# Hybrid and inorganic plumbo-halide perovskites for solar cells

by **Silvia Mariotti**

Department of Physics

Stephenson Institute for Renewable Energy


Thesis submitted in accordance with the requirements of the

University of Liverpool for the degree of Doctor in Philosophy

January 2019

# Abstract

This thesis explores the hybrid and inorganic lead halide perovskite compounds methylammonium lead iodide (MAPI) and caesium lead iodide-bromide ($CsPbI_2Br$) with regard to their synthesis, stability and use in thin film solar photovoltaic devices.

MAPI thin films were prepared using two different approaches: the one-step and the two-step solution processes to determine which gives better films, in terms of physical-chemical properties, environmental stability and device performance. The best device efficiency obtained by devices prepared with MAPI (glass/ITO/$TiO_2$/MAPI/spiro-OMeTAD/Au) was of 11.8% *PCE*, however the device stability toward environmental conditions was poor, showing degradation effects in environments containing UV light combined with oxygen. In order to circumvent the instability issue, the fully inorganic $CsPbI_2Br$ compound was studied for direct comparison, as an alternative, more stable perovskite compound. Once the synthesis of $CsPbI_2Br$ thin films was optimised, devices were fabricated (glass/ITO/$TiO_2$/$CsPbI_2Br$/spiro-OMeTAD/Au) and measured, giving a champion device *PCE* of 9.1%. However, while the $CsPbI_2Br$ devices were found to present higher environmental stability compared to MAPI devices, they showed high susceptibility towards humid conditions. Unlike MAPI, however, the degradation of $CsPbI_2Br$ was caused by phase instability, rather than chemical degradation, which was demonstrated to be reversible.

Most devices in this work were fabricated using a superstrate *n-i-p* device architecture commonly used for perovskite solar cells. In addition, a new device structure was created, with the aim of forming a heterojunction between MAPI and silicon. First the device structure was studied (contact/Si/MAPI/transporting material/contact) using both *n*- and *p*-doped silicon wafers, to determining the ideal Ohmic contacts, the nature of MAPI deposited onto silicon and by understanding the electrical behaviours of each interface. Solar cells of this type produced efficiencies up to 2.1% *PCE*. It was demonstrated that these Si/MAPI heterojunction devices form a single-sided junction in the silicon. Recommendations for improvement are given.

# Acknowledgements

First, I would like to thank the Centre of Doctoral Training in New and Sustainable Photovoltaics (CDT-PV) and EPSRC for the opportunity and the funding.
My gratitude goes to my supervisor, Prof. Ken Durose, for the guidance given me during these years, the keenness to correct this thesis, and the help in accomplishing this challenging, life-changing step in the kindest way possible.
I would like to thank my amazing research group, from whom I gained a great amount of knowledge, for their kindness and willingness to help, in particular my second supervisor Dr. Jon Major, Dr. Asim Mumtaz, Dr. Laurie Phillips, Dr. Oliver S. Hutter, Dr. Mohammed Al Turkestani, Dr. Georgios Papageorgiou, Dr. Annette Pressman, Dr. Enzo Peccerillo, Dr. Isabel Vázquez Fernández, Peter Yates, Tom Baines, Jack Swallow, Tom Shalvey, Theo Hobson and Huw Shiel. Particular thanks to Laurie for introducing me to the PV and the perovskite world in my first year, to Oliver for taking the trouble to help me by checking this thesis, the papers and for making the multiple SEM and DSC measurements, and Mohammed for giving me directions in the experimental challenges encountered for one particular chapter of this Thesis and for his perseverance on trying to give a kick to my self-confidence. My special thanks go to “the office guys” (Tom, Pete, Jack, Tom and Huw) with whom I’ve spent loads of time (maybe too much) chatting and laughing, and to my great friends Georgios, Oliver, Enzo for the multiple coffee/tea breaks; thanks to you all for singing with me in the lab and making normal days memorable moments. Thanks to Gloria the Glovebox, my life partner in these 4 years, for creating the perfect atmosphere in the lab!
My heartfelt thanks to Gaia and Stefano, for listening to my multiple complains and for trying to bring me to my senses during the (numerous) moaning moods, having long discussions, laughs, coffees, long shopping sessions, wine, beer and loads of great food! I couldn’t have survived this PhD without you! Many thanks to Isabel, Claudia, Charlotte, Ebe, Marios, Mar, Paula, Maria and all the Stephenson colleagues for being always nice and bringing back a smile on my face when needed.. but also for the numerus pints at the pub and the great times! Thanks to the CDT-PV friends Pete, Lana, Giacomo, James, Giulio and Mike for making me survive the 14 weeks travelling the UK and for the great (and crazy) moments spent at showcases and conferences together.

I would also like to thank the great friends who I have met during my stay in Liverpool, in particular Michela, Danilo, Aitor, Sara, Luca, Giulia, Diego, Emma, Federica, Tommaso, Clara, Riccardo, Caitlin, Ilaria, Luigi and all the other amazing people I have met during these years in the UK, who gave me strength and made this stay unforgettable.
Last but not least, I would like to thank my old friends too, who, no matter the distance, kept being supportive and beloved friends, in particular Lucia and Nicole who always encouraged me and gave me the energy to carry on, my "Bologna" friends Grazia, Paddo, Santa, Nicola, Agnese, Francesca, Sara, Ruggero, Carlotta, Chiara, Valerio and Martina, with whom I've spent spectacular moments during the last years, and my hometown friends, in particular Veronica, Molly, Max, Teo, Marco, Camilla, Topo, Elisa, Alessandro, Pietro, Silvia, Mik and Ruzze, who made me always feel welcome, like no time has passed, when I was going back home.
I am particularly grateful to the most important women of my life, my mom, sister and grandma, for being *always* on my side, for supporting me even during my stressed moods and for spoiling me shamelessly. Warm thanks also to the "acquired" relatives, in particular Beppe, Pier and Cristina, who nevertheless became family.
Finally, thanks to my grandpa, who thankfully passed on his love for science and whose wisdom has always been a great example for me, and to my father, who has always believed in my potential. I wish they would be proud of me.

# Table of Contents

# Declaration

All the measurements in this thesis have been performed by the author, apart from:

1. SEM pictures by Dr. Oliver S. Hutter and Peter J. Yates from the Department of Physics in the Engineering Department, University of Liverpool;
2. DSC-TGA by Dr. Oliver S. Hutter from the Department of Physics in the Stephenson Institute for Renewable Energy, University of Liverpool;
3. STM by Biswajit Kundu, Department of Solid State Physics, Indian Association for the Cultivation of Science, Jadavpur, Kolkata, India;
4. XPS by Jack Swallow and Dr. Vinod R. Dhanak, Stephenson Institute for Renewable Energy, Department of Physics, University of Liverpool

# 1. Introduction

During the industrial revolution an increasing energy resources supply was needed to support the rapid economic growth, which lead to a more common use of coal and oil. Hence, during the 19$^{th}$ century, the so called Oil Age, refinement techniques and engines working with gasoline were developed.[1] Since then, huge environmental impact derived from the fossil fuel consumption for energy production. Large changes to the environment have been recorded producing threats to the stability and safety of the environment in which we live. In particular the emission of carbon dioxide ($CO_2$), a greenhouse gas, results in a rise of the temperature and hence climate change.[2] The rapid consumption of the limited fossil fuel sources (due to the population growth) and the significant changes of the environmental conditions, which may be not reversible, demonstrate the urgent need of new, sustainable, clean energy resources.

In 1997 a first important step was taken by 192 countries (EU included) who signed the Kyoto protocol,[3] with the aim of reducing the greenhouse gases. Further progress followed with the adoption by 195 countries to the Paris agreement in 2015,[4] which aims to

limit the global warming well below 2°C on average before the end of this century, reducing the impacts of climate change. In addition, the governments agreed to meet every 5 years to plan more ambitious targets. In 2016, 86% of the EU power installations were based on renewable technologies and in 2018 an even larger global investment in renewable power was observed in particular from China, Europe and United States.[5] Although the use of renewable energies has shown its largest annual increase in 2018, these technologies are not advancing quickly enough to meet the world energy needs caused by a global economic growth.[5] In addition, issues are still encountered in terms of energy system integration, political will and technology energy efficiency.[5]

Nevertheless, renewable energy systems have grown rapidly in recent years, mainly due to the important cost reduction, in particular in the solar photovoltaic (PV) and wind power fields.[6] PV has shown to be the most important contributing technology for the development of efficient renewable energy systems. Its main potential is given by the presence of a continuous and reliable solar irradiation: in 2010 it was estimated that the total annual solar irradiation potential amounts to 6000 times the global energy consumption per annum (~12,000 million tons of oil equivalent), which is of an order of magnitude greater compared to all non-renewable energy sources.[7] Furthermore, PV manufacturing is scalable and PV itself may be used from portable or domestic applications to large solar parks, which require minimal maintenance and guarantee 90% of their efficiency over 25 years.[8] There are numerous technologies for solar PV, however the most influential material in the market is silicon, accounting 95% of the total PV production in 2017.[9] Silicon is generally used in both crystalline (c-Si) and multicrystalline (poly-Si) forms, however the crystalline wafers produce the highest efficiencies, achieving up to 26.1%.[10,11] Although silicon is abundant in Earth's crust (in the form of quartzite) it shows limitations, such as the expensive fabrication processes (in particular for purification) and physical-chemical issues (indirect band gap and

low absorption coefficient). Therefore, new technologies have emerged, including thin film technologies. Some of these have matched or exceeded silicon's device performance but do not necessarily match silicon in terms of stability and warranty for such long periods (25 years). The thin film technologies that have produced major interest, hence those that were used for module production and commercialisation, are the chalcogenides cadmium telluride (CdTe) and copper indium gallium (di)selenide (CIGS) compounds, which achieved high lab efficiencies, being 22.1% and 22.9% for CdTe and CIGS respectively.[10,11] Fig. 1.1 shows the record efficiencies of the main PV technologies that have emerged and developed in the last 42 years. Among the emerging materials for PV technologies, perovskite materials have shown astonishing achievements from their first application in PV (2009):[12] in less than ten years these materials have achieved a record certified efficiency of 23.3% (Fig. 1.1), achieving device performances that are very close of those accomplished by the CdTe and CIGS.[13] Perovskite materials show low cost processes and exceptional physical-chemical properties: they have high absorption coefficients, direct and, very importantly, easily tunable band gaps.[14,15] This specific property allows the creation of perovskite materials with a large range of band gaps which can be used for tandem solar cells applications,[16] thus these materials are appealing for alternative photovoltaic technologies. However, perovskite materials present substantial issues, such as instability to environmental conditions, toxicity (as most of the perovskite materials for PV applications contain lead) and electrical hysteresis.[17] Numerous research groups are focussing on solving these issues.[18] In particular, the stability and hysteresis issues have shown great improvement by using multication mixed halide perovskite materials,[19] and it was shown that lead may be replaced with tin for the production of environmental friendly materials, with fewer issues related to disposal and/or recycling processes.[13] The main aim of the perovskite research community is

therefore to fulfil the "golden triangle" of the solar cell technology, this being cost, efficiency and stability properties for the fast commercialisation of the product.[20]

As perovskite materials are the subject of this Thesis, more information is presented in the review in chapter 3, whereas chapter 2 introduces the reader to the main concepts of the basic theory of solar cells and chapter 4 describes the main techniques used for the synthesis and characterisation of perovskite thin films and solar cell devices. chapter 5 presents studies on the main causes of degradation of methylammonium lead iodide (MAPI, the first perovskite material to be studied in PV), since, as mentioned above, perovskite materials showed high degradation rates and are not able to achieve commercial standards.[21] Furthermore, since the presence of organic compounds in MAPI's crystal structure has shown to contribute to the material's instability,[22] the synthesis of a fully-inorganic perovskites, $CsPbI_2Br$, was performed with the aim of synthesising a stable perovskite solar cell. The stability of this material and its devices were studied using the same experimental protocols as for MAPI, allowing a direct comparison of the underlying degradation processes to be made. This study is presented in chapter 6. Chapter 7 presents work performed on the fabrication of a new perovskite device architecture, not known in the literature. Recently, silicon was used in the fabrication of tandem solar cells with perovskite materials,[23] however it is shown in this Thesis that it is possible to form a direct heterojunction between MAPI and silicon.

Result chapters 5, 6 and 7 are followed by overall discussions and conclusions in chapters 8 and 9.

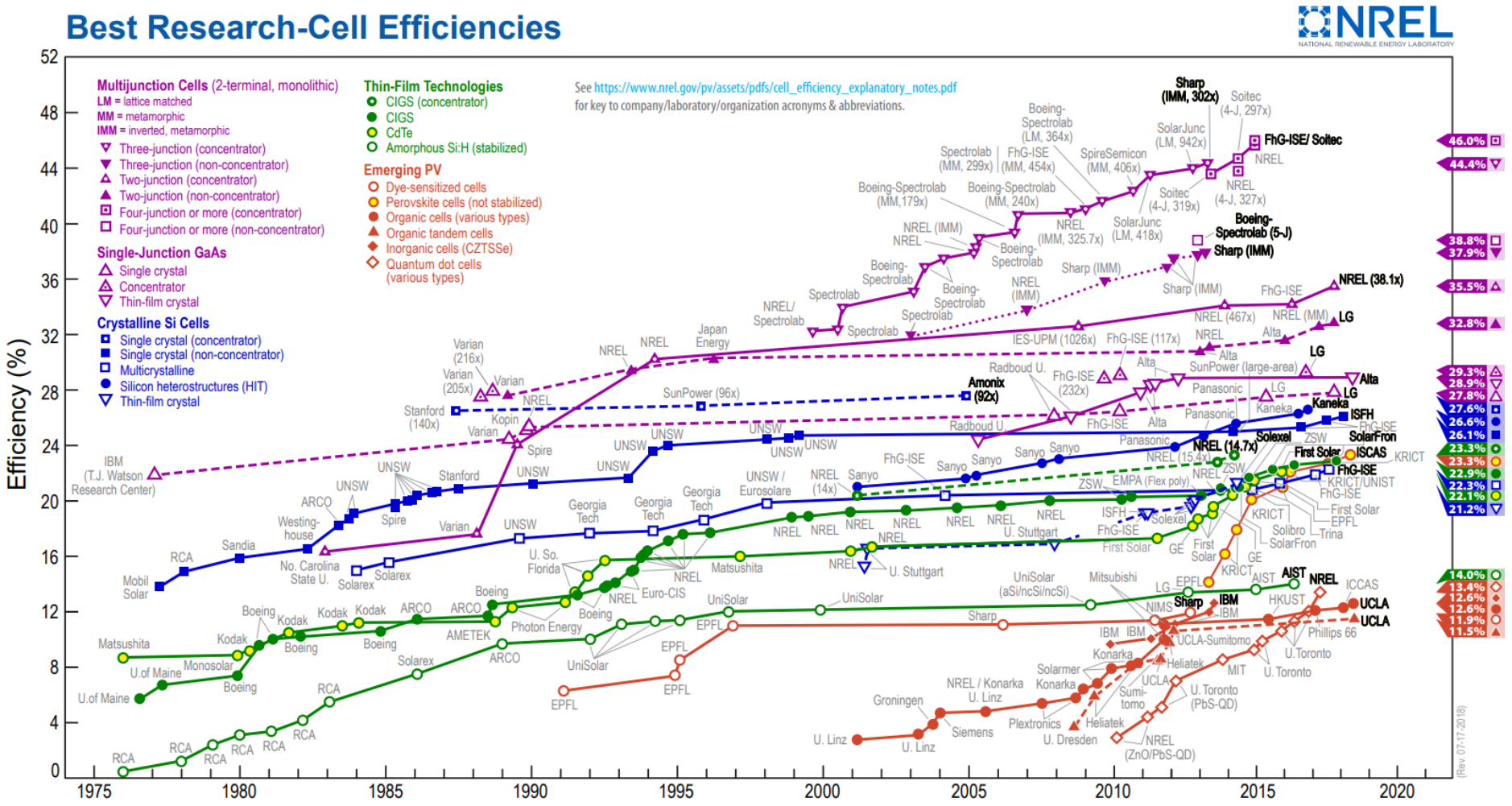


**Fig. 1.1.** NREL efficiency chart (2018), showing the certified efficiencies achieved by the most important PV technologies. This plot is courtesy of the National Renewable Energy Laboratory, Golden, CO.[11]

## 1.1 References


(1) Maugeri, L. *The Age of Oil: The Mythology, History, and Future of the World's Most Controversial Resource*; Lyons Press, 2006.

(2) Internation Energy Agency, I. E. A. Climate Change http://www.iea.org/topics/climatechange/ (accessed Sep 6, 2018).

(3) UN. *Kyoto Protocol To the United Nations Framework Kyoto Protocol To the United Nations Framework*; 1998; Vol. 7.

(4) Framework Convention on Climate Change. Paris Agreement. United Nations Treaty Collection https://ec.europa.eu/clima/policies/international/negotiations/paris_en (accessed Aug 7, 2018).

(5) Renewables Global Status Report REN21 http://www.ren21.net/status-of-renewables/global-status-report/ (accessed Aug 7, 2018).

(6) Internation Energy Agency, I. E. A. *Renewables*; 2017.

(7) Tress, W. *Organic Solar Cells: Theory, Experiment, and Device Simulation*; Springer, Ed.; 2014.

(8) The Renewable Energy Hub. Solar Panel Warranty, Insurance and Maintenance - The Renewable Energy Hub https://www.renewableenergyhub.co.uk/solar-panels/solar-panel-warranty-insurance-maintenance.html (accessed Aug 7, 2018).

(9) Fraunhofer, I. S. E. Photovoltaics Report. *Fraunhofer Inst. Sol. Energy Syst. www. ise. fraunhofer. de/mwginternal/de5fs23hu73ds/progress* **2018**, 45.

(10) Green, M. A.; Hishikawa, Y.; Warta, W.; Dunlop, E. D.; Levi, D. H.; Hohl-Ebinger, J.; Ho-Baillie, A. W. H. Solar Cell Efficiency Tables (Version 50). *Prog. Photovoltaics Res. Appl.* **2017**, *25* (7), 668–676.

(11) NREL. Efficiency chart https://www.nrel.gov/pv/assets/images/efficiency-chart.png (accessed Feb 12, 2018).

(12) Kojima, A.; Teshima, K.; Shirai, Y.; Miyasaka, T. Organometal Halide Perovskites as Visible-Light Sensitizers for Photovoltaic Cells. *J. Am. Chem. Soc.* **2009**, *131* (17), 6050–6051.

(13) Konstantakou, M.; Stergiopoulos, T. A Critical Review on Tin Halide Perovskite Solar Cells. *J. Mater. Chem. A* **2017**, *5* (23), 11518–11549.

(14) Hao, F.; Stoumpos, C. C.; Chang, R. P. H.; Kanatzidis, M. G. Anomalous Band Gap Behavior in Mixed Sn and Pb Perovskites Enables Broadening of Absorption Spectrum in Solar Cells. *J. Am. Chem. Soc.* **2014**, *136* (22), 8094–8099.

(15) Noh, J. H.; Im, S. H.; Heo, J. H.; Mandal, T. N.; Seok, S. Il. Chemical Management for Colorful, Efficient, and Stable Inorganic-Organic Hybrid Nanostructured Solar

Cells. *Nano Lett.* **2013**, *13* (4), 1764–1769.

(16) Sutton, R. J.; Eperon, G. E.; Miranda, L.; Parrott, E. S.; Kamino, B. A.; Patel, J. B.; Hörantner, M. T.; Johnston, M. B.; Haghighirad, A. A.; Moore, D. T.; Snaith, H. J. Bandgap-Tunable Cesium Lead Halide Perovskites with High Thermal Stability for Efficient Solar Cells. *Adv. Energy Mater.* **2016**, *6*, 150258–150464.

(17) Green, M. A.; Ho-Baillie, A.; Snaith, H. J. The Emergence of Perovskite Solar Cells. *Nat. Photonics* **2014**, *8* (7), 506–514.

(18) Ansari, M. I. H.; Qurashi, A.; Nazeeruddin, M. K. Frontiers, Opportunities, and Challenges in Perovskite Solar Cells: A Critical Review. *J. Photochem. Photobiol. C Photochem. Rev.* **2018**, *35*, 1–24.

(19) Grätzel, M. The Rise of Highly Efficient and Stable Perovskite Solar Cells. *Acc. Chem. Res.* **2017**, *50* (3), 487–491.

(20) Docampo, P.; Ball, J. M.; Darwich, M.; Eperon, G. E.; Snaith, H. J. Efficient Organometal Trihalide Perovskite Planar-Heterojunction Solar Cells on Flexible Polymer Substrates. *Nat. Commun.* **2013**, *4*, 2761.

(21) Grätzel, M. The Light and Shade of Perovskite Solar Cells. *Nat. Mater.* **2014**, *13* (9), 838–842.

(22) Conings, B.; Drijkoningen, J.; Gauquelin, N.; Babayigit, A.; D'Haen, J.; D'Olieslaeger, L.; Ethirajan, A.; Verbeeck, J.; Manca, J.; Mosconi, E.; Angelis, F. De; Boyen, H.-G. Intrinsic Thermal Instability of Methylammonium Lead Trihalide Perovskite. *Adv. Energy Mater.* **2015**, *5* (15), 1500477–1500485.

(23) Werner, J.; Niesen, B.; Ballif, C. Perovskite/Silicon Tandem Solar Cells: Marriage of Convenience or True Love Story? – An Overview. *Adv. Mater. Interfaces* **2018**, *5* (1), 1700731–1700750.

# 2.Physics of semiconductors and solar cells

This chapter presents the main concepts of semiconductors, their junctions and the characteristics of solar cells with the emphasis being on the concepts most closely related to the work in this Thesis. However, the basic concepts of semiconductor physics and solar photovoltaic cells are the subject of book-length reviews to which the reader is referred for further information (ref.[1–4]).

## 2.1. Fundamentals of semiconductor materials

In a bulk solid the electron energy states form bands. The valence band is fully occupied by electrons. Above the Fermi level electron states are unoccupied (at 0K). In a semiconductor, above the Fermi level, there is a conduction band which may be considered to be either empty or else partially occupied by electrons which are free to move. In the case of metals, the valence and conduction bands overlap, hence electrons move freely and conduction is high. In the case of insulators there is a wide gap between the valence and

conduction bands, hence electrons cannot reach the conduction band by thermal promotion and hence conduction is low. In the case of semiconductors, the band gap between valence and conduction bands is in an intermediate range being from 0.5 – 4 eV,[4] and hence conductivity may arise from thermal promotion (in the case of intrinsic semiconductors) or more importantly from doping.

Semiconductors are classified according to their band gap, as direct and indirect semiconductors. This depends on the crystal momentum (k-vector) in the Brillouin zone: if the k-vectors of valence and conduction bands are similar the band gap is called “direct”, whereas if these are different the band gap is “indirect”. This is explained in the schematic shown in Fig. 2.1. The indirect band gap is disadvantageous for semiconductors in PV, since an electron needs both energy and momentum to favour the transition to the conduction band. This effect produces poor photon absorption of the semiconductor (since photons cannot carry crystal momentum) and hence indirect semiconductors require thick films to absorb enough light for the solar cell to work. For this reason, silicon for PV applications is thick (100 – 500 μm) whereas thin film technologies are usually less than 1 μm thick since they use direct semiconductor materials.

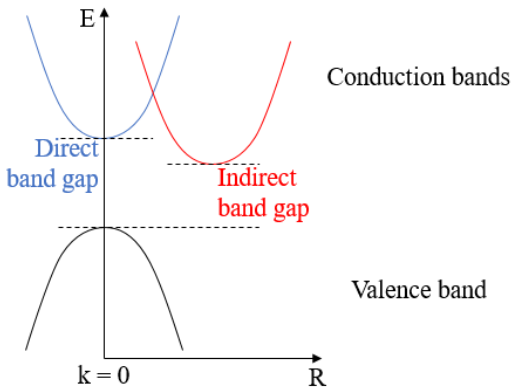


**Fig. 2.1.** Schematic showing the difference in direct and indirect band gaps in semiconductors.

The conductivity of semiconductors may be changed by doping the material with impurities. According to the nature of the impurities, *n*-type doping (negative doping, when additional electrons are introduced) or *p*-type doping (positive doping, when impurities containing a reduced number of electrons are introduced) exist. While for intrinsic semiconductors the number of holes (*p*) and electrons (*n*) at thermal equilibrium is identical, in the case of *n*-doped semiconductors, the number of electrons at thermal equilibrium is approximately equal to the donor concentration ($N_D$, $cm^{-3}$) and similarly for *p*-doped semiconductors, the number of holes is approximately equal to the acceptor concentration ($N_A$, $cm^{-3}$). The doping levels influence the Fermi level position, by shifting this closer to the conduction band in the case of *n*-doped semiconductors and closer to the valence band in the case of *p*-doped semiconductors, with the shift being dependent to the doping concentration.

### 2.1.1. *p-n* junctions

A *p-n* junction comprises neighbouring semiconductors with different doping. The *p-n* junction may be classified as a homojunction and a heterojunction according to the semiconductors used. These are described in the following subsections. *p-n* junctions are used in numerous devices, such as diodes and solar cells, having the electrical symbol shown in Fig. 2.2. The arrow in the diagrams indicate that current flows from the anode to the cathode, but not in the opposite direction.

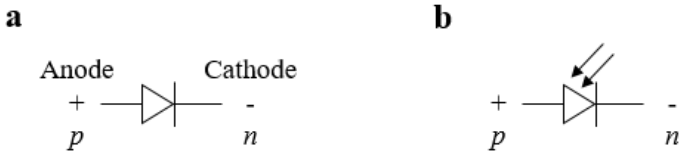


**Fig. 2.2.** Schematic of electrical symbols for a) diode and b) photodiode.

*a) The homojunction*

The homojunction is formed when *n*-doped and *p*-doped regions are made of the same semiconductor, as shown in Fig. 2.3. The electron and hole concentration gradients in the two doped regions induce electrons to diffuse from the *n*-region to the *p*-region, and holes to diffuse from the *p*-region toward the *n*-region (Fig. 2.3, middle). A region depleted of free charge particles is formed, leaving behind the ionised impurities from which the electrons and holes come from, these being negative in the *p*-doped semiconductor and positive in the *n*-doped semiconductor. This field opposes the diffusion and is called the depletion region, characterised by a depletion width (*W*), which is given by Equation 2.1.

$$W = w_n + w_p = \sqrt{\frac{2\varepsilon_S}{\mathrm{e}}\left(\frac{N_A+N_D}{N_A N_D}\right)V_{bi}} \tag{2.1}$$

where: $\varepsilon_S$ = permittivity of the semiconductor, e is the electron charge, $N_A$ and $N_D$ are the doping concentrations of the acceptor and donor respectively, and $V_{bi}$ is the built in voltage.

The depletion region creates an electric field, which is associated with an electron potential, called the built in voltage ($V_{bi}$), which acts as a barrier to prevent the displacement of electrons and holes. The electric field opposes the diffusion current until it reaches equilibrium (diffusion current equals the drift current), which determines the alignment of the Fermi level (Fig. 2.3, bottom).

The $V_{bi}$ is calculated by subtracting the work functions of the *n*-doped ($\Phi_n$) and the *p*-doped regions ($\Phi_p$). Its value however, may be increased or decreased by applying a reverse or a forward external voltage. A large $V_{bi}$ prevents the electron/hole diffusion, hence it produces negligible current, whereas when the potential barrier is lowered the current increases.

An alternative method for the calculation of $V_{bi}$ is presented in Equation 2.2 and considers the carrier concentrations in equilibrium, rather than the work functions.

$$V_{bi} = \frac{k_B T}{e} \ln\left(\frac{N_a N_d}{n_i^2}\right) \quad (2.2)$$

where: $k_B$ = Boltzmann's constant, $T$ is the temperature, and $n_i$ is the intrinsic carrier concentration.

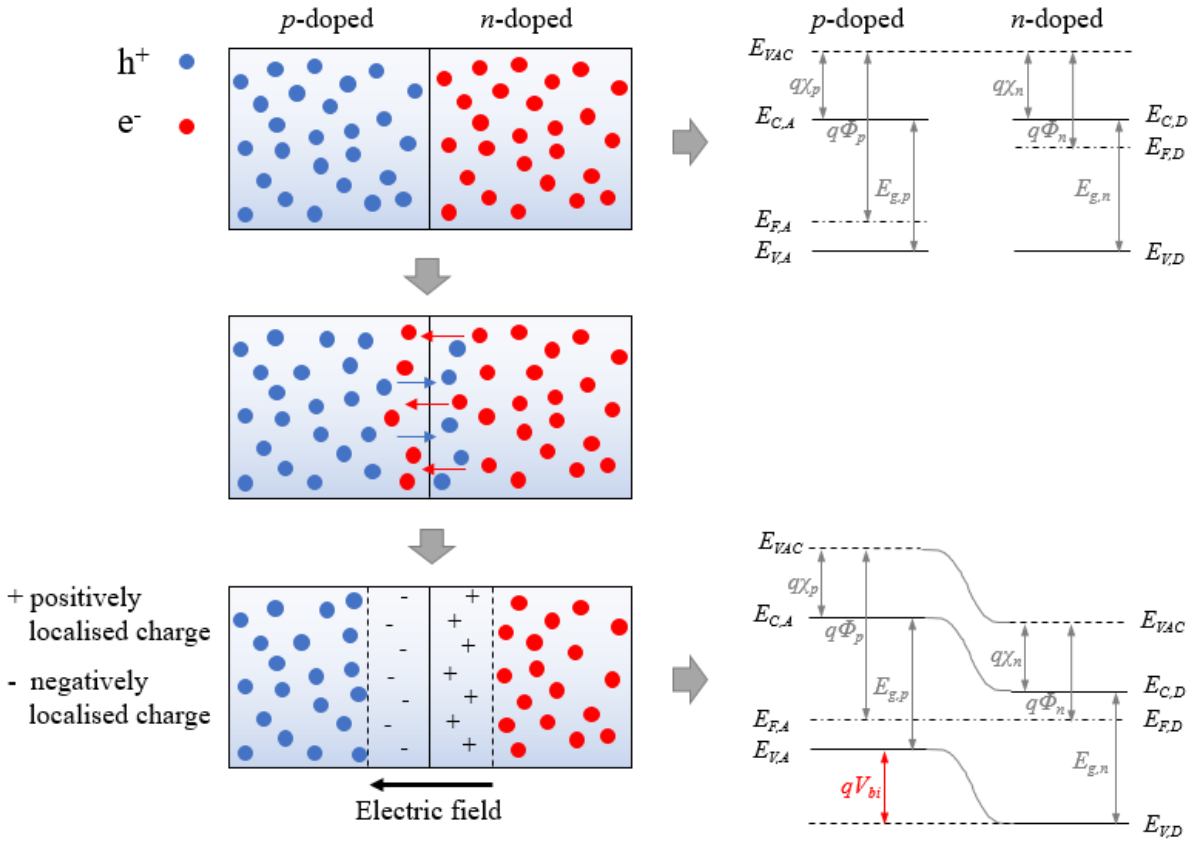


**Fig. 2.3.** Schematic of a *p*-*n* homojunction showing, from top to bottom (left side), *p*- and *n*-doped semiconductors after approach, holes and electron diffusion, formation of the depletion region with the electric field. The schematics are accompanied by the band diagrams of the homojunction (right side), showing the initial state where vacuum levels of *p*-doped (acceptor, *A*) and *n*-doped (donor, *D*) materials are aligned (top right), and the equilibrium state, where the Fermi levels are aligned (bottom right). Here, the built in potential of the depletion region is shown ($qV_{bi}$), which intensity may vary by an applied external voltage. $\chi$ is the electron affinity, $\Phi$ is the work function, $E_F$ is the Fermi level, $E_g$ is the band gap, $E_C$ is the conduction band and $E_V$ is the valence band.

*b) The heterojunction*

A *p*-*n* junction may be formed by different semiconductor materials (*i.e.* different band gaps). Due to the difference of the band gaps, a discontinuity in the conduction between valence and conduction bands is established. Hence, the band alignment is dependent on the

differences in electron affinity and work function of these materials, and form potential steps that may act as barriers, that can lead to recombination sites in the junction. These barriers are strictly related to the difference in the electron affinities and work functions of the semiconductors involved in the junction and they may be described as “spikes” or “cliffs” in the band line-up, as shown in Fig. 2.4a.

### 2.1.2. *p-i-n* junctions

A variant of the *p-n* junction is the *p-i-n* junction which contains an intrinsic (*i*) or undoped material, sandwiched between the *p*- and the *n*-doped semiconductors.

Compared to a *p-n* junction, the depletion region width is larger in the *p-i-n* junction. The intrinsic material may also act as the absorber material in a solar cell, where the photo-generation of carriers occurs. These carriers ideally have long carrier diffusion lengths, as they must be transported through the doped materials to reach the contacts. The *p*- and *n*-doped regions contribute to the solar cell functioning by forming the electric field required for the carrier diffusion.

Also *p-i-n* junctions may comprise homojunction and heterojunctions. An example of homo- *p-i-n* junction is shown in the diagram in Fig. 2.4b.

The *p-i-n* junction presents some disadvantages, such as:

- The intrinsic “*i*” region has lower conductivity compared to the *p*- and *n*-regions, which may determine the series resistance in the device;
- Recombination processes between electrons and holes may occur in the “*i*” region;
- The presence of impurities in the “*i*” region may cause the electric field to break down.

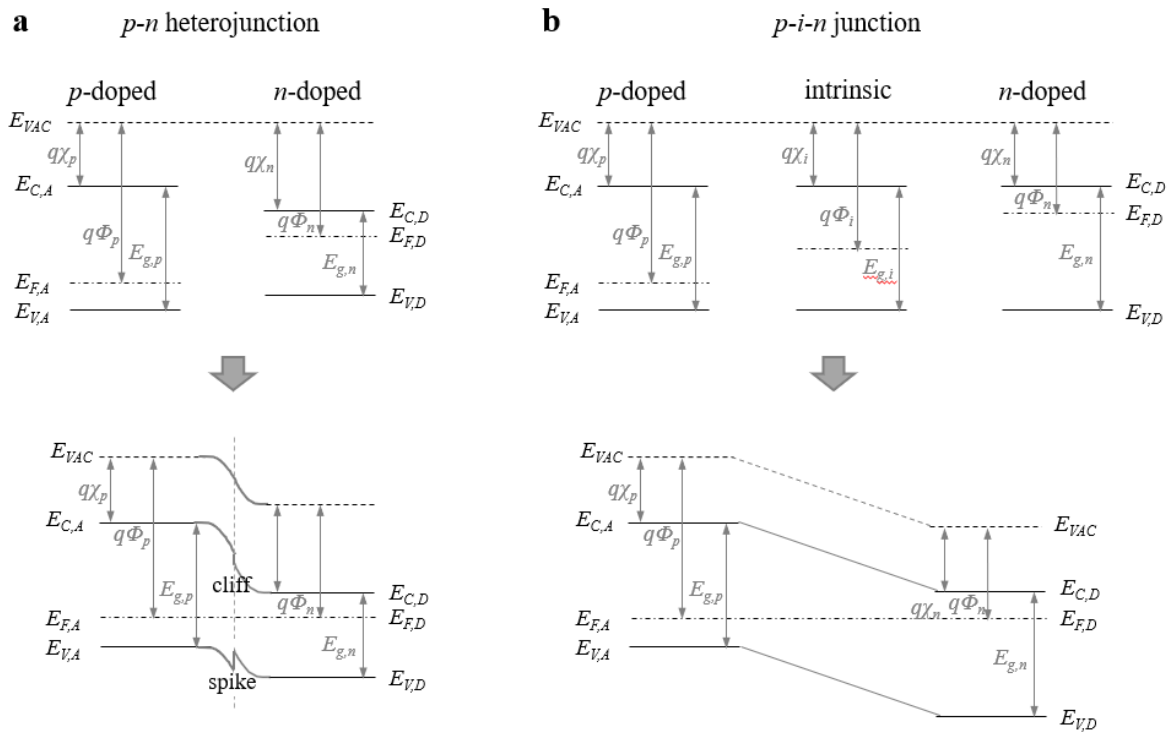


**Fig. 2.4.** Schematic of a) *p-n* heterojunction and b) *p-i-n* junction (homojunction) showing, the isolated bands (top) and the bands in equilibrium (bottom). The alignment of the Fermi level in the *p-n* heterojunction (a) produces a cliff between the conduction bands and a spike between the valence bands of the two semiconductors.

### 2.1.3. The Schottky junction

Metal-semiconductor contacts may form Ohmic contacts (non-rectifying junction, having a linear current - voltage behaviour), or a Schottky junction. The type of junction that is formed depends on the work functions of the metal and the semiconductor considered. An example of a common Schottky junction is the one between *p*-CdTe and most metals, since the electron affinity of CdTe is very large (producing a large work function of ~5.9 eV) and greater compared to that of any metal.[1] Hence, in the case of a *p*-semiconductor, a surface barrier (Schottky junction) is formed when $\Phi_{metal} < \Phi_p$, and vice versa for *n*-doped semiconductors $\Phi_{metal} > \Phi_n$, as shown in Fig. 2.5.

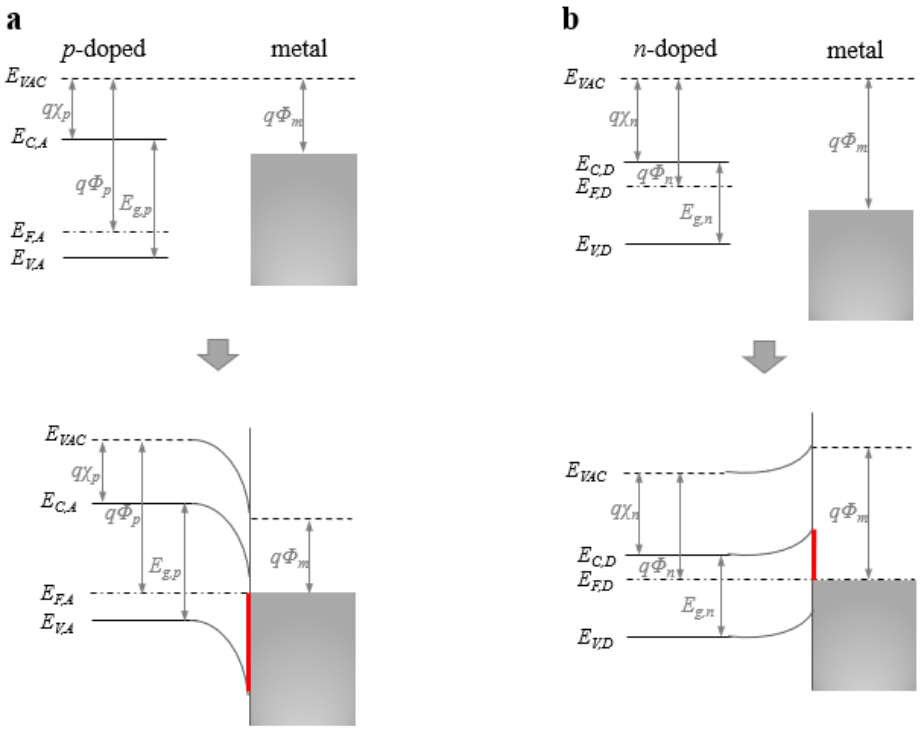


**Fig. 2.5.** Schematic of a Schottky junction formed between a) a *p*-doped semiconductor and a metal, and b) an *n*-doped semiconductor and a metal. The Schottky barriers are shown in red.

## 2.2. Fundamental of solar cells

### 2.2.1. Solar radiation

The energy generated by the Sun's nuclear fusion reactions, is emitted and reaches Earth with an intensity of 1353 W/m$^2$ in free space. This is attenuated by absorption and scattering caused by the atmosphere and is dependent on the latitude considered on Earth. The evaluation of solar cell devices has been therefore standardised using the AM1.5 irradiance spectrum, shown in Fig. 2.6, which corresponds to an irradiance of ~1000 W/m$^2$ (after atmosphere attenuation) with a tilt of 37° compared to the equator.

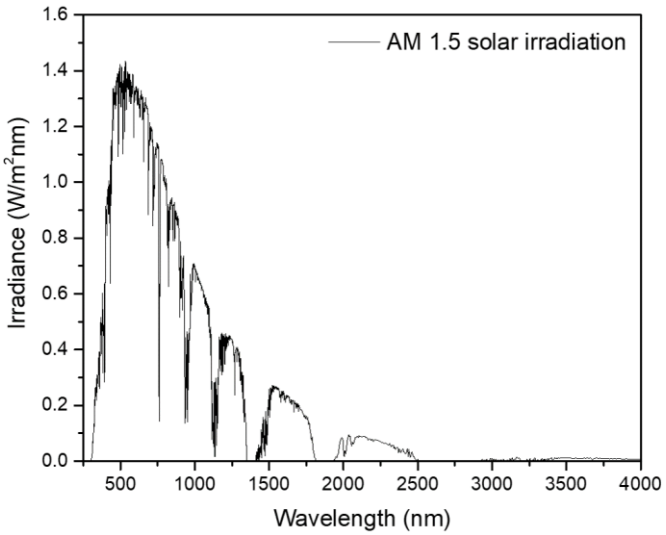


**Fig. 2.6.** Solar spectrum irradiance at Air Mass 1.5, plotted using the ASTM G137-03 reference spectra.[5]

The highest irradiance occurs in the visible range with a peak at ~500 nm, whereas at low wavelengths (< 300 nm) absorption is caused by oxygen, ozone and nitrogen and at high wavelengths in the infrared region, absorption is caused by water and carbon dioxide molecules. It is these absorptions that cause the attenuation of the radiation, and determine the 'air mass' (AM) factor. For this reason, outside the atmosphere the solar radiation is called AM0, which is used for space applications.

### 2.2.2. The photovoltaic effect

The photovoltaic effect is the phenomenon that converts light into electrical energy. A photon is absorbed by a medium and generates an electron/hole pair. It differs from the photoelectric effect in which an electron is ejected out of the material into the vacuum, whereas in the photovoltaic effect the electron is excited from the valence band to the conduction band of a semiconductors. The photon is absorbed in the material only if the photon energy $h\nu \geq E_g$. Photo-excited electrons with $h\nu > E_g$, quickly relax to the conduction

band and lose their surplus energy by thermalisation. On the contrary, photons with h$\nu < E_g$ are not absorbed and are therefore transmitted by the material.

In a solar cell, after light absorption, the generated electron/hole pair must reach the depletion region in order to avoid recombination. Due to the presence of the electric field, these $e^-/h^+$ pairs are separated and drift: the electrons toward the *n*-part and the holes toward the *p*-part of the diode. By connecting the device to an external circuit, the electron flow will produce electric current.

### 2.2.3. Current-Voltage *I-V* characteristics

*a) Equivalent circuit of a solar cell*

The equivalent circuit of a single junction solar cell is shown in Fig. 2.7 and it considers an ideal (a) and a real solar cell model (b). Under dark conditions a *p-n* junction can be described using a single diode model, which current – voltage (*I* – *V*) response is given by the Shockley equation. The Shockley equation (Eq. 2.3) describes the density current (*I*/area = *J*) in an ideal diode.

$$J = J_0 \left( e^{\frac{eV}{nk_BT}} - 1 \right) \tag{2.3}$$

where: $J_0$ is the reverse saturation current, *V* is the voltage across the diode and *n* is the diode ideality factor, a parameter which indicates how close the diode follows the ideal diode equation. The ideality factor is strictly related to the quality of the solar cell material and the recombination processes, and has typical values between 1 and 2.

In the case of a solar cell however, the diode is connected in parallel to a current source (light) and hence the *J-V* response is:

$$J = J_0 \left( e^{\frac{eV}{nk_BT}} - 1 \right) - J_L \tag{2.4}$$

where: $J_L$ is the photocurrent.

Real solar cells however, are affected by both shunt ($R_{SH}$) and series ($R_S$) resistances (Fig. 2.7b), which must be taken into consideration in the *J-V* response. Hence, Equation 2.5 should be considered:

$$J = J_0\left(e^{\frac{e(V-AJR_S)}{nk_BT}} - 1\right) - J_L + \frac{V-AJR_S}{R_{SH}} \quad (2.5)$$

where: *A* is the area of the solar cell and $[(V\text{-}AJR_S)/R_{SH}] = J_{SH}$. The resistances act in series ($R_S$) and in parallel ($R_{SH}$) with the cell, as shown in Fig. 2.7b.

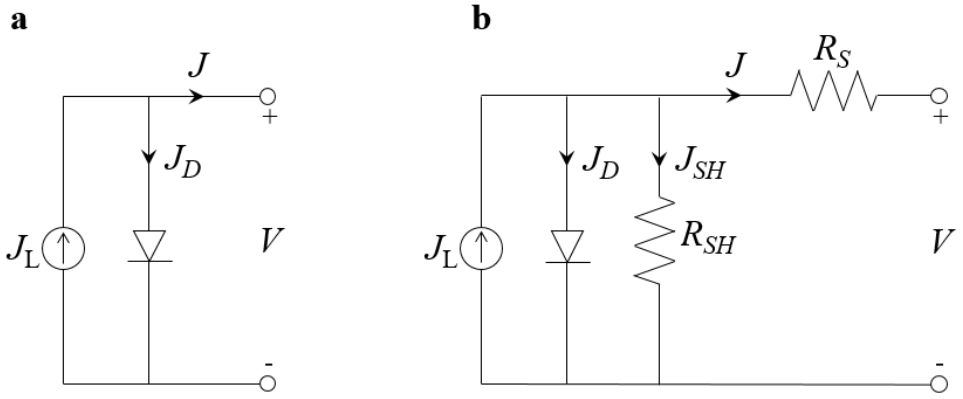


**Fig. 2.7.** Equivalent circuit of a) an ideal cell and b) a real (non-ideal) solar cell. Both are formed by a diode ($J_D$) and a current generator ($J_L$), however the real solar cell contains parasitic series and shunt resistances ($R_S$ and $R_{SH}$).

*b) Solar cell parameters*

The main PV characterisation is performed by illuminated (AM1.5) *J-V* analysis, which provides a characteristic curve (*J-V* curve) from which the short circuit current ($J_{SC}$), open circuit voltage ($V_{OC}$), and the fill factor (*FF*) are extracted. These values are important as from these it is possible to measure the power conversion efficiency (*PCE* or $\eta$) of the solar cell.

A typical *J-V* curve is shown in Fig. 2.8, which shows the main parameters of a solar cell measured in the dark and under illumination. The main parameters for the illuminated *J-V* curve are described as follows:

- $J_{SC}$ is the current density flowing in the external circuit when the voltage is zero (short circuited solar cell). In an ideal solar cell $J_{SC} = J_L$;

- $V_{OC}$ is the open circuit voltage and it corresponds to the maximum voltage available for the solar cell, at which no current can flow ($J$ = 0). The $V_{OC}$ is expressed as follows:

$$V_{OC} = \frac{k_B T n}{e} \ln\left(\frac{J_L}{J_0} + 1\right) \quad (2.6)$$

- *MPP* is the maximum power point, and it corresponds to the maximum power output of the device ($P_m = J_{MPP} \cdot V_{MPP}$);
- *FF* is the fill factor. This parameter defines the 'squareness' of the *J-V* curve and corresponds to the ratio of the maximum power density ($P_m$ at *MPP*) and the $V_{OC} \cdot J_{SC}$ product, as shown in Eq. 2.7. Typical *FF* values range between 40% and 80%.

$$FF = \frac{J_{MPP} V_{MPP}}{J_{SC} V_{OC}} \quad (2.7)$$

- *PCE* is the power conversion efficiency and it is defined as the ratio of the generated power and the input power ($P_{in}$ at AM1.5 = 1000 W/m$^2$) and it is therefore calculated as follows:

$$PCE\ (\%) = \frac{P_{out}}{P_{in}} \cdot 100 = \frac{J_{SC} V_{OC} FF}{P_{in}} \cdot 100 = \frac{J_{MPP} V_{MMP}}{P_{in}} \cdot 100 \quad (2.8)$$

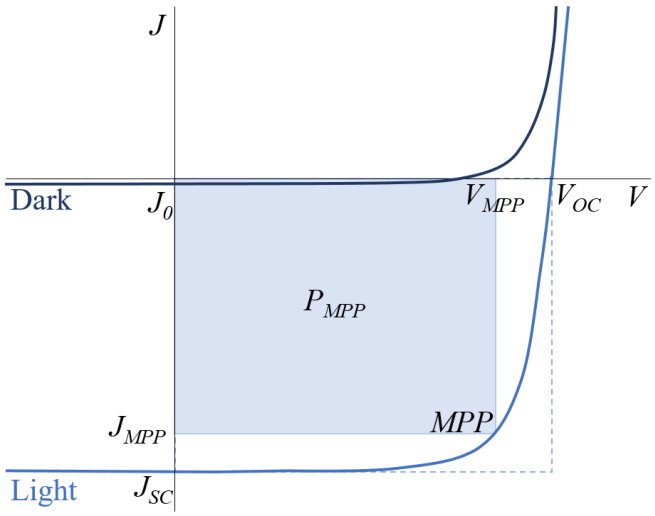


**Fig. 2.8.** Example of a *J-V* curve of a solar cell device under dark and light conditions.

*c) Shockley-Queisser limit*

The maximum theoretical efficiency of a single-junction solar cell is determined by the Shockley-Queisser limit and is a function of the band gap and the incident spectrum.[6] Since the incident spectrum is standardised (AM1.5), the efficiency ($\eta$) is determined only by the $E_g$, as shown in Fig. 2.9. Lower values of the efficiency are produced with small and large band gaps, since small $E_g$ produce devices having small working voltages, whereas large $E_g$ produce small photocurrents. On the contrary, a maximum efficiency of 33.7% is achieved by materials having $E_g$ of ~1.4 eV. The main energy loss mechanism in solar devices is thermalisation (absorption for h$\nu \geq E_g$).

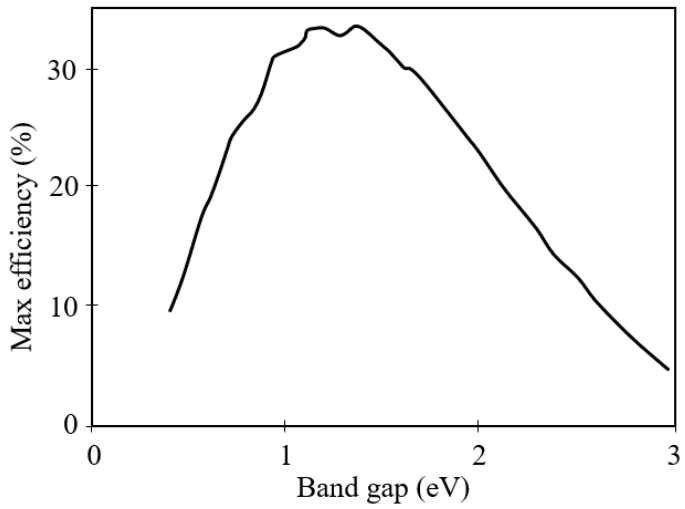


**Fig. 2.9.** Shockley-Queisser limit for a single junction solar cell at AM1.5. Graph re-drawn from ref.[7]

*d) Losses in solar cell devices*

The efficiency of solar cell device may be negatively influenced by energy losses. The main reasons for these losses are described below.

*i) Optical losses*

A solar cell comprises numerous layers, some of which can contribute to parasitic photon absorption or absorption that does not contribute in the formation of the electron/hole

pair. Hence during the fabrication of solar cells, it is important to evaluate the absorbance of the front-layers. An example may be the parasitic absorption of transparent conductive oxide (TCO) materials.

In addition, reflection may contribute in optical losses. In modern silicon solar cells this effect is avoided using anti-reflective coatings.

*ii) Resistive losses (shunt and series resistance)*

Section 2.2.3.a, showed that the Shockley equation in real solar cells is influenced by shunt ($R_{SH}$) and series ($R_S$) resistances, as these allow power dissipation. Their effect on the shapes of the *J-V* curves, is shown in Fig. 2.10. The series resistance is commonly associated with thick absorbing layers, low doping levels and low conductivity of the front transparent contact, whereas the shunt resistance may occur in case of layers with pin-holes and weak diode regions.

The resistances values may be determined by measuring the inverse of the slope close to the $V_{OC}$ and $J_{SC}$ for $R_S$ and $R_{SH}$ respectively. In order to have the smallest influence on the solar cell, $R_S$ should approach 0, whereas $R_{SH}$ should tend toward infinity.

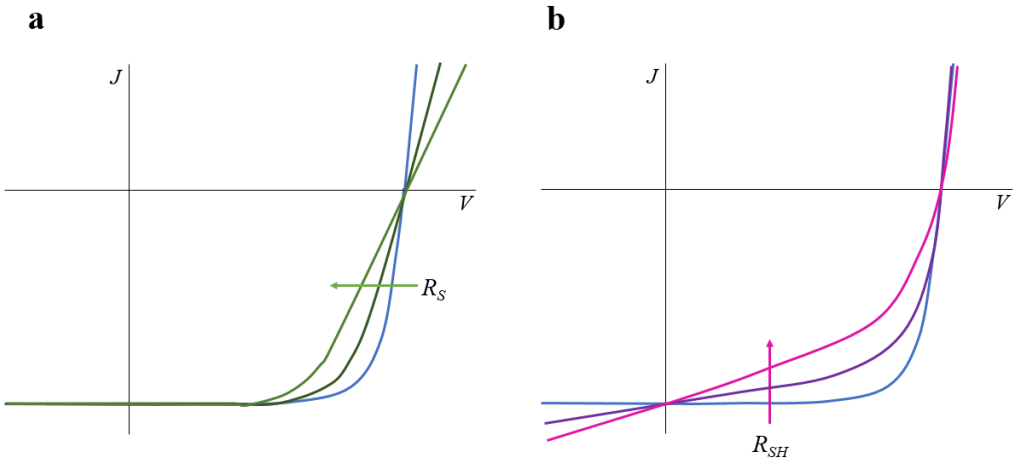


**Fig. 2.10.** *J-V* curves showing the effect of series (a) and shunt (b) resistances on the curve.

*iii) Recombination losses*

Electron/hole pair generated by photon absorption, may be subjected to recombination in the bulk, on the surface or in the depletion region. Recombination losses affect both $J_{SC}$ and $V_{OC}$ and are caused by native defects, impurities, or dangling bonds.

*Bulk* recombination effects may occur in three different ways: radiative, non-radiative and Auger recombination. Fig. 2.11 shows these mechanisms which are briefly explained as follows.

- Radiative recombination is a relaxation phenomenon where an electron recombines with a hole, releasing a photon. This photon has similar energy to the band gap, hence it is weakly absorbed by the material, and thus the radiation is emitted. Radiative recombination is suppressed in indirect semiconductors because it would require momentum *k* (see section 2.1).
- Non-radiative recombination occurs through defects with energy states within the band gap. Free carriers may be trapped by such energy states and either be released by thermal activation, or the trap may host both an electron and a hole which recombine.
- Auger recombination involves three carriers, in which an electron and a hole recombine releasing energy. This energy, rather than being emitted as a photon, is released by exciting an electron. This electron thermalises back to the edge of the conduction band. Since Auger recombination conserves both momentum and energy, this type or recombination can occur in indirect semiconductors.

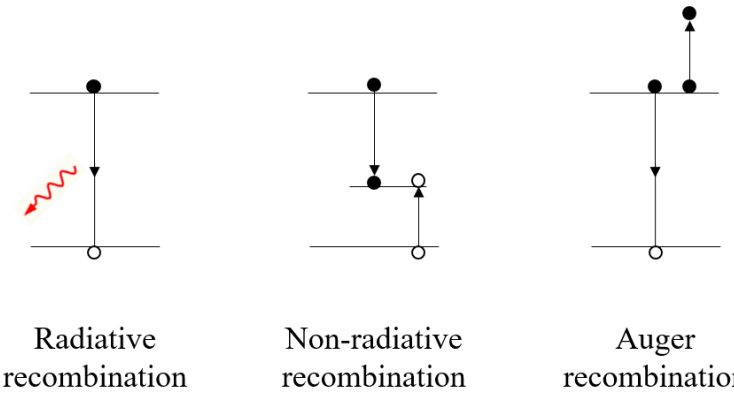


**Fig. 2.11.** Electron/hole recombination mechanisms.

*iv) Metal-semiconductor interface losses*

While for Ohmic contacts electrons and holes are free to move in and out of a semiconductor with minimal energy losses, in Schottky junctions (rectifying contacts) the potential barrier causes a reduction in the carrier flow. Since in a solar cell the Schottky junction behaves similarly to a second diode, a 'roll-over' at forward bias may be recorded in a *J*-*V* curve (Fig. 2.12), which may affect the $V_{OC}$ of the solar cell.

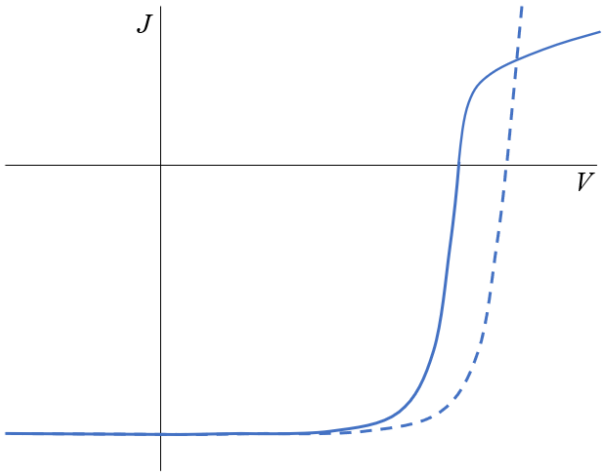


**Fig. 2.12.** 'Roll-over' effect caused by a back contact junction diode.

### 2.2.4. External quantum efficiency

External quantum efficiency (*EQE*) is defined as the ratio of the photogenerated charge carriers that are collected by the solar cell, to the number of incident photons, as shown in Equation 2.9.

$$EQE = \frac{electrons/sec}{photons/sec} \tag{2.9}$$

If all photons are absorbed and generate charge carriers that are collected in the circuit, the *EQE* is 100%. Unfortunately this ideal case is rare, as carrier recombination and optical losses (caused for example by glass or window layers) play an important role in reducing the solar cell quantum efficiency. The measurement is usually made as a function of wavelength using a monochromated beam. Devices are illuminated by a light beam at different wavelengths, and the current produced by the solar cell at each wavelength is measured.

The *EQE* analysis may be used to support the *J-V* analysis, since by measuring the area underneath the *EQE* curve the $J_{SC}$ may be determined.

### 2.2.5. Capacitance-voltage *C-V* characteristics

Capacitance - voltage (*C-V*) measurement is used for the characterisation of *p-n* junctions and Shottky barriers or, in general, semiconductor materials forming a depletion region. The depletion region is commonly compared to a capacitor sandwiched between two semiconductors, having a capacitance of:

$$C = \frac{dQ}{dV} \tag{2.10}$$

where:

$$Q = WAeN = A\sqrt{2e\varepsilon_r\varepsilon_0 N(V_{bi} - V)} \tag{2.11}$$

where: $Q$ is the total charge, $W$ is the width of the depletion region, $A$ is the contact area, e is the electron charge, $N$ is the carrier concentration, $\varepsilon_r$ is the dielectric constant of the

semiconductor/s involved in the junction, $\varepsilon_0$ is the permittivity in free space, $V_{bi}$ is the built in voltage and $V$ is voltage. The total depletion width is calculated as the sum of the widths in both semiconductors involved in the junction ($w_1$ and $w_2$), as shown in Eq. 2.12:

$$W = w_1 + w_2 \tag{2.12}$$

By applying a voltage it is possible to vary the depletion width, which provides information about electrical properties, such as carrier concentration ($N$) and the built in voltage ($V_{bi}$). In order to determine $N$ and $V_{bi}$ it is first necessary to determine the Mott Schottky plot, a graph showing $1/C^2$ versus voltage. However, at this point it is important to know if the junction is one-sided or two-sided in order to avoid misinterpretation of the $C$-$V$ results.

*a) The one-sided junction*

Typically a junction is considered one-sided when the doping concentration of one of the two semiconductors is greater of at least two orders of magnitude compared to the other. Since the depletion region is positioned in the semiconductor with less carriers, $V_{bi}$ and $N$ are calculated solely in this semiconductor.

In the case of a one-sided abrupt junction, the most common case in PV devices, the determination of the depletion region properties is simplified, since this is buried inside one of the two semiconductors involved in the junction. Hence, the capacitance is calculated as:

$$C = \frac{\varepsilon_r \varepsilon_0 A}{W} \tag{2.13}$$

where: $C$ is capacitance, $\varepsilon_r$ is the dielectric constant of the semiconductor containing the depletion region, $\varepsilon_0$ is the permittivity in free space, $A$ is the contact area and $W$ is the width of the depletion region, which for a one-sided junction is $W = w_1$. Hence, the $W$ calculation is derived from Eq. 2.13:

$$W = \frac{\varepsilon_r \varepsilon_0 A}{C} \tag{2.14}$$

From the *C-V* plot, the Mott-Shottky plot is calculated and the $1/C^2$ equation is obtained from Eq. 2.10 and 2.11, through Eq. 2.15:

$$C = \frac{dQ}{d(V_{bi}-V)} = \frac{A}{2}\sqrt{\frac{2e\varepsilon_r\varepsilon_0 N}{(V_{bi}-V)}} \tag{2.15}$$

$$\frac{1}{C^2} = \frac{2(V_{bi}-V)}{A^2 e\varepsilon_r\varepsilon_0 N} \tag{2.16}$$

$$\frac{1}{C^2} = \frac{2\,V_{bi}}{A^2 e\varepsilon_r\varepsilon_0 N} - \frac{2\,V}{A^2 e\varepsilon_r\varepsilon_0 N} \tag{2.17}$$

where: $N$ is the carrier concentration of the semiconductor containing the depletion region, hence either $N_A$ or $N_D$.

From the fitting in the Mott-Shottky plot (having formula $y = mx + b$, where $y = 1/C^2$ and $x = V$), the $V_{bi}$ may be determined by the intercept ($x$):

$$V_{bi} = -\frac{b}{m} + \left(\frac{T k_B}{e}\right) \tag{2.18}$$

where: $T$ is temperature, $k_B$ is Boltzmann's constant and the slope ('$m$') is determined as:

$$m = -\frac{2}{A^2 e\varepsilon_r\varepsilon_0 N} \tag{2.19}$$

from which the carrier concentration is derived:

$$N = \frac{2}{m\,A^2 e\varepsilon_r\varepsilon_0} \tag{2.20}$$

*b) The two-sided junction*

When the carrier concentration of the two media is similar (less than two orders of magnitude difference), the junction is positioned between the two semiconductors, forming a two-sided junction.

In the case of the two-sided junction the total dielectric constant of the junction must be calculated, as shown in the following Equations (2.21 – 2.27):

$$\frac{1}{C} = \frac{1}{C_1} + \frac{1}{C_2} \tag{2.21}$$

$$C = \frac{C_1 C_2}{C_1 + C_2} \tag{2.22}$$

For simplicity it is assumed that the junction is positioned half in one semiconductor and half in the second semiconductor. Hence, the capacitance for each side is described as:

$$C_1 = \frac{\varepsilon_{r_1}\varepsilon_0 A}{\omega/2} \quad \text{and} \quad C_2 = \frac{\varepsilon_{r_2}\varepsilon_0 A}{\omega/2} \tag{2.23}$$

where: $\varepsilon_{r1}$ = dielectric constant of one semiconductor, $\varepsilon_{r2}$ = dielectric constant of second semiconductor. Hence, by replacing Eq. 2.23 in Eq. 2.22:

$$C = \frac{\frac{\varepsilon_{r_1}\varepsilon_0 A}{\omega/2}\frac{\varepsilon_{r_2}\varepsilon_0 A}{\omega/2}}{\frac{\varepsilon_{r_1}\varepsilon_0 A}{\omega/2}+\frac{\varepsilon_{r_2}\varepsilon_0 A}{\omega/2}} \tag{2.24}$$

Eq. 2.24 may be simplified to:

$$C = \frac{2\varepsilon_{r_1}\varepsilon_{r_2}\varepsilon_0}{(\varepsilon_{r_1}+\varepsilon_{r_2})}\frac{A}{\omega} \tag{2.25}$$

$$C = \varepsilon\frac{A}{\omega} \tag{2.26}$$

Where:

$$\varepsilon = \frac{2\varepsilon_{r_1}\varepsilon_{r_2}\varepsilon_0}{(\varepsilon_{r_1}+\varepsilon_{r_2})} \tag{2.27}$$

The depletion width in equilibrium is calculated as:

$$W = \sqrt{\frac{2\varepsilon V_{bi}}{\mathrm{e}}\frac{N_a+N_d}{N_a N_d}} \tag{2.28}$$

which, under applied bias is:

$$W = \sqrt{\frac{2\varepsilon(V_{bi}-V)}{\mathrm{e}}\frac{N_a+N_d}{N_a N_d}} \tag{2.29}$$

Since the total charge, $Q$ is described as follows:

$$Q = W\mathrm{e}A\frac{N_a+N_d}{N_a N_d} = A\sqrt{2\mathrm{e}\varepsilon\,(V_{bi}-V)\frac{N_a N_d}{N_a+N_d}} \tag{2.30}$$

the capacitance is derived as:

$$C = \frac{dQ}{d(V_{bi}-V)} = \frac{A}{2}\sqrt{\frac{2\mathrm{e}\varepsilon}{(V_{bi}-V)}\frac{N_a N_d}{N_a+N_d}} \tag{2.31}$$

At this point the carrier concentration of the acceptor or of the donor may be determined from the Mott-Shottky plot. This is only possible if the carrier concentration of

one material is known, from which it is possible to extract the carrier concentration of the second material involved in the junction.

For example, for the determination of $N_A$ (but the equivalent applies for $N_D$):

$$C^2 = \frac{A^2}{4}\frac{2e\varepsilon}{(V_{bi}-V)}\frac{N_aN_d}{N_a+N_d} \tag{2.32}$$

$$\frac{1}{C^2} = \frac{4\,V_{bi}}{A^2 2e\varepsilon}\frac{N_a+N_d}{N_aN_d} - \frac{4\,V}{A^2 2e\varepsilon}\frac{N_a+N_d}{N_aN_d} \tag{2.33}$$

by knowing "*b*" from the fitting in the Mott-Shottky plot (having formula $y = mx + b$), $N_A$ may be determined as follows:

$$b = \frac{4\,V_{bi}}{A^2 2e\varepsilon}\frac{N_a+N_d}{N_aN_d} \tag{2.34}$$

$$b\,N_a = \frac{4\,V_{bi}}{A^2 2e\varepsilon}\frac{N_a+N_d}{N_d} \tag{2.35}$$

Solving Eq. 2.35, $N_A$ yields:

$$N_a = \frac{4\,V_{bi}N_d}{bA^2 2e\varepsilon N_d - 4\,V_{bi}} \tag{2.36}$$

The carrier concentration unit is $cm^{-3}$.

## 2.3. References


(1) Sze, S. M.; Ng, K. K. *Physics of Semiconductor Devices*; John Wiley & Sons, Inc.: Hoboken, NJ, USA, 2006.

(2) Nelson, J. *The Physics of Solar Cells*; Imperial College, UK, 2003.

(3) Blood, P.; Orton, J. W. *The Electrical Characterization of Semiconductors:Majority Carriers and Eletron States*; Academic Press, 1992.

(4) Tress, W. *Organic Solar Cells: Theory, Experiment, and Device Simulation*; Springer, Ed.; 2014.

(5) National Renewable Energy Laboratory. Reference Air Mass 1.5 Spectra https://www.nrel.gov/grid/solar-resource/spectra-am1.5.html (accessed Sep 11, 2018).

(6) Shockley, W.; Queisser, H. J. Detailed Balance Limit of Efficiency of P-n Junction Solar Cells. *J. Appl. Phys.* **1961**, *32* (3), 510–519.

(7) Obayes, H. R.; Al-Gebori, A. M.; Khazaal, S. H.; Jarad, A. J.; Alwan, G. H.; Al-Amiery, A. A. Hypothetical Design of Carbon Nanotube Materials Based on [8]Circulene. *J. Nanoelectron. Optoelectron.* **2015**, *10* (5), 711–716.

# 3. Perovskite materials and solar cell devices – Literature review

Perovskite materials have been demonstrated to have multiple applications in the literature, for instance in the production of lasers, light emitting diodes, in catalysis and photocatalysis.[1–3] However, this thesis will focus on their use in photovoltaic applications and in particular on those materials inspired by the hybrid organic-inorganic perovskite class, that have shown exceptional PV performance.

## 3.1. Rate of publications on perovskite materials and solar cells

Starting from the early stages of the twentieth century, perovskite materials have attracted a considerably interest in the scientific community. A graph presenting the number of publications on the topic between 1900 and 2017 is shown in Fig. 3.1a (data acquired from Web of science Core Collection).[4] The graph shows that literature about perovskite materials started to be published at the beginning of the twentieth century (1911) but began

to produce wider interest in the scientific community around 1990. However, since it was demonstrated that perovskite materials may be used for solar cell applications in 2009,[5] an abrupt increment of the publications was recorded year after year, as shown in Fig. 3.1b. The total number of publications in the years 1990 – 2017 is 65,752 for the material research and 9,285 for the material used solely in solar cell applications, and further increment is expected in 2018.

It is therefore understandable that a full literature review on perovskite materials cannot be reported in this work, and hence only the fundamental topics that are relevant for this thesis are presented.

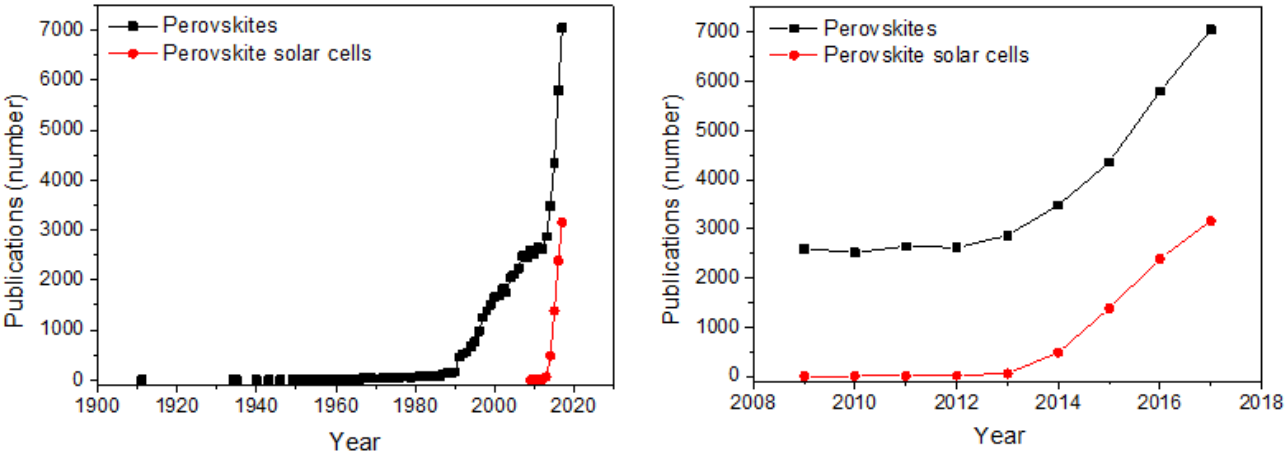


**Fig. 3.1.** Number of publications about perovskite materials (black) and perovskite solar cells (red) published from 1900 (a) and between 2009 and 2017 (b). Source: Web of science Core Collection.[4]

## 3.2. Perovskite materials

Perovskites are a family of materials which adopt the same crystal structure as the mineral $CaTiO_3$ perovskite, a compound that was discovered by Gustav Rose in the Ural Mountains of Russia in 1839 who named it after L. A. Perovski (1792 – 1856), a Russian mineralogist.[6]

All perovskite materials have in common the general formula $ABX_3$, where A is a large cation (which can be an atom or a molecule), B is a smaller cation and X is the anion,

typically oxygen or a halide, and they adopt the structure shown in Fig. 3.2a. Perovskites are generally classified as metal oxide perovskites ($ABO_3$) and halide perovskites ($ABX_3$). Halide perovskites (X = F, Cl, Br, I) are used for solar cell applications, and can be further sub-divided as alkali halide perovskites and organo-metal halide perovskites. Both types will be examined in this thesis, in particular $CsPbI_2Br$ and methylammonium lead iodide ($CH_3NH_3PbI_3$ or MAPI).

Alkali halide perovskites were synthesised for the first time in 1893,[7] however they were classified as perovskite materials only in 1958 by Christian Møller,[8] who studied the crystal structure of $CsPbX_3$ (X = Cl, Br or I) compounds and found that they were photoconductive. Later, in 1978 Dieter Weber synthesised the first organic-inorganic perovskite by replacing the caesium with methylammonium ($CH_3NH_3^+$) and forming MAPI,[9] which was the first and most studied perovskite material used in solar cell applications.[10]

Perovskite materials have a cubic structure (space group *Pm3m*),[11] formed by cuboctahedral inorganic $[BX_6]^{4-}$ cages which are connected in a 3D framework through corner-sharing. These cages contain the $A^+$ cation at their centre. A representation of the unit cell is shown in Fig. 3.2a, whereas the unit cell projection is shown in Fig. 3.2b. The cubic structure can tilt forming an orthorhombic or tetragonal perovskite structure, according to the temperature and/or pressure,[11,12] until the structure is too unstable and collapses, becoming an amorphous material.[13] Conventionally the cubic structure is called the α-phase and the *non*-perovskite-like structure is the δ-phase.[13,14]

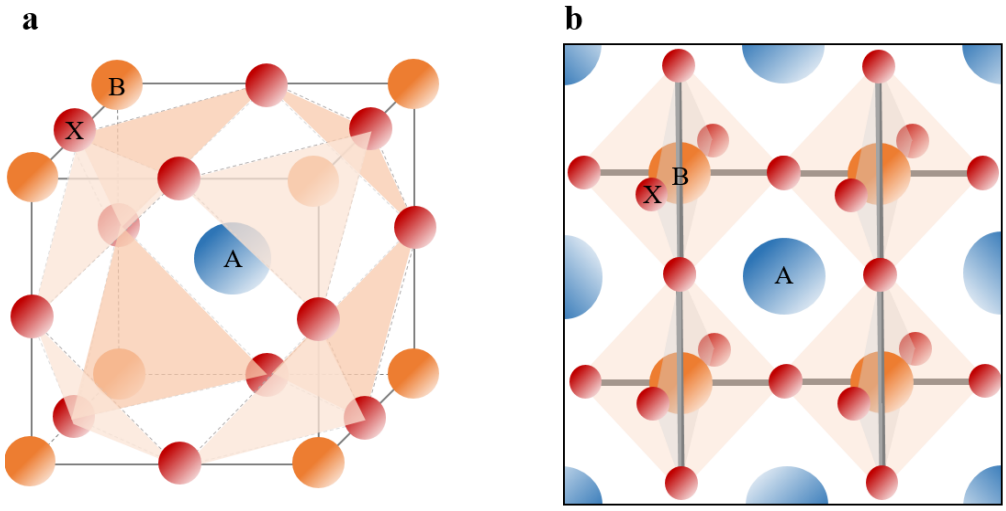


**Fig. 3.2.** $ABX_3$ perovskite cubic structure (example: A = $CH_3NH_3^+/Cs^+$, B = $Pb^{2+}/Sn^{2+}$, X = $I^-/Br^-/Cl^-$). a) Representation of the unit cell and b) the unit cell projection.

The stability and distortion of the perovskite materials is governed by the atomic radii of A, B and X. In 1926, V. M. Goldschmidt described a parameter to determine the stability of preparing perovskite compounds known as Goldschmidt's tolerance factor.[15] This method was initially used for oxide perovskites, but it has been shown to be suitable also for organic-inorganic and alkali halide perovskite compounds.[13] The tolerance factor is defined as:

$$t = \frac{r_A + r_B}{\sqrt{2}\,(r_B + r_X)} \tag{3.1}$$

where: $t$ = tolerance factor and $r$ = radius of the constituents A, B and X.

Tolerance factors in the range of 0.71 – 1 indicate that the perovskite structure may be formed.[13,16] In addition, by analysing the values of $t$, it is possible to identify the phase that is formed: this relationship is described in Table 3.1.

While it is established that perovskite structures are formed for $0.71 < t < 1$, some research in the literature disagrees in the threshold between orthorhombic and cubic phases, this being 0.9 (instead of 0.8).[17]

| *t* | Phase | Notes |
|---|---|---|
| < 0.71 | Non-perovskite | A and B have similar radii |
| 0.71 – 0.8 | Orthorhombic or rhombohedral | A is too small |
| 0.8 - 1 | Cubic | A and B have ideal size |
| > 1 | Hexagonal, tetragonal or single chained | A is too big or B is too small |

**Table 3.1.** Goldschmidt tolerance factor values determining the perovskite structure.[13,16]

## 3.3. Origin and evolution of perovskite solar cells

Perovskite materials were used for the first time as semiconductors in dye sensitised solar cells (DSSC) by Myasaka's group in 2009, using a $TiO_2$ electrode (anode) and an FTO/glass counter electrode (cathode), obtaining 3.8% efficient devices with $CH_3NH_3PbI_3$ and 3.1% with $CH_3NH_3PbBr_3$.[5] In 2011 Park and co-workers produced a 6.5% efficient quantum-dot-sensitised solar cell, by spin-coating an equimolar solution of $PbI_2$ and $CH_3NH_3I$ in γ-butyrolactone onto nanocrystalline $TiO_2$ (electron transporting material, ETM).[18] An example of these device structures is shown in Fig. 3.3a. However, all these devices showed great instability.

In 2012, Grätzel and Park's groups, and shortly after Miyasaka and co-workers in collaboration with Snaith's group, fabricated perovskite solar cells using a $TiO_2$ mesoporous layer (mp-$TiO_2$) and replaced the liquid electrolyte of the DSSC with a compact layer made with spiro-OMeTAD (hole transporting material, HTM, 2,2',7,7'-Tetrakis-(N,N-di-4-methoxyphenylamino)-9,9'-spirobifluorene), which radically improved the stability of the solar cells. With this configuration (Fig. 3.3b) the efficiency exceeded 9%.[19,20] In addition, Miyasaka and Snaith's groups showed that by replacing the mesoporous $TiO_2$ with an $Al_2O_3$ scaffold formed on a compact $TiO_2$ layer (c-$TiO_2$), the device efficiency further improved reaching 10.9% *PCE*.[20] By using the insulating $Al_2O_3$

scaffold, a higher $V_{OC}$ was achieved compared to the titania scaffold devices, which implied that the perovskite is able to transport both holes and electrons and does not need an adjacent electron transporting material, revealing that perovskites were more than normal sensitisers.[20] This discovery was an important turning point, as from that moment the mesoporous titania scaffold onto a compact-electron transporting materials, or only the planar (scaffold-free) compact layers, were covered with a thicker perovskite layer (200 – 400 nm). Examples are shown in Fig. 3.3c and d respectively. These last two configurations were the most used for the development of perovskite solar cells.

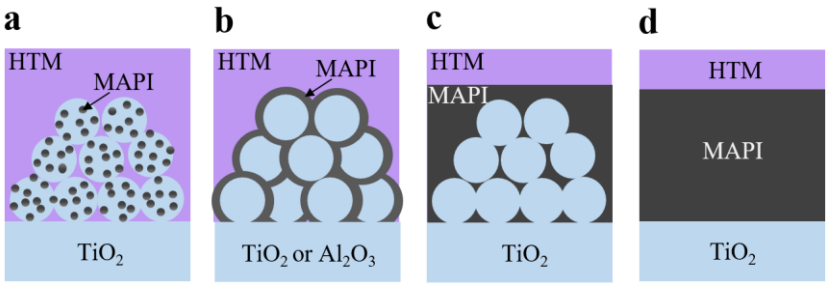


**Fig. 3.3.** Evolution of MAPI device structure. a) DSSC using a perovskite-dye in liquid electrolyte. b) Perovskite thin layer covering the mesoporous scaffold layer and using a solid state hole conductor. c) Perovskite infiltrated into the mesoporous scaffold. d) Perovskite thin film deposited on compact titania (planar device).

In only a few years the device efficiency improved greatly, not only due to an improvement in the device architecture but also due to altering the composition of the perovskite material. In particular, by using perovskite material composed of formamidinium with multiple cations and mixed halide anions, in 2017 W. S. Yang *et al.* achieved a *PCE* of 22.1% - the highest performing device fabricated up to now.[21] Nevertheless, the scientific community seems to be confident that perovskite solar cells will exceed 22% *PCE* shortly.[22]

The rapid evolution of champion efficiencies achieved by perovskite solar cells is shown in Fig. 3.4. It can be observed that in only 8 years these devices have shown an improvement of the *PCE* of 18.3 percentage points.

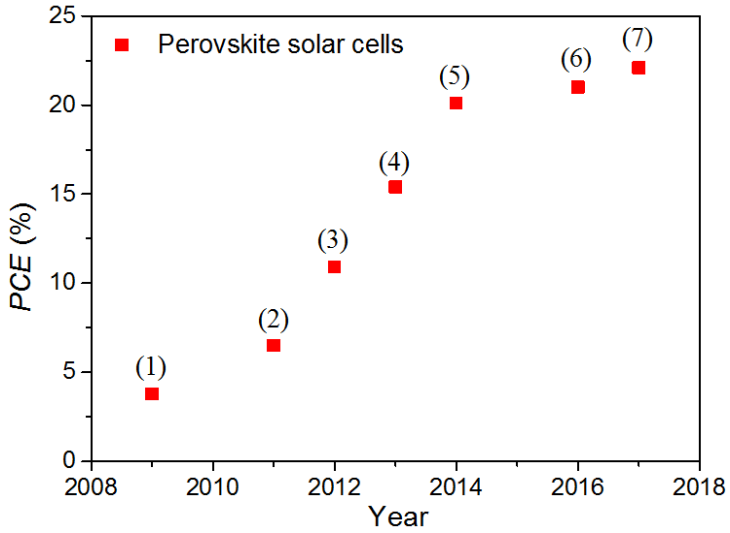


**Fig. 3.4.** Record perovskite solar cell efficiencies in the year gap 2009 – 2018, the numbers in brackets give information about the highest *PCE* % achieved. These are listed: (1) 3.8%,[5] (2) 6.5%,[18] (3) 10.9%,[20] (4) 15.4%,[23] (5) 20.1%,[24] (6) 21%,[25] and (7) 22.1%.[21,24]

In addition, in the last few years tandem solar cells were fabricated using perovskite solar cells. Perovskite-perovskite tandems, using compounds with significantly different bandgaps, achieved up to 18.5% *PCE* with a 2-terminal configuration[26] and 20.3% with a 4-terminal configuration,[27] whereas silicon-rubidium multication perovskite tandems have achieved up to 26.4% *PCE* in 2017.[28]

### 3.3.1. MAPI perovskites

Generally speaking, perovskite materials have produced interest in the scientific community due to their low temperature and therefore low cost, facile deposition processes. MAPI was the first perovskite used in solar cell applications and since it showed very promising results, it was widely studied in recent years. Therefore, the main properties can be easily found in the literature and are described next.

MAPI presents a direct band gap (1.55 – 1.6 eV)[10,29] with high absorption coefficient ($10^4$ – $10^5$ $cm^{-1}$)[30] and good light absorption in the whole visible spectrum, which makes it very suitable as absorber material for PV applications. Furthermore it presents weak exciton

binding energy (~16 meV at room temperature,[31,32] dissociating rapidly into $e^-$ and $h^+$) with charges showing moderate mobility (10 $cm^2 V^{-1}s^{-1}$ for solution processed MAPI)[33] and high carrier diffusion lengths (up to 175 μm for single crystals in full sunlight and in the range of 100 – 1000 nm in thin films)[10,34,35] suggesting that the recombination times are very high (hundreds of nanoseconds).[33,36] These characteristics allow planar and efficient device configurations for thin film PV technologies with high $V_{OC}$ values (up to 1.23 V),[22,37] however they may greatly vary according to the fabrication processes of the films.

MAPI shows a pseudocubic crystal structure due to the asymmetric methylammonium cation, but nevertheless in the literature it is still considered as cubic due to dynamic disorder.[38] However, the cubic structure is not stable at room temperature. X-ray diffraction analysis performed during cooling revealed that MAPI undergoes a phase change at ~54°C from cubic to tetragonal structure and by further decreasing the temperature the tetragonal structure converts into an orthorhombic structure at ~-110°C.[39,40] Table 3.2 summarises the phase transition temperatures for MAPI, with the room temperature phase being tetragonal.

| MAPI phase | Crystal system | Space group | Temperature (°C) |
|---|---|---|---|
| $\alpha$ | Cubic | *Pm3m* | >54.25 |
| $\beta$ | Tetragonal | *I4/mcm* | -110.95 – 54.25 |
| $\gamma$ | Orthorhombic | $Pna2_1$ | <-110.95 |

**Table 3.2.** MAPI phases and temperature of transition.[11]

While very much is known about the crystal structure of MAPI, the doping properties show conflicting results in the literature since some research groups have shown *p*-doping features[41] and some others have shown *n*-doping properties.[42] However, Wang *et al.* suggested that the doping level of the material is strictly related to the preparation processes.[43] In particular, depending on the excess of MAI or $PbI_2$ precursor reagents, MAPI

could become *p*-type on *n*-type respectively.[43–45] For the same reason, stoichiometric MAPI was suggested to be intrinsic.[44] However, theoretical calculations showed that the intrinsic doping may be influenced by the presence of iodine vacancies, which are the defects that form more spontaneously, compared to other defects.[44] The defect chemistry of MAPI was studied by many research groups worldwide, but it showed great complexity due to the presence of overlapping factors, such as ionic point defects, and delocalised and localised charges. However, despite the low defect formation energy, it was measured that the intrinsic carrier concentration is low, this being in the region of $10^9$ - $10^{14}$ $cm^{-3}$.[44,46] The main analysis performed in order to determine the carrier concentration was the Hall effect measurement which was difficult to implement, perhaps explaining the large range of carrier concentrations determined in the literature.

An interesting feature of MAPI is its easy band gap tunability. Initially most changes were effected by mixing the iodine with other halides (bromine and chlorine in particular),[47,48] then by mixing or swapping lead with tin (mainly for toxicity issues),[49,50] and finally by using different organic compounds (formamidinium) or inorganic atoms (caesium and/or rubidium).[51,52] In this way it is possible to tune the band gap from 1.2 to 2.3 eV.[53,54] These compositional changes produced improvements of both device efficiency and stability of the material. Furthermore, the band gaps obtained make the materials useful for the fabrication of tandem solar cells.

Nevertheless, MAPI also has some disadvantageous properties for solar cell applications, and for this reason their commercialisation has not yet been realised. In particular, the main issues with MAPI (and also other organic-inorganic perovskites) are related to material stability and hysteresis in the *J*-*V* analysis. These two important aspects are addressed next. Particular focus was given to the stability of MAPI, as this aspect is important for the understanding of the results chapters 5 and 6.

*a) Stability issue in MAPI perovskites*

In the literature the stability of perovskite *solar cells* has been investigated by evaluating the changes in performance with time and the subsequent effects of degradation of the material. In service evaluation monitors the degradation of the perovskite device continuously during the measurement. As perovskite devices are currently moving toward commercialisation, the environmental stability of perovskite materials and devices will need to be tested by monitoring the *J-V* parameters as a function of time under extreme conditions of continuous light, humidity (85% relative humidity or RH) and over large temperature ranges (-40°C to 85°C), as devices need to meet the IEC 61646 testing standards for thin-film terrestrial photovoltaic modules.[55,56] These specifications need to be followed in order to guarantee stability of the commercial product for 20 - 25 years, retaining 80% of the initial performances after this amount of time (≤ 1% *PCE*/year).[57] In addition, post-degradation deconstructive analysis is performed on deliberately degraded devices.[58]

Stability of perovskite solar cells can also be categorised into intrinsic and extrinsic stability. The *intrinsic stability* relates solely to the stability of the perovskite material that can undergo structural changes due to UV, oxygen, humidity, temperature or electric bias exposure. In turn the intrinsic stability can be further classified by considering two main factors: the chemical stability, considering reacting species such as water and oxygen and organic solvents, and the structural stability, which considers the ability of the crystal to be stable at certain temperatures, pressures etc. On the contrary, the *extrinsic stability* is referred to the conditions independent from the perovskite material that affect the solar cell. For example, researchers have recently shown that the stability of perovskite solar cell devices is also strictly related to the choice of front and back contacts, as they may migrate into the perovskite layers,[59,60] and the type of electron and hole transporting materials used,[61] as they

may cause interfacial degradation with the perovskite[62–65] or show intrinsic degradation.[58,66–68] Other examples can be related to the choice of the encapsulation material and its sealing.[58]

Researchers have shown that there are ways to produce perovskite materials with higher intrinsic stability, for example by mixing $CH_3NH_3PbI_3$ with different cations or anions[58] (such as formamidinium, as organic cation),[69] using tin as inorganic cation and mixed halide anions ($I^-$, Br- and $Cl^-$).[70,71] With particular regard to the halides, it was shown that the use of iodine as the halide (X) anion in the perovskite structure decreases the stability of the perovskite compounds and by completely exchanging iodine with bromine an improvement of the structural stability is achieved.[71,72] The reason for this may be related to the formation of better, more uniform crystallites, reduction of the grain boundary surface area, which also determine an increased efficiency. Conversely, the mixed halide compounds containing both iodine and bromine, show segregation of iodide and bromide domains when the material is exposed to light soaking, thus leading to recombination and limited voltages in the devices.[73] In general, using different cations or anions produces a change in the Goldschmidt tolerance factor[15] that leads to lattice distortion. This may be beneficial or disadvantageous for the perovskite crystal structure stabilisation. Furthermore, it has been shown that since perovskite materials contain $CH_3NH_3^+$, $Pb_2^+$ and $I^-$ vacancies at room temperature, they may all contribute to pathways for ion transportation, leading to degradation, and hence influencing the long-term stability of these materials.[46,74]

Apart from the perovskite instability towards some solvents,[75] which lead to numerous issues regarding the choice of hole or electron transporting materials and their deposition methods, the other main aspects of the perovskite's degradation are discussed in the following subsections. However, it should be considered that for any type of degradation, there is an important equilibrium between MAPI and its salts, *i.e.*:

$$PbI_2\ (s) + CH_3NH_3I\ (aq) \leftrightarrow CH_3NH_3PbI_3\ (s) \qquad (3.2)$$

As shown by the double directional arrow, the chemical reaction is reversible and therefore it can synthesise or decompose $CH_3NH_3PbI_3$. Similar reactions occur for perovskites composed of different or mixed halides.[76]

Organic-inorganic perovskite instability towards ambient conditions was observed at very early stages, however the rapid progress in the increasing device efficiency induced researchers to focus mainly on the improvement of the solar cell performances.[77,78] In 2014, Grätzel stated that only few works about the perovskite stability were published and new studies were urgently required, to understand if the perovskite materials could have met the international norms essential for future commercialisation.[10] Later in the same year, M. A. Green, A. Ho-Baillie and H. J. Snaith commented for the first time on the intrinsic instability of perovskite materials, showing that methylammonium lead iodide undergoes degradation in a short time when exposed to moisture and ultraviolet radiation,[71] this being highly undesirable for photovoltaic applications. However, the exact conditions or mechanism of the degradation were not known but, as predicted by M. D. McGehee in 2014,[79] numerous studies about the stability of $CH_3NH_3PbI_3$ and similar perovskites were ultimately initiated and published in the last few years. These showed insight into the roles of moisture and UV light combined to oxygen in the degradation processes.

*i) Stability to moisture*

As presented in literature, organic-inorganic perovskite materials have shown extreme receptivity towards water, even in the form of water vapour. In particular, it was seen that the higher the humidity level, the faster the degradation,[80] especially for MAPI.

In 2014 and 2015 G. Niu *et al.* proposed that the chemical stability of MAPI materials is irreversibly compromised by moisture and oxygen.[76,81] In particular, water induces the

hydrolysation of the perovskite (3.3) caused by the negative Gibbs free energy, producing a cascade of reactions that are described as follows:

$$CH_3NH_3PbI_3\ (s) \leftrightarrow PbI_2\ (s) + CH_3NH_3I\ (aq) \quad (3.3)$$

$$CH_3NH_3I\ (aq) \leftrightarrow CH_3NH_2\ (aq) + HI\ (aq) \quad (3.4)$$

$$4HI\ (aq) + O_2\ (g) \leftrightarrow 2I_2\ (s) + 2H_2O\ (l) \quad (3.5)$$

$$2HI\ (aq) \leftrightarrow H_2\ (g) + I_2\ (s) \quad (3.6)$$

However, for this proposed series of reactions to happen, it is essential that moisture, oxygen and light are present together. For example, the equilibrium of the Reaction 3.4 shifts to the right if there is a redox reaction in presence of oxygen (3.5) or if there is a photochemical reaction induced by UV radiation (3.6). Finally, if HI consumption takes place (Reactions 3.5 and 3.6), the whole process is favoured. Recently, J. M. Frost *et al.* showed a similar schematic degradation of the perovskite catalysed by water and forming HI, MAI and $PbI_2$. It was claimed that since all these products are soluble in water the process is irreversible, thus invoking the additional issue related to the toxicological danger of lead.[82]

Humidity not only produces MAPI's degradation, it also affects the absorption coefficient. Yang *et al.* monitored films exposed to humidity, and observed that the higher the RH values the faster the reduction of the film absorption. For example, using 98% RH the absorption value halved in only 4.5 hours, but nevertheless it was calculated that using only 20% RH this would take 10,000 hours. They speculated that the perovskite degrades in presence of water, forming the hydrated phase $(CH_3NH_3)_4PbI_6 \cdot 2H_2O$.[80] In 2015 this dihydrated phase was purposely synthesised by J. A. Christians *et al.* in order to compare this phase with the degraded phase of MAPI. They proved that the speculation from Yang *et al.* was correct: they observed matching XRD patterns between hydrated and degraded MAPI, indicating that the hydrated phase was formed. Furthermore, they demonstrated that

this phase was formed in the dark and hence the transformation occurred without UV light. They postulated that the opportunity for water to interact with the perovskite is a consequence of the weak bond of methylammonium with $PbI_6$, which allows the lead compound to interact easily with water.[83]

However, in the same year A. Leguy *et al.* found that MAPI hydration is reversible.[84] They showed that a reversible monohydrated phase is formed first, which converts to a dihydrated form.

$$4CH_3NH_3PbI_3 + 4H_2O \leftrightarrow 4[CH_3NH_3PbI_3 \cdot H_2O] \leftrightarrow$$

$$\leftrightarrow (CH_3NH_3)_4PbI_6 \cdot 2H_2O + 3PbI_2 + 2H_2O \qquad (3.7)$$

However, the dihydrated phase irreversibly decomposes to MAI, $PbI_2$ and $H_2O$ after long exposures to humidity. Also, they showed that initially the hydration of the perovskite occurs mainly at the grain boundaries and by exposing the devices to dry nitrogen for 6 hours, the material recrystallizes in the original form, while when water fully penetrates the grains, the decomposition is irreversible. Despite this result, recovered devices showed increased hysteresis, probably related to the increased defect density of the recovered material.

Yang *et al.* have also confirmed the hydrated phases and observed the formation of isolated $PbI_6^{4-}$ octahedra (a degradation product), which breaks down to $PbI_2$ and $I_2$.[80] However, since $CH_3NH_3^+$ bonds more strongly to water than iodine,[85] the reversibility is limited.

In addition, it was shown that the effect of moisture with an electric field increases the rate of $PbI_2$ segregation, *i.e.* the combination of factors increase the rate of irreversible degradation processes.[86,87]

*ii) Stability to oxygen and UV light*

Most studies focussed solely on the degradation of organic-inorganic perovskites induced by moisture. However, some groups observed sensitivity of perovskite materials, towards UV light, this being known for other PV technologies, such as polymer and dye-sensitised solar cells.[88,89]

In 2013 Leijtens *et al.* proposed that perovskite solar cell degradation was induced by UV degradation of the mesoporous $TiO_2$ layer.[90] Later, by introducing a $Sb_2S_3$ blocking layer, Ito *et al.* showed a reduction of the photo-degradation: the $CH_3NH_3PbI_3$ did not decompose in $PbI_2$, maintaining its crystal structure.[91] They proposed that MAPI's decomposition starts from $I^-$ ions present at the interface between MAPI and $TiO_2$, in the same direction where electrons (generated after light absorption) are drifting:

$$2I^- \leftrightarrow I_2 + 2e^- \quad (3.8)$$

$$3CH_3NH_3^+ \leftrightarrow 3CH_3NH_2\,(g) + 3H^+ \quad (3.9)$$

$$I^- + I_2 + 3H^+ + 2e^- \leftrightarrow 3HI\,(g) \quad (3.10)$$

Despite the $pK_a$ (10.80) of reaction 3.9, the evaporation of $CH_3NH_2$ (3.9) and the consumption of $H^+$ (3.10) shifts reaction 3.9 towards the products.[91]

However, later on S. A. Haque's group (2015) demonstrated that fast degradation occurs when the material is exposed to both UV light and oxygen, due to the formation of a superoxide ($O_2^-$) species.[92–94] In particular, they showed that the two degradation factors together act on the perovskite layer and form methylamine, lead iodide, molecular iodine and water. However, it was mentioned that it is very likely that the grain size of the perovskite crystals may influence the diffusion of oxygen in the material and hence the speed of the degradation process.

In 2017, S. A. Haque and M. S. Islam's groups presented the latest and most detailed degradation mechanism for MAPI which was obtained by a range of experimental and

computational experiments.[95] They calculated using DFT (density functional theory), that MAPI's degradation reaction in absence of light (3.11) (*i.e.* without the photo-generation of electrons in the lattice), is energetically *not* favourable (the enthalpy calculated per $O_2$ molecule is +1.60 eV).

$$4CH_3NH_3PbI_3 + O_2 \rightarrow 4PbI_2 + 2I_2 + 2H_2O + 4CH_3NH_2 \quad (3.11)$$

On the contrary, if light is present, the methylammonium lead iodide molecule is photo-activated ($CH_3NH_3PbI_3$*) with a negative free Gibbs energy, forming an electron and a hole. If oxygen is present and finds a vacancy in the lattice, the photo-generated electron will contribute to the formation of a superoxide species ($O_2 + e^- \rightarrow O_2^-$), which irreversibly forms the perovskite degradation products. Reaction 3.12 and Fig. 3.5 describe the reaction mechanism.[95]

$$4CH_3NH_3PbI_3^* + O_2^- \rightarrow 4PbI_2 + 2I_2 + 2H_2O + 4CH_3NH_2 \quad (3.12)$$

The reaction is similar to (3.11), however the main difference is related to the enthalpy of this reaction (-1.4 eV per $O_2$ molecule) implying that the reaction is now favourable. Furthermore, since small grains were degraded more rapidly than larger crystallites, it was proved that the formation of the superoxide species is controlled by the size of the perovskite grains.

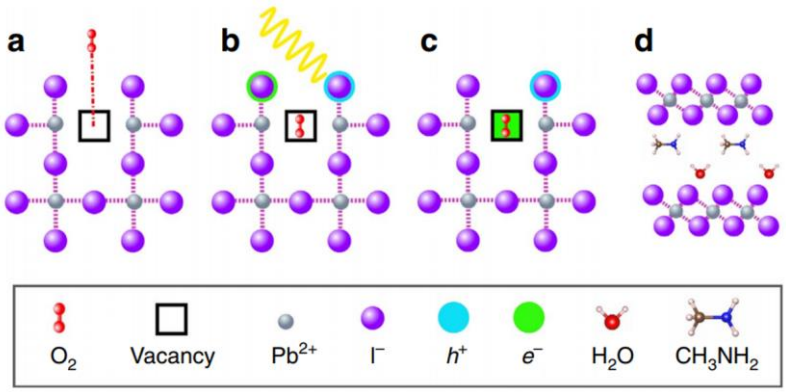


**Fig. 3.5.** $O_2$/UV induced degradation of MAPI represented in four steps: a) oxygen diffusion in the lattice, b) light absorption in MAPI generating an electron/hole pair, c) formation of the superoxide species ($O_2^-$) and d) degradation of the perovskite structure. Reproduced with permission from Nature Comm., ref.[95]

Later, further simulations performed by the same group predicted that the superoxide species forms preferentially at the iodide vacancies, as shown in Fig. 3.6, because the relative sizes of the iodide ion and the superoxide anion are very similar (4.40 Å and 3.42 Å respectively): the $Pb^{2+}$ octahedral coordination is restored making this process the most energetically favoured. Hence, passivation of the halide vacancies may improve the stability of perovskite thin films.

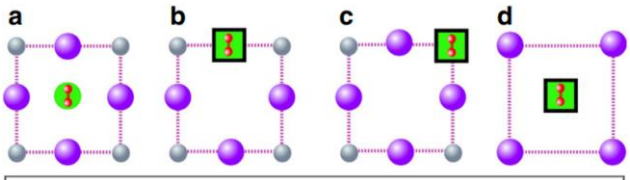


| Site | a) face | b) $V_I^x$ | c) $V''_{Pb}$ | d) $V'_{MA}$ |
|---|---|---|---|---|
| $O_2^-$ formation energy (eV) | −1.19 | −1.94 | +0.29 | −0.23 |

**Fig. 3.6.** Possible sites for the formation of the superoxide species in MAPI: a) face site, b) iodide vacancy, c) lead and d) methylammonium sites. The relative formation energies are included in the inset table. The preferred formation site is in the iodide vacancy, as the formation energy is the most advantageous. Reproduced with permission from Nature Comm., ref.[95]

Equally, studies have shown that MAPI exposed to dry air in the dark did not show any degradation[19,20] demonstrating that the presence of oxygen alone is not harmful for the organic-inorganic perovskite. The danger of exposure to oxygen only occurs when UV light is involved, as it produces a photo-oxidation process.[96,97]

Following the description of the harmful effect of UV radiation and oxygen, developments on the encapsulation processes were performed[98,99] and UV filters were proposed.[58] However, these filters are expensive, degrade irreversibly after 24 hours of exposure and they decrease the PV performances, as they reduce the width of the absorption spectra of the solar cell.

The stability of MAPI towards water and UV/oxygen was improved by interface passivation and by changing the chemical composition.[100–106] Furthermore, effective encapsulations for protection towards these instability factors were developed: encapsulated devices exposed to the stressing tests for thin films PV (85°C and 85% RH) under light soaking for typically 1000 hours, performed at constant rates under light for long amount of time.[87,107–110]

*iii) Thermal stability*

Thermal instability is an intrinsic property of organic-inorganic perovskite materials. In particular, MAPI has shown to be affected by temperatures > 85°C, but nevertheless temperatures between 85°C and 100°C are necessary for the formation of the crystal structure. DSC-TGA measurements showed that exposure to heating induces an initial phase change of the crystal structure[85] and then sublimation at temperatures between 247 - 300°C, caused by the separation of $CH_3NH_3^+$ and HI.[111,112] Therefore, the thermal degradation is mainly recognisable by the formation of $PbI_2$ caused by the partial volatile properties of some of MAPI's constituents,[113,114] suggesting that this degradation mechanism produces the same products formed by degradation caused by water and oxygen/UV.[111] Thermal degradation is slower in the range of 85 - 100°C, compared to $T$ > 100°C where degradation is rapid.

The temperature dependence has been shown to be related to the substrate on which the perovskite is deposited on. For example, ZnO showed accelerated decomposition processes compared to ITO or $TiO_2$.[115] However, heat-treated ZnO improved the thermal stability of the perovskite, suggesting that the reason for this accelerated mechanism is related to water absorbed on the material's surface. But nevertheless, it is not advantageous

to use ZnO as electron transporting material, as this produces lower device performances and higher hysteresis.[116]

Thermal degradation was studied under different environments by Supasai *et al.*, who showed that degradation at 100°C occurs only on MAPI layers that are exposed to air, whereas if samples are kept under vacuum thermal degradation occurs between 140 – 160°C.[117] Furthermore, it must be mentioned that for MAPI prepared using coevaporation processes, the thermal stability increases up to 200°C, as shown by P. Pistor *et al*.[118]

The thermal stability issue in organic-inorganic perovskite solar cells is relevant to the working temperature of solar panels. In some geographical areas, operational temperature ranges of -40°C to +85°C can be easily reached.[119] Therefore, MAPI cannot yet be commercialised as it does not meet the International Standards (IEC 61646).[116] As the main cause of the perovskite thermal instability is due to the presence of the organic components[120] this was improved first by replacing formamidinium (FA) with MA,[50,52] and then further by using Cs and Rb cations. These are effective since their atomic radii are smaller and form a stable high-temperature cubic perovskite phase.[85,121] However, the issue with FA and Cs is their very low chemical stability towards humidity.[50,52,122]

### *b) Hysteresis in MAPI perovskites*

Hysteresis can be seen during *J-V* scans, with differences when measuring in forward (from negative to positive voltages) and reverse (from positive to negative voltages) directions. This behaviour was also found in organic thin film, dye-sensitised and silicon solar cells when the voltage scan is performed too quickly.[123] In perovskite solar cells, and in particular MAPI, hysteresis typically resulted in higher device performances during measurements in the reverse scan direction compared to the performance measured in the forward scan direction, revealing that the charge collection is more effective in the reverse

scan. Furthermore, it was shown that devices often present higher hysteresis in planar $TiO_2$ configurations compared to mesoporous devices.[124] More importantly, hysteresis has been shown to depend strictly on the preparation process and the choice of the materials used as hole and electron transporting layers. For example, perovskite layers with large, well connected grains show less hysteresis compared to smaller and disconnected grains,[125,126] and thicker MAPI layers produce larger hysteresis.[127] Furthermore, the usage of insulating mesoporous alumina on top of compact $TiO_2$ (the electron transporting material) produces larger hysteresis compared to $TiO_2$ alone,[127] but [6,6]-phenyl-$C_{61}$-butyric acid methyl (PCBM) produces negligible hysteresis.[128] Yet, it has been demonstrated that fabricating devices in different laboratories results in large differences in hysteresis, suggesting that this property may be strictly related to the interfaces in the device rather than being a property of the bulk perovskite material.[124] Numerous papers have been published on the understanding of the origin of hysteresis. In particular, four main mechanisms were suggested, these being ion migration (in particular $I^-$),[127,129,130] interfacial carrier dynamics,[127] trap states,[127] and ferroelectricity[50,131,132] (in common with $BaTiO_3$ and $PbTiO_3$ perovskites).[124] However, recent studies converge on the hypothesis involving the ion migration and ion vacancies, for which the degree of hysteresis depends on the scan rate used.[133,134]

### 3.3.2. Inorganic perovskites

Since the main cause of the perovskite thermal instability is related to the presence of volatile organic components,[120] researchers have tried to replace the organic molecules with inorganic atoms. In order to fulfil the tolerance factor requirements, the choice of the cation is restricted to large monovalent cations which are able to fit into the perovskite cubic structure. Caesium lead halide perovskites have been explored, and both iodide and bromide

fulfil the Goldschmidt tolerance condition ($0.81 < t < 1.11$).[71] Single halide and mixed halide compounds have also been studied, as described in this section.

In 2016 - 2017 caesium perovskites were studied in order to replace the organic-inorganic perovskites, in particular with the aim of using them for tandem solar cell devices - due to their wider band gap (> 1.7 eV).[120] However, today caesium is mainly used as an additive in mixed cation perovskites (methylammonium – formamidinium – caesium – rubidium), in order to improve the performance of the perovskite solar cells while also increasing the device's environmental and thermal stability.[51,135,136]

*a) $CsPbI_3$, $CsPbBr_3$ and $CsPbI_2Br$*

Although the caesium tin and plumbo halides were known since 1893[7] and their physical-chemical properties were determined between 1959 and 2013,[8,137–145] they were proposed for photovoltaic and light emission applications only recently.[16,120,154–160,146–153] For example, Chen et. al. demonstrated a $CsSnI_3$ PV device in 2012.[160] In 2015 Beal *et al.* demonstrated a 2.9% efficient $CsPbI_3$ *p-i-n* solar cell device.[146] In the same year, $CsPbBr_3$ achieved a 5.95% efficient PV device.[148] However both iodine and bromine perovskites have shown both advantageous and disadvantageous properties, as explained below.

$CsPbI_3$ has the most appropriate band gap (1.73 eV), however it is stable in its dark cubic phase only at $T > 310$°C. At room temperature it remains metastable in the dark-coloured phase for a short time[8,137,139] before assuming its stable yellow orthorhombic δ-phase (2.85 eV band gap).[139,152] This yellow phase shows edge-shared octahedral chains (similarly to $NH_4CdCl_3$),[16,161] and is a poor absorber for PV applications. Although the material's stability made it difficult to measure devices, an efficiency of 1.7% was achieved.[146] The metastability of the dark cubic phase was slightly improved by adding HI to the precursor solution, but the devices did not exceed a *PCE* of 2.9%.[146]

On the other hand, $CsPbBr_3$ has higher band gap (2.25 eV)[144,152] and despite this being unsuitable for single junction solar cells, it yielded higher efficiencies (5.95% *PCE*) than the pure iodide compound.[148] The advantage of this bromide perovskite is that it is stable in air and at room temperature in its perovskite orthorhombic phase.[120] This improved stability compared to the iodide structure may be due to a better electrostatic stability imparted by the smaller atomic radius of the bromine within the perovskite structure. However, when moderate heating is applied (around 88°C) the phase changes to tetragonal, and then above 130°C to a cubic orange phase. Therefore, despite being more suitable for applications in tandem devices compared to $CsPbI_3$, $CsPbBr_3$ (which is stable at room temperature), is not thermally stable at solar cell working temperatures. Hence, both $CsPbI_3$ and $CsPbBr_3$ are not ideal materials for photovoltaic applications.

However, it has been observed that by mixing the halide composition the band gap can be tuned and the phase stability of the perovskite structure may be improved.[120,150,152] The goal was to find a compound with a lower band gap, imparted by the iodine, but with a better stability at room temperature, imparted by the bromine.

For example, studies on $CsPbIBr_2$ ($E_g$ = 2.05 eV), have led to interesting results. W. Y. Ho-Baillie and her group fabricated spray-assisted devices with 6.3% stabilised conversion efficiency.[154,162] However among the series of $CsPbI_{(3-x)}Br_x$ compounds, the compound that attracted major interest was $CsPbI_2Br$. This was investigated since the inclusion of bromide should make it sufficiently environmentally stable while the inclusion of iodide should give it a usable band gap. $CsPbI_2Br$ has been reported for solar cell applications. Using a classic perovskite device structure FTO/$TiO_2$/$CsPbI_2Br$/Spiro-OMeTAD/Ag, in 2016 Sutton *et al.* fabricated devices with 9.8% *PCE*,[120] indicating the potential of all-inorganic perovskite PV: the Shockley-Queisser limit predicted for this type of perovskite has efficiencies up to 21%, 1.63 V $V_{OC}$ and 16.3 mA/cm$^2$ $J_{SC}$.[120,163,164]

A summary of the main characteristics presented in the literature before 2018, regarding the single halide compounds ($CsPbI_3$ and $CsPbBr_3$) and the most used mixed halide compound ($CsPbI_2Br$), is shown in Table 3.3.

| **Material** | **Room temperature phase** | **Other phases** | **PV results** | **Notes** |
|---|---|---|---|---|
| **$CsPbBr_3$** | Black orthorhombic phase<br><br>$E_g$ = 2.25 eV[144] | $T$ > 88°C<br>Tetragonal phase<br><br>$T$ > 130°C<br>Orange cubic phase[144] | 5.95%[148] | Room temperature phase is stable however its large band gap is not suitable for a PV absorber. |
| **$CsPbI_2Br$** | Brown phase<br><br>$E_g$ = 1.92 eV | Yellow phase<br><br>$E_g$ = 2.85 eV | 9.84% [120] | Ideal compromise between band gap and room temperature stability. |
| **$CsPbI_3$** | Yellow orthorhombic phase<br><br>$E_g$ = 2.85 eV[146] | $T$ > 310°C<br>Black cubic phase (metastable at room temperature - stabilised with HI for few hours only).<br><br>$E_g$ = 1.73 eV[146] | 1.7% and<br>2.9% (with HI)[146] (in the metastable black phase) | Metastable at room temperature in the cubic phase, but its band gap is suitable for PV applications. |

**Table 3.3.** Summary of the main phases, band gaps and device performances of the most used compounds of the $CsPbI_{(3-x)}Br_x$ series studied in the literature. Since the pure iodide compound is unstable at room temperature and the bromide compound has a large band gap not suitable for PV applications, $CsPbI_2Br$ fulfils the best combination of factors.

However, a few incidental comments in the literature[120] indicated the poor stability of $CsPbI_2Br$ in air, but without including deeper analysis on the factors that induce the degradation of the material, nor the mechanism of degradation of the compound. This is therefore explored in Chapter 6.

Fig. 3.7 shows the phase diagram produced by Sharma *et al.*[139] in 1992 which helps to better understand the temperature ranges of the single and the mixed halide $CsPbI_{(3-x)}Br_x$ chemical structures, and in particular the composition dependent orthorhombic - cubic phase transition points. The graph shows an orthorhombic – cubic transition at ~135°C and ~320°C

and melting points at ~560°C and ~485°C for the pure $CsPbBr_3$ and $CsPbI_3$ compounds respectively. It can be noted that mixed halide compounds do not show linear changes in the phase transition temperature and the melting points with composition.

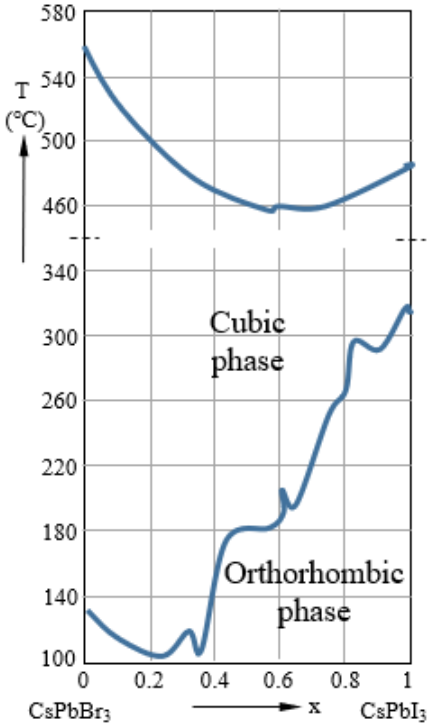


**Fig. 3.7.** Phase diagram for $CsPbI_{(3-x)}Br_x$ re-drawn from the graph reported by Sharma *et al*. (1992).[139] The graph shows the phase transition from orthorhombic to cubic phase for different halide composition in $CsPbX_3$,[139] where x = molar fraction of $CsPbI_3$.

After the experimental work for Chapter 6 was finished in 2017, new articles have been published on $CsPbI_2Br$ and $CsPbIBr_2$,[165–168] showing increased efficiencies and phase stability up to 13.3% for an encapsulated novel structured device ($FTO/NiO_x/CsPbI_2Br/ZnO/C_{60}/Ag$), with a $V_{OC}$ of 1.14 V, $J_{SC}$ of 15.2 $mA/cm^2$ and *FF* of 77%.[166] The large band gap of $CsPbI_2Br$ (1.92 eV) makes it a feasible absorber for combination with silicon or low-band gap perovskite solar cells to fabricate tandem devices in the future.

## 3.4 Deposition methods and principal device architectures for perovskite PV

### 3.4.1. Deposition methods

Perovskite thin films were prepared since 1998 by Mitzi's[169] and Kitazawa's groups[170] who presented a one-step solution spin-coating process from dimethylformamide (DMF) solution to form films for optical and electrical applications.[47,170] With the same deposition method (but using γ-butyrolactone) Miyasaka *et al.*[5] produced the first perovskite solar cell in 2009, and since then optimisation of film deposition was carried out by numerous research groups worldwide. A short description of the main methods used in the literature follows.

The deposition of perovskite thin films initially started using a solution process, which is still the most commonly adopted technique. It involves the preparation of one or more homogenous solutions containing the perovskite precursors, which are spin-coated or dip-coated to form layers which are finally heat-treated at low-temperature to dry the films and promote crystallisation. Depending on the perovskite composition, the annealing temperature may vary to optimise crystallisation.[171] This solution deposition method may be performed by using a one-step process or a sequential two-step deposition process.[5,18,77,172–175] For MAPI, the one-step solution process uses a single solution containing both $PbI_2$ and MAI precursors, normally dissolved in DMF, dimethyl sulfoxide (DMSO) or γ-butyrolactone (GBL) solvent or a mixture of these, which is then deposited to form a thin film.[5,18,172,173] The two-step process comprises the sequential deposition of two solutions. In the case of MAPI for example, the solutions are typically lead iodide in DMF and methylammonium iodide in isopropyl alcohol (IPA): the $PbI_2$ solution is deposited and later covered with the MAI solution that, by interdiffusion, interacts with $PbI_2$, and after solvent

evaporation forms MAPI. The two-step solution process may be either the sequential deposition of two solutions,[174,175] or it can be performed by dipping the first layer in the solution of the second precursor, for example the $PbI_2$ layer in a MAI solution.[77,176,177] A further technique is VASP (vapour-assisted solution process), which involves the preparation of a first layer *via* a solution process (for instance $PbI_2$) and then exposing this to an organic vapour of the second precursor (MAI).[178,179] In addition to the hybrid solution-vapour synthesis, Liu *et al.* fabricated MAPI layers by co-evaporating powders of lead iodide and methylammonium iodide.[23,180] Other more recent techniques, mainly aimed to scale-up processes, involve spray coating,[181,182] doctor blading[183,184] and die deposition techniques for roll-to-roll production.[185] All techniques produced the required compound and showed promising results in solar cell devices. However, the one-step and the two-step solution processes, and the vapour deposition are the most common techniques used up to now.[186]

Furthermore, besides the thin film deposition, perovskites have also been synthesised in the form of single crystals, in particular for the understanding physical-chemical properties,[187] such as charge diffusion length measurements,[35] or to narrow down their optical band gap without changing the composition,[188] or for the fabrication of solar cells, which however have shown poor *PCE*s up to now (0.01%).[189]

Various papers address opportunities for the improvement of deposition techniques. In the case of MAPI for example, the main problems were the concentration of the precursor solution (typically used from 10% to 40% wt.), the annealing time (from 0 to 60 min) and the annealing temperature (in the range of 40°C - 160°C).[18,190–192] For example, it was shown that the higher the annealing *T*, the lower the concentration of pores and the larger the crystals. However beyond 100°C the perovskite decomposes. Another important technique was to improve the perovskite film quality by solvent engineering. In addition to the most

common solvent used (DMF), other solvents and combinations are effective. The most important examples are GBL and DMSO, which were either mixed with DMF or were used to replace it. In addition to this, the anti-solvent method involves the dripping of an anti-solvent on the spinning perovskite layer to improve the crystallinity of the film, with the most successful choice for this procedure being toluene.[173,193,194]

By changing all these variables during the preparation of the films, the perovskite surface coverage and crystallinity may be improved, contributing to an improvement of the device current density and hence its performance.

### 3.4.2. Perovskite device architecture

When the first perovskite *dye sensitised* solar cell was constructed by Miyasaka's group, the perovskite solution was deposited onto a $TiO_2$ layer to form a photoelectrode (anode), which was surrounded by organic electrolyte solution that permitted redox reaction with a Pt-coated FTO cathode.[5] Later, perovskite *thin film* solar cells were fabricated, by maintaining the perovskite film on the scaffolding of the mesoporous titania layer (the electron transporting material) and adding a solid-state hole-transporting material (spiro-OMeTAD) on top, replacing the electrolyte.[19,20] This $TiO_2$/MAPI/spiro-OMeTAD architecture is still the most common *n-i-p* device configuration for perovskite solar cell devices, using $TiO_2$ as the electron transporting material (*n*), MAPI as the photon absorber ("*i*", intrinsic) and spiro-OMeTAD as the hole transporting material (*p*) which structure is shown in Fig. 3.8.

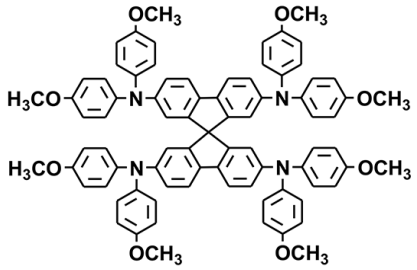

**Fig. 3.8.** Chemical structure of spiro-OMeTAD, commonly used as hole transporting material in *n-i-p* perovskite solar cell devices.

Despite the literature reports that the presence of the hole-transporting material improves the device performance, it was proved that its presence is not necessary for the device to work: devices without spiro-OMeTAD produced a *PCE* of about 5%,[195] which increased to 12.8% *PCE* when a double layer of mp-$TiO_2$ and mp-$ZrO_2$ were used as scaffold.[78] Edri *et al.*, believed that the *p-i-n* junction is in fact a sum of two heterojunctions: the *p-i* and the *n-i* junctions in series, which together contribute to increase the $V_{OC}$, explaining the high efficiency achieved by these devices.[196] Once the photons are absorbed in the perovskite material, electron-hole pairs are generated by the weakly bounded excitons, and carriers drift towards the hole and electron transporting materials and then to the contacts. Fig. 3.9 shows the band alignment of the device configuration (ITO/$TiO_2$/MAPI/spiro-OMeTAD/Au) that is reported here in order to explain why the choice of these transporting materials is appropriate. The band diagram shows the energy levels of the semiconductors and Ohmic contacts before and after equilibrium (Figs. 3.9a and b respectively), which is supported by theoretical data from the literature.[197] The band bending between the conduction bands of MAPI and $TiO_2$ allows electrons formed after the photo-absorption in MAPI to drift towards the electron transporting material, which in turn passes the electrons to the front contact (ITO) without energetic losses. Similarly, a second field is located between the MAPI and spiro-OMeTAD, which allows holes to easily drift towards the hole transporting material and further to the Ohmic back contact (Au). An abrupt

discontinuity can be observed between MAPI and spiro-OMeTAD's conduction bands and between MAPI and titania's valence bands: these are beneficial as they block electrons and holes to go in the direction where recombination would take place. Therefore this device architecture appears ideal for MAPI perovskite solar cells.

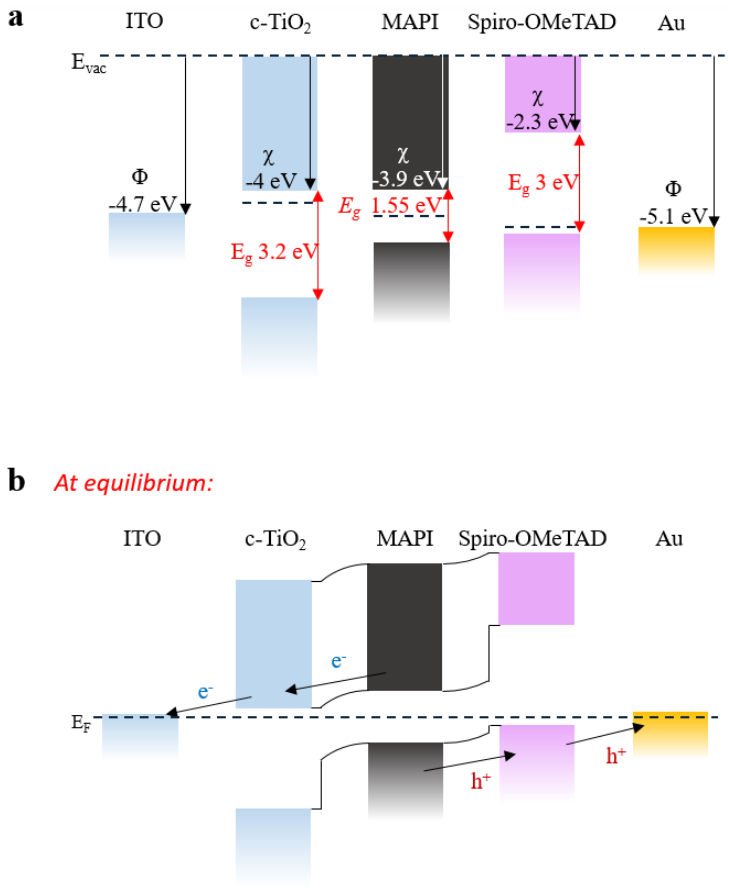


**Fig. 3.9.** Band diagrams of perovskite solar cells with the device structure glass/ITO/$TiO_2$/MAPI/spiro-OMeTAD/Au, made by using energy data from the literature and assuming MAPI an intrinsic material.[197] Fermi levels of titania and spiro-OMeTAD are assumed relative to their doping. a) Band energy details for each device component before equilibrium, and b) band diagram of the components in equilibrium: the Fermi level is aligned and cliffs are drawn between conduction and valence bands.

This device architecture is still commonly used for perovskite solar cells. However, issues related to the hole and electron transporting materials were found. For example, the high annealing temperature required for the preparation of the $TiO_2$ layer does not permit the development of flexible solar cell fabrication (since it requires processing temperatures < 150°C for deposition on transparent plastic films, such as PET or PET/ITO) limiting the

fabrication of perovskite solar cells to only glass substrates.[198,199] Another example relates to the presence of dopants in spiro-OMeTAD that are needed for the improvement of its conductivity, but dramatically reduce the stability of the perovskite material.[76,80,200] Therefore, in the last years new electron and hole transporting materials have been employed. Since the perovskite absorber material was maintained sandwiched between the hole and the electron materials, the new structure could form both *n-i-p* (substrate/TCO/HTM/perovskite/ETM/metal contact) or *p-i-n* (substrate/TCO/ETM/perovskite/HTM/metal contact) architectures by simply inverting the polarity of the device. The main device architectures used in the literature are shown in Fig. 3.10.[186] Fig. 3.10a shows the most common *n-i-p* structure with $TiO_2$ as ETM and spiro-OMeTAD as HTM. In the case of *p-i-n* devices, or the *inverted* device structure, P. Docampo's group has shown in 2013 that it was possible to replace the most common transporting material with those used more conventionally in organic solar cell devices, these being poly(3,4-ethylenedioxythiophene) poly(styrenesulphonate) (PEDOT:PSS) as the *p*-semiconductor and [6,6]-phenyl-$C_{61}$-butyric acid methyl (PCBM) as the *n*-seminconductor.[201] With the following device architecture: substrate/FTO/PEDOT:PSS/$CH_3NH_3PbI_{3-x}Cl_x$/PCBM/$TiO_x$/Al (Fig. 3.10b) they produced a solar cell having 10% *PCE*.[201] The advantage of using these polymers is that the processing temperatures for perovskite devices decreases.[202,203] Furthermore, researchers proved that these alternative organic transporting materials produce devices with negligible hysteresis,[204–207] but unfortunately the device performances are lower compared to the traditional *n-i-p* configuration, the best *PCE* reported being in the range 12 – 18%.[208–212]

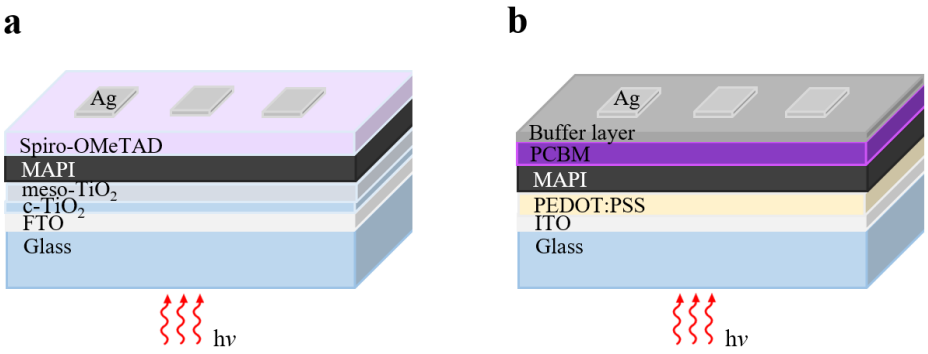


**Fig. 3.10.** Typical a) *n-i-p* and b) *p-i-n* device architectures.

## 3.5. References


1. Veldhuis, S. A. *et al.* Perovskite Materials for Light-Emitting Diodes and Lasers. *Adv. Mater.* **28**, 6804–6834 (2016).
2. Moniruddin, M. *et al.* Recent progress on perovskite materials in photovoltaic and water splitting applications. *Mater. Today Energy* **7**, 246–259 (2018).
3. Voorhoeve, R. J. H., Johnson, D. W., Remeika, J. P. & Gallagher, P. K. Perovskite oxides: Materials science in catalysis. *Science.* **195**, 827–833 (1977).
4. Rose, G. Web of Science Core Collection - Clarivate. *Ann. Phys.* **124**, 551573 (2018).
5. Kojima, A., Teshima, K., Shirai, Y. & Miyasaka, T. Organometal halide perovskites as visible-light sensitizers for photovoltaic cells. *J. Am. Chem. Soc.* **131**, 6050–6051 (2009).
6. Rose, G. Beschreibung einiger neun Mineraliem des Urals. *Ann. der Phys. und Chemie* **124**, 551–577 (1839).
7. Wells, H. L. Über die Cäsium- und Kalium-Bleihalogenide. *Zeitschrift für Anorg. Chemie* **3**, 195–210 (1893).
8. Møller, C. K. Crystal Structure and Photoconductivity of Cæsium Plumbohalides. *Nature* **182**, 1436–1436 (1958).
9. Weber, D. $CH_3NH_3PbX_3$, ein Pb(II)-System mit kubischer Perowskitstruktur $CH_3NH_3PbX_3$, a Pb(II)-System with Cubic Perovskite Structure. **33**, 1443–1445 (1978).
10. Grätzel, M. The light and shade of perovskite solar cells. *Nat. Mater.* **13**, 838–842 (2014).
11. Poglitsch, A. & Weber, D. Dynamic disorder in methylammoniumtrihalogenoplumbates (II) observed by millimeter-wave spectroscopy. *J. Chem. Phys.* **87**, 6373–6378 (1987).
12. Onoda-Yamamuro, N., Yamamuro, O., Matsuo, T. & Suga, H. p-T phase relations of $CH_3NH_3PbX_3$(X = Cl, Br, I) crystals. *J. Phys. Chem. Solids* **53**, 277–281 (1992).

13. Stoumpos, C. C. & Kanatzidis, M. G. The Renaissance of Halide Perovskites and Their Evolution as Emerging Semiconductors. *Acc. Chem. Res.* **48**, 2791–2802 (2015).

14. Lee, J.-W., Seol, D.-J., Cho, A.-N. & Park, N.-G. High-Efficiency Perovskite Solar Cells Based on the Black Polymorph of $HC(NH_2)_2PbI_3$. *Adv. Mater.* **26**, 4991–4998 (2014).

15. Goldschmidt, V. M. Die Gesetze der Krystallochemie. *Naturwissenschaften* **14**, 477–485 (1926).

16. Dastidar, S. *et al.* High Chloride Doping Levels Stabilize the Perovskite Phase of Cesium Lead Iodide. *Nano Lett.* **16**, 3563–3570 (2016).

17. Li, Z. *et al.* Stabilizing Perovskite Structures by Tuning Tolerance Factor: Formation of Formamidinium and Cesium Lead Iodide Solid-State Alloys. *Chem. Mater.* **28**, 284–292 (2016).

18. Im, J.-H., Lee, C.-R., Lee, J.-W., Park, S.-W. & Park, N.-G. 6.5% efficient perovskite quantum-dot-sensitized solar cell. *Nanoscale* **3**, 4088–93 (2011).

19. Kim, H.-S. *et al.* Lead Iodide Perovskite Sensitized All-Solid-State Submicron Thin Film Mesoscopic Solar Cell with Efficiency Exceeding 9%. *Sci. Rep.* **2**, 591–603 (2012).

20. Lee, M. M., Teuscher, J., Miyasaka, T., Murakami, T. N. & Snaith, H. J. Efficient hybrid solar cells based on meso-superstructured organometal halide perovskites. *Science.* **338**, 643–647 (2012).

21. Yang, W. S. *et al.* Iodide management in formamidinium-lead-halide-based perovskite layers for efficient solar cells. *Science.* **356**, 1376–1379 (2017).

22. Correa-Baena, J.-P. *et al.* Identifying and suppressing interfacial recombination to achieve high open-circuit voltage in perovskite solar cells. *Energy Environ. Sci.* **10**, 1207–1212 (2017).

23. Liu, M., Johnston, M. B. & Snaith, H. J. Efficient planar heterojunction perovskite solar cells by vapour deposition. *Nature* **501**, 395–398 (2013).

24. NREL efficiency chart 2018. Available at: https://www.nrel.gov/pv/assets/images/efficiency-chart.png. (Accessed: 5th July 2018)

25. Bi, D. *et al.* Polymer-templated nucleation and crystal growth of perovskite films for solar cells with efficiency greater than 21%. *Nat. Energy* **1**, 16142–16147 (2016).

26. Rajagopal, A. *et al.* Highly Efficient Perovskite–Perovskite Tandem Solar Cells Reaching 80% of the Theoretical Limit in Photovoltage. *Adv. Mater.* **29**, 1702140–1702150 (2017).

27. Eperon, G. E. *et al.* Perovskite-perovskite tandem photovoltaics with optimized band gaps. *Science.* **354**, 861–865 (2016).

28. Duong, T. *et al.* Rubidium Multication Perovskite with Optimized Bandgap for Perovskite-Silicon Tandem with over 26% Efficiency. *Adv. Energy Mater.* **7**, 1700228–1700239 (2017).

29. Yamada, Y., Nakamura, T., Endo, M., Wakamiya, A. & Kanemitsu, Y. Near-band-edge optical responses of solution-processed organic-inorganic hybrid perovskite $CH_3NH_3PbI_3$ on mesoporous $TiO_2$ electrodes. *Appl. Phys. Express* **7**, 032302–032306 (2014).

30. Phillips, L. J. *et al.* Maximizing the optical performance of planar $CH_3NH_3PbI_3$ hybrid perovskite heterojunction stacks. *Sol. Energy Mater. Sol. Cells* **147**, 327–333 (2016).

31. Even, J., Pedesseau, L. & Katan, C. Analysis of Multivalley and Multibandgap Absorption and Enhancement of Free Carriers Related to Exciton Screening in Hybrid Perovskites. *J. Phys. Chem. C* **118**, 11566–11572 (2014).

32. Miyata, A. *et al.* Direct measurement of the exciton binding energy and effective masses for charge carriers in organic–inorganic tri-halide perovskites. *Nat. Phys.* **11**, 582–587 (2015).

33. Wehrenfennig, C., Eperon, G. E., Johnston, M. B., Snaith, H. J. & Herz, L. M. High charge carrier mobilities and lifetimes in organolead trihalide perovskites. *Adv. Mater.* **26**, 1584–1589 (2014).

34. Stranks, S. D. *et al.* Electron-hole diffusion lengths exceeding 1 micrometer in an organometal trihalide perovskite absorber. *Science* **342**, 341–4 (2013).

35. Dong, Q. *et al.* Electron-hole diffusion lengths > 175mum in solution-grown $CH_3NH_3PbI_3$ single crystals. *Science.* **347**, 967–970 (2015).

36. Azarhoosh, P., McKechnie, S., Frost, J. M., Walsh, A. & Van Schilfgaarde, M. Relativistic origin of slow electron-hole recombination in hybrid halide perovskite solar cells. *APL Mater.* **4**, 1–19 (2016).

37. Du, T. *et al.* Elucidating the Origins of Subgap Tail States and Open-Circuit Voltage in Methylammonium Lead Triiodide Perovskite Solar Cells. *Adv. Funct. Mater.* 1801808–1801819 (2018). doi:10.1002/adfm.201801808

38. Soe, C. M. M. *et al.* Room Temperature Phase Transition in Methylammonium Lead Iodide Perovskite Thin Films Induced by Hydrohalic Acid Additives. *ChemSusChem* **9**, 2656–2665 (2016).

39. Baikie, T. *et al.* Synthesis and crystal chemistry of the hybrid perovskite $(CH_3NH_3)PbI_3$ for solid-state sensitised solar cell applications. *J. Mater. Chem. A* **1**, 5628–5641 (2013).

40. Onoda-Yamamuro, N., Matsuo, T. & Suga, H. Calorimetric and IR spectroscopic studies of phase transitions in methylammonium trihalogenoplumbates (II). *J. Phys. Chem. Solids* **51**, 1383–1395 (1990).

41. Harwell, J. R. *et al.* Probing the energy levels of perovskite solar cells: Via Kelvin probe and UV ambient pressure photoemission spectroscopy. *Phys. Chem. Chem. Phys.* **18**, 19738–19745 (2016).

42. Miller, E. M. *et al.* Substrate-controlled band positions in $CH_3NH_3PbI_3$ perovskite films. *Phys. Chem. Chem. Phys.* **16**, 22122–22130 (2014).

43. Wang, Q. *et al.* Qualifying composition dependent p and n self-doping in $CH_3NH_3PbI_3$. *Appl. Phys. Lett.* **105**, 163508–163516 (2014).

44. Zohar, A. *et al.* What Is the Mechanism of $MAPbI_3$ p-Doping by $I_2$? Insights from Optoelectronic Properties. *ACS Energy Lett.* **2**, 2408–2414 (2017).

45. Yin, W.-J., Shi, T. & Yan, Y. Unusual defect physics in $CH_3NH_3PbI_3$ perovskite solar cell absorber. *Appl. Phys. Lett.* **104**, 063903–063908 (2014).

46. Walsh, A., Scanlon, D. O., Chen, S., Gong, X. G. & Wei, S. H. Self-regulation mechanism for charged point defects in hybrid halide perovskites. *Angew. Chemie - Int. Ed.* **54**, 1791–1794 (2015).

47. Kitazawa, N., Watanabe, Y. & Nakamura, Y. Optical properties of $CH_3NH_3PbX_3$ (X = halogen) and their mixed-halide crystals. *J. Mater. Sci.* **37**, 3585–3587 (2002).

48. Protesescu, L. *et al.* Nanocrystals of Cesium Lead Halide Perovskites ($CsPbX_3$, X = Cl, Br, and I): Novel Optoelectronic Materials Showing Bright Emission with Wide Color Gamut. *Nano Lett.* **15**, 3692–3696 (2015).

49. Noel, N. K. *et al.* Lead-Free Organic-Inorganic Tin Halide Perovskites for Photovoltaic Applications. *Energy Environ. Sci.* **7**, 3061–3068 (2014).

50. Stoumpos, C. C., Malliakas, C. D. & Kanatzidis, M. G. Semiconducting tin and lead iodide perovskites with organic cations: Phase transitions, high mobilities, and near-infrared photoluminescent properties. *Inorg. Chem.* **52**, 9019–9038 (2013).

51. Saliba, M. *et al.* Incorporation of rubidium cations into perovskite solar cells improves photovoltaic performance. *Science.* **354**, 206–209 (2016).

52. Eperon, G. E. *et al.* Formamidinium lead trihalide: a broadly tunable perovskite for efficient planar heterojunction solar cells. *Energy Environ. Sci.* **7**, 982–988 (2014).

53. Hao, F., Stoumpos, C. C., Chang, R. P. H. & Kanatzidis, M. G. Anomalous band gap behavior in mixed Sn and Pb perovskites enables broadening of absorption spectrum in solar cells. *J. Am. Chem. Soc.* **136**, 8094–9 (2014).

54. Noh, J. H., Im, S. H., Heo, J. H., Mandal, T. N. & Seok, S. Il. Chemical management for colorful, efficient, and stable inorganic-organic hybrid nanostructured solar cells. *Nano Lett.* **13**, 1764–1769 (2013).

55. CENELEC. Review of Performance Testing Requirements for Photovoltaic Modules - Quality Digest. (2015). Available at: https://www.qualitydigest.com/inside/twitter-ed/review-performance-testing-requirements-photovoltaic-modules.html. (Accessed: 10th May 2018)

56. Cincinnati Sub-Zero Industrial. Photovoltaic Module & Solar Panel Environmental Testing Guide. 1–12 (2016). Available at: http://www.cszindustrial.com/portals/1/pdf/Solar_Panel_Testing_Guide.pdf. (Accessed: 10th May 2018)

57. Roesch, R. *et al.* Procedures and practices for evaluating thin-film solar cell stability. *Adv. Energy Mater.* **5**, 1501407–31 (2015).

58. Asghar, M. I., Zhang, J., Wang, H. & Lund, P. D. Device stability of perovskite solar cells – A review. *Renewable and Sustainable Energy Reviews* **77**, 131–146 (2017).

59. Domanski, K. *et al.* Not All That Glitters Is Gold: Metal-Migration-Induced Degradation in Perovskite Solar Cells. *ACS Nano* **10**, 6306–6314 (2016).

60. Kato, Y. *et al.* Silver Iodide Formation in Methyl Ammonium Lead Iodide Perovskite Solar Cells with Silver Top Electrodes. *Adv. Mater. Interfaces* **2**, 1500195–1500201 (2015).

61. You, J. *et al.* Improved air stability of perovskite solar cells via solution-processed metal oxide transport layers. *Nat. Nanotechnol.* **11**, 75–81 (2015).

62. Guerrero, A. *et al.* Interfacial Degradation of Planar Lead Halide Perovskite Solar Cells. *ACS Nano* **10**, 218–224 (2016).

63. Guarnera, S. *et al.* Improving the Long-Term Stability of Perovskite Solar Cells with a Porous $Al_2O_3$ Buffer Layer. *J. Phys. Chem. Lett.* **6**, 432–437 (2015).

64. Zhang, H. *et al.* Pinhole-Free and Surface-Nanostructured $NiO_x$ Film by Room-Temperature Solution Process for High-Performance Flexible Perovskite Solar Cells with Good Stability and Reproducibility. *ACS Nano* **10**, 1503–1511 (2016).

65. Li, W. *et al.* Enhanced UV-light stability of planar heterojunction perovskite solar cells with caesium bromide interface modification. *Energy Environ. Sci.* **9**, 490–498 (2016).

66. Wei, D. *et al.* Photo-induced degradation of lead halide perovskite solar cells caused by the hole transport layer/metal electrode interface. *J. Mater. Chem. A* **4**, 1991–1998 (2016).

67. Zhang, F., Yang, X., Cheng, M., Wang, W. & Sun, L. Boosting the efficiency and the stability of low cost perovskite solar cells by using CuPc nanorods as hole transport material and carbon as counter electrode. *Nano Energy* **20**, 108–116 (2016).

68. Abate, A. *et al.* Silolothiophene-linked triphenylamines as stable hole transporting materials for high efficiency perovskite solar cells. *Energy Environ. Sci.* **8**, 2946–2953 (2015).

69. Binek, A., Hanusch, F. C., Docampo, P. & Bein, T. Stabilization of the Trigonal High-Temperature Phase of Formamidinium Lead Iodide. *J. Phys. Chem. Lett.* **6**, 1249–1253 (2015).

70. Jiang, J., Onwudinanti, C. K., Hatton, R. A., Bobbert, P. A. & Tao, S. Stabilizing Lead-Free All-Inorganic Tin Halide Perovskites by Ion Exchange. *Journal of Physical Chemistry C* **122**, 17660–17667 (2018).

71. Green, M. A., Ho-Baillie, A. & Snaith, H. J. The emergence of perovskite solar cells. *Nat. Photonics* **8**, 506–514 (2014).

72. Ansari, M. I. H., Qurashi, A. & Nazeeruddin, M. K. Frontiers, opportunities, and challenges in perovskite solar cells: A critical review. *J. Photochem. Photobiol. C Photochem. Rev.* **35**, 1–24 (2018).

73. Hoke, E. T. *et al.* Reversible photo-induced trap formation in mixed-halide hybrid perovskites for photovoltaics. *Chem. Sci.* **6**, 613–617 (2015).

74. Yuan, H. *et al.* Degradation of Methylammonium Lead Iodide Perovskite Structures through Light and Electron Beam Driven Ion Migration. *J. Phys. Chem. Lett.* **7**, 561–566 (2016).

75. Jin, Y. & Chumanov, G. Fabrication of Lead Halide Perovskite Film by Controlling

Reactivity at Room Temperature in Mixed Solvents. *Chem. Lett.* **43**, 1722–1724 (2014).

76. Niu, G., Guo, X. & Wang, L. Review of recent progress in chemical stability of perovskite solar cells. *J. Mater. Chem. A* **3**, 8970–8980 (2015).

77. Burschka, J. *et al.* Sequential deposition as a route to high-performance perovskite-sensitized solar cells. *Nature* **499**, 316–319 (2013).

78. Mei, A. *et al.* A hole-conductor-free, fully printable mesoscopic perovskite solar cell with high stability. *Science*, **345**, 295–298 (2014).

79. McGehee, M. D. Perovskite solar cells: Continuing to soar. *Nat. Mater.* **13**, 845–846 (2014).

80. Yang, J., Siempelkamp, B. D., Liu, D. & Kelly, T. L. Investigation of $CH_3NH_3PbI_3$ degradation rates and mechanisms in controlled humidity environments using in situ techniques. *ACS Nano* **9**, 1955–1963 (2015).

81. Niu, G. *et al.* Study on the stability of $CH_3NH_3PbI_3$ films and the effect of post-modification by aluminum oxide in all-solid-state hybrid solar cells. *J. Mater. Chem. A* **2**, 705–710 (2014).

82. Frost, J. M. *et al.* Atomistic origins of high-performance in hybrid halide perovskite solar cells. *Nano Lett.* **14**, 2584–90 (2014).

83. Christians, J. A., Miranda Herrera, P. A. & Kamat, P. V. Transformation of the Excited State and Photovoltaic Efficiency of $CH_3NH_3PbI_3$ Perovskite upon Controlled Exposure to Humidified Air. *J. Am. Chem. Soc.* **137**, 1530–1538 (2015).

84. Leguy, A. M. A. *et al.* Reversible Hydration of $CH_3NH_3PbI_3$ in Films, Single Crystals, and Solar Cells. *Chem. Mater.* **27**, 3397–3407 (2015).

85. Leijtens, T. *et al.* Stability of metal halide perovskite solar cells. *Adv. Energy Mater.* **5**, 1500963–1500986 (2015).

86. Leijtens, T. *et al.* Mapping electric field-induced switchable poling and structural degradation in hybrid lead halide perovskite thin films. *Adv. Energy Mater.* **5**, 1500962–1500973 (2015).

87. Habisreutinger, S. N. *et al.* Carbon nanotube/polymer composites as a highly stable hole collection layer in perovskite solar cells. *Nano Lett.* **14**, 5561–5568 (2014).

88. Jørgensen, M., Norrman, K. & Krebs, F. C. Stability/degradation of polymer solar cells. *Sol. Energy Mater. Sol. Cells* **92**, 686–714 (2008).

89. Hinsch, A. *et al.* Long-term stability of dye-sensitised solar cells. *Prog. Photovoltaics Res. Appl.* **9**, 425–438 (2001).

90. Leijtens, T. *et al.* Overcoming ultraviolet light instability of sensitized $TiO_2$ with meso-superstructured organometal tri-halide perovskite solar cells. *Nat. Commun.* **4**, 2885–2893 (2013).

91. Ito, S., Tanaka, S., Manabe, K. & Nishino, H. Effects of surface blocking layer of $Sb_2S_3$ on nanocrystalline $TiO_2$ for $CH_3NH_3PbI_3$ perovskite solar cells. *J. Phys. Chem. C* **118**, 16995–17000 (2014).

92. Aristidou, N. *et al.* The Role of Oxygen in the Degradation of Methylammonium Lead Trihalide Perovskite Photoactive Layers. *Angew. Chemie - Int. Ed.* **54**, 8208–8212 (2015).

93. O'Mahony, F. T. F. *et al.* Improved environmental stability of organic lead trihalide perovskite-based photoactive-layers in the presence of mesoporous $TiO_2$. *J. Mater. Chem. A* **3**, 7219–7223 (2015).

94. Bryant, D. *et al.* Light and oxygen induced degradation limits the operational stability of methylammonium lead triiodide perovskite solar cells. *Energy Environ. Sci.* **9**, 1655–1660 (2016).

95. Aristidou, N. *et al.* Fast oxygen diffusion and iodide defects mediate oxygen-induced degradation of perovskite solar cells. *Nat. Commun.* **8**, 15218–15227 (2017).

96. Kautsky, H. Quenching of luminescence by oxygen. *Trans. Faraday Soc.* **35**, 216–219 (1939).

97. Abdou, M. S. A., Orfino, F. P., Son, Y. & Holdcroft, S. Interaction of Oxygen with Conjugated Polymers: Charge Transfer Complex Formation with Poly(3-alkylthiophenes). *J. Am. Chem. Soc.* **119**, 4518–4524 (1997).

98. Han, Y. *et al.* Degradation observations of encapsulated planar $CH_3NH_3PbI_3$ perovskite solar cells at high temperatures and humidity. *J. Mater. Chem. A* **3**, 8139–8147 (2015).

99. Weerasinghe, H. C., Dkhissi, Y., Scully, A. D., Caruso, R. A. & Cheng, Y.-B. Encapsulation for improving the lifetime of flexible perovskite solar cells. *Nano Energy* **18**, 118–125 (2015).

100. Correa-Baena, J.-P. *et al.* The rapid evolution of highly efficient perovskite solar cells. *Energy Environ. Sci.* **10**, 710–727 (2017).

101. Grätzel, M. The Rise of Highly Efficient and Stable Perovskite Solar Cells. *Acc. Chem. Res.* **50**, 487–491 (2017).

102. Zhu, X. *et al.* Superior stability for perovskite solar cells with 20% efficiency using vacuum co-evaporation. *Nanoscale* **9**, 12316–12323 (2017).

103. Abate, A. *et al.* Supramolecular Halogen Bond Passivation of Organic–Inorganic Halide Perovskite Solar Cells. *Nano Lett.* **14**, 3247–3254 (2014).

104. Li, X. *et al.* Improved performance and stability of perovskite solar cells by crystal crosslinking with alkylphosphonic acid ω-ammonium chlorides. *Nat. Chem.* **7**, 703–711 (2015).

105. Noel, N. K. *et al.* Enhanced Photoluminescence and Solar Cell Performance via Lewis Base Passivation of Organic–Inorganic Lead Halide Perovskites. *ACS Nano* **8**, 9815–9821 (2014).

106. Grancini, G. *et al.* One-Year stable perovskite solar cells by 2D/3D interface engineering. *Nat. Commun.* **8**, 15684–15692 (2017).

107. Matteocci, F. *et al.* Solid-state solar modules based on mesoscopic organometal halide perovskite: a route towards the up-scaling process. *Phys. Chem. Chem. Phys.* **16**, 3918–3923 (2014).

108. Tran, C. D. T., Liu, Y., Thibau, E. S., Llanos, A. & Lu, Z.-H. Stability of organometal perovskites with organic overlayers. *AIP Adv.* **5**, 087185–087192 (2015).

109. Najafi, M. *et al.* Highly Efficient and Stable Flexible Perovskite Solar Cells with Metal Oxides Nanoparticle Charge Extraction Layers. *Small* **14**, 1702775–1702785 (2018).

110. Christians, J. A. *et al.* Tailored interfaces of unencapsulated perovskite solar cells for >1,000 hour operational stability. *Nat. Energy* **3**, 68–74 (2018).

111. Conings, B. *et al.* Intrinsic Thermal Instability of Methylammonium Lead Trihalide Perovskite. *Adv. Energy Mater.* **5**, 1500477–1500485 (2015).

112. Dualeh, A., Gao, P., Seok, S. Il, Nazeeruddin, M. K. & Grätzel, M. Thermal behavior of methylammonium lead-trihalide perovskite photovoltaic light harvesters. *Chem. Mater.* **26**, 6160–6164 (2014).

113. Bi, C. *et al.* Understanding the formation and evolution of interdiffusion grown organolead halide perovskite thin films by thermal annealing. *J. Mater. Chem. A* **2**, 18508–18514 (2014).

114. Philippe, B. *et al.* Chemical and electronic structure characterization of lead halide perovskites and stability behavior under different exposures-A photoelectron spectroscopy investigation. *Chem. Mater.* **27**, 1720–1731 (2015).

115. Yang, J., Siempelkamp, B. D., Mosconi, E., De Angelis, F. & Kelly, T. L. Origin of the Thermal Instability in $CH_3NH_3PbI_3$ Thin Films Deposited on ZnO. *Chem. Mater.* **27**, 4229–4236 (2015).

116. Wang, D., Wright, M., Elumalai, N. K. & Uddin, A. Stability of perovskite solar cells. *Sol. Energy Mater. Sol. Cells* **147**, 255–275 (2016).

117. Supasai, T., Rujisamphan, N., Ullrich, K., Chemseddine, A. & Dittrich, T. Formation of a passivating $CH_3NH_3PbI_3/PbI_2$ interface during moderate heating of $CH_3NH_3PbI_3$ layers. *Appl. Phys. Lett.* **103**, 183906–183909 (2013).

118. Pistor, P., Borchert, J., Fränzel, W., Csuk, R. & Scheer, R. Monitoring the phase formation of coevaporated lead halide perovskite thin films by in situ x-ray diffraction. *J. Phys. Chem. Lett.* **5**, 3308–3312 (2014).

119. Osterwald, C. R. & McMahon, T. J. History of accelerated and qualification testing of terrestrial photovoltaic modules: A literature review. *Prog. Photovoltaics Res. Appl.* **17**, 11–33 (2009).

120. Sutton, R. J. *et al.* Bandgap-Tunable Cesium Lead Halide Perovskites with High Thermal Stability for Efficient Solar Cells. *Adv. Energy Mater.* **6**, 150258–150464 (2016).

121. Trots, D. M. & Myagkota, S. V. High-temperature structural evolution of caesium and rubidium triiodoplumbates. *J. Phys. Chem. Solids* **69**, 2520–2526 (2008).

122. Mariotti, S. *et al.* Stability and Performance of $CsPbI_2Br$ Thin Films and Solar Cell Devices. *ACS Appl. Mater. Interfaces* **10**, 3750–3760 (2018).

123. Koide, N., Chiba, Y. & Han, L. Methods of Measuring Energy Conversion Efficiency in Dye-sensitized Solar Cells. *Jpn. J. Appl. Phys.* **44**, 4176–4181 (2005).

124. Park, N. G., Grätzel, M. & Miyasaka, T. *Organic-inorganic halide perovskite photovoltaics: From fundamentals to device architectures*. *Organic-Inorganic Halide Perovskite Photovoltaics: From Fundamentals to Device Architectures* (Springer, 2016). doi:10.1007/978-3-319-35114-8

125. Kim, H.-S. & Park, N.-G. Parameters Affecting I – V Hysteresis of $CH_3NH_3PbI_3$ Perovskite Solar Cells: Effects of Perovskite Crystal Size and Mesoporous $TiO_2$ Layer. *J. Phys. Chem. Lett.* **5**, 2927–2934 (2014).

126. Chen, S., Lei, L., Yang, S., Liu, Y. & Wang, Z. S. Characterization of Perovskite Obtained from Two-Step Deposition on Mesoporous Titania. *ACS Appl. Mater. Interfaces* **7**, 25770–25776 (2015).

127. Snaith, H. J. *et al.* Anomalous hysteresis in perovskite solar cells. *J. Phys. Chem. Lett.* **5**, 1511–1515 (2014).

128. Kim, H.-S. *et al.* Control of *I–V* Hysteresis in $CH_3NH_3PbI_3$ Perovskite Solar Cell. *J. Phys. Chem. Lett.* **6**, 4633–4639 (2015).

129. Zhang, H. *et al.* Dynamic interface charge governing the current-voltage hysteresis in perovskite solar cells. *Phys. Chem. Chem. Phys.* **17**, 9613–9618 (2015).

130. Correa-Baena, J.-P. *et al.* Promises and challenges of perovskite solar cells. *Science.* **358**, 739–744 (2017).

131. Chen, H. W., Sakai, N., Ikegami, M. & Miyasaka, T. Emergence of hysteresis and transient ferroelectric response in organo-lead halide perovskite solar cells. *J. Phys. Chem. Lett.* **6**, 164–169 (2015).

132. Frost, J. M., Butler, K. T. & Walsh, A. Molecular ferroelectric contributions to anomalous hysteresis in hybrid perovskite solar cells. *APL Mater.* **2**, 081506–081517 (2014).

133. Tress, W. Metal Halide Perovskites as Mixed Electronic-Ionic Conductors: Challenges and Opportunities - From Hysteresis to Memristivity. *J. Phys. Chem. Lett.* **8**, 3106–3114 (2017).

134. Li, C. *et al.* Iodine Migration and its Effect on Hysteresis in Perovskite Solar Cells. *Adv. Mater.* **28**, 2446–2454 (2016).

135. Yi, C. *et al.* Entropic stabilization of mixed A-cation $ABX_3$ metal halide perovskites for high performance perovskite solar cells. *Energy Environ. Sci.* **9**, 656–662 (2016).

136. Saliba, M. *et al.* Cesium-containing triple cation perovskite solar cells: improved stability, reproducibility and high efficiency. *Energy Environ. Sci.* **9**, 1989–1997 (2016).

137. Møller, C. K. The structure of perovskite-like cæsium plumbo trihalides. *Mat. Fys. Medd. Dan. Vid. Selsk* **32**, (1959).

138. Kondo, S., Tanaka, H. & Saito, T. Optical absorption and localized electronic states in amorphous $CsPbX_3$ , $PbX_2$ and TlX (X = Cl, Br). *J. Phys. Condens. Matter* **11**, 8155–8162 (1999).

139. Sharma, S., Weiden, N. & Weiss, A. Phase Diagrams of Quasibinary Systems of the Type: $ABX_3$ - $A'BX_3$; $ABX_3$ - $AB'X_3$, and $ABX_3$ — $ABX_3$; X = Halogen Crystal

structure / Phase diagrams / Phase transitions / X-ray diffraction. **175**, 63–80 (1992).

140. Kondo, S., Sakai, T., Tanaka, H. & Saito, T. Amorphization-induced strong localization of electronic states in $CsPbBr_3$ and $CsPbCl_3$ studied by optical absorption measurements. *Phys. Rev. B* **58**, 11401–11407 (1998).

141. Rodová, M., Brožek, J., Knížek, K. & Nitsch, K. Phase transitions in ternary caesium lead bromide. *J. Therm. Anal. Calorim.* **71**, 667–673 (2003).

142. Trots, D. M. & Myagkota, S. V. High-temperature structural evolution of caesium and rubidium triiodoplumbates. *J. Phys. Chem. Solids* **69**, 2520–2526 (2008).

143. Murtaza, G. & Ahmad, I. First principle study of the structural and optoelectronic properties of cubic perovskites $CsPbM_3$ (M=Cl, Br, I). *Phys. B Condens. Matter* **406**, 3222–3229 (2011).

144. Stoumpos, C. C. *et al.* Crystal Growth of the Perovskite Semiconductor $CsPbBr_3$: A New Material for High-Energy Radiation Detection. *Cryst. Growth Des.* **13**, 2722–2727 (2013).

145. Somma, F. *et al.* The growth, structure and optical properties of CsI-$PbI_2$ co-evaporated thin films. *Superf. y Vacío* **9**, 62–64 (1999).

146. Eperon, G. E. *et al.* Inorganic caesium lead iodide perovskite solar cells. *J. Mater. Chem. A* **3**, 19688–19695 (2015).

147. Shahiduzzaman, M. *et al.* Improved Reproducibility and Intercalation Control of Efficient Planar Inorganic Perovskite Solar Cells by Simple Alternate Vacuum Deposition of $PbI_2$ and CsI. *ACS Omega* **2**, 4464–4469 (2017).

148. Kulbak, M., Cahen, D. & Hodes, G. How Important Is the Organic Part of Lead Halide Perovskite Photovoltaic Cells? Efficient $CsPbBr_3$ Cells. *J. Phys. Chem. Lett.* **6**, 2452–2456 (2015).

149. Zhang, D., Eaton, S. W., Yu, Y., Dou, L. & Yang, P. Solution-Phase Synthesis of Cesium Lead Halide Perovskite Nanowires. *J. Am. Chem. Soc.* **137**, 9230–9233 (2015).

150. Song, J. *et al.* Quantum Dot Light-Emitting Diodes Based on Inorganic Perovskite Cesium Lead Halides ($CsPbX_3$). *Adv. Mater.* **27**, 7162–7167 (2015).

151. Protesescu, L. *et al.* Nanocrystals of Cesium Lead Halide Perovskites ($CsPbX_3$, X = Cl, Br, and I): Novel Optoelectronic Materials Showing Bright Emission with Wide Color Gamut. *Nano Lett.* **15**, 3692–3696 (2015).

152. Beal, R. E. *et al.* Cesium lead halide perovskites with improved stability for tandem solar cells. *J. Phys. Chem. Lett.* **7**, 746–751 (2016).

153. Ma, Q. *et al.* The Effect of Stoichiometry on the Stability of Inorganic Cesium Lead Mixed-Halide Perovskites Solar Cells. *J. Phys. Chem. C* **121**, 19642–19649 (2017).

154. Lau, C. F. J. *et al.* $CsPbIBr_2$ Perovskite Solar Cell by Spray-Assisted Deposition. *ACS Energy Lett.* **1**, 573–577 (2016).

155. Yakunin, S. *et al.* Low-threshold amplified spontaneous emission and lasing from colloidal nanocrystals of caesium lead halide perovskites. *Nat. Commun.* **6**, 8056–8064 (2015).

156. Liang, J. *et al.* $CsPb_{0.9}Sn_{0.1}IBr_2$ Based All-Inorganic Perovskite Solar Cells with Exceptional Efficiency and Stability. *J. Am. Chem. Soc.* **139**, 14009–14012 (2017).

157. Lau, C. F. J. *et al.* Strontium-Doped Low-Temperature-Processed $CsPbI_2Br$ Perovskite Solar Cells. *ACS Energy Lett.* **2**, 2319–2325 (2017).

158. Chang, X. *et al.* Carbon-Based $CsPbBr_3$ Perovskite Solar Cells: All-Ambient Processes and High Thermal Stability. *ACS Appl. Mater. Interfaces* **8**, 33649–33655 (2016).

159. Yantara, N. *et al.* Inorganic Halide Perovskites for Efficient Light-Emitting Diodes. *J. Phys. Chem. Lett.* **6**, 4360–4364 (2015).

160. Chen, Z., Wang, J. J., Ren, Y., Yu, C. & Shum, K. Schottky solar cells based on $CsSnI_3$ thin-films. *Appl. Phys. Lett.* **101**, 093901 (2012).

161. Brasseur, H. & Pauling, L. The Crystal Structure of Ammonium Cadmium Chloride, $NH_4CdCl_3$. *J. Am. Chem. Soc.* **60**, 2886–2890 (1938).

162. Ma, Q. *et al.* Hole Transport Layer Free Inorganic $CsPbIBr_2$ Perovskite Solar Cell by Dual Source Thermal Evaporation. doi:10.1002/aenm.201502202

163. Bi, D. *et al.* Efficient luminescent solar cells based on tailored mixed-cation perovskites. *Sci. Adv.* **2**, e1501170–e1501170 (2016).

164. Shockley, W. & Queisser, H. J. Detailed Balance Limit of Efficiency of p-n Junction Solar Cells. *J. Appl. Phys.* **32**, 510–519 (1961).

165. Swarnkar, A., Mir, W. J. & Nag, A. Can B-Site Doping or Alloying Improve Thermal- and Phase-Stability of All-Inorganic $CsPbX_3$ (X = Cl, Br, I) Perovskites? *ACS Energy Lett.* **3**, 286–289 (2018).

166. Liu, C. *et al.* All-Inorganic $CsPbI_2Br$ Perovskite Solar Cells with high efficiency exceeding 13%. *J. Am. Chem. Soc.* **140**, 3825–3828 (2018).

167. Lin, J. *et al.* Thermochromic halide perovskite solar cells. *Nat. Mater.* **17**, 261–267 (2018).

168. Duan, J., Zhao, Y., He, B. & Tang, Q. High-Purity Inorganic Perovskite Films for Solar Cells with 9.72 % Efficiency. *Angew. Chemie* **130**, 3849–3853 (2018).

169. Liang, K., Mitzi, D. B. & Prikas, M. T. Synthesis and Characterization of Organic-Inorganic Perovskite Thin Films Prepared Using a Versatile Two-Step Dipping Technique. *Chem. Mater.* **10**, 403–411 (1998).

170. Kashiwamura, S. & Kitazawa, N. Thin films of microcrystalline $(CH_3NH_3)(C_6H_5C_2H_4NH_3)_2Pb_2Br_7$ and related compounds: fabrication and optical properties. *Synth. Met.* **96**, 133–136 (1998).

171. Schwartz, R. W. Chemical Solution Deposition of Perovskite Thin Films. *Chem. Mater.* **9**, 2325–2340 (1997).

172. Hwang, I. & Yong, K. Novel CdS Hole-Blocking Layer for Photostable Perovskite Solar Cells. *ACS Appl. Mater. Interfaces* **8**, 4226–4232 (2016).

173. Ahn, N. *et al.* Highly Reproducible Perovskite Solar Cells with Average Efficiency of 18.3% and Best Efficiency of 19.7% Fabricated via Lewis Base Adduct of Lead(II)

Iodide. *J. Am. Chem. Soc.* **137**, 8696–8699 (2015).

174. Ko, H.-S., Lee, J.-W. & Park, N.-G. 15.76% efficiency perovskite solar cells prepared under high relative humidity: importance of PbI2 morphology in two-step deposition of CH3NH3PbI3. *J. Mater. Chem. A* **3**, 8808–8815 (2015).

175. Im, J. H., Kim, H. S. & Park, N. G. Morphology-photovoltaic property correlation in perovskite solar cells: One-step versus two-step deposition of CH3NH3PbI3. *APL Mater.* **2**, 081510–081518 (2014).

176. Liu, D., Gangishetty, M. K. & Kelly, T. L. Effect of $CH_3NH_3PbI_3$ thickness on device efficiency in planar heterojunction perovskite solar cells. *J. Mater. Chem. A* **2**, 19873–19881 (2014).

177. Zhang, W. *et al.* Thermal Stability-Enhanced and High-Efficiency Planar Perovskite Solar Cells with Interface Passivation. *ACS Appl. Mater. Interfaces* **9**, 38467–38476 (2017).

178. Chen, Q. *et al.* Planar Heterojunction Perovskite Solar Cells via Vapor-Assisted Solution Process. *J. Am. Chem. Soc.* **136**, 622–625 (2014).

179. Peng, Y., Jing, G. & Cui, T. High-performance perovskite solar cells fabricated by vapor deposition with optimized $PbI_2$ precursor films. *RSC Adv.* **5**, 95847–95853 (2015).

180. Momblona, C. *et al.* Efficient methylammonium lead iodide perovskite solar cells with active layers from 300 to 900nm. *APL Mater.* **2**, 081504–081511 (2014).

181. Jung, Y. S. *et al.* Differentially pumped spray deposition as a rapid screening tool for organic and perovskite solar cells. *Sci. Rep.* **6**, 20357–20366 (2016).

182. Das, S. *et al.* High-Performance Flexible Perovskite Solar Cells by Using a Combination of Ultrasonic Spray-Coating and Low Thermal Budget Photonic Curing. *ACS Photonics* **2**, 680–686 (2015).

183. Deng, Y. *et al.* Scalable fabrication of efficient organolead trihalide perovskite solar cells with doctor-bladed active layers. *Energy Environ. Sci.* **8**, 1544–1550 (2015).

184. Deng, Y., Wang, Q., Yuan, Y. & Huang, J. Vividly colorful hybrid perovskite solar cells by doctor-blade coating with perovskite photonic nanostructures. *Mater. Horizons* **2**, 578–583 (2015).

185. Hwang, K. *et al.* Toward Large Scale Roll-to-Roll Production of Fully Printed Perovskite Solar Cells. *Adv. Mater.* **27**, 1241–1247 (2015).

186. Dubey, A. *et al.* Strategic Review on Processing Routes towards Highly Efficient Perovskite Solar Cells. *J. Mater. Chem. A* **6**, 2406–2431 (2018).

187. Kollek, T. *et al.* Porous and shape-anisotropic single crystals of the semiconductor perovskite $CH_3NH_3PbI_3$ from a single-source precursor. *Angew. Chemie - Int. Ed.* **54**, 1341–1346 (2015).

188. Chen, Z. *et al.* Thin single crystal perovskite solar cells to harvest below-bandgap light absorption. *Nat. Commun.* **8**, 1890–1897 (2017).

189. Schlipf, J. *et al.* Top-Down Approaches Towards Single Crystal Perovskite Solar Cells. *Sci. Rep.* **8**, 4906–4914 (2018).

190. Etgar, L. *et al.* Mesoscopic $CH_3NH_3PbI_3/TiO_2$ Heterojunction Solar Cells. *J. Am. Chem. Soc.* **134**, 17396–17399 (2012).

191. Kim, H. B. *et al.* Mixed solvents for the optimization of morphology in solution-processed, inverted-type perovskite/fullerene hybrid solar cells. *Nanoscale* **6**, 6679–6683 (2014).

192. Kim, M. *et al.* High-Temperature-Short-Time Annealing Process for High-Performance Large-Area Perovskite Solar Cells. *ACS Nano* **11**, 6057–6064 (2017).

193. Paek, S. *et al.* From Nano- to Micrometer Scale: The Role of Antisolvent Treatment on High Performance Perovskite Solar Cells. *Chem. Mater.* **29**, 3490–3498 (2017).

194. Choi, Y. C., Lee, S. W. & Kim, D. H. Antisolvent-assisted powder engineering for controlled growth of hybrid $CH_3NH_3PbI_3$ perovskite thin films. *APL Mater.* **5**, 026101–026107 (2017).

195. Etgar, L. *et al.* Mesoscopic $CH_3NH_3PbI_3/TiO_2$ heterojunction solar cells. *J. Am. Chem. Soc.* **134**, 17396–9 (2012).

196. Edri, E. *et al.* Elucidating the charge carrier separation and working mechanism of $CH_3NH_3PbI_{3-x}Cl_x$ perovskite solar cells. *Nat. Commun.* **5**, 3461–3469 (2014).

197. Elumalai, N. K., Mahmud, M. A., Wang, D. & Uddin, A. Perovskite solar cells: Progress and advancements. *Energies* **9**, 861–881 (2016).

198. Di Giacomo, F., Fakharuddin, A., Jose, R. & Brown, T. M. Progress, challenges and perspectives in flexible perovskite solar cells. *Energy Environ. Sci.* **9**, 3007–3035 (2016).

199. Liu, D. & Kelly, T. L. Perovskite solar cells with a planar heterojunction structure prepared using room-temperature solution processing techniques. *Nat. Photonics* **8**, 133–138 (2014).

200. Li, W. *et al.* Montmorillonite as bifunctional buffer layer material for hybrid perovskite solar cells with protection from corrosion and retarding recombination. *J. Mater. Chem. A* **2**, 13587–13592 (2014).

201. Docampo, P., Ball, J. M., Darwich, M., Eperon, G. E. & Snaith, H. J. Efficient organometal trihalide perovskite planar-heterojunction solar cells on flexible polymer substrates. *Nat. Commun.* **4**, 2761 (2013).

202. Jeng, J.-Y. *et al.* $CH_3NH_3PbI_3$ perovskite/fullerene planar-heterojunction hybrid solar cells. *Adv. Mater.* **25**, 3727–32 (2013).

203. Liang, P.-W. *et al.* Additive Enhanced Crystallization of Solution-Processed Perovskite for Highly Efficient Planar-Heterojunction Solar Cells. *Adv. Mater.* **26**, 3748–3754 (2014).

204. Shao, Y., Xiao, Z., Bi, C., Yuan, Y. & Huang, J. Origin and elimination of photocurrent hysteresis by fullerene passivation in $CH_3NH_3PbI_3$ planar heterojunction solar cells. *Nat. Commun.* **5**, 5784–5791 (2014).

205. Xue, Q. *et al.* Efficient and Stable Perovskite Solar Cells via Dual Functionalization of Dopamine Semiquinone Radical with Improved Trap Passivation Capabilities. *Adv. Funct. Mater.* **28**, 1707444 (2018).

206. Bai, Y., Meng, X. & Yang, S. Interface Engineering for Highly Efficient and Stable Planar p-i-n Perovskite Solar Cells. *Adv. Energy Mater.* **8**, 1701883–1701901 (2018).

207. Bryant, D. *et al.* Observable Hysteresis at Low Temperature in 'hysteresis Free' Organic-Inorganic Lead Halide Perovskite Solar Cells. *J. Phys. Chem. Lett.* **6**, 3190–3194 (2015).

208. Li, Y. *et al.* Highly Efficient p-i-n Perovskite Solar Cells Utilizing Novel Low-Temperature Solution-Processed Hole Transport Materials with Linear π-Conjugated Structure. *Small* **12**, 4902–4908 (2016).

209. Gong, X. *et al.* Controllable Perovskite Crystallization by Water Additive for High-Performance Solar Cells. *Adv. Funct. Mater.* **25**, 6671–6678 (2015).

210. Huang, X., Wang, K., Yi, C., Meng, T. & Gong, X. Efficient Perovskite Hybrid Solar Cells by Highly Electrical Conductive PEDOT:PSS Hole Transport Layer. *Adv. Energy Mater.* **6**, 1501773–1501780 (2016).

211. Huang, D. *et al.* Perovskite solar cells with a DMSO-treated PEDOT:PSS hole transport layer exhibit higher photovoltaic performance and enhanced durability. *Nanoscale* **9**, 4236–4243 (2017).

212. Zhou, L. *et al.* Enhanced planar perovskite solar cell efficiency and stability using a perovskite/PCBM heterojunction formed in one step. *Nanoscale* **10**, 3053–3059 (2018).

# 4. Experimental methods

An overview of the main techniques and instruments used for the synthesis and characterisation of the samples is presented in this chapter.

## 4.1. Cleaning procedures and substrate preparation

### 4.1.1. Glass cleaning

Quartz coated glass (20 nm of synthetic quartz covering a glass substrate 20 x 15 $mm^2$, Ossila Ltd.) or ITO coated glass (ITO thickness 100 nm, resistance 14-16 Ω/□, 20 x 15 $mm^2$ glass slides, Ossila Ltd.) were cleaned with the following procedure: the substrates were sonicated in water for 5 - 10 minutes and then isopropyl alcohol (IPA) for other 5 - 10 minutes. The slides were dried with flowing nitrogen, taking particular care to eliminate all droplets on the sample's surface, and finally they were treated in an UV-ozone ($UV/O_3$, Ossila Ltd.) cleaner for 10 minutes to remove possible organic contaminants from the surface. At this point samples were ready to use for the deposition of materials.

*a) The UV/$O_3$ cleaner*

UV/$O_3$ cleaner uses a photo-sensitised oxidation process (adopting short wavelengths and ozone molecules), with which organic molecules are dissociated from the surface. This cleaning treatment is commonly adopted as it removes traces of solvents and oils, without causing significant surface damage. The substrates are illuminated using two wavelengths (185 nm and 254 nm). The shortest wavelength is absorbed by the oxygen present in the system and produces radicals (4.1), which react with molecular oxygen to produce ozone (4.2.).

$$O_2 \rightarrow 2O\cdot \quad (4.1)$$

$$O_2 + O\cdot \rightarrow O_3 \quad (4.2)$$

The longest wavelength is absorbed by organic molecules, forming organic radicals. These reactive species then react with the unstable ozone, forming volatile compounds ($CO_2$, $H_2O$, $N_2$ and short chain organic molecules) which desorb from the surface.

### 4.1.2. Silicon wafers

Both *n*-doped and *p*-doped crystalline silicon wafers were used for the fabrication of heterojunctions with MAPI (chapter 7) and were the following:

- *n*-Si, (100) ± 0.5°, phosphorous doped, 1 – 10 Ω·cm, 355 – 405 μm thickness, Pi-KEM Ltd;
- *n*-Si (100) ± 0.5°, phosphorous doped, 1 – 5 Ω·cm, 5 – 10 Ω·cm and 10 – 15 Ω·cm, 355 – 405 μm thickness, Mi-Net Technology Ltd;
- *p*-Si (100) ± 0.5°, boron doped, 380 μm thickness, 1-10 Ω·cm, Pi-KEM Ltd.

The wafers were cut in pieces (~2 x 1 $cm^2$) and then cleaned using an RCA procedure, which was developed by Werner Kern in 1965 while working for the *Radio Corporation of America*. This procedure is still used for cleaning the surface of silicon wafers from organic

and particle residues, and it is followed by the so called ‘oxide strip’, which is the removal of the insulating silicon oxide ($SiO_2$) surface layer (few nanometre thickness) that forms on the wafer when this is in contact with air. The RCA procedure consists in a series of treatments which are here described.

The silicon pieces were soaked in acetone at 55°C for 10 minutes and then in methanol for 5 minutes. After rinsing with abundant DI water and drying with flowing nitrogen, they were soaked for 15 minutes in a solution of $H_2O_2$ : $NH_4OH$ : $H_2O$ solution (1 : 1 : 5 by volume) that was previously boiled at 70°C until it showed distinct bubbling for ~2 minutes. After copious amounts of water were used to rinse the samples, they were dried and transferred to a water-flushed fume hood for the following ‘oxide strip’. A 2% hydrofluoric acid (HF, 49%, Merck) solution in water was prepared. The silicon wafers were then immersed in the solution for 2 minutes, using appropriate polytetrafluoroethylene (PTFE) containers. Rinsing with water followed. The effectiveness of the silicon oxide removal can be tested with an hydrophobicity check: if the HF treatment was conducted properly, water forms rounded droplets with a high contact angle on the silicon that run off, whereas if the silicon oxide is still present on the wafer surface the water creates a uniform film due to the $SiO_2$ being hydrophilic. The wafers were finally dried with a nitrogen flow and immediately transferred into a nitrogen glovebox to protect the wafer from the fast surface re-oxidation. Although this oxidation is not avoidable, it can be limited to a minimum.

## 4.2. Thin film deposition

### 4.2.1. Spin-coating technique

Spin-coating technique was the main deposition technique used in this thesis and was used for depositing perovskite, spiro-OMeTAD and $TiO_2$ thin films. While normal spin-coaters hold samples using a vacuum, the spin-coater used here (Ossila Ltd.) has a spinning disk with a well where the samples can be located (either 50 x 50 $mm^2$ or 20 x 15 $mm^2$). Spin coating was conducted in a nitrogen glovebox.

The spin-coating technique uses solutions of the material in a solvent (or ink) which are dropped onto a substrate to form a film with thicknesses in the nm – μm range. The deposition can be done a) statically, by depositing the solution on the substrate when this is in a steady position, or b) dynamically, when the solution is dropped onto a moving substrate. Normally, the dynamic spin-coating provides higher uniformity of the films, since the static spin-coating may be affected by an initial solvent evaporation before the spinning, which gives lower conformity. By applying high speed of the substrate (from 1000 rpm to 6000 rpm, rpm = revolution per minute) most of the solution is flung off the side, and the airflow promotes the solvent evaporation leaving a highly uniform thin film on the substrate surface, as shown in Fig. 4.1. The thickness is inversely proportional to the square root of the spinning velocity used, as shown in the following Equation:

$$t \propto \frac{1}{\sqrt{\omega}} \tag{4.3}$$

where: $t$ = thickness, ω = angular velocity.

Nevertheless, the thickness of the film is strictly related to the concentration of the solution and the boiling point of the solvent used, depending in turn on the temperature, viscosity and vapour pressure. Furthermore, since the spin-coater is equipped with levelling feet, the films show even thickness over the whole surface.

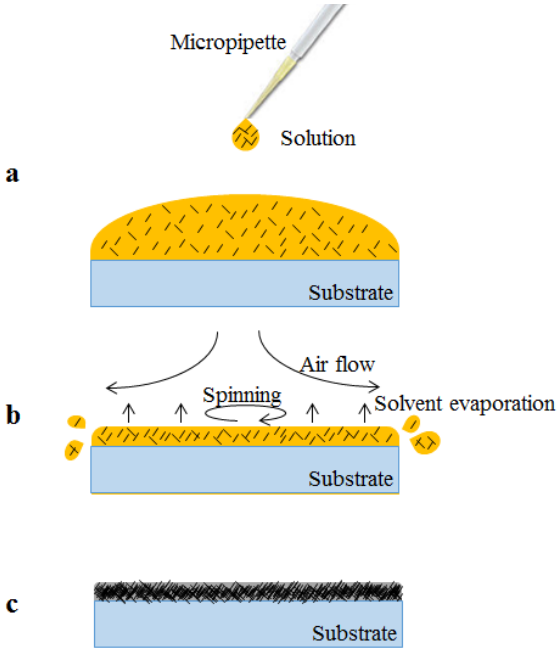


**Fig. 4.1.** Spin-coating stages: a) solution dripping, b) rotation and air flow removing the excess solution and evaporating the solvent for the formation of the thin film (c).

### 4.2.2. Thermal evaporation

Thermal evaporation was used for the deposition of metal contacts. This deposition technique is one of the most common physical vapour deposition (PVD) methods. In particular, gold (Au, 99.95%, Advent) was evaporated using a tungsten boat (W, Kurt J. Lesker) in a dedicated evaporator (Oerlikon, Univex 300), and aluminium (Al, 99.99%, Merk) was evaporated in a belljar evaporator (Moorfield M307). A piece of pure Au or Al wire was cut and deposited onto the W boat (W does not react with either metal). Evaporation took place at $10^{-5}$ – $10^{-6}$ Torr. Rotation was used for the deposition of Al, but not Au.

### 4.2.3. RF sputtering

Magnetron sputtering is a PVD technique which consists in ejecting a material from a target and depositing it onto a substrate, placed above the target at a certain distance. In

this thesis magnetron sputtering was used for the deposition of zinc oxide (ZnO target, 99.99%, Pi-KEM) films and a transparent conductive material (TCO), this being aluminium-doped zinc oxide (AZO target, 99.99%, Pi-KEM), using an AJA International Inc. ATC Orion chamber, with the chamber pumped to a base pressure of $10^{-7}$ Torr initially and then set at a working pressure of 2-10 mTorr.

The process is initiated by ionising an inert gas (in this work argon) forming a plasma. Then a high potential (direct current, DC or radio frequency, RF) is applied between the target and the substrate. Since the materials deposited in this work are semiconductors, RF sputtering was adopted, which can be used also for insulators, whereas in the case of deposition of conductive materials DC sputtering should be adopted. This potential creates ions that are accelerated toward the target, causing the ejection of particles from the target which condense on the surfaces (these that are directly pointing at the target, including the sample positioned on top of the target). Samples were rotated during deposition for higher film uniformity.

Since the chamber contains multiple sputtering 'guns' it was possible to deposit films stacks without removing the substrate from the chamber. This advantage allows also to co-sputter different compounds simultaneously, however this technique was not used in this work.

## 4.3. Intentional film degradation: conditions

Perovskite thin films prepared in the glovebox showed rapid degradation when exposed to air. Since the degradation causes were not yet understood, studies on the films were performed by separating environmental conditions which may be causing this degradation. Later by analysing the films visually, by X-ray diffraction and spectrophotometry, the damaging factors were identified.

The segregation environments chosen for the intentional degradation experiments were the following:

- "UV/$N_2$": samples were exposed to UV radiation (2 x 9W UV lamps, LED source, $\lambda$ = 365 nm) inside a nitrogen glovebox (< 10 ppm $H_2O$), therefore in inert atmosphere. This condition has been used to study the effect of UV light only.
- "Dark/air": films were kept in the dark and covered with aluminium foil to avoid illumination, but without being sealed and therefore exposed to air. In this way, the samples would be exposed only to water and/or oxygen (*i.e.* the main reacting molecules in air).
- "Desiccator": perovskite layers were kept in dry atmosphere (relative humidity < 15%) but being still exposed to the ambient light of the laboratory (although UV rays are strongly reduced since these are absorbed by the thick plastic walls of the desiccator container). This condition evaluated the effect of reduced humidity but in the presence of oxygen.
- "UV/$O_3$": samples were put in an UV-ozone cleaner (section 4.1.1) in order to expose the material to UV and oxygen. As explained in the literature review (section 3.3.1.a, *ii*) these factors are the main degradation factors for MAPI's degradation.[1–3] Since the UV/$O_3$ cleaner is positioned in a fume hood, the water vapour level is low.

Table 4.1 summarises the test conditions used to identify the origin of degradation of perovskite films. Through the use of this logic table it is possible to exclude potential causes: for example, if the sample shows degradation effects when exposed to "UV/$N_2$" and "UV/$O_3$" only (but not "dark/air" or "desiccator"), the degradation factor must be related to UV radiation since this is the only common factor.

| Test | Degradation factor | | | | |
|---|---|---|---|---|---|
| | **UV** | **$O_2$** | **$H_2O$ (vap)** | **$O_3$** | **Ambient light** |
| **UV/$N_2$** | Yes | No | No | No | No |
| **Dark/air** | No | Yes | Yes | No | No |
| **Desiccator** | No | Yes | Low | No | Yes |
| **UV/$O_3$** | Yes | Yes | Low | Yes | No |

**Table 4.1.** Test conditions for the degradation experiments used for MAPI and $CsPbI_2Br$. Each test has a small number of characteristics so that making all four test allows the factors causing degradation to be uniquely identified.

## 4.4. Material characterisation

This section presents the techniques used for the characterisation of the material in terms of physical, optical, structural and chemical properties, and is divided into film and powder characterisation.

### 4.4.1. Thin film characterisation

*a) Profilometry*

A stylus profilometer was used for the determination of thicknesses and roughness of films. A probe is moved on the surface of the sample, using a continuous predefined force between the probe and the sample, following the surface of the sample. The vertical displacement of the probe is revealed either optically or electrically.

The profilometer used for the measurements presented in this thesis was an AMBIOS, XP-200 and was mainly used for the determination of the thickness of thin films, by measuring the step in height between the substrate's surface and the film's. This step was

made by mechanically scribing the films' surface (if the material was soft enough) or by masking a small part of the substrate during the deposition.

*b) UV-Vis spectrophotometry*

Optical measurements are commonly used for the determination of the band gap of materials and can be performed in both liquid and solids. In particular in the case of UV-Vis-IR spectrophotometry (also called UV-Vis-IR for simplicity) a monochromated beam of light hits the sample and appropriate detectors detect the transmitted and reflected light and measure the ratio of light reaching the detector to the incident light. In the case of thin films, the absorption coefficient may be calculated as follows:

$$\alpha = \frac{1}{d} \ln\left[\frac{1-R^2}{T}\right] \quad (4.3)$$

Where: $\alpha$ = absorption coefficient, $d$ = film thickness, $R$ = reflectance, $T$ = transmittance.

From the absorption coefficient it is possible to measure the band gap ($E_g$) using the Tauc plot,[4] which plots $(\alpha h\nu)^n - h\nu$, where $h\nu$ is the photon energy, and $n$ is an exponent dependent on the nature of the electron transition. If the band gap is direct (vertical transition in the $E - k$ diagram, hence advantageous path in materials such as MAPI and CdTe) then $n = ½$, whereas if the band gap is indirect (not vertical in the $E - k$ diagram, such as in silicon) then $n = 2$.

In this work a Shimadzu SolidSpec-3700 UV-Vis-IR Spectrophotometer was utilised for the measurement of transmittance and reflectance of thin films, typically in a wavelength range of 300 – 1100 nm.

*c) X-ray diffraction*

X-ray diffraction (XRD) is commonly used for the structural characterisation and phase identification of crystalline materials. The most common setup for X-ray

diffractometers is the Bragg-Brentano, shown in Fig. 4.2, where a monochromatic X-ray beam is directed towards the sample with an angle θ. The beam divergence and collection angle are controlled by slits after the X-ray source and before the detector. The incident X-rays are then diffracted from the sample and reach the detector with angle 2θ. This is θ - 2θ diffractometry. The working principle is that the sample is irradiated with X-rays, and the scattering gives constructive and deconstructive interference.[5] Bragg's Law describes this effect,[6] by relating the incident X-ray wavelength ($\lambda$) to the incident angle (θ) in a lattice plane with spacing $d_{hkl}$ (*hkl* are Miller indices denoting the planes in the crystal lattice), as shown by Equation 4.4.

$$n\lambda = 2d_{hkl}\sin\theta \tag{4.4}$$

where *n* describes the order of diffraction.

When the interference is constructive the intensity of the diffracted X-rays is maximised and Bragg's peaks are recorded. Each individual compound produces a characteristic pattern ("fingerprint") and therefore this technique is used for the identification of materials and their crystallographic phases. Reference tables (JCPDS or X'pert HighScore/ICDD) may be used for comparison.

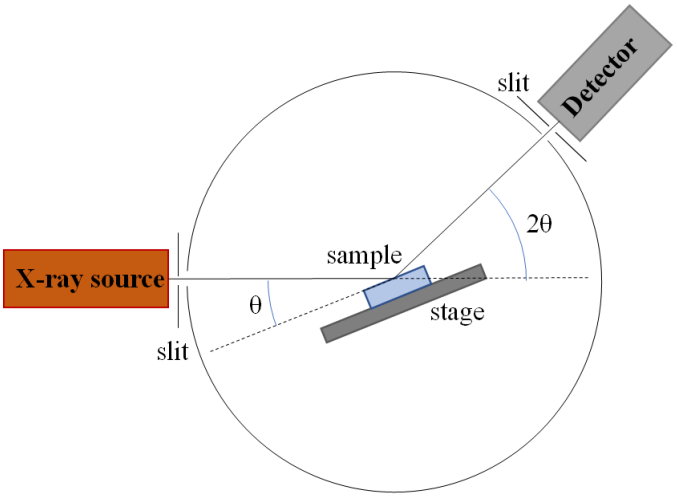


**Fig. 4.2.** Schematic representation of a Bragg-Brentano X-ray diffractometer, showing the incident angle (θ) deriving from the monochromatic X-ray source and the reflective angle (2θ) of X-rays that reach the detector from the sample.

XRD instruments may be used on both powders and thin films, however the resulting patterns may not show identical peak intensities as their crystal textures may differ. In the case of powder XRD the orientation is random, resulting in full set of peaks with different intensities, whereas thin films may have a preferred orientation, and hence a reduced number of diffraction peaks with different intensities than in the random case.

In this work both thin film and powder XRD instruments were utilised. In the case of thin film XRD two instruments were used: initially an X'Pert PRO X-ray diffraction system – Philips Analytical and later a Rigaku, SmartLab (both with a Cu X-ray tube), whereas in the case of the powder XRD a Brucker D8 Venture (Cu source) was utilised.

*d) Optical microscopy*

A Nikon eclipse LV100 optical microscope with a digital camera was used to examine the films produced in this work.

*e) Scanning electron microscopy*

Scanning electron microscopy (SEM) provides images of a sample, using an electron probe. The beam is generated by an electron source (for example a tungsten filament), the electrons are accelerated by an anode, and a series of electromagnetic lenses are used for focussing the beam onto the sample. Electrons emerging from the sample are then collected by detectors.[7] In particular, secondary electrons - low-energy electrons generated from the sample - are the main electrons collected in this technique for routine imaging. However SEM instruments may be equipped with other types of detectors (for example for the collection of back scattered electrons, transmitted electrons, X-rays, etc.) from which elemental and crystallographic information can be recorded. Secondary electrons yield high-resolution images, with down to nm resolution. In order to produce secondary electrons the

sample must be conductive whereas insulating materials must be covered with conductive material before measurement.

In this work a JEOL JSM-7001F SEM instrument was used for secondary electron imaging. Samples were mounted on a stage for the imaging of both surface and cross section, and contacted with conductive tape. According to the sample an accelerated voltage in the range of 5 – 30 kV was used. No coating was necessary for imaging the perovskite films and devices.

*f) X-ray photoelectron spectroscopy*

X-ray photoelectron spectroscopy (XPS) is a spectroscopic quantitative technique that measures the elemental composition of a compound and determines its chemical formula and the electronic state. X-rays impinge on the sample (under vacuum at $10^{-8}$ mbar or $10^{-10}$ mbar) and a detector measures the kinetic energy and the number of electrons escaping the material. This technique is used to determine the surface chemistry of a material. Here it was also used to estimate the valence band energies of the materials studied in this work.

In this work X-ray photoemission spectroscopy was performed using a PSP Vacuum Technology Al Kα X-ray source ($h\nu$ = 1486.6 eV) operating at 144 W, with a PSP electron-energy analyser operating at a pass energy of 20 eV. Photoemission measurements were performed in a standard ultrahigh vacuum chamber with a base operating pressure of ~$10^{-10}$ mbar. Samples were mounted to metallic plates and tantalum straps were spot welded to the plates contacting the sample surface to minimise charging under illumination. A small charge correction was applied to spectra using the C1s (284.8 eV) as the reference peak.

*g) Scanning tunnelling spectroscopy*

Scanning tunnelling spectroscopy (STS) is an extension of a scanning probe microscopy UHV-STM. STS is used for the determination of density of states. An atomically sharp tip is positioned very closely (a few Ångstroms) over the surface of a conductive or semiconductive sample, with the height of the tip fixed and a bias voltage applied between the tip and the sample, allowing current to flow. This is called electron tunneling current which changes accordingly to the energy of the electrons: since the electron energy is a function of the electrical potential difference (voltage) between the tip and the sample, an *I*-*V* curve is obtained. Then, by measuring the differential conductance of the *I*-*V* curve (d*I*/d*V*, Eq. 4.5), the local electron density of states (LDOS), referred to a particular position of the sample, can be calculated.[8]

$$\frac{dI}{dV}\Big|_{V=V_{bias}} \propto \int_{-\infty}^{\infty} \rho_s(E) \frac{\partial f(E-eV)}{\partial(eV)}\Big|_{V=V_{bias}} dE \qquad (4.5)$$

where: $\rho_s$ are the density of states (DOS) and $f$ is the Fermi distribution.

In this work STS was measured on a RHK Pan-style UHV-STM instrument (Department of Solid State Physics, Indian Association for the Cultivation of Science, Jadavpur, Kolkata, India).

*h) Van der Pauw method*

This measurement uses a four-point probe to measure the resistivity of a semiconductor. The instrument has four equidistant probes, positioned at the corners of a square. A current is injected in two facing probes ($I_{12}$), and the voltage is measured across the remaining probes ($V_{34}$). The resistance is therefore measured using Ohm's Law ($R_{34,12} = V_{34} / I_{12}$) and the resistivity ($\rho$) can be calculated through numerical techniques, by knowing the area measured and the thickness of the film ($t$). Since in the four point probe this area is

a square, the sheet resistance is calculated ($R_s$, Ω/□), knowing that $\rho = R_s \cdot t$. For more information about this technique consult ref.[9]

In this work an Advanced Instrument Technology CMT-SR2000N four-point probe kit was used for the determination of the resistivity of thin films of gold.

### 4.4.2. Powder characterisation

Some μl of perovskite precursor solutions (typically in DMF) were dropped onto glass slides (without spinning) and annealed at the temperature required for the material formation inside a glovebox. When the film was completely dry, this was scraped off forming perovskite powders that were used for characterisation using the following techniques.

*a) Differential scanning calorimetry – thermogravimetric analysis*

Differential scanning calorimetry (DSC) is a thermoanalytical technique which determines the difference in energy required to heat a sample (in a crucible) and a reference (typically an empty crucible). Generally the temperature is increased linearly as a function of time, therefore the spectra shows a heat flux versus temperature (or sometimes versus time), showing peaks in correspondence of exothermic or endothermic reactions with temperature. The convention for the peaks to be positive or negative relative to the exothermic or endothermic reaction depends on each instrument. Eventually the compound reaches the melting temperature, which results in an endothermic peak. This method is very useful for the determination of transition temperatures and for the fabrication of phase diagrams.

Thermogravimetric analysis (TGA) is a thermal analysis used for the determination of the mass loss over time while changing the temperature. It consists in a precision balance located in a furnace, using a temperature control which generally increases the temperature

at constant rates. This heating process may occur in air, inert gas or vacuum or specific gases for oxidation, reduction, etc. This method is useful for the determination of absorption and desorption, as well as chemisorption and thermal decomposition. Furthermore, information about the thermal stability may be obtained, as thermally unstable compounds show a mass change before melting.

Often, the DSC and TGA techniques are combined for a better understanding of the sample analysis. In this work a combined DSC-TGA instrument was used, this being a TA Instruments, SDT Q600, with powders placed in alumina crucibles with a heating rate of 10ºC/min in argon.

*b) Nuclear magnetic resonance*

Nuclear magnetic resonance spectroscopy (NMR) is a technique used for the determination of atomic environments. In the presence of an external magnetic field, the spin states of the nuclei orient in alignment or in opposite direction relative to the external magnetic field (spin up or spin down). The difference in energy between the spin states at a given magnetic field is proportional to their magnetic moment. NMR analysis not only recognises the type of atoms within the molecule, it also gives information about the position and type of chemical bond. This is possible since the electronic environment of each nucleus is different and affects the magnetic field differently, requiring slightly different energies of the applied field, hence generating a shift on the spectra (although these energetic shifts are very small, usually in parts per million). Since the signals are dependent on the solvent and the strength of the external magnetic field, it is common use to report the peaks relative to a reference signal (usually tetramethylsilane or TMS which is set at 0 ppm).

The NMR technique is mainly used for the determination of the compounds of organic molecules and produces well-resolved spectra which are easily predictable for small

molecules. The most common types of liquid NMR are the proton ($^{1}H$) and the carbon ($^{13}C$) spectra. When the nuclei are placed in a magnetic field, they absorb electromagnetic radiation at a characteristic frequency which depends on the isotope. Since the vast majority of solvents are organic solvents (hydrocarbons, which therefore contain NMR-active atoms), special solvents are utilised in order to remove the excess signal that they would generate. In the case of $^{1}H$-NMR for example, deuterated solvents are used to replace the majority of the protons with deuterium ($^{2}H$) which is much less sensitive. In this way, only the signals from the residual protons of the sample under measurement are observed. Although there are different deuterated solvent that may be used, the most common are $CDCl_3$, $D_2O$ and DMSO-$d_6$.

In this work the spectrometer used to collect $^{1}H$-NMR spectra was a 400 MHz Bruker NMR spectrometer and analysis were performed using deuterated dimethyl sulfoxide (DMSO-$d_6$).

### *c) Fourier-transform infrared spectroscopy*

Infrared spectroscopy (IR) involves the absorption of infrared radiation by matter for the study of the chemical composition. Typically this spectroscopy uses the Fourier-transform (FT), a mathematical process that allows to reduce the noise during the acquisition of high resolution data over a wide spectral range (without the need of using a monochromatic beam). The spectrum can be visualised in both transmittance and absorbance versus either wavelength or frequency. The main principle of this technique is that specific chemical structures absorb at specific frequencies, producing spectra which describe the chemical properties of the molecule, for which the main functional groups can be easily recognised. This signals are therefore called ‘fingerprints’ as they are specific for

certain chemical bonds, however, the energies may be affected by the potential energy surface, the masses of atoms, the shape of the molecule and the strength of the bond.

In order for the chemical to be infrared active it must have a dipole moment: a molecule can vibrate in numerous ways (vibrational modes), which can be detected in different parts of the spectra. The main vibrations involve stretching (radial vibrations that can be symmetric and asymmetric) and bending (scissoring and rocking for the latitudinal bending and wagging and twisting for the longitudinal bending). Therefore molecules having only one bond and only one vibrational band will not be recognised (for example $N_2$ since it is diatomic, linear and symmetrical). Usually FT-IR is measured in liquid or in solid states. In the case of liquid IR, a liquid-cell can be employed whereas the solid state measurement is performed on a small quantity of powders (in order to avoid saturation of the signal) mixed in a material transparent to IR radiation (for example KBr), which is then pressed into a compact tablet. However, modern instruments enable the measurement of solid powders and liquid directly in their state, using and attenuated total reflection (ATR) technique, avoiding the problem of the attenuation by highly absorbing materials. By using an ATR crystal (which requires to have higher reflective index compared to that of the sample) and adopting a certain angle, the changes and the attenuation of the IR light that reflects when the beam reaches the sample, are measured with a detector.

In this work powders were analysed on a Thermo Scientific Nicolet iS50 FT-IR spectrophotometer provided with diamond crystal/built in all-reflective diamond ATR. All spectra were obtained in absorbance mode and then converted to transmittance mode.

## 4.5. Solar cell characterisation

This section presents the main techniques used in this thesis for the characterisation of solar cell devices and describes how perovskite solar cells were protected by the environmental degradation during these measurements.

### 4.5.1. *J-V* measurement

Current-voltage (*I-V*) or current density-voltage (*J-V*) measurement were performed to evaluate the rectification behaviour and the efficiency of solar cell devices using AM1.5 illumination spectrum with an intensity of 1000 W/m$^2$. The calibration of the light intensity was performed using a GaAs reference cell.

The *J-V* curves were obtained measuring the current from the device during a voltage sweep from -1 to +1 V and using a scan rate of 0.19 V/s. Scans were performed in both forward (from -1 V to +1 V) and reverse (from +1 V to -1 V) directions, in order to evaluate the hysteretical behaviour of the perovskite devices. Rectification trials were performed in the dark, whereas efficiency evaluations were performed under light. In this work a TS Space Systems and an Oriel Instrument 81160 solar simulator calibrated at AM 1.5 were utilised and device measurements were carried out using a Keithley 2400 source meter and LabView software to extract the *J-V* parameters: *PCE*, $V_{OC}$, $J_{SC}$ and *FF*.

*a) Stabilised efficiency measurements*

In perovskite solar cells the efficiency of the devices requires a steady-state reading, since the efficiency measured by common *J-V* curves has been found to vary with the voltage sweep rate, the scanning direction (positive or negative) and the history of light exposure of the sample (*i.e.* whether cells were in the dark or under light soaking just before the reading).[10] In order to determine the stability of the efficiency over time, measurements of

the current density were performed by measuring 1000 consecutive points, resulting in ~70 seconds of measurement time (depending on the scan rate). The measured points were limited to a maximum of 1000, by the *J-V* software used. The voltage used for this purpose was a set value corresponding to the voltage at maximum power point ($V_{mpp}$) obtained from a *J-V* curve measurement. Therefore the current measured at the maximum power point ($I_{mpp}$) is easily transformed into $J_{mpp}$ dividing by the contact area. Hence the *PCE*, is given by $PCE = (J_{mpp} \cdot V_{mpp})/P_{in}$.

### 4.5.2. *EQE* measurement

In this work a Bentham PVE300 *EQE* system operating with a 0.75 $mm^2$ slit and using a BenWin+ remote control software was utilised. The typical wavelength range was 300 – 900 nm.

### 4.5.3. *C-V* measurement

Capacitance-Voltage (*C-V*) measurement was used in this thesis for the determination of the carrier concentration (*N*) of MAPI/silicon heterojunctions. *C-V* measurements were performed in the dark using Solartron SI 1260 impedance analyser using an interface SmartLab software from which the impedance was calculated applying a frequency of $10^5$ Hz and a voltage sweep (DC) from -1 V to +1.5V.

Once the measurements were taken, the data were introduced in a self-made Origin template for the fabrication of *C-V* and $1/C^2$ plots, from which it was possible to determine the carrier concentration (using Equations 2.20 and 2.44 for the one-sided and two-sided junctions respectively). The following dielectric constants were utilised:

- In the case of the one-sided junction the dielectric constant of the silicon was used, this being 11.7.[11]

- In the case of the two-sided junction the dielectric constant of both silicon and MAPI were used these being 11.7 and 24.1 respectively.[11,12] The junction was assumed to be half in the silicon and half in the MAPI, although this is a simplification as the exact depletion width in each part is not known.

### 4.5.4. The air-tight box

The air-tight box was built with the intention to protect perovskite devices that are easily affected (degraded) by environmental conditions, such as oxygen and water. Samples were introduced in the box inside a glovebox and therefore remained sealed in a nitrogen (inert) environment when the box was taken to air for the device measurement. In particular, the box was utilised for the measurement of MAPI and $CsPbI_2Br$ solar cells with the *p-i-n* superstrate device configuration, whereas silicon/MAPI heterojunctions could not be used within the box due to their substrate configuration.

Fig. 4.3, shows a photograph of the box, which may contain up to 4 samples: for each sample there are 5 gold coated pins, 1 for the front contact (ITO) and 4 for the back contact (gold). Each pin is connected to wires that through a feedthrough are connected to a box (Fig. 4.3, top right) that allows to select one contact at the time. The samples are positioned in the box and then pushed onto the pins using an aluminium plate which is hold in place using 4 screws. This aluminium plate masks the samples, except for the holes of 2 mm Ø which are positioned in correspondence of the gold contacts of the devices. During the measurement, light from the solar simulator or the *EQE* kit passes through a quartz plate positioned on top of the sample holder. Quartz was favoured to glass because it is more transparent. Once light reaches the samples, the current that is produced from the devices is sent through electrical connections to the measurement kits.

This nitrogen filled box was helpful for the measurement of devices: results were not affected by environmental degradation and could protect samples for up to 3 days, allowing further measurements to be taken.

For *J-V* measurements with the air-tight box only the Oriel Instrument 81160 solar simulator was utilised.

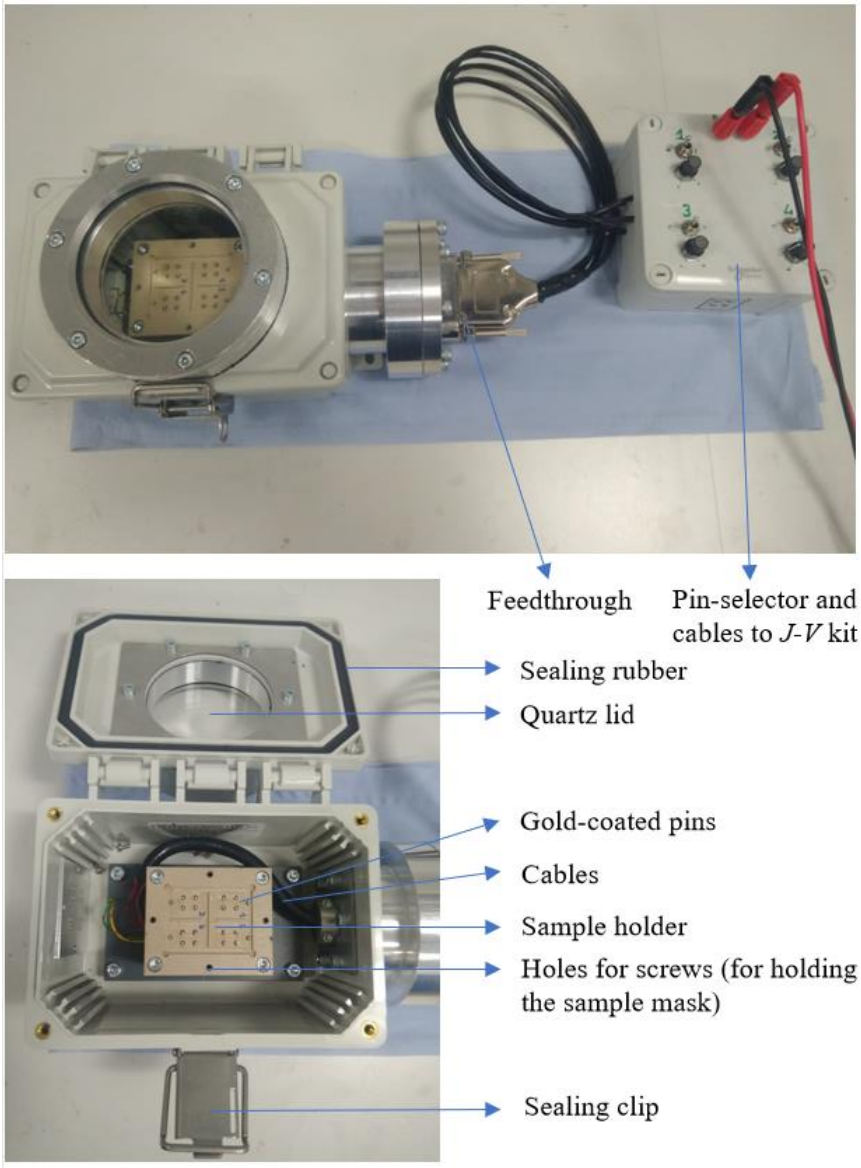


**Fig. 4.3.** Photograph of the air tight box used for *J-V* or *EQE* measurements with closed (top) and open (bottom) lid. The solar cells were loaded into the box in the glovebox and transferred to the solar simulator or *EQE* apparatus for measurement. The sample are held down by an aluminium plate with holes to allow light to reach the sample in correspondence of the spring gold pins.

## 4.6. References


(1) Aristidou, N.; Sanchez-Molina, I.; Chotchuangchutchaval, T.; Brown, M.; Martinez, L.; Rath, T.; Haque, S. A. The Role of Oxygen in the Degradation of Methylammonium Lead Trihalide Perovskite Photoactive Layers. *Angew. Chemie - Int. Ed.* **2015**, *54* (28), 8208–8212.

(2) Aristidou, N.; Eames, C.; Sanchez-Molina, I.; Bu, X.; Kosco, J.; Islam, M. S.; Haque, S. A. Fast Oxygen Diffusion and Iodide Defects Mediate Oxygen-Induced Degradation of Perovskite Solar Cells. *Nat. Commun.* **2017**, *8*, 15218–15227.

(3) Bryant, D.; Aristidou, N.; Pont, S.; Sanchez-Molina, I.; Chotchunangatchaval, T.; Wheeler, S.; Durrant, J. R.; Haque, S. A. Light and Oxygen Induced Degradation Limits the Operational Stability of Methylammonium Lead Triiodide Perovskite Solar Cells. *Energy Environ. Sci.* **2016**, *9* (5), 1655–1660.

(4) Tauc, J.; Grigorovici, R.; Vancu, A. Optical Properties and Electronic Structure of Amorphous Germanium. *Phys. status solidi* **1966**, *15* (2), 627–637.

(5) Waseda, Y.; Matsubara, E.; Shinoda, K. *X-Ray Diffraction Crystallography; Introduction, Examples and Solved Problems*; Springer, 2011.

(6) Bragg, W. H.; Bragg, W. L.; H Bragg, B. W. The Reflection of X -Rays by Crystals. *Proc. Camb. Phil. Soc. Nat.* **1913**, *5* (23), 428–438.

(7) Goldstein, J. I.; Newbury, D. E.; Echlin, P.; Joy, D. C.; Lyman, C. E.; Lifshin, E.; Sawyer, L.; Michael, J. R. *Scanning Electron Microscopy and X-Ray Microanalysis*; Springer US: Boston, MA, 2003.

(8) Pavarini, E.; Koch, E.; Van Den Brink, J.; Sawatzky, G. *Quantum Materials: Experiments and Theory*; 2016; Vol. Volume 6.

(9) Sze, S. M.; Ng, K. K. *Physics of Semiconductor Devices*; John Wiley & Sons, Inc.: Hoboken, NJ, USA, 2006.

(10) Snaith, H. J.; Abate, A.; Ball, J. M.; Eperon, G. E.; Leijtens, T.; Noel, N. K.; Stranks, S. D.; Wang, J. T. W.; Wojciechowski, K.; Zhang, W. Anomalous Hysteresis in Perovskite Solar Cells. *J. Phys. Chem. Lett.* **2014**, *5* (9), 1511–1515.

(11) Dunlap, W. C.; Watters, R. L. Direct Measurement of the Dielectric Constants of Silicon and Germanium. *Phys. Rev.* **1953**, *92* (6), 1396–1397.

(12) Walsh, A.; Scanlon, D. O.; Chen, S.; Gong, X. G.; Wei, S. H. Self-Regulation Mechanism for Charged Point Defects in Hybrid Halide Perovskites. *Angew. Chemie - Int. Ed.* **2015**, *54* (6), 1791–1794.

# 5. Methylammonium lead iodide films, devices and degradation studies

## 5.1. Introduction

This chapter presents a study on methylammonium lead iodide ($CH_3NH_3PbI_3$ or 'MAPI') perovskite materials conducted mainly between 2014 and 2015. During these years, research on finding the best deposition methods was still ongoing and more importantly, it was not clear how the degradation of MAPI was taking place, *i.e.* the factors responsible for material degradation were unknown. This chapter therefore presents a study focused on the preparation and characterisation of MAPI films and their degradation processes. Whilst a full literature review on this perovskite material is presented in chapter 3, the main concepts necessary for understanding the experiments conducted in this work are summarised below.

Since Miyasaka's group[1] produced the first perovskite solar cell in 2009, MAPI film deposition was improved by numerous research groups worldwide. The deposition technique most widely used at the time was spin-coating and the main aspects for the improvement of the perovskite film's quality addressed in the literature were the

concentration of the precursor solution, the annealing time and the annealing temperature of the perovskite thin films.[2–5] In particular, it was found that the higher the annealing temperature, the lower the concentration of pores in the structure and the bigger the crystal grains were. However, beyond 100°C decomposition of MAPI occurs – an indication of the low thermal stability of these organic-inorganic perovskites. Another important technique that was used in the literature to improve the film quality was the anti-solvent method, which involved the dripping of an anti-solvent on the spinning perovskite precursor layer to improve the crystallinity of the film. One of the best solvents used for this purpose was toluene.[6–8] By changing all these variables during the preparation of the films, the perovskite surface coverage and crystallinity were improved and strongly contributed to an improvement of the device current density, increasing the device performance.

In this chapter, MAPI films were prepared using one-step and two-step solution processed spin-coating techniques in order to identify which produced the best devices. First, the film's crystallinity was optimised by using different annealing conditions and anti-solvent treatment and then the MAPI thin films were used for the fabrication of perovskite solar cells. A *p-i-n* device configuration was employed, using spiro-OMeTAD as the hole transporting material (*p*), MAPI as the photon absorber (*i*) and $TiO_2$ as the electron transporting material (*n*). This device architecture (glass/TCO/$TiO_2$/MAPI/spiro-OMeTAD/metal contact) was the main used in literature for the fabrication of MAPI perovskite solar cell devices[9,10] and is still used frequently.

While organic-inorganic perovskite materials showed great perspectives for the fabrication of highly performing solar cell devices, their instability under ambient conditions was observed at very early stages of research.[11] Nevertheless, the initial success of these materials made researchers focus mainly on the improvement of the solar cell performances[12,13] rather than trying to understand the causes of the perovskite's degradation

and its mechanism. In 2014 Grätzel *et al.*[11] stated that it was important to determine the perovskite environmental stability and in the same year, M. A. Green *et al.* demonstrated that organic-inorganic perovskites underwent degradation in a short time when exposed to moisture and ultraviolet radiation,[14] but without mentioning the exact conditions or mechanism of the degradation. Numerous studies about the stability of $CH_3NH_3PbI_3$ and similar perovskites were ultimately initiated,[15] one of which was performed at the University of Liverpool and is presented in this chapter.

A preliminary study of the *degradation* of $CH_3NH_3PbI_3$ was performed on films prepared with the two different deposition techniques. Once the film type that showed higher predisposition towards degradation was identified, detailed studies on the degradation processes were performed. The reason for this was to a) identify which deposition technique showed better stability and b) to study the perovskite stability on the most susceptible MAPI. Therefore, a comprehensive study of the degradation of the one-step solution processed films was conducted by isolating suspected degrading factors, such as oxygen, water vapour and light.

The degradation experiments were performed only on MAPI layers and not on the solar cell devices, as the goal of this study was to identify the cause of the intrinsic degradation of the perovskite material, without considering the other components of the solar cell device.

## 5.2. Experimental methods

### 5.2.1. Methylammonium iodide synthesis

MAPI's organic precursor, methylammonium iodide ($CH_3NH_3^+I^-$ or MAI), was synthesised by adding HI (57% wt. in $H_2O$, Merk) drop by drop to a $CH_3NH_2$ solution (33% wt. in EtOH, Merk), until a molar ratio of HI/$CH_3NH_2$ 1:1 was reached.[16]

The reaction was conducted in a round bottom flask covered with ice (~0°C) for 2 hours, using fast stirring as the reaction is exothermic. The products were recovered by evaporating the solvent and diethyl ether was added drop by drop as anti-solvent to start the crystallisation. The white crystals were then recovered by filtering. A second crystallisation with anti-solvent was then performed to improve MAI's purity and the crystals were filtered with a Büchner filter. Finally, the crystals were dried overnight in a vacuum oven at 70°C and then stored in a nitrogen glovebox, due to the material's hygroscopic properties.

The purity of the synthesised material was verified on the powders using X-ray diffraction and infrared spectroscopy (FT-IR).

As the material synthesis was time consuming, commercial MAI (Solaronix) was later purchased and used for perovskite synthesis. FT-IR and XRD analyses of the commercial product were performed, for comparison with the synthesised MAI.

### 5.2.2. Fabrication of MAPI thin films

Thin films of MAPI were deposited onto either quartz covered glass (20 nm of synthetic quartz covering a glass substrate, Ossila Ltd.) or ITO covered glass (20 x 15 $mm^2$ glass slides, 14-16 Ω/□, Ossila Ltd.) for the material characterisation and for degradation studies. The substrates were cleaned (as described in section 4.1.1) and then the perovskite solution was deposited inside a nitrogen filled glovebox. The deposition was performed using spin-coating (section 4.2.1) using two different methods: the one-step solution process, which involves the spin-coating of one single precursor solution on top of the substrate, and the two-step interdiffusion process or two-step solution process, where first a precursor solution of $PbI_2$ was deposited followed by the spin-coating of MAI. In both cases, fresh solutions were prepared each time, to avoid ageing effects that may influence the properties of the MAPI films.

The procedures are explained in detail below. It is acknowledged that the recipes were inspired by procedures presented in the literature and then adjusted.

*a) One-step solution process*

Lead iodide ($PbI_2$, 99%, Merk, 461 mg), methylammonium iodide (MAI, Solaronix, 159 mg), dimethyl sulfoxide (DMSO, anhydrous ≥ 99.9%, Merk, 78 mg) were mixed in 1:1:1 molar ratio in *N*,*N*-dimethylformamide (DMF, anhydrous 99.8%, Merk, 600 mg).[6,17] The solution was stirred at 50°C for 30 minutes, filtered using a 0.22 µl polytetrafluoroethylene (PTFE) filter and then dynamically spin coated (50 µl) at 4000 rpm for 25 seconds onto a quartz coated glass slide for film characterisation, or on glass/ITO/$TiO_2$ substrate for device fabrication. Immediately after the spin-coating process, the samples were placed on a hot plate for annealing, for 1 minute at 65°C and then 2 minutes at 100°C.[17] Contrarily to Hwang *et al.* (ref. 17) the recipe adopted in this work did not use diethyl ether during the spinning of the sample.

For simplicity this technique is called 'one-step process' from here on.

*i) One-step process with anti-solvent treatment*

The quality of one-step films was improved by using an anti-solvent treatment. A $PbI_2$/MAI/DMSO (1:1:1) solution was prepared in DMF as described above. During the spin-coating process (50 µl, 6000 rpm for 50 seconds, dynamic), 500 µl toluene was spun over the film, 250 µl immediately after the perovskite precursor solution and 250 µl after 10 seconds. Annealing on a hotplate at 100°C for 1 hour followed.

*b) Two-step solution process*

The two-step process is named as such since the perovskite film is formed by depositing two different precursor solutions, one on top of the other: only when the second solution is spin-coated on top of the first layer a chemical reaction takes place forming the MAPI perovskite film.

The two solutions are: a) $PbI_2$ 40% wt. in DMF and b) MAI 4% wt. in isopropyl alcohol (IPA, > 99.7%, Merck). Both were stirred at 50°C and then the $PbI_2$ solution was filtered with a 0.22 μl PTFE filter because the solution was turbid. While the preparation of the solution was prepared with our own recipe, the deposition technique was inspired by Z. Xiao *et al*.[18] 50 μl of the pre-heated $PbI_2$ solution (75°C) was dynamically spin-coated at 6000 rpm for 35 seconds on a pre-heated quartz coated glass or glass/ITO/$TiO_2$ sample (75°C). Following the first deposition, the samples were immediately annealed on a hot plate at 100°C for 10 minutes. When the samples were cooled to room temperature, 70 μl of pre-heated MAI solution (~50°C) was spin-cast on to them (static, 6000 rpm, 35 seconds) followed by annealing at 100°C for 15 - 60 minutes: the annealing temperature study is shown in section 5.3.2.

For simplicity this technique is called 'two-step process' from here on.

MAPI layers were finally characterised by XRD, UV-Vis-IR spectrophotometry and SEM. Furthermore, XPS measurements were performed on MAPI films deposited onto molybdenum foil (section 4.4.1).

### 5.2.3. Thin film degradation conditions and analysis

In order to identify the degradation factors of MAPI layers, selected environments were chosen in order to systematically identify the causes of degradation. The conditions

described as ‘dark/air’, ‘desiccator’, ‘UV/$N_2$’ and ‘UV/$O_3$’ are described in detail in chapter 4 and are summarised in Table 5.1.

Preliminary studies performed on films prepared with the one-step and the two-step process involved the study of the effect of ‘dark/air’ and ‘UV/$N_2$’ conditions after one week of exposure. These were compared to ‘as grown’ samples (*i.e.* freshly prepared MAPI films) and ‘ambient’ samples, hence films left in the lab environment conditions for one week. Once it was determined which perovskite layer was most affected by the degradation effects, a full range of experiments were utilised. Films were exposed to ‘UV/$O_3$’, ‘UV/$N_2$’, ‘dark/air’ and ‘desiccator’ conditions for one week and one month before being analysed.

MAPI degraded layers were characterised visually, by XRD and UV-Vis spectrophotometry (section 4.4.1).

### 5.2.4. Device fabrication

A total of 145 devices were fabricated using different procedures, but the most successful recipe was as follows: all device layers were spin-coated onto an unpatterned ITO covered glass substrate (20 x 15 $mm^2$, 14-16 Ω/□, Ossila Ltd.), one by one to form the superstrate device. After gold evaporation, the structure was: glass/ITO/$TiO_2$/MAPI/spiro-OMeTAD/Au, as shown in Fig. 5.1a. The perovskite layers were deposited as explained in 5.2.2, and the recipes for preparing the electron and hole transporting material layers, $TiO_2$ and spiro-OMeTAD, are described below.

#### *a) c-$TiO_2$ preparation and deposition*

Two solutions with different concentrations (0.15 M and 0.3 M) of titanium(IV)-isopropoxide (97%, Merk) in ethanol (95%, Merk) were prepared inside a glovebox. Starting with the lower concentrated solution and proceeding with the higher, 50 µl of each solution

was dynamically spin-coated onto the ITO covered glass at 3000 rpm for 30 seconds and then annealed at 100°C for 10 minutes. Between the first annealing and the spin-coating of the second solution, the samples were left to cool down. Finally, samples were annealed at 550°C inside a box furnace in air for 30 minutes. This produced layers with a thickness of 100 - 130 nm. The compact titania (c-$TiO_2$) covered samples were finally cooled down in air and re-introduced in the glovebox for the perovskite layer deposition.

$TiO_2$ layers were also prepared by depositing only the 0.3 M Ti-isopropoxide solution, which produced layers ~50 nm thick. Both thicker and thinner layers of $TiO_2$ were used to prepare MAPI devices and the optimal thickness of $TiO_2$ was finally chosen by analysing the *J-V* responses of each one-step and two-step solution processed MAPI devices.

*b) Spiro-OMeTAD preparation and deposition*

Once the perovskite layer was deposited onto $TiO_2$, a spiro-OMeTAD solution was prepared and then spin-coated inside a nitrogen glovebox.

First, 1 ml of chlorobenzene (anhydrous 99.8%, Merk) was added to 92 mg of spiro-OMeTAD powder (2,2',7,7'-Tetrakis-(N,N-di-4-methoxyphenylamino)-9,9'-spirobifluorene, 99%, Merk) and then dopants were added to the solution: 13 μl of 4-tert-butylpyridine (96%, Merk) and 13 μl of a solution of lithium bis(trifluoromethane)sulfonimide (Li-TFSI, 99.9%, Merk) in acetonitrile (anhydrous 99.8%, Merk) (520 mg/ml).[19] The solution was quickly stirred and, as soon as the solution became limpid, 50 μl were dynamically spin-coated at 3000 rpm for 30 seconds. No annealing was used. Finally, the device was moved inside a desiccator overnight (RH ≤ 15%) to allow spiro-OMeTAD's oxygen doping, which increases the polymer's conductivity.[20]

50 nm thick gold contacts were deposited by thermal evaporation, in 3 mm Ø dots. However, as the contacts were masked to provide accurate results during the *J-V* and *EQE* measurements, the final contact area was of 0.0314 $cm^2$ (2 mm Ø dots). Normally, each sample had four metal contacts, as shown in the photograph of a device seen from the back contact side, in Fig. 5.1b.

Devices were loaded in a nitrogen filled box (section 4.5.4) and then measured by *J-V* (with AM1.5 illumination, using a scan rate of 0.19 V/s) and *EQE* (section 4.5.1, 4.5.2) analyses.

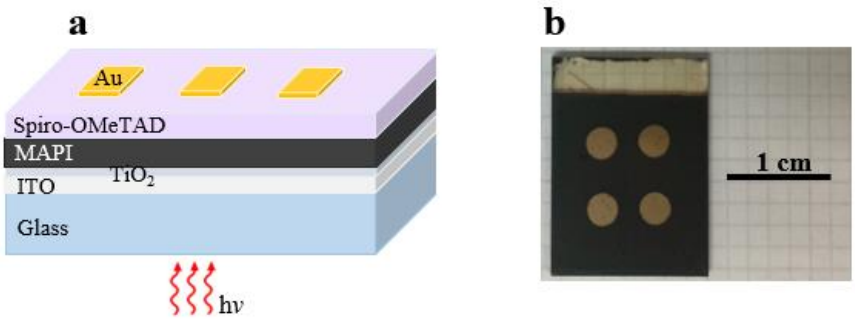


**Fig. 5.1.** MAPI device structure fabricated in this work. a) Diagram of the 'superstrate' device architecture. b) Photograph of a device (20 x 15 $mm^2$), showing four gold dots (back contacts) on the glass/ITO/$TiO_2$/MAPI/spiro-OMeTAD/Au device. The top strip is the bare ITO area used for contacting (front contact).

## 5.3. Results

### 5.3.1. Methylammonium iodide characterisation

Methylammonium iodide (MAI), also called methylamine hydroiodide ($CH_3NH_3^+I^-$ or $CH_3NH_2 \cdot HI$) is MAPI's organic precursor which was initially synthesised in the laboratory and later purchased for simplicity. The synthesis, described in section 5.2.1 was followed by characterisation of MAI powders by XRD and FT-IR, with results shown in Fig. 5.2.

Fig. 5.2a presents the powder XRD analysis comparing the synthesised and the commercial MAI compounds to the reference peaks of the tetragonal crystal system of MAI, reported by the XRD software database. The reference peaks match perfectly the ones from synthesised and commercial products with there being only inconsequential difference in preferred orientations.

FT-IR results obtained from the synthesised and commercial powders present similarities to the reference spectra, as shown in Fig. 5.2b.[21] All compounds show the same main peaks, these being N-H, C-H and C-N stretching (~3100 $cm^{-1}$, 2960 $cm^{-1}$ and 1400 $cm^{-1}$ respectively) and N-H and C-H bending (1560 - 1480 $cm^{-1}$ and ~1460 $cm^{-1}$ respectively).[22] The broad peaks at around ~900 $cm^{-1}$, 1500 - 1650 $cm^{-1}$, 2750 – 3500 $cm^{-1}$ correspond to water, meaning that the products were not properly dried, in particular in the case of the commercial MAI. The small peak at ~3900 $cm^{-1}$ for the commercial product and the intense peak present in both commercial and synthesised MAI at ~2400 $cm^{-1}$ corresponds to $CO_2$, due to the measurement being performed in air. Furthermore, it should be noted that the different intensities of the peaks are related to the quantity of powder used for the measurement.

XRD and FT-IR results reveal that the synthesis of MAI was performed correctly, producing a pure crystalline product. Therefore both commercial and synthesised MAI were usable for the preparation of MAPI, leading to perovskite thin films with similar properties.

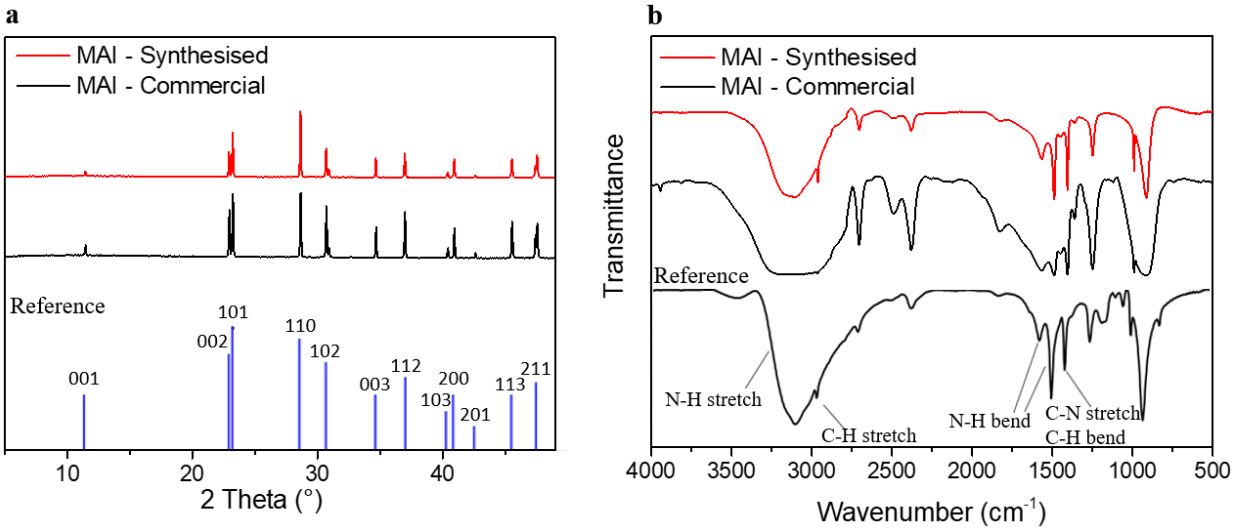


**Fig. 5.2.** Commercial and synthesised MAI powder characterisation and comparison with reference data. a) Powder XRD analysis showing tetragonal crystal system peaks for both powders, matching the reference pattern (X'Pert HighScore PANalytical reference code: 00-010-0737). b) FT-IR analysis indicating the main stretching and bending bonds of MAI: reference peaks[21] matching for both synthesised and commercial materials.

### 5.3.2. Methylammonium lead iodide thin films

*a) One-step process vs two-step process*

The characterisation of MAPI thin films commenced using XRD to confirm the crystal structure and to identify the suitability of the preparation procedures of the films. As little was known about MAPI perovskite properties when this study was started, the determination of the perovskite crystal structure was performed by comparison with XRD patterns presented in the literature, rather than by comparison with a reference spectrum from X-ray diffraction databases. The thin film XRD patterns obtained from MAPI prepared with the one-step and the two-step processes are shown in Fig. 5.3. The patterns were comparable to those found in the literature and were indexed by comparison, as shown in Fig. 5.3a.[23,24] The most intense Bragg peaks (110) and (220) at 14.1° and 28.5° 2θ respectively, in combination with the less intense (310) at 31.93° 2θ and (330) at 43.2° 2θ peaks, confirmed the tetragonal structure with a preferred orientation. This is the stable structure of MAPI at room temperature.[24,25]

The peak at 12.6° 2θ, present solely in the XRD pattern of the MAPI produced with the two-step deposition method (Fig. 5.3a), corresponds to $PbI_2$. The same $PbI_2$ peak can be observed also in Fig. 5.3b, which shows the effect of increasing the annealing time. In addition to the lead iodide peak, the pattern also contains a broad peak at ~44° 2θ, which is related to second precursor: methylammonium iodide. Both peaks progressively decrease with increasing the annealing time and almost disappear after 60 min of heating at 100°C. These results reveal that at annealing times < 60 minutes the precursors did not have time to react and therefore the minimum time necessary to complete the reaction between $PbI_2$ and MAI to form MAPI using the two-step solution process is one hour. Therefore this was the annealing time chosen to use for the preparation of the two-step interdiffusion process MAPI for all experiments shown next.

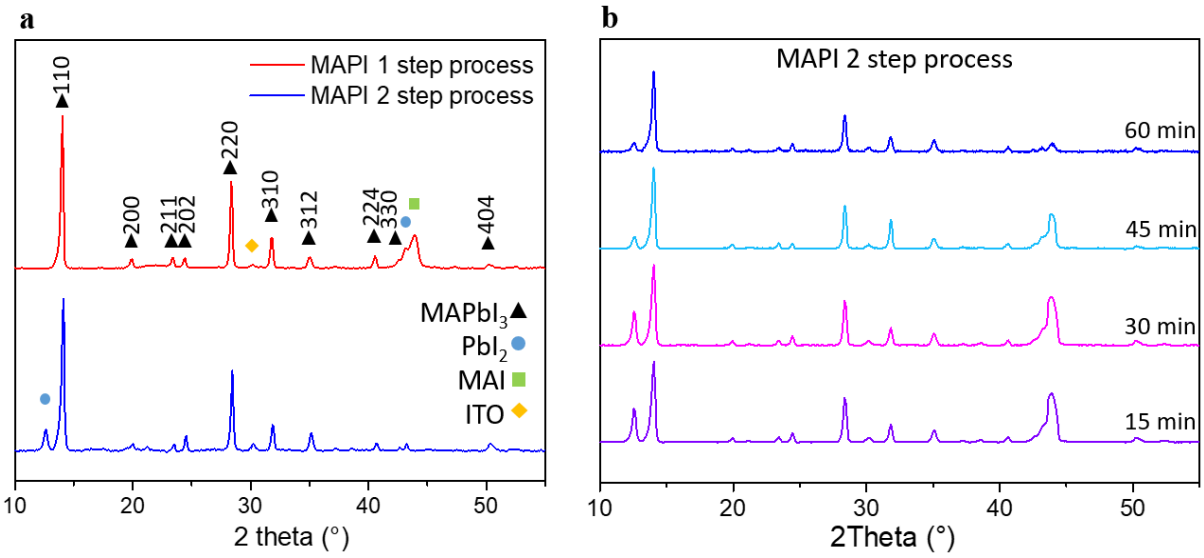


**Fig. 5.3.** XRD analysis on MAPI films. a) The graph shows the XRD patterns obtained with the one-step and the two-step recipes, revealing for both that a tetragonal structure was formed, this being consistent with literature reports for MAPI. Miller indices are assigned for the main perovskite peaks[24,26] and the legend shows all assignments. b) MAPI films prepared with the two-step process using different annealing times, showing a progressive reduction of the $PbI_2$ peak at 12.6° 2θ to the minimum obtained at 60 minutes.

Following the analysis of the crystal structure, optical characterisation was performed by UV-Vis spectrophotometry, as shown in Fig. 5.4. The transmittance and reflectance curves in Fig. 5.4a show that higher transmittance was achieved with MAPI films prepared with the two-step process. These data were used to calculate the absorption coefficient (for 300 nm thick films for both deposition techniques), and the curves are shown in Fig. 5.4b. The absorption coefficients are of $7.5 \cdot 10^4 – 1.2 \cdot 10^5$ $cm^{-1}$ and $2.5 \cdot 10^4$ - $9 \cdot 10^5$ $cm^{-1}$ in the visible range for MAPI prepared with the one-step and two-step processes respectively. Moreover, Fig. 5.4a and b show a distinctive absorbance cut off for both samples at ~780 nm, which corresponds to the band edge. A more precise estimate of the band gap was made using a Tauc plot using the relation appropriate for a direct-gap semiconductor, which has been shown to be appropriate for MAPI.[27] The Tauc plots of MAPI perovskites prepared with the two different recipes (Fig. 5.4c), show that the band gap of samples prepared with the one-step process was 1.57 eV, while the band gap of the MAPI made with the two-step process was 1.61 eV. These are both self-consistent and comparable to literature values.[28]

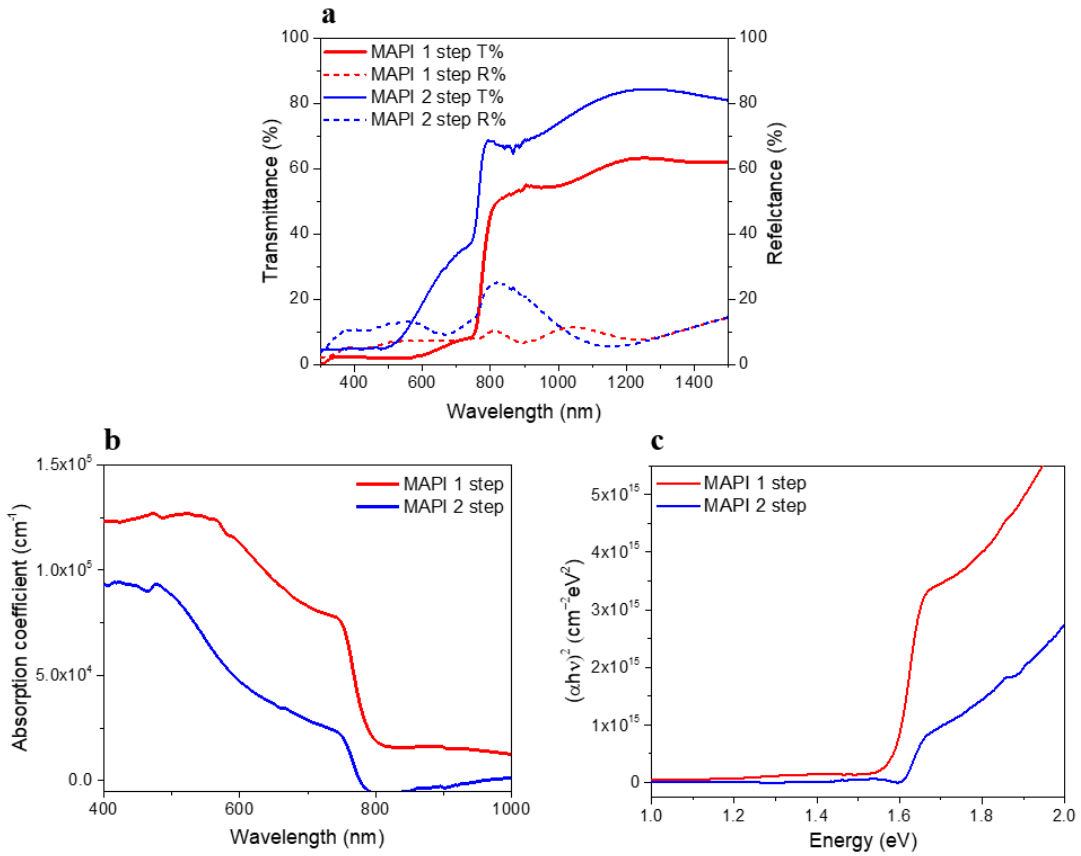


**Fig. 5.4.** Optical measurements on MAPI thin films made with the one-step and the two-step process: a) transmittance and reflectance, b) calculated absorption coefficient and c) Tauc plot, yielding band gaps of 1.57 eV and 1.61 eV for MAPI prepared with the one-step and the two-step deposition methods respectively.

XPS measurements were performed on MAPI thin films with the aim of understanding the band properties of the material, and the results are shown in Fig. 5.5. While XPS measurements are normally used for chemical environment analysis, in this particular experiment it was used to evaluate the valence band position ($V_B$) relative to the Fermi level ($E_F$) which is arbitrarily positioned at 0 eV. The evaluation of the difference between these energies provides information on the Fermi level position in the band gap, which was measured optically. The difference was of 0.89 eV and 0.87 eV (± 0.01 eV) for the one and two-step process respectively, as shown in Fig. 5.5. Since the optical band gaps were 1.57 eV and 1.61 eV for the one and two-step process respectively, and considering that for a material to be intrinsic the Fermi energy should be positioned in the middle of the

band gap ($E_g$/2), it may be concluded that the Fermi level of the two perovskites is positioned slightly above mid gap for both samples. Therefore both may be considered slightly *n*-type, but nearly intrinsic, as shown in Fig. 5.5c and d.

However, the XPS measurement determines the properties of the surface, hence the position of the Fermi level may differ in the bulk. In addition, the position of the Fermi level is calculated in respect to the band gap, which was determined optically. Since optical measurements are affected by error (depending on which linear part of the Tauc plot is fitted), the overall determination of the Fermi level position may be affected by error.

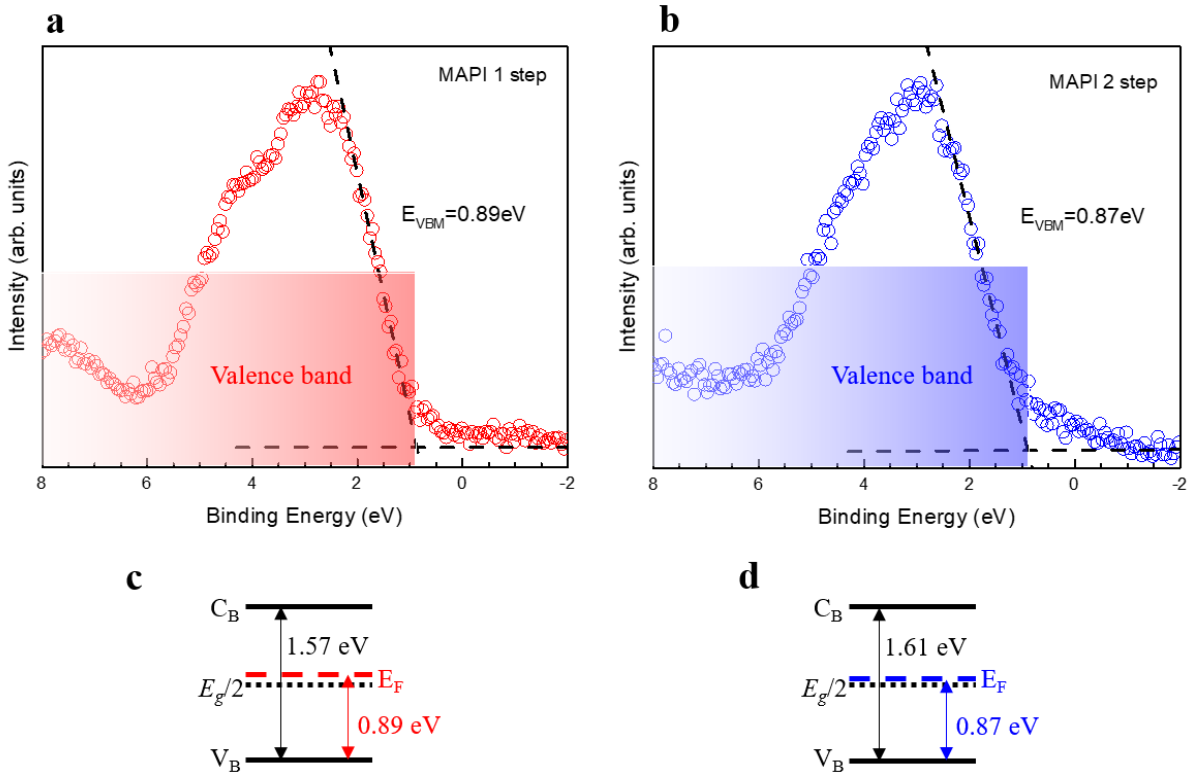


**Fig. 5.5.** XPS determination of the valence band energy. As the Fermi level is considered to be at 0 eV, the difference between valence band (last peak before 0 eV) and Fermi energy can be measured, this being 0.89 eV for the MAPI prepared with the one-step process (a) and 0.87 eV for the MAPI prepared with the two-step process (b). c) and d) show the band diagram of MAPI using the optical band gaps and XPS Fermi level positions for both one and two-step materials.

Electron micrographs of MAPI made with the one-step and the two-step processes are shown in Fig. 5.6. A comparison of the films shows that those fabricated with the two-

step process produce higher quality films. Crystal grains are discernible in both layers, in particular form Figs. 5.6c and f. These show large crystals, but with numerous pin-holes for MAPI one-step (up to ~500 nm) and small but highly uniform crystals for the MAPI films prepared with the two-step process (~100 – 150 nm). However, the two-step thin films show bright spots uniformly located on the film's surface, these being ~100 nm Ø. Since the films contain unreacted lead iodide (see XRD in Fig. 5.3), these spots may be due to bright atomic number contrast from this.

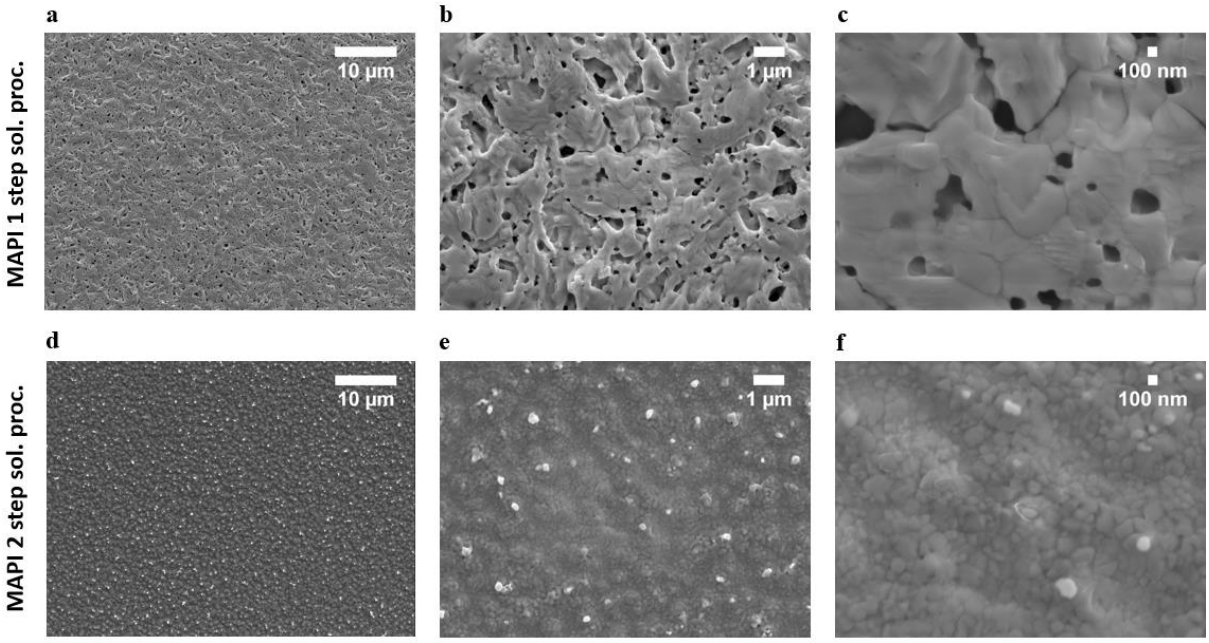


**Fig. 5.6.** SEM images of MAPI produced with the one-step and the two-step processes. The electron micrographs show that larger crystals were produced with the one-step process, but higher uniformity in layers was produced with the two-step process.

*b) Anti-solvent treatment on MAPI one-step solution process*

MAPI thin films prepared with the one-step process using an anti-solvent treatment (toluene) showed a different visual appearance compared with the films without the addition of toluene, these being black but presenting a shiny mirror-like surface, as shown in the inset of Fig. 5.7a. The highly reflective layer and the camera used to take the picture can be seen. The films were compared to the simple one-step process by XRD and SEM analysis as shown in Figs. 5.7a-c. The XRD pattern shows the presence of sharp MAPI peaks which are

comparable to those shown in Fig. 5.3, confirming that the crystal structure does not change. The crystallinity observed in Figs. 5.7b and c is higher than for that observed in Figure 5.6a-c, with the toluene treated MAPI films showing highly compact crystals with size of ~100 nm Ø and without pin-holes.

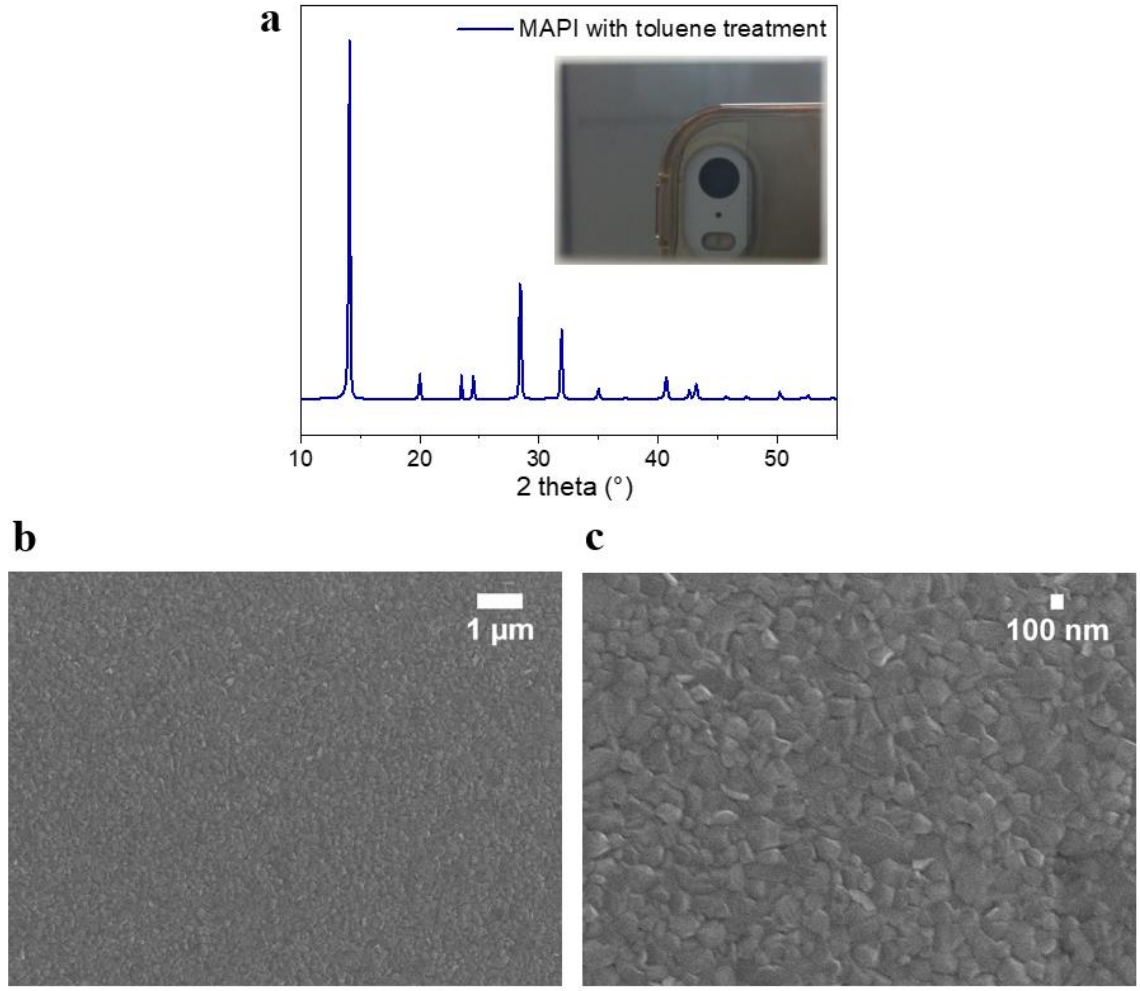


**Fig. 5.7.** Characterisation of MAPI prepared with the one-step process and treated with toluene. a) XRD pattern showing MAPI peaks with inset showing the visual appearance of a black, shiny MAPI layer deposited on a 20 x 15 $mm^2$ substrate. b,c) SEM analysis conducted on MAPI one-step process thin films treated with toluene, showing different magnifications: 1 µm (b) and 100 nm where well defined and stacked crystals can be observed (c).

### 5.3.3. Methylammonium lead iodide thin film degradation

MAPI thin films were observed to have poor stability when removed from the nitrogen environment and exposed to air, which was easily observed as the appearance of the films changed from black to yellow after few days in air, as shown in Fig. 5.8.

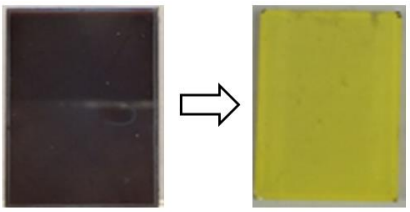


**Fig. 5.8.** Photographs of a fresh MAPI layer (black) and degraded MAPI layer (yellow). The samples are 20 x 15 $mm^2$.

Preliminary studies on the stability of MAPI were conducted on layers prepared with both deposition processes presented in the previous sections. The main goal of these introductory experiments was to identify the MAPI layer which could better withstand degradation conditions. In addition, the least stable MAPI layer was used for further studies on the stability, as the lower stability perovskite was easier and quicker to use to ascertain the degradation factors that influence the structure of the material. Additional studies on the most unstable MAPI perovskite are shown in section 5.3.3.b.

*a) Comparison between stability of one-step and two-step MAPI films*

MAPI films prepared with the one-step and the two-step processes were exposed to 'UV/$N_2$', 'dark/air' and 'ambient' conditions for one week and were then characterised by XRD and UV-Vis analysis, along with an 'as grown' control, as shown in Fig. 5.9.

*i) MAPI one-step processed layers*

From both XRD and optical measurements on MAPI prepared with the single step process (Fig. 5.9a, b, c) it can be observed that samples left in 'UV/$N_2$' and 'dark/air' conditions showed only minor variations compared to the 'as grown' sample. On the contrary, films left in 'ambient' for one week showed a complete degradation, visually detectable by the formation of a yellow layer. The XRD pattern of the 'ambient' degraded sample showed only a $PbI_2$ peak at 12.6° 2θ, and the optical measurements showed a shift of MAPI's band edge from ~780 nm towards ~530 nm, corresponding to the absorption edge of $PbI_2$ (2.3 eV band gap).

*ii) MAPI two-step processed layers*

The analysis of MAPI two-step processed layers (Fig. 5.9d, e, f) showed some changes occurring on films exposed to 'UV/$N_2$' and 'dark/air' and severe degradation occurring for films in 'ambient'. For all conditions the XRD analysis showed an increase of the $PbI_2$ peak at 12.6° 2θ and a shift of the material's band gap. However, while for 'UV/$N_2$' and 'dark/air' these changings are less noticeable, in the case of samples left in 'ambient' the effect of degradation is very pronounced: the main XRD peak at 12.6° 2θ and the shift of the band edge towards ~530 nm show the prevalent presence of $PbI_2$, but nevertheless MAPI peaks and band edges are still recognisable.

Comparing the changes detected for the one-step and the two-step MAPI layers it can be noted that they both showed smaller changes occurring on films exposed to 'UV/$N_2$' and 'dark/air' compared to the severe degradation occurring for films in 'ambient'. However, the degradation to these isolated environments ('UV/$N_2$' and 'dark/air') is more pronounced in the case of MAPI prepared with the two-step process. On the contrary,

considering the ‘ambient’ degradation conditions, the one-step processed MAPI is completely degraded after one week, whereas the two-step deposited MAPI shows a predominant but not complete degradation, as the XRD and UV-Vis analysis still show peaks and a band edge belonging to the perovskite material. Nevertheless, both samples left in ambient conditions appeared completely yellow coloured.

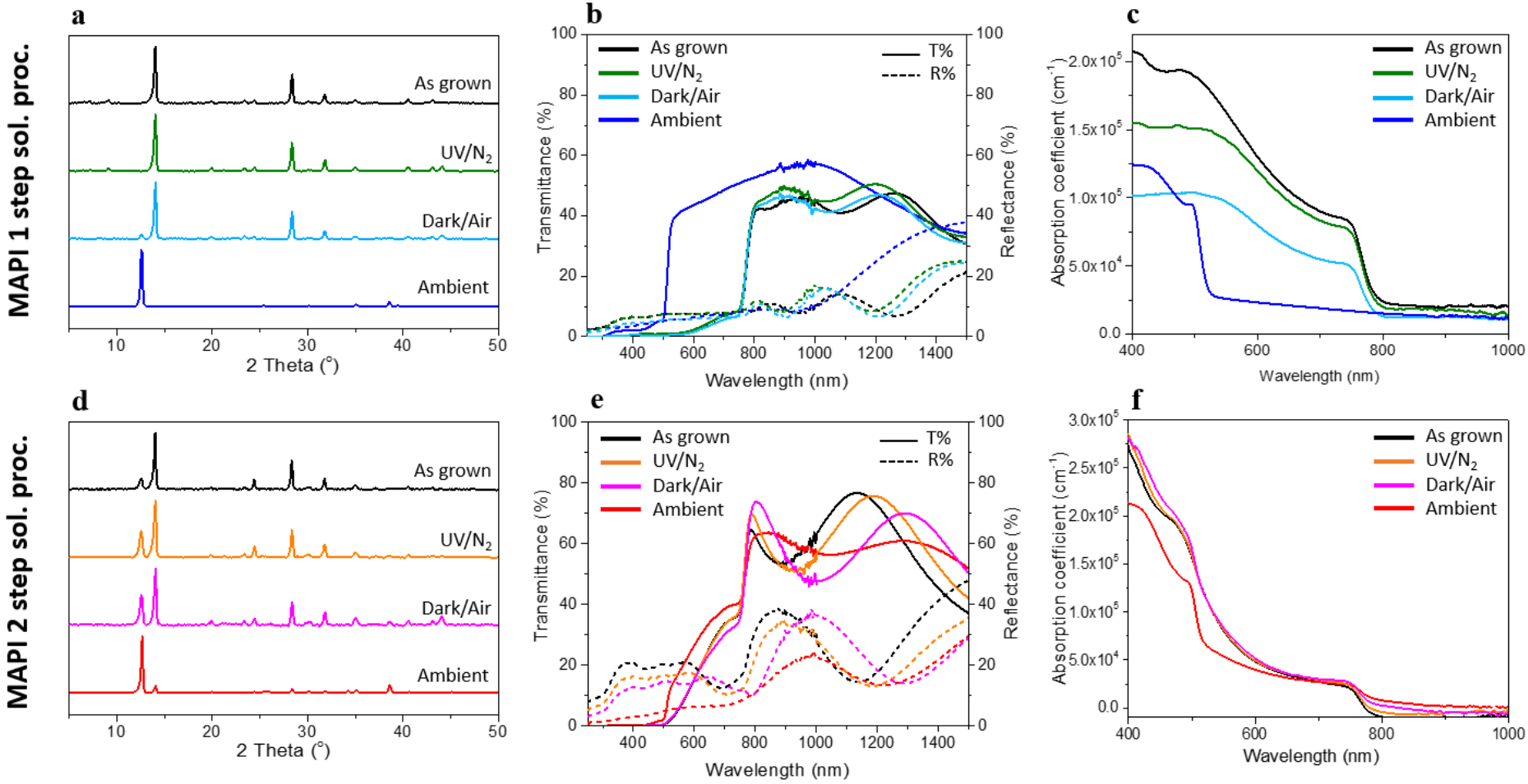


**Fig. 5.9.** *One week* degradation analysis on one-step (a, b, c) and two-step (d, e, f) MAPI films, considering 'UV/$N_2$', 'dark/air' and 'ambient' degradation processes, compared with the results of 'as grown' samples. These analysis refer to XRD (a, d), transmittance and reflectance measurements ((b, e) and the calculated absorption coefficient (c, f).

As the index of the degradation of films may be expressed by the increased concentration of $PbI_2$, it was possible to quantitatively compare the degradation of the films prepared with the different deposition techniques. In order to determine this quantity it was chosen to use the area of the XRD peaks of $PbI_2$ at 12.6° 2θ and compare it to the most intense MAPI peak at 14.1° 2θ, corresponding to the (110) orientation. The ratio between these X-ray peaks was used to determine the amounts of $PbI_2$ in each film, using the XRD patterns shown in Fig. 5.9a and d. The concentrations of lead iodide determined in this way for MAPI layers produced with the two deposition processes, on fresh films and on films exposed to degradation conditions, are shown in Fig. 5.10.

The histogram shows that $PbI_2$ does not exist in *fresh* MAPI films prepared with the one-step solution process, but its presence is detected in the fresh two-step MAPI layers, amounting to 22%. This amount reveals unreacted reagent, as it was shown previously in the XRD analysis (Fig. 5.3) and speculated in the SEM analysis (Fig. 5.6). After one week of degradation in 'UV/$N_2$', where the main degrading issue is represented by UV radiation (as $N_2$ is inert), the situation is similar for the one-step processed MAPI (0% $PbI_2$), while in the case of the two-step solution MAPI the lead iodide concentration increases to 41%. Similarly, in the case of 'dark/air' (where the main degrading factors are water and oxygen present in air) the $PbI_2$ concentration rises to 9% for the one-step process and to 34% for the two-step process. However, in the case of 'ambient' conditions, the amount of $PbI_2$ reaches 100% in the layer prepared with the one-step process, hence no MAPI is left in this sample, and 89% $PbI_2$ in the case of the two-step solution process, revealing that small quantities of MAPI are still present in the sample.

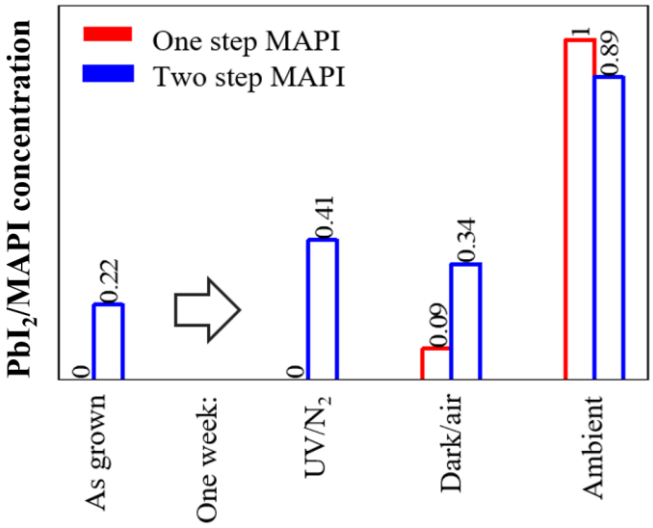


**Fig. 5.10.** Lead iodide concentration ratios referred to the ratio of the XRD peak areas of $PbI_2$ at 12.6° 2θ and the (110) MAPI peak area at 14.1° 2θ. Ratios are shown for MAPI made by the one-step and the two-step processes before and after exposure to specific degradation conditions.

Therefore, higher stability towards isolated confinements ('UV/$N_2$' and 'dark/air') was shown from MAPI made with the one-step process, however a greater stability towards 'ambient' conditions was recognised for the two-step material. Nevertheless, both MAPI perovskites showed similar behaviours towards all degrading conditions, hence the procedure used to prepare the layers does not produce great influence on the stability towards degrading agents.

To conclude this section, although it is clear that the preliminary study on one-step MAPI films indicates that 'ambient' conditions degrade the films but 'UV/$N_2$' and 'dark/air' conditions do not, further studies are required to identify the exact causes of the degradation. These follow below.

*b) Further degradation approaches on one-step processed MAPI*

Degradation studies on MAPI prepared with the one-step process were conducted by exposing films to 'UV/$N_2$', 'dark/air' and 'desiccator' conditions and by analysing these films after one week and after one month of exposure. In addition, 'UV/$O_3$' analysis was

chosen to simulate the accelerated effects of UV and oxygen and hence it was conducted for only 19 minutes. All the details of the techniques used for the degradation environments are explained in section 4.3.

This section shows visual appearances of the films before and after the degradation conditions, as well as XRD and optical analysis after one week and one month of exposure to the isolated environments (Fig. 5.11, 5.12 and 5.13). Furthermore a comprehensive summary of the degradation conditions and results of the analysis is presented in Table 5.1.

*i) Films with up to one week of degradation*

The fastest degradation was observed when MAPI layers were subjected to an $UV/O_3$ cleaner. Fig. 5.11 shows photographs of the layers taken every minute for a total of 19 minutes (a), and the photograph of a layer kept in the $UV/O_3$ cleaner for 19 minutes continuously (b). Both Fig. 5.11a and b show that the result of 19 minutes of exposure is deleterious for MAPI films, which completely change their colour from black to yellow/orange. This result reveals a strong response of the material towards UV-radiation combined with oxygen, which is confirmed by the results of the XRD and optical characterisation shown in Fig. 5.12a, b and c (orange curves). The XRD analysis on a layer kept in '$UV/O_3$' conditions shows a different pattern compared to the 'as grown' layer. It shows a prevalent peak at 43.8° 2θ corresponding to methylammonium iodide, and different band edges on the transmittance and reflectance curves, which do not correspond to those of MAPI. MAPI is therefore completely degraded after only 19 minutes in the UV-ozone cleaner. However, it should be noted that the curves obtained by the '$UV/O_3$' conditions do not resemble the 'yellow phase' curves, revealing that 19 minutes using this degradation condition produce degradation effects that go beyond the formation of lead iodide films.

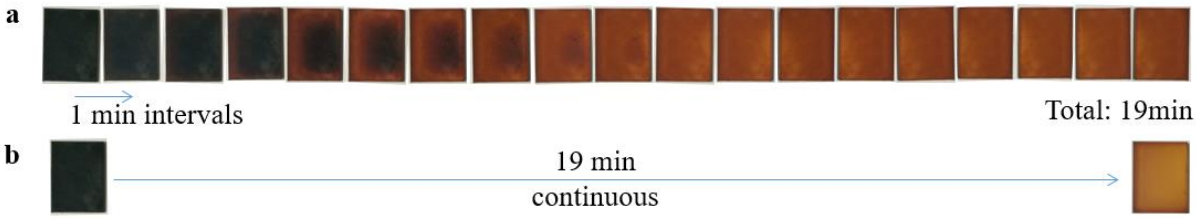


**Fig. 5.11.** Photographs of MAPI layers produced with a one-step process, exposed to 'UV/$O_3$' conditions. a) Images of the layers introduced inside a UV/$O_3$ cleaner taken every minute, for 19 minutes in total. b) Photograph of a MAPI layer before and after introducing it in a UV/$O_3$ cleaner for 19 minutes continuously, showing higher degradation compared to (a).

Further films were exposed to degradation factors for one week these being 'UV/$N_2$', 'dark/air' and 'desiccator'. The effects of 'UV/$N_2$' and 'dark/air' after one week were already explored in section 5.3.3.a, showing only minor changes in the MAPI properties mainly recognisable from a decrease in the absorption coefficient in the visible range. Layers kept in the desiccator also showed low levels of degradation, only recognisable by an increase in the $PbI_2$ and the MAI peak intensities in the XRD analysis (12.6° and 43.8° 2θ respectively) and a small drop in the absorption coefficient, compared to the 'as grown' response (Fig. 5.12a and c). Therefore, little information was discovered from the analysis of MAPI films after one week and hence longer periods of exposure were necessary. This is described below.

*ii) Films after one month of degradation*

After one month of exposure in 'UV/$N_2$', 'dark/air' and 'desiccator' more changes were detectable, as shown by the analysis presented in Fig. 5.12d, e and f and the photographs of the layers shown in Fig. 5.13. Starting from 'UV/$N_2$', it is shown from both XRD and optical characterisation that films underwent considerable degradation. The XRD pattern becomes completely different, with a predominant peak at 43.8° 2θ corresponding to MAI, whereas the transmittance curve shows a band edge, which corresponds to neither

MAPI nor $PbI_2$, and the absorption coefficient shows a drop in the whole wavelength range considered. In addition, the photograph of the layer exposed to 'UV/$N_2$' shown in Fig. 5.13, appears white. Visual inspection of the sample reveals that the degradation under UV light in the glovebox produced a different degradation mechanism compared to a layer exposed to ambient, as the film turned white rather than yellow. This may be related to the fact that the UV-radiation used in the glovebox was very strong and positioned very closely to the sample, which may have produced a thermal degradation of the material over the long period of time considered.

On the contrary, the 'dark/air' degradation did not show any effect beyond the weak degradation noticed after one week of exposure and remained fairly unchanged. This was confirmed by the appearance of the MAPI films, shown in Fig. 5.13, which appear black but less uniform that the 'as grown' films. Finally, the layer left in 'desiccator' conditions for one month, showed degradation detectable in the XRD pattern, showing increased $PbI_2$ and MAI peaks, while the transmittance only showed a small decrease in the signal intensity. The same occurs for the absorption coefficient spectra, where the band edge of $PbI_2$ is detectable around 500 - 550 nm, confirming the X-ray analysis and the visual appearance: Fig. 5.13 shows that yellow areas formed mainly in the corners of the sample, and these correspond to $PbI_2$.

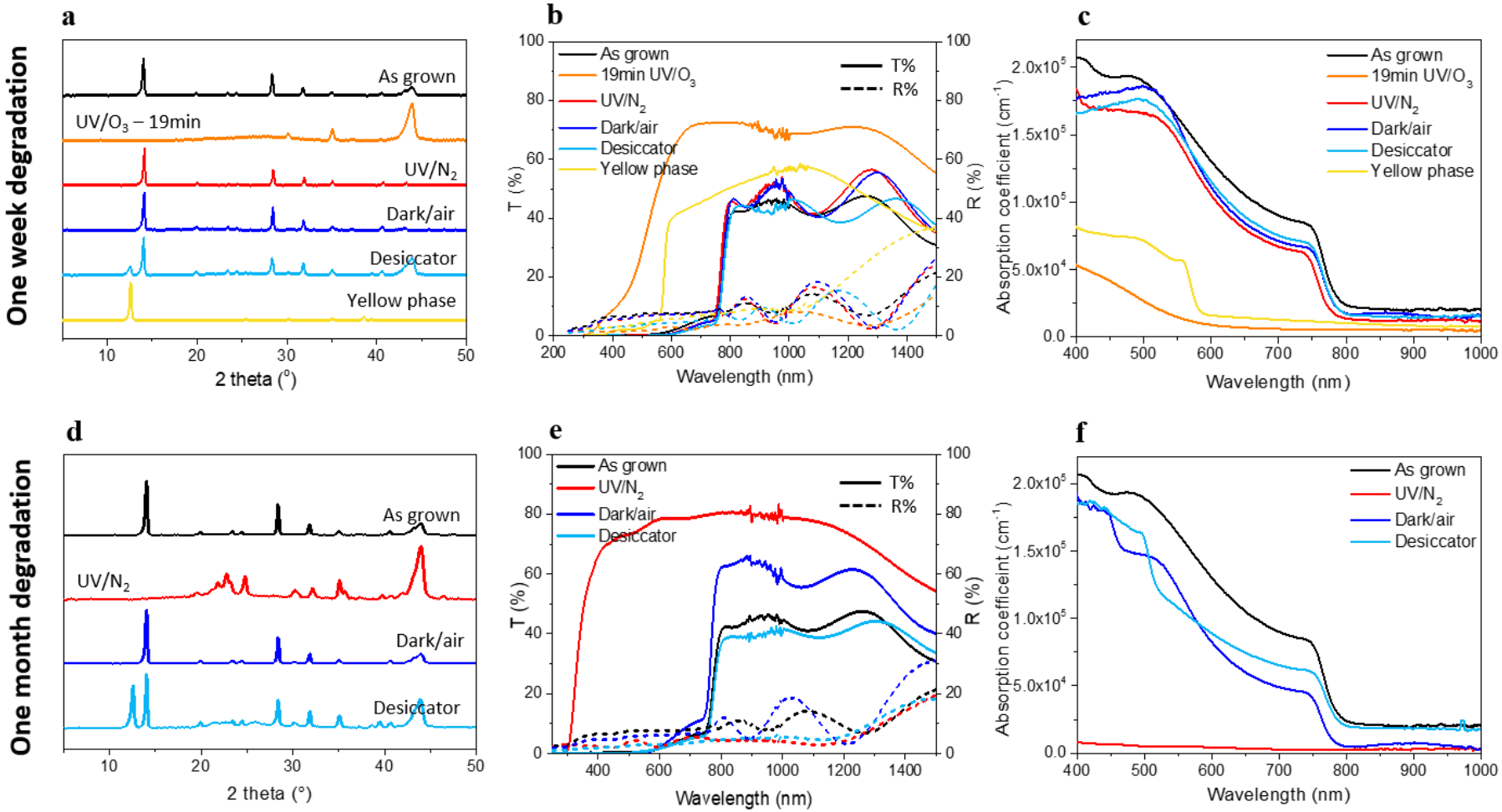


**Fig. 5.12.** XRD analysis (a, d), transmittance and reflectance measurements (b, e) and calculated absorption coefficient (c, f) of MAPI prepared with a one-step process, after one week (a, b, c) and one month (d, e, f) of exposure to degradation conditions. 'As grown' and 'yellow phase' are used as references for an easier interpretation of the results obtained with the isolated conditions.

The photographs of the ‘as grown’ and degraded films in Fig. 5.13 show the overall trends very clearly, with the most significant changes being caused by ‘UV/$N_2$’ and ‘UV/$O_3$’ conditions which completely transformed the black MAPI phase to its degraded products.

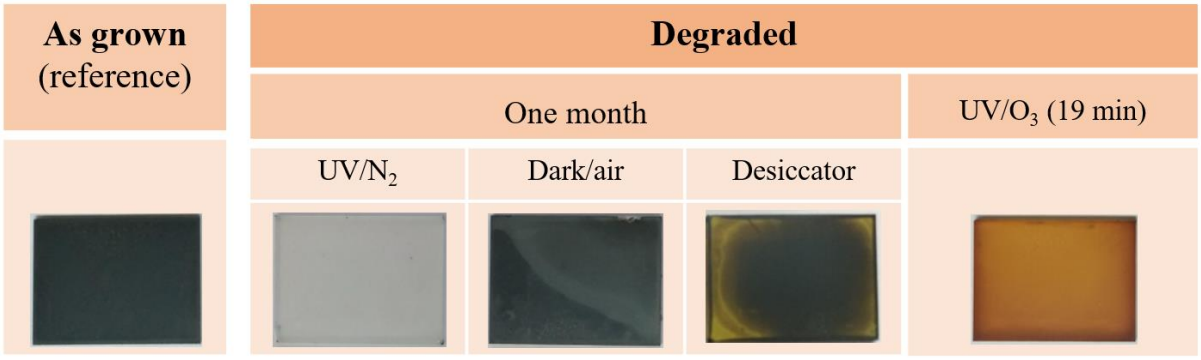


**Fig. 5.13.** Photographs of MAPI layers (20 x 15 $mm^2$) prepared with the one-step process, comparing the ‘as grown’ black layer with the layers after one month of exposure to degradation conditions, with the exception of ‘UV/$O_3$’ which lasted 19 minutes.

Table 5.1 follows, presenting a final summary of all experiments involved in the degradation study on MAPI one-step films and the results obtained by confining these to each degradation condition. By analysing the results in Table 5.1 it is easy to identify the main conditions in which MAPI showed phase instability. Since the damaging effect of one month in ‘UV/$N_2$’ is related to the exposure to strong UV-radiation which produced considerable heat, to which MAPI is unstable, by considering the effect after only one week it can be concluded that UV-radiation by itself does not cause severe degradation, but heat does. For this reason, samples after one month exposure to UV/$N_2$ appear white (Fig. 5.13) rather than yellow (MAPI’s degradation colour). Furthermore, MAPI films left in the dark in air, do not show any degradation even after one month. This infers that MAPI degradation is not caused by air, and therefore water or oxygen alone, which are the most reactive molecules present in air, are not responsible for degrading the material. However, when light and air are combined the effect on MAPI is different. Samples left in the desiccator (lab lighting and air with reduced water concentration) show little degradation after one week

and significant degradation after one month, revealing that the combination of even limited UV-radiation in the presence of air (*i.e.* $O_2$), is capable of producing changes in MAPI's structure. Concordantly, samples introduced in a UV-$O_3$ cleaner show quick and remarkable degradation even after few minutes. This aggressive environment was purposely selected to confirm the effects of UV-radiation with extremely reactive oxygen and results have shown that this environment produced the most degradation in MAPI. The use of such intense conditions however, caused the MAPI films to go beyond normal degradation processes, showing XRD pattern and absorption curves that do not match the 'conventionally' degraded ones (yellow phase).

It can be therefore stated that the main degradation conditions for MAPI were identified, these being the combination of UV light and oxygen, confirming the results in the most recent literature. However, moisture which is the other important condition that in the literature was found to influence MAPI's stability,[29] did not show an effect on the MAPI layers prepared in this work. It should be noted however that the effect of the material's exposure to high quantities of water vapour was limited, as none of the isolated degradation conditions used in this work presented high levels of water vapour to the samples.

| **Degradation conditions** | | | | | | **Characterisation** | | | |
|---|---|---|---|---|---|---|---|---|---|
| **Test** | **Illumination** | **Containment** | **Atmosphere** | **UV, $O_2$ and/or $H_2O$** | **Duration** | **Visual** | **XRD** | **Optical** | **Conclusion** |
| **"UV/$O_3$"** | UV lamp | UV-ozone cleaner | Dry air with ozone | UV, $O_2$ | 19 minutes | Yellow/Orange | MAI peak prevailing | Complete change | UV and oxygen quickly and radically change the MAPI structure |
| **"UV/$N_2$"** | UV lamp | Glovebox | $N_2$ | UV | One week | Slightly discoloured but black | No change | No change | Long exposure to UV radiation completely changes the MAPI structure |
| | | | | | One month | Decoloured, white | MAI peak prevailing | Complete change | |
| **"Dark/air"** | None | Wrapped petridish in drawer | Air (RH > 15%) | $O_2$, $H_2O$ | One week | No change | No change | No change | Humidity and/or oxygen do not affect the MAPI structure |
| | | | | | One month | No change | No change | Slightly shifted $E_g$ | |
| **"Desiccator"** | Lab lighting | Desiccator (silica gel in transparent container) | Air (RH < 15%) | $O_2$ (low [$H_2O$]) | One week | Some yellow phase on corners | MAI peak start to appear | No change | Combination of ambient light and oxygen change the MAPI structure |
| | | | | | One month | Yellow phase on corners | MAI peaks prevailing | Slightly shifted $E_g$ | |

**Table 5.1.** Summary of the result of degradation trials on MAPI prepared with a one-step process. The most important degradation factor was identified as 'UV/$O_3$', with only 19 minutes needed to completely change the MAPI appearance and film analysis.

This section may be therefore concluded by stating that MAPI layers showed high susceptibility to combined light and oxygen, but either factor on its own does not affect the perovskite. A further discussion on the suggested mechanism for the degradation of MAPI is deferred to section 5.4.

### 5.3.4. Methylammonium lead iodide devices

Devices were fabricated with the following structure: glass/ITO/c-$TiO_2$/MAPI/spiro-OMeTAD/Au for both MAPI one-step and two-step processed thin films.

Table 5.2 presents the average and best *J-V* device parameters for the one-step and the two-step process devices. Averages were measured from 25 devices fabricated on different days using the same procedure (see section 5.2.4), but showed considerable consistency. The best *J-V* curves obtained with these devices are shown in Fig. 5.14.

The average device results were affected by the $TiO_2$ thicknesses. In the case of MAPI prepared with the one-step process, devices produce higher average performances with thinner $TiO_2$ layer (50 nm), these being 3.63% compared to the 1.15% *PCE* obtained using the thicker $TiO_2$. The best *J-V* curve for MAPI one-step process devices (Fig. 5.14a) showed 8.22% *PCE*, $V_{OC}$ = 0.88 V, $J_{SC}$ = 20.83 mA/cm$^2$, *FF* = 44.8% using the 50 nm $TiO_2$ layer, and 3.59% *PCE*, $V_{OC}$ = 0.70 V, $J_{SC}$ = 11.15 mA/cm$^2$, *FF* = 45.9% using the 100 nm layer of $TiO_2$. Nevertheless, both curves shapes indicate poor shunt and series resistance and this is manifested by the average *FF* values being extremely low: 29.4% and 27.8% for 50 nm and 100 nm $TiO_2$ thickness respectively.

In the case of MAPI prepared with the two-step process, the *J-V* parameters (Table 5.2) show that the highest device performances are reached in devices containing 100 nm $TiO_2$. An example is shown from the *J-V* curves (Fig. 5.14b), in which the highest *PCE* (8.45%, $V_{OC}$ = 0.98 V, $J_{SC}$ = 16.57 mA/cm$^2$, *FF* = 52.1%) of the 100 nm $TiO_2$ device

outperforms the devices with the 50 nm layer (1.28% best *PCE*, $V_{OC}$ = 0.82 V, $J_{SC}$ = 6.65 mA/cm$^2$, *FF* = 23.3%). As shown in Table 5.2, the main reason for the considerable rise in performance in the devices with the thicker $TiO_2$ layer, is due to the increased $V_{OC}$ and $J_{SC}$: averages show 0.58 V and 2.91 mA/cm$^2$ for the devices with thinner $TiO_2$, compared to 0.87 V and 15.14 mA/cm$^2$ for the device with the thicker $TiO_2$. Furthermore, Fig. 5.14b shows that while the *J-V* curve for the device with 100 nm $TiO_2$ has high series resistance, the 50 nm $TiO_2$ device shows extremely low shunt and high series resistances, leading to important losses.

In conclusion, while devices prepared with the MAPI one-step process work best with thinner layers of $TiO_2$ (50 nm), devices with MAPI prepared with the two-step process produces higher performances with thicker $TiO_2$ layers (~100 nm). Therefore, devices that are shown in the next sections will use these optimised $TiO_2$ thicknesses.

| **MAPI process** | **$TiO_2$ thickness** | | ***PCE* (%)** | **$V_{OC}$ (V)** | **$J_{SC}$ (mA/cm$^2$)** | ***FF* (%)** |
|---|---|---|---|---|---|---|
| **one-step process** | 50 nm | AVG | 3.63 (±2.38) | 0.64 (±0.15) | 16.49 (±3.96) | 29.4 (±9.1) |
| | | Best | 8.22 | 0.88 | 20.83 | 44.8 |
| | 100 nm | AVG | 1.15 (±1.48) | 0.39 (±0.24) | 7.02 (±5.17) | 27.8 (±9.1) |
| | | Best | 3.59 | 0.70 | 11.15 | 45.9 |
| **two-step process** | 50 nm | AVG | 0.46 (±0.60) | 0.58 (±0.37) | 2.91 (±2.77) | 32.6 (±10.3) |
| | | Best | 1.28 | 0.82 | 6.65 | 23.3 |
| | 100 nm | AVG | 4.17 (±1.62) | 0.87 (±0.11) | 15.14 (±2.50) | 31.0 (±7.0) |
| | | Best | 8.45 | 0.98 | 16.57 | 52.1 |

**Table 5.2.** *J-V* parameters of MAPI devices prepared using the perovskite deposited with the one-step and the two-step processes. For each deposited layer, the results of single and double $TiO_2$ layered devices are shown, presenting both average ($N \approx 25$) and best performances.

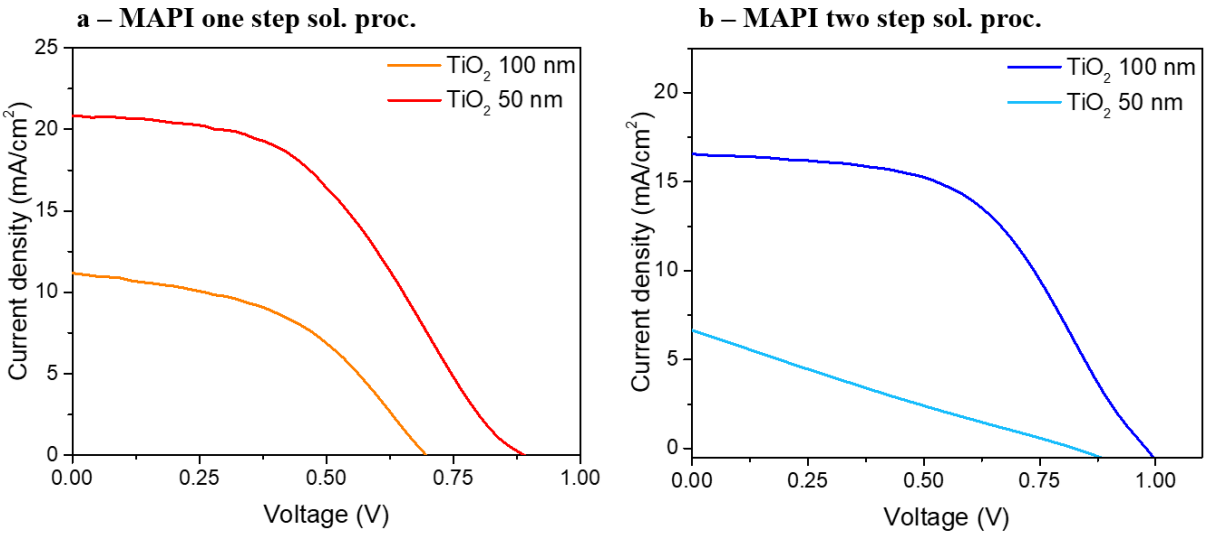


**Fig. 5.14.** Best *J-V* curves obtained from a) MAPI one-step devices and b) MAPI two-step devices, using different $TiO_2$ thicknesses. Highest device performances were obtained with 50 nm of $TiO_2$ for MAPI one-step process devices and 100 nm $TiO_2$ layer for the MAPI two-step solution devices.

The *J-V* properties and statistics obtained by the one-step and two-step optimised devices, in combination with the *EQE* measurements of these, are presented in Fig. 5.15 and Table 5.3.

Fig. 5.15a-d shows the *J-V* parameters of the best device and the average performances for both the one-step and two-step processes. In addition, the averages of results obtained with the forward and reverse sweeps are presented, to give information about their hysteretic behaviour. While the peak *PCE* values for both deposition processes are similar (8.22% and 8.45% for the one and two-step process respectively), the averages show a higher efficiency for the two-step processed devices (4.17% *PCE* against 3.63% *PCE* of the one-step process). This difference is not significant, however the standard deviation shows that the devices prepared with the two-step process are more consistent, indicating higher uniformity of the films as shown in the SEM in Fig. 5.6. The device trends are revealed by the $V_{OC}$ and $J_{SC}$ graphs (Fig. 5.15b and c). Higher $V_{OC}$ values were measured for the two-step process devices (0.87 V average) with the highest $V_{OC}$ reaching 0.98 V, and

lower in the one-step process devices (0.64 V average, 0.88 V highest). Although, the one-step process produced higher $J_{SC}$ values than the two-step process (16.49 mA/cm$^2$ and 15.14 mA/cm$^2$ respectively), data are spread out (large error bars). Similarly to the $V_{OC}$, the *FF* (Fig. 5.15d) shows higher values for the two-step process, with an average of 31%, compared to 29.4% for the one-step process devices and, as before, error bars are considerably larger for the latter.

Fig. 5.15a-d also reports the average data for forward and reverse *J-V* measurements, which explains the wide variation in performance of the devices and Table 5.3 presents the average data for MAPI devices prepared with the one-step and two-step processes. While all *J-V* parameters show that reverse scans outperform the forward data (a common phenomenon broadly presented in the literature for perovskites),[30] it is easily recognisable that devices with MAPI prepared with the one-step process suffer more from hysteretic behaviour, compared to the two-step process devices (4.20% and 1.65% Δ*PCE* for the one-step and the two-step process respectively, being Δ*PCE* the difference between forward and reverse scans). In the case of the one-step process devices, the larger discrepancy in the *J-V* parameters is observed in the current density, as shown by the large error bars in Fig. 5.15c. However, important differences are seen also in *FF* and $V_{OC}$. On the contrary, in the case of MAPI prepared with the two-step process, the discrepancies between *J-V* parameters are smaller, and they are mainly controlled by the $J_{SC}$, whereas the difference in $V_{OC}$ is extremely low.

Finally, Fig. 5.15e and f compare the stabilised efficiency and the *EQE* spectra of MAPI one-step and two-step process devices. The maximum power point tracking (Fig. 5.15e) shows a drop in the efficiency (from 6.5% to 3.4% *PCE* and from 7.5% to 5.3% *PCE* for the one-step and two-step process devices respectively) in the first ten seconds and then a slow stabilisation which reaches a steady state after 70 seconds, for both devices. MAPI

prepared with the two-step process shows higher performance, as from 7.5% *PCE* the efficiency drops to 4.7% after 70 seconds, whereas for MAPI prepared with the one-step process, the *PCE* changes from 6.5% to 3.1%. Therefore the *PCE* drop after light soaking is 2.8 percentage points for the two-step and 3.4 percentage points for the one-step process, indicating that the two-step process produces higher stability towards light soaking.

The *EQE* spectra shown in Fig. 5.15f present two main cut-offs, one at low wavelength (~300 nm) corresponding to the absorption edge of the ITO transparent conductive oxide used as front contact (> 4.1 eV),[31] and a shoulder at ~780 - 800 nm, corresponding to the MAPI band absorption edge. (In the case of the MAPI one-step process devices, there is an apparent feature at 735 nm which was found to be caused by the lamp exchange during the *EQE* measurement and is not device related). Both *EQE* spectra present low quantum efficiencies demonstrating that the device performances could be improved.

| **MAPI devices** | | ***PCE* (%)** | ***$V_{OC}$* (V)** | ***$J_{SC}$* (mA/cm$^2$)** | ***FF* (%)** |
|---|---|---|---|---|---|
| **One-step process** | AVG Forward | 1.53 (± 0.52) | 0.54 (± 0.11) | 13.08 (± 2.36) | 21.7 (± 3.6) |
| | AVG Reverse | 5.73 (± 1.49) | 0.75 (± 0.11) | 19.90 (± 1.61) | 37.2 (± 5.6) |
| **Two-step process** | AVG Forward | 3.17 (± 0.83) | 0.85 (± 0.08) | 13.53 (± 2.12) | 27.6 (± 4.3) |
| | AVG Reverse | 4.82 (± 1.68) | 0.89 (± 0.12) | 16.02 (± 2.27) | 33.0 (± 7.64) |

**Table 5.3.** Average *J-V* parameters of devices prepared using MAPI with the one-step and the two-step processes, focussing on the results of forward and reverse scans to show the important hysteretic behaviour of the devices ($N \approx 25$).

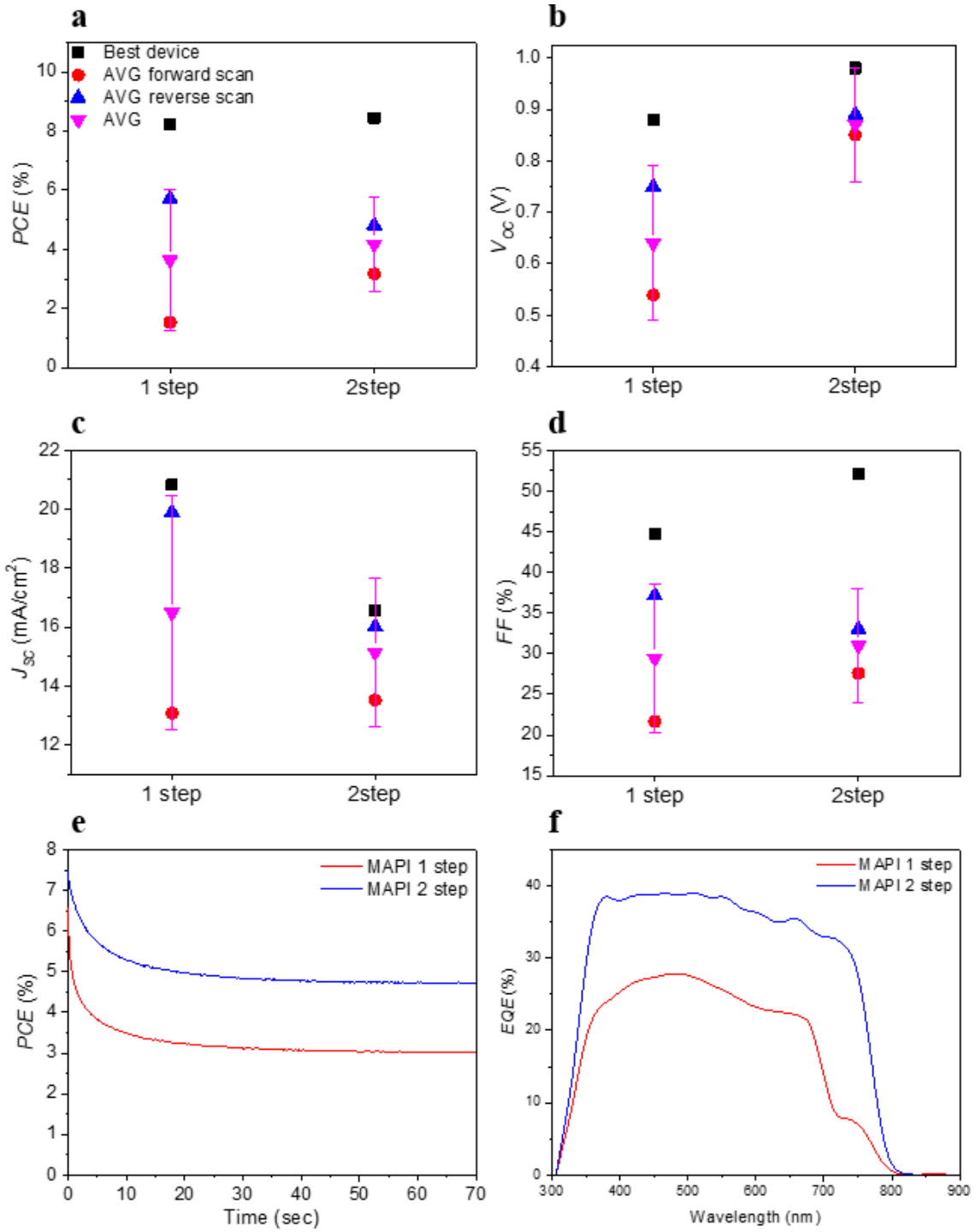


**Fig. 5.15.** Comparison between *J-V* parameters of devices prepared with MAPI one-step and two-step processes. Statistics showing the highest, average, average of forward and average of reverse scans of a) *PCE*, b) $V_{OC}$, c) $J_{SC}$ and d) *FF*. The 'best' values refer to the device with the highest *PCE* recorded. e) Stabilised efficiencies and f) *EQE* spectra of representative devices prepared with the one-step and two-step processes, showing higher performances for devices prepared using the two-step solution process.

*a) Time effect on MAPI two-step process devices*

MAPI devices prepared with the two-step process showed an increased efficiency when they were stored for some time in a desiccator (lab lighting and RH < 15%), a phenomenon that was not observed in the one-step process devices. Therefore a separate batch of two-step process devices was fabricated and their efficiency monitored on the first, second and fourth days after fabrication.

Table 5.4 shows the average and best *J-V* parameters calculated for 16 contacts and Fig. 5.16 shows the best *J-V* curves and the statistical behaviour of these devices.

Performances of average and best devices in this batch were not dissimilar from the results of MAPI two-step process devices shown previously in Table 5.2 (3.71% *PCE* for this batch, against 4.17% *PCE* as shown in section 5.3.4) which demonstrates the consistency of the device performance. However, the *J-V* parameters re-measured on the second day showed unexpected behaviour. The average *PCE* was increased by 1.26% (absolute), rising up to 4.97% *PCE*, while the best *PCE* recorded was 11.80% ($V_{OC}$ = 1 V, $J_{SC}$ = 20.87 mA/cm$^2$, *FF* = 56.5%). This was the champion device fabricated with MAPI in this work. However, increasing the storage time in the desiccator up to four days produced a decrease of the efficiency of the devices, showing a *PCE* of 2.93%. Since this was lower than the *PCE* recorded on the first day (3.71%) the ageing study was ended, as this decreasing trend indicated that a slow degradation in the MAPI was occurring. *PCE* results shown in Fig. 5.16b, indicate that although devices measured on the second day perform better, the improvement of the device performance was not uniform in all cells, since they present large error bars.

| MAPI two-step devices | | *PCE* (%) | $V_{OC}$ (V) | $J_{SC}$ (mA/cm$^2$) | *FF* (%) |
|---|---|---|---|---|---|
| 1st day | AVG | 3.71 (± 1.32) | 0.84 (± 0.11) | 14.97 (± 2.70) | 29.3 (± 5.16) |
| | Best | 7.02 | 0.97 | 19.2 | 37.5 |
| 2nd day | AVG | 4.97 (± 3.20) | 0.78 (± 0.23) | 17.44 (± 5.95) | 33.1 (± 7.71) |
| | Best | 11.80 | 1.00 | 20.87 | 56.5 |
| 4th day | AVG | 2.93 (± 2.03) | 0.69 (± 0.19) | 12.14 (± 3.84) | 31.1 (± 7.0) |
| | Best | 8.19 | 0.95 | 18.94 | 45.4 |

**Table 5.4.** Average and best *J-V* parameters of MAPI two-step process devices measured on the first, second and fourth day ($N \approx 16$). Samples were kept in the desiccator in the meantime.

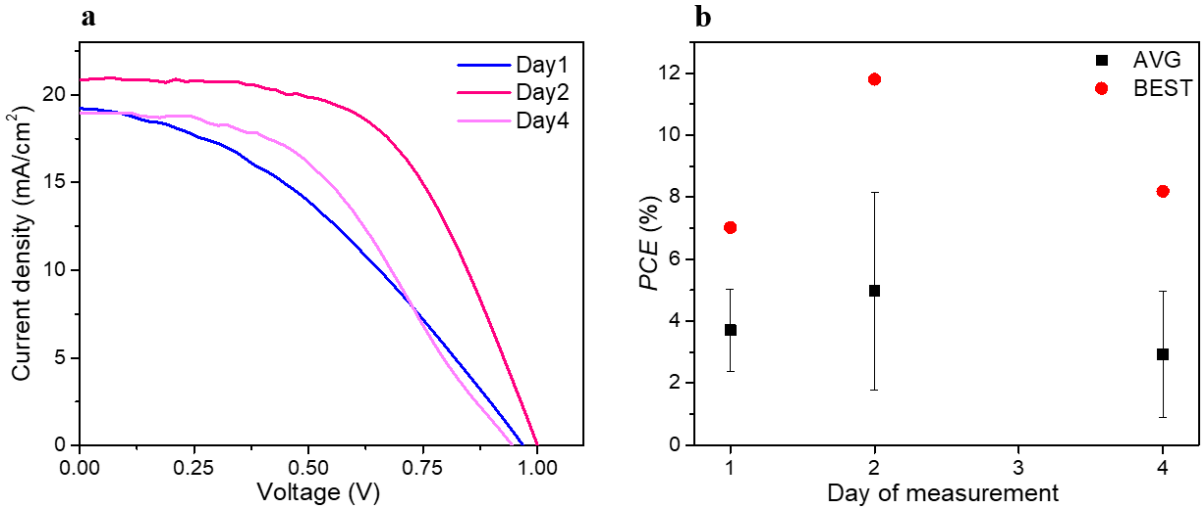


**Fig. 5.16.** Efficiency measured on devices using a two-step process, on the first day (as grown), on the second and on the fourth day, of desiccator storage (lab lighting, RH < 15%). a) *J-V* curves of the highest performing devices and b) best and average efficiencies.

*b) MAPI one-step process devices with anti-solvent treatment*

One-step process MAPI devices showed lower performance compared to two-step devices. However, using an anti-solvent treatment on the perovskite surface showed increased film uniformity which lead to higher device performance, as shown by the *J-V* analysis of toluene-treated one-step process devices and those without the toluene treatment,

shown in Fig. 5.17. As shown previously in Table 5.2, non-treated devices showed an average *PCE* of 3.63% ($V_{OC}$ = 0.64 V, $J_{SC}$ = 16.49 mA/cm$^2$, *FF* = 29.4%) with the highest performing device producing a *PCE* of 8.22% ($V_{OC}$ = 0.88 V, $J_{SC}$ = 20.83 mA/cm$^2$, *FF* = 44.8%). However, with the toluene treatment the average *PCE* rose by 1.33% (absolute), showing an average 4.96% *PCE* ($V_{OC}$ = 0.82 V, $J_{SC}$ = 16.72 mA/cm$^2$, *FF* = 34.6%), with the best device yielding a 9.36% *PCE* ($V_{OC}$ = 0.92 V, $J_{SC}$ = 20.23 mA/cm$^2$, *FF* = 50.3%). The best curves obtained by the two sets of devices are shown in Fig. 5.17a. The main improvement observed for MAPI devices treated with toluene was observed in the rise of the $V_{OC}$ (from 0.64 V to 0.82 V), whereas a small increment was observed in the *FF* (from 29.4% to 34.6%) and almost no difference was detected in the current (from 16.49 mA/cm$^2$ to 16.72 mA/cm$^2$).

The trend shown by the stabilised efficiencies in Fig. 5.17b is very similar between the two sets of devices (see Fig. 5.15 for the non-toluene treated device). The toluene treated device showed an initial *PCE* of 12.4% which dramatically dropped in 5 seconds of illumination. For a further 5 seconds the *PCE* continued to decrease, until it reached a steady state at 4.5% *PCE*. Therefore, light soaking produced a decrease of 7.9% *PCE* (absolute) in a very short time but, nevertheless, the final efficiency is higher than the one from the non-toluene treated devices.

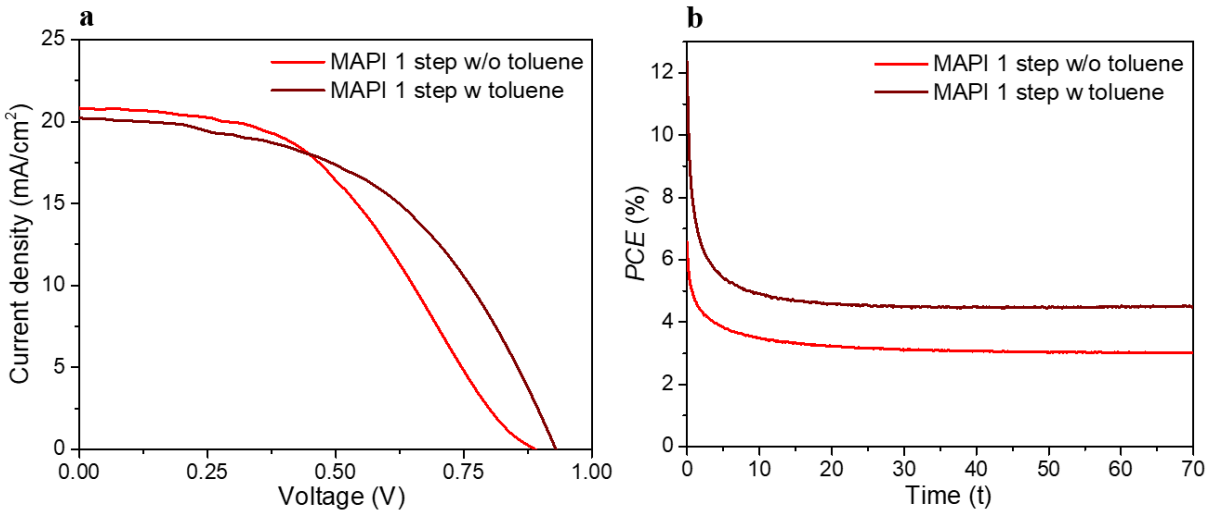


**Fig. 5.17.** *J-V* analysis on one-step process devices with and without the anti-solvent treatment: comparison between a) best *J-V* curves (9.36% and 8.22% *PCE* respectively) and b) stabilised efficiencies showing steady state behaviour at 4.50% and 3.0% *PCE* for toluene and non-toluene treated devices respectively.

## 5.4. Discussion

This chapter presents a study on the preparation and characterisation of MAPI thin films using two main deposition techniques: the one-step and the two-step process. The first involves the spin-coating of a single methylammonium iodide precursor solution, whereas the second involves the deposition of two solutions which are consecutively spin-coated one on top of the other to form the perovskite. Although it was demonstrated by XRD analysis that both techniques produced MAPI thin films, the properties of the material varied. For instance, the X-ray patterns showed that layers were not identical, as the MAPI prepared with the two-step process showed a peak corresponding to the lead iodide precursor, absent in the case of the MAPI prepared with the one-step procedure. However, this $PbI_2$ peak intensity was shown to be easily reduced by increasing the annealing time to 60 minutes – a considerably longer time compared to the one-step perovskite (3 minutes), which is an important factor to consider for materials that may be used for scale-up processes. In

addition to the X-ray analysis, SEM images of the two-step process films (Fig. 5.6) revealed lighter-coloured particles on the surface (~100 nm Ø), which may be related to the presence of the unreacted reagent $PbI_2$. If this hypothesis is correct, by using a higher concentration of the MAI precursor solution, the unreacted $PbI_2$ may react with MAI forming MAPI. Furthermore, longer annealing times may help to completely remove the unreacted precursors in the two-step MAPI film. Nevertheless, the electron micrographs showed that MAPI prepared with the two-step process showed higher uniformity, with small, compact crystals (~100 - 150 nm), whereas MAPI prepared with the one-step process forms larger crystals (up to ~500 nm) with numerous pin-holes. These large crystal grains in the one-step perovskite films produced a higher absorption coefficient compared to two-step processes films ($1.25 \cdot 10^5$ $cm^{-1}$ and $9 \cdot 10^4$ $cm^{-1}$ respectively), whereas in terms of intrinsic properties of the material the band gap showed extremely similar results, these being 1.57 eV and 1.61 eV for the one-step and the two-step processed MAPI respectively. In addition, both perovskites showed nearly intrinsic properties with the Fermi level position being close to the mid-band gap position.

Another common characteristic of both MAPI layers, is that they degraded when exposed to ambient conditions for some time. This degradation was revealed by the change in the visual appearance of the films, which turned from the 'as grown' black films into bright yellow coloured layers, this colour being due to $PbI_2$, as confirmed by the X-ray analysis (Fig. 5.9a, d). A study was therefore conducted to determine the causes of this ageing process. Both MAPI films were subjected to controlled degradation conditions, these being UV-radiation in nitrogen and dark conditions in air, in order to isolate the effects of UV light and air to identify their effects on the perovskite films. Little effect was observed on layers of the two different films, however the perovskite prepared with the two-step procedure showed higher resistance toward degradation in ambient compared to the one-

step MAPI film. This greater sensitivity of the one-step processed MAPI may be related to the presence of numerous pin-holes in the film that, with their high surface area, permitted the degrading agent to easily infiltrate between the perovskite grains.

As the one-step MAPI demonstrated higher susceptibility to degradation, this material was selected for degradation trials. In particular, additional degrading environments ('UV/$O_3$' and 'desiccator') and longer periods of exposure (up to one month) were employed. Even considering longer periods of time, no degradation was detected for samples left in 'dark/air conditions', suggesting that the main degradation factor for MAPI is UV-radiation. Concordantly, the most important degradation was detected in 'UV/$O_3$', which affected the MAPI composition in a very short time (19 minutes). Therefore, in this work, the presence of oxygen combined to the UV-radiation appeared to be the predominant degradation effect for MAPI perovskite materials. The mechanism suggested for this phenomenon was that the UV-rays produced radicals on the organic part of the perovskite (methylammonium), which then reacted with oxygen creating volatile compounds that left $PbI_2$ on the sample. The instability towards UV and oxygen was confirmed by other research groups as shown in the literature, and the more detailed mechanism recently proposed from S. Islam's group[32] is presented in chapter 3 (multistage reaction, forming the superoxide species). Although the susceptibility of MAPI towards UV and oxygen was confirmed also by the literature, the experiment shown in this thesis adopting UV/$O_3$ could have been improved by adding a short wavelength filter on the UV lamp (184 nm), in order to remove the reaction forming $O_3$ (see section 4.1.1), unnecessary for the purpose of the experiment, and leaving the higher wavelength used to form the radicals solely on the organic molecules. In this way, the experiment used to study the degradation of MAPI in presence of UV/$O_2$ would be determined more accurately.

In addition to this degradation factor, numerous research groups stated that MAPI shows high sensitivity towards water vapour, however this was not observed in this work. A possible reason for this may be related to the exposure conditions used in this study: the highest humidity level used was the ambient humidity, which in a working environment in the United Kingdom is normally between 40% and 60% RH. Therefore, samples were not exposed to extreme RH values and this may be why the effect of moisture was not detected on the samples during the 'dark/air' degradation studies.

MAPI films prepared with the one and two-step processes were further analysed and compared in devices, using the following device architecture: glass/ITO/c-$TiO_2$/MAPI/spiro-OMeTAD/Au. Both films achieved low performances compared to those shown in the literature. However the goal of fabricating devices in this work was mainly focussed on showing that MAPI films used for the degradation studies were functional. For device development, the $TiO_2$ thickness was optimised initially, and 50 nm for the MAPI one-step process devices and 100 nm for the MAPI two-step process devices were found to be optimal. For one-step process devices, an average *PCE* of 3.63% ($V_{OC}$ = 0.64 V, $J_{SC}$ = 16.49 mA/cm$^2$, *FF* = 29.4%) with the highest performing device producing 8.22% *PCE* ($V_{OC}$ = 0.88 V, $J_{SC}$ = 20.83 mA/cm$^2$, *FF* = 44.8%) was achieved. These *J-V* performances were surpassed by the two-step process devices, showing an average *PCE* of 4.17% ($V_{OC}$ = 0.87 V, $J_{SC}$ = 15.14 mA/cm$^2$, *FF* = 31.0%), with the highest *PCE* being 8.45% ($V_{OC}$ = 0.98 V, $J_{SC}$ = 16.57 mA/cm$^2$, *FF* = 52.1%). While the main reason for the two-step process devices reaching higher performances was mainly recognised to be the higher $V_{OC}$, both devices showed poor *FF*, which was the main cause of the low performances presented in this work. A possible reason for this may be the parasitic resistive losses in the device, which in turn are suggested by the presence of numerous pin-holes in the case of the MAPI one-step

process devices and the weak diode regions caused by the presence of unreacted $PbI_2$ (large band gap semiconductor) in the two-step process devices.

Interestingly however, Table 5.3 showed that if only the average *PCE* data of the *reverse scans* of the two sets of devices are compared, one-step process devices reach higher efficiencies, with an average *PCE* of 5.73% against 4.82% *PCE* of two-step process devices. Both sets of devices showed high hysteretic behaviour but this was shown to be larger in one-step process devices, showing a $\Delta PCE$ of 4.2% (absolute) between forward and reverse scans, compared to only $\Delta PCE$ of 1.65% (absolute) in the two-step processed devices.

Two-step process devices, showed an improvement in the device performance between the first and second day of measurement, reaching an average of 4.97% ($V_{OC}$ = 0.78 V, $J_{SC}$ = 17.44 mA/cm$^2$, *FF* = 33.8%) and a best *PCE* of 11.80% ($V_{OC}$ = 1 V, $J_{SC}$ = 20.87 mA/cm$^2$, *FF* = 56.5%), which is the champion device measured in this work. The main improvement of the devices measured on the second day is an increase of the $J_{SC}$ and the *FF*, whereas the $V_{OC}$ decreases. The reduction in the $V_{OC}$ indicates the reduction in the absorber material's quality which may be due to a slow degradation process, which is also indicated by the decreased $V_{OC}$ measured on the fourth day (0.69 V) (Table 5.3). Also, since an improved $J_{SC}$ is normally attributed to improved surface coverage, it may be speculated that the MAPI perovskite prepared with the two-step process may need settling time to improve its crystallinity. Furthermore, since samples were left in the desiccator in air it may be speculated that these conditions increased the oxygen doping of the spiro-OMeTAD layer, hence its conductivity and the hole transport toward the contacts.

An improvement in the device performances was also observed for MAPI prepared with the one-step process by using an anti-solvent treatment. As shown in the SEM image (Fig. 5.7b, c) the effect of toluene spin-coated on MAPI films is remarkable: the free-pin hole layer shows numerous crystals (~100 nm Ø) and high uniformity. In devices, this

beneficial effect was observed with an increase in the *PCE*, this being 1.33% (absolute) on average higher than the one of samples prepared *without* the anti-solvent treatment and producing the highest efficiency for devices prepared with the one-step process (9.36% *PCE*). It was observed that the beneficial effect was mainly due to an increase in the $V_{OC}$, as the treatment produced more uniform films with fewer pin-holes compared to the classic one-step process that supressed non-radiative charge recombination. However, one of the main advantages of the one-step process for hypothetical scale-up process is its extremely short annealing time (3 minutes), which in the case of the anti-solvent treatment increased to one hour – which is the same time needed for the two-step process.

For the anti-solvent treated one-step and the non-treated two-step process, it is possible to note that the highest performances are now reversed: MAPI prepared with the one-step process using the anti-solvent treatment showed higher efficiency compared to two-step process devices, these being 4.96% and 4.17% average *PCE* respectively. However, the same comparison cannot be implied for devices fabricated using the MAPI two-step solution process measured on day two (4.97% average *PCE*).

Nevertheless, as the results given by the best MAPI devices prepared with the two-step process (*PCE* = 11.80%) outperformed all other devices fabricated in this work, it may be concluded that this is the best procedure to use.

## 5.5. Conclusions

Chapter 5 presented a study on MAPI thin films and devices.

MAPI thin films were deposited using two main spin-coating techniques, the one-step and the two-step process depositions. Both techniques produced MAPI thin films with a ~1.6 eV direct band gap and intrinsic properties. The two different depositions techniques mainly influenced the morphological appearance of the films, which in turn contributed to

influence the device performances. In particular, while the one-step process films show grains of different sizes and numerous pin-holes, the films prepared with the two-step process formed highly uniform films, made of small grains but sporadic particles of unreacted reagent. While the crystallinity of films made with the one-step process were improved by treating the surface with an anti-solvent (toluene), for the two-step process the annealing time was increased to 60 minutes to permit a complete reaction between the two reagents: $PbI_2$ and MAI. The films were introduced into devices with the following architecture: glass/ITO/c-$TiO_2$/MAPI/spiro-OMeTAD/Au to study the effect of the different deposition on the device performance. Once the thickness of the electron transporting material was optimised, the best device efficiencies recorded were 8.22% *PCE* ($V_{OC}$ = 0.88 V, $J_{SC}$ = 20.83 mA/cm$^2$, *FF* = 44.8%) for one-step process devices and 8.45% *PCE* ($V_{OC}$ = 0.98 V, $J_{SC}$ = 16.57 mA/cm$^2$, *FF* = 52.1%) for the two-step devices. Further improvement of the MAPI films showed an increased efficiency of the devices, these being 9.36% *PCE* ($V_{OC}$ = 0.92 V, $J_{SC}$ = 20.23 mA/cm$^2$, *FF* = 50.3%) for one-step process devices treated with toluene, and 11.80% ($V_{OC}$ = 1 V, $J_{SC}$ = 20.87 mA/cm$^2$, *FF* = 56.5%) for two-step process devices measured on the second day. Hysteresis was found in all devices, but was a larger issue in the case of one-step process devices.

Therefore, according to results presented in this work, it may be concluded that the best MAPI deposition technique is the two-step process. In terms of scale-up processes, however, the one-step process allows a simplified device fabrication, adoption of smaller quantities of solutions and solvents, fewer depositions steps, and shorter annealing times and it is therefore better for PV applications.

However, both MAPI films and devices have shown low stability towards ambient conditions. In this work a systematic study to find the cause of degradation was performed, and showed that MAPI is particularly subjected to degradation when it is exposed to a

combination of UV-radiation and oxygen. When this work was ongoing, the same subject was investigated by numerous research groups worldwide and the hypothesis of the degradation mechanism was confirmed. The shelf life of these perovskite materials is therefore tolerable, however a protection towards UV-radiation is necessary. MAPI is therefore not an adequate material for solar cell applications. Encapsulation may be a solution for short periods of time, but long exposures of these devices to sunlight may be an issue. However, recent research has shown incredible improvements in terms of stability and device performance by using mixed-compound perovskites, showing a better perspective for perovskites in the PV field.[33–35]

## 5.6. References


(1) Kojima, A.; Teshima, K.; Shirai, Y.; Miyasaka, T. Organometal Halide Perovskites as Visible-Light Sensitizers for Photovoltaic Cells. *J. Am. Chem. Soc.* **2009**, *131* (17), 6050–6051.

(2) Im, J.-H.; Lee, C.-R.; Lee, J.-W.; Park, S.-W.; Park, N.-G. 6.5% Efficient Perovskite Quantum-Dot-Sensitized Solar Cell. *Nanoscale* **2011**, *3* (10), 4088–4093.

(3) Etgar, L.; Gao, P.; Xue, Z.; Peng, Q.; Chandiran, A. K.; Liu, B.; Nazeeruddin, M. K.; Grätzel, M. Mesoscopic $CH_3NH_3PbI_3/TiO_2$ Heterojunction Solar Cells. *J. Am. Chem. Soc.* **2012**, *134* (42), 17396–17399.

(4) Kim, H. B.; Choi, H.; Jeong, J.; Kim, S.; Walker, B.; Song, S.; Kim, J. Y. Mixed Solvents for the Optimization of Morphology in Solution-Processed, Inverted-Type Perovskite/Fullerene Hybrid Solar Cells. *Nanoscale* **2014**, *6* (12), 6679–6683.

(5) Kim, M.; Kim, G. H.; Oh, K. S.; Jo, Y.; Yoon, H.; Kim, K. H.; Lee, H.; Kim, J. Y.; Kim, D. S. High-Temperature-Short-Time Annealing Process for High-Performance Large-Area Perovskite Solar Cells. *ACS Nano* **2017**, *11* (6), 6057–6064.

(6) Ahn, N.; Son, D.-Y.; Jang, I.-H.; Kang, S. M.; Choi, M.; Park, N.-G. Highly Reproducible Perovskite Solar Cells with Average Efficiency of 18.3% and Best Efficiency of 19.7% Fabricated via Lewis Base Adduct of Lead(II) Iodide. *J. Am. Chem. Soc.* **2015**, *137* (27), 8696–8699.

(7) Paek, S.; Schouwink, P.; Athanasopoulou, E. N.; Cho, K. T.; Grancini, G.; Lee, Y.; Zhang, Y.; Stellacci, F.; Nazeeruddin, M. K.; Gao, P. From Nano- to Micrometer Scale: The Role of Antisolvent Treatment on High Performance Perovskite Solar

Cells. *Chem. Mater.* **2017**, *29* (8), 3490–3498.

(8) Choi, Y. C.; Lee, S. W.; Kim, D. H. Antisolvent-Assisted Powder Engineering for Controlled Growth of Hybrid $CH_3NH_3PbI_3$ Perovskite Thin Films. *APL Mater.* **2017**, *5* (2), 026101–026107.

(9) Lee, M. M.; Teuscher, J.; Miyasaka, T.; Murakami, T. N.; Snaith, H. J. Efficient Hybrid Solar Cells Based on Meso-Superstructured Organometal Halide Perovskites. *Science.* **2012**, *338* (6107), 643–647.

(10) Kim, H.-S.; Lee, C.-R.; Im, J.-H.; Lee, K.-B.; Moehl, T.; Marchioro, A.; Moon, S.-J.; Humphry-Baker, R.; Yum, J.-H.; Moser, J. E.; Grätzel, M.; Park, N.-G. Lead Iodide Perovskite Sensitized All-Solid-State Submicron Thin Film Mesoscopic Solar Cell with Efficiency Exceeding 9%. *Sci. Rep.* **2012**, *2* (1), 591–603.

(11) Grätzel, M. The Light and Shade of Perovskite Solar Cells. *Nat. Mater.* **2014**, *13* (9), 838–842.

(12) Burschka, J.; Pellet, N.; Moon, S.-J.; Humphry-Baker, R.; Gao, P.; Nazeeruddin, M. K.; Grätzel, M. Sequential Deposition as a Route to High-Performance Perovskite-Sensitized Solar Cells. *Nature* **2013**, *499* (7458), 316–319.

(13) Mei, A.; Li, X.; Liu, L.; Ku, Z.; Liu, T.; Rong, Y.; Xu, M.; Hu, M.; Chen, J.; Yang, Y.; Grätzel, M.; Han, H. A Hole-Conductor-Free, Fully Printable Mesoscopic Perovskite Solar Cell with High Stability. *Science,* **2014**, *345* (6194), 295–298.

(14) Green, M. A.; Ho-Baillie, A.; Snaith, H. J. The Emergence of Perovskite Solar Cells. *Nat. Photonics* **2014**, *8* (7), 506–514.

(15) McGehee, M. D. Perovskite Solar Cells: Continuing to Soar. *Nat. Mater.* **2014**, *13* (9), 845–846.

(16) Heo, J. H.; Song, D. H.; Han, H. J.; Kim, S. Y.; Kim, J. H.; Kim, D.; Shin, H. W.; Ahn, T. K.; Wolf, C.; Lee, T.-W.; Im, S. H. Planar $CH_3NH_3PbI_3$ Perovskite Solar Cells with Constant 17.2% Average Power Conversion Efficiency Irrespective of the Scan Rate. *Adv. Mater.* **2015**, *27* (22), 3424–3430.

(17) Hwang, I.; Yong, K. Novel CdS Hole-Blocking Layer for Photostable Perovskite Solar Cells. *ACS Appl. Mater. Interfaces* **2016**, *8* (6), 4226–4232.

(18) Xiao, Z.; Bi, C.; Shao, Y.; Dong, Q.; Wang, Q.; Yuan, Y.; Wang, C.; Gao, Y.; Huang, J. Efficient, High Yield Perovskite Photovoltaic Devices Grown by Interdiffusion of Solution-Processed Precursor Stacking Layers. *Energy Environ. Sci.* **2014**, *7* (8), 2619–2623.

(19) Schölin, R.; Karlsson, M. H.; Eriksson, S. K.; Siegbahn, H.; Johansson, E. M. J.; Rensmo, H. Energy Level Shifts in Spiro-OMeTAD Molecular Thin Films When Adding Li-TFSI. *J. Phys. Chem. C* **2012**, *116* (50), 26300–26305.

(20) Wang, X.; Sarvari, H.; Dang, H.; Chen, Z.; Singh, V. Evolution Characteristics of Perovskite Solar Cells in Air and Vacuum Environments. *Optik*, **2017**, *150*, 111–116.

(21) Jeon, N. J.; Noh, J. H.; Kim, Y. C.; Yang, W. S.; Ryu, S.; Seok, S. Il. Solvent Engineering for High-Performance Inorganic-Organic Hybrid Perovskite Solar Cells. *Nat. Mater.* **2014**, *13* (9), 897–903.

(22) Socrates, G. *Infrared and Raman Characteristic Group Frequencies*; John Wiley & Sons, 2004.

(23) Pham, N. D.; Tiong, V. T.; Yao, D.; Martens, W.; Guerrero, A.; Bisquert, J.; Wang, H. Guanidinium Thiocyanate Selective Ostwald Ripening Induced Large Grain for High Performance Perovskite Solar Cells. *Nano Energy* **2017**, *41*, 476–487.

(24) Jia, E. D.; Lou, X.; Zhou, C. L.; Hao, W. C.; Wang, W. J. $O_3$ Fast and Simple Treatment-Enhanced p-Doped in Spiro-MeOTAD for $CH_3NH_3I$ Vapor-Assisted Processed $CH_3NH_3PbI_3$ Perovskite Solar Cells. *Chinese Phys. B* **2017**, *26* (6), 068803(1)-068803(6).

(25) Whitfield, P. S.; Herron, N.; Guise, W. E.; Page, K.; Cheng, Y. Q.; Milas, I.; Crawford, M. K. Structures, Phase Transitions and Tricritical Behavior of the Hybrid Perovskite Methyl Ammonium Lead Iodide. *Sci. Rep.* **2016**, *6*, 35685–35710.

(26) Pham, N. D.; Tiong, V. T.; Yao, D.; Martens, W.; Guerrero, A.; Bisquert, J.; Wang, H. Guanidinium Thiocyanate Selective Ostwald Ripening Induced Large Grain for High Performance Perovskite Solar Cells. *Nano Energy* **2017**, *41*, 476–487.

(27) Milot, R. L.; Eperon, G. E.; Snaith, H. J.; Johnston, M. B.; Herz, L. M. Temperature-Dependent Charge-Carrier Dynamics in $CH_3NH_3PbI_3$ Perovskite Thin Films. *Adv. Funct. Mater.* **2015**, *25* (39), 6218–6227.

(28) Yamada, Y.; Nakamura, T.; Endo, M.; Wakamiya, A.; Kanemitsu, Y. Near-Band-Edge Optical Responses of Solution-Processed Organic-Inorganic Hybrid Perovskite $CH_3NH_3PbI_3$ on Mesoporous $TiO_2$ Electrodes. *Appl. Phys. Express* **2014**, *7* (3), 032302–032306.

(29) Leguy, A. M. A.; Hu, Y.; Campoy-Quiles, M.; Alonso, M. I.; Weber, O. J.; Azarhoosh, P.; van Schilfgaarde, M.; Weller, M. T.; Bein, T.; Nelson, J.; Docampo, P.; Barnes, P. R. F. Reversible Hydration of $CH_3NH_3PbI_3$ in Films, Single Crystals, and Solar Cells. *Chem. Mater.* **2015**, *27* (9), 3397–3407.

(30) Yang, D.; Zhou, X.; Yang, R.; Yang, Z.; Yu, W.; Wang, X.; Li, C.; Liu, S. (Frank); Chang, R. P. H. Surface Optimization to Eliminate Hysteresis for Record Efficiency Planar Perovskite Solar Cells. *Energy Environ. Sci.* **2016**, *9* (10), 3071–3078.

(31) Farhan, M. S.; Zalnezhad, E.; Bushroa, A. R.; Sarhan, A. A. D. Electrical and Optical Properties of Indium-Tin Oxide (ITO) Films by Ion-Assisted Deposition (IAD) at Room Temperature. *Int. J. Precis. Eng. Manuf.* **2013**, *14* (8), 1465–1469.

(32) Aristidou, N.; Eames, C.; Sanchez-Molina, I.; Bu, X.; Kosco, J.; Islam, M. S.; Haque, S. A. Fast Oxygen Diffusion and Iodide Defects Mediate Oxygen-Induced Degradation of Perovskite Solar Cells. *Nat. Commun.* **2017**, *8*, 15218–15227.

(33) Saliba, M.; Matsui, T.; Domanski, K.; Seo, J.-Y.; Ummadisingu, A.; Zakeeruddin, S. M.; Correa-Baena, J.-P.; Tress, W. R.; Abate, A.; Hagfeldt, A.; Gratzel, M. Incorporation of Rubidium Cations into Perovskite Solar Cells Improves Photovoltaic Performance. *Science.* **2016**, *354* (6309), 206–209.

(34) Duong, T.; Wu, Y.; Shen, H.; Peng, J.; Fu, X.; Jacobs, D.; Wang, E.-C.; Kho, T. C.; Fong, K. C.; Stocks, M.; Franklin, E.; Blakers, A.; Zin, N.; McIntosh, K.; Li, W.; Cheng, Y.-B.; White, T. P.; Weber, K.; Catchpole, K. Rubidium Multication Perovskite with Optimized Bandgap for Perovskite-Silicon Tandem with over 26% Efficiency. *Adv. Energy Mater.* **2017**, *7* (14), 1700228–1700239.

(35) Snaith, H. J. Present Status and Future Prospects of Perovskite Photovoltaics. *Nat. Mater.* **2018**, *17* (5), 372–376.

# 6. $CsPbI_2Br$ perovskite films, devices and degradation studies

*This work has been published as:*

*Mariotti, S.; Hutter, O. S.; Phillips, L. J.; Yates, P. J.; Kundu, B.; Durose, K., Stability and Performance of $CsPbI_2Br$ Thin Films and Solar Cell Devices, ACS Appl. Mater. Interfaces,* ***2018****, 10 (4), 3750–3760, DOI: 10.1021/acsami.7b14039.*

## 6.1. Introduction

A full literature review on all-inorganic perovskites, with particular emphasis on caesium perovskites, has been presented in chapter 3. The main points relevant to this chapter are now summarised: all-inorganic perovskites, such as $CsPbI_3$ and $CsPbBr_3$, and their mixed compositions $CsPbI_{(1-x)}Br_x$, are of interest since their thermal and chemical stabilities under PV operating conditions are superior to that of most organic-inorganic perovskites.[1–4] Nevertheless, the *single halide* caesium perovskites have some limitations:

- The dark brown cubic phase of $CsPbI_3$ has a useful band gap for PV applications (1.73 eV) but it is not stable in this form at room temperature.[5–8]
- The orthorhombic $CsPbBr_3$ has a wider band gap (2.25 eV) which is unsuitable for highly efficient solar cells, but is stable at room temperature.[5,9,10]

Caesium lead *mixed halide* perovskites on the other hand have the potential to offer a compromise of these properties, such as a tuned band gap and improved stability at room temperature. Therefore their potential for use in PV applications may be more realistic.[5,10,11]

In particular, $CsPbI_2Br$ (1.92 eV) has received attention: Sutton *et al.*, demonstrated $CsPbI_2Br$ solar cell devices with 9.8% efficiency,[5] however the environmental stability of this material was only marginally considered until the present work was published in 2018. This chapter presents a study of $CsPbI_2Br$ thin films, devices and their environmental stability.

Films were prepared by spin-coating a precursor solution and then by annealing them at a range of temperatures (150 - 350°C). In the literature the annealing temperature used to prepare $CsPbI_2Br$ films is 350°C,[5] but this range of 200°C enabled the evaluation of the minimum temperature required to form the brown perovskite phase to use in devices and scaled-up processes. The resulting $CsPbI_2Br$ films were characterised and used for fabrication and characterisation of devices having the following structure: glass/ITO/$TiO_2$/$CsPbI_2Br$/spiro-OMeTAD/Au.

Similarly to the study in chapter 5, this work includes the study on the stability of films to environmental factors. As $CsPbI_2Br$ is closer in composition to $CsPbI_3$ than $CsPbBr_3$, the Goldschmidt tolerance factor[12] for $CsPbI_3$ should be considered, and is reported as being calculated as 0.78[13] or 0.85.[14,15] The first appears more accurate as the tolerance factor in the range of 0.71 - 0.8 corresponds to orthorhombic structures stable at room temperature. For this reason, it is possible to infer that $CsPbI_2Br$, despite having an improved stability in its perovskite phase compared to $CsPbI_3$, may energetically prefer the orthorhombic state. Nevertheless, since the experimental stability of the $CsPbI_2Br$ compound had not been investigated, a full study of the causes and the mechanism of degradation was performed and is presented in this chapter. Experiments were performed to isolate and identify the factors having the most deleterious effects on the material. The factors investigated were chosen with reference to those known to influence MAPI. These were: UV radiation combined with oxygen,[16–19] and water.[20–23] A further study on MAPI

relevant to the present work is that of Leguy *et al.*[20] who identified a hydrated MAPI perovskite phase $(CH_3NH_3)_4PbI_6 \cdot 2H_2O$. This is relevant since $CsPbI_2Br$ proved to be sensitive to moisture raising the possibility that it too has a hydrated phase.

The role of water on $CsPbI_2Br$ was therefore investigated and a mechanism for its degradation was postulated. All work on the degradation on $CsPbI_2Br$ was performed on the timescale of one week to one month in order to allow a direct comparison with the study of MAPI degradation presented in chapter 5. In addition, the degradation study was extended to devices and their recovery.

## 6.2. Experimental methods

### 6.2.1. Fabrication and characterisation of $CsPbI_2Br$ thin films

$CsPbI_2Br$ films were deposited onto quartz coated glass or glass/ITO substrates previously cleaned using the method described in section 4.1.1.

To prepare the films a 40% w/v solution of $CsI : PbI_2 : PbBr_2$ (1 : 0.5 : 0.5 molar concentration) in DMF/DMSO (9:1 vol.) was prepared inside a nitrogen glovebox. The solution was then stirred for one hour at 50°C and finally filtered using a 0.22 µl PTFE filter. Deposition was accomplished by dynamically spin-coating 50 µl of the solution at 2000 rpm for 25seconds onto cleaned quartz coated glass (15 x 20 $mm^2$) and placing the samples onto a hotplate for annealing immediately afterwards. The annealing was performed for 10 minutes at temperatures in the range of 150°C - 350°C, in steps of 50°C. Photographs of the solution and the resulting film are shown in Fig. 6.1.

The films were analysed by UV-Vis-IR spectrophotometry, XRD, SEM and spectroscopic STS analysis (see section 4.4.1 for details).

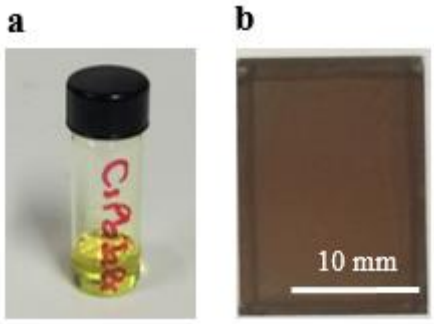


**Fig. 6.1.** Photographs of a) $CsPbI_2Br$ solution obtained after stirring at 50°C, and b) $CsPbI_2Br$ thin film deposited on quartz glass (15 x 20 $mm^2$).

### 6.2.2. Device fabrication and characterisation

Among the 158 $CsPbI_2Br$ devices that were prepared, an optimised device fabrication procedure was stipulated and is here described.

Devices were prepared with the following device structure: glass/ITO/$TiO_2$/$CsPbI_2Br$/spiro-OMeTAD/Au, as shown in the diagram in Fig. 6.2. On commercial ITO covered glass a layer of compact $TiO_2$ was deposited by spin-coating a 0.15 M followed by a 0.3 M solution of Ti-isopropoxide in ethanol, as described in the previous chapter (section 5.2.4.a). A small $TiO_2$-free area was left on the ITO to allow electrical contacting. After annealing and cooling of the $TiO_2$, a 350 nm layer of $CsPbI_2Br$ was deposited, using the same procedure described in section 6.2.1. Afterwards, a layer of doped spiro-OMeTAD was spin-coated on the perovskite's surface at 3000 rpm for 30 seconds (see section 5.2.4.b). Finally, the samples were quickly transferred to an evaporator where 50 nm of gold was deposited in 3 mm Ø dots, providing the back contacts. Each rectangular sample (20 x 15 $mm^2$), was usually contacted with four gold dots.

Initial device measurements were carried out in air, but since samples degraded quickly only *J-V* measurements were performed. To allow extensive *J-V* and *EQE* measurements, later devices were loaded into a measurement box under dry nitrogen for transfer to the measurement stations, as described in section 4.5.4.

For measurements in air, the full dot area of 0.07 $cm^2$ was illuminated, whereas when the air-tight box was used, the sample holder had a mask with 2 mm Ø holes, making the effective illuminated area 0.0314 $cm^2$.

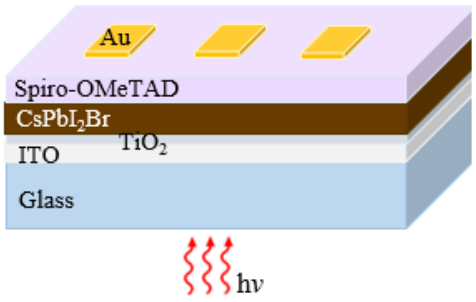


**Fig. 6.2.** Diagram of the "superstrate" device structure of the $CsPbI_2Br$ solar cells fabricated in this work.

### 6.2.3. Intentional degradation of $CsPbI_2Br$ films

After realising that brown $CsPbI_2Br$ layers that were prepared in a nitrogen glovebox would quickly degrade into yellowish films when exposed to air, the causes and chemical mechanism of the transformation were investigated.

A set of trial degradation conditions were selected in order to systematically identify the factors that promote degradation. These were the same as those selected for the study of MAPI degradation as described in section 4.3 and were 'UV/$O_3$', 'UV/$N_2$', 'dark/air' and 'desiccator'.

*a) Analysis of degraded films and powders*

After being subjected to each test, $CsPbI_2Br$ thin films were analysed visually (as the colour of the film changes from brown to yellow after degradation), by UV-Vis-IR spectrophotometry (band gap evaluation) and by XRD (crystal structure identification).

In order to investigate the mechanism of the process, powder samples of the material were synthesises for further analysis: bulk powders were prepared by dripping 1 ml of the

perovskite precursor solution onto a glass slide and heating at 300°C for 10 minutes. The film was then scraped off to yield ~16 mg of $CsPbI_2Br$ powder. This allowed measurement by differential scanning calorimetry/thermo-gravimetric analysis (DSC-TGA) and proton nuclear magnetic resonance ($^1H$ NMR). For the DSC-TGA an alumina crucible with a heating rate of 10°C/min was used, while for the NMR measurements a few milligrams of the powders were introduced in NMR tubes inside an argon glovebox and dissolved in deuterated dimethyl sulfoxide (DMSO-$d_6$).

See section 4.4.1 and 4.4.2 for more information about the instruments used.

*b) Film recovery*

After degradation, yellowish films were recovered by re-annealing at $T > 250$°C, preferably at 350°C, for 10 minutes. Immediately, the films regained their dark uniform brown appearance. The characterisation of the recovered layers was performed visually and by XRD analysis.

### 6.2.4. Device degradation and recovery

Devices were intentionally degraded by leaving them in the open air in the lab. Since one of the active degradation factors was found to be atmospheric moisture (see section 6.3.3) and the humidity was not controlled, the time taken for degradation varied from minutes to hours. The device recovery was performed by re-annealing the glass/ITO/$TiO_2$/yellow-$CsPbI_2Br$ films at 350°C, under nitrogen conditions whereupon the perovskite recovered its dark phase. The device performance of recovered films was tested by applying a fresh layer of spiro-OMeTAD (since this hole transporting material is not stable at 350°C).

## 6.3. Results

### 6.3.1. $CsPbI_2Br$ thin films

$CsPbI_2Br$ films deposited on glass, showed a different visual appearance according to the annealing temperature used, as shown in the photographs in Fig. 6.3a. Temperatures above 150°C were necessary to begin to form the brown perovskite phase. However, the films annealed at 150°C and 200°C show orange areas, which became smaller and less prevalent when the temperature was increased. This phase is most likely to be the orange cubic phase of $CsPbBr_3$,[5] which forms at $T$ > 130°C (see review in section 3.3.2.a). Upon increasing the preparation temperature, the films appear gradually more uniform, and assume a dark-brown colour, consistent with the cubic phase of $CsPbI_2Br$. The film's superior quality at $T$ > 250°C was demonstrated by SEM (Fig. 6.3b), forming crystals of 1 - 2 μm Ø at 350°C annealing.

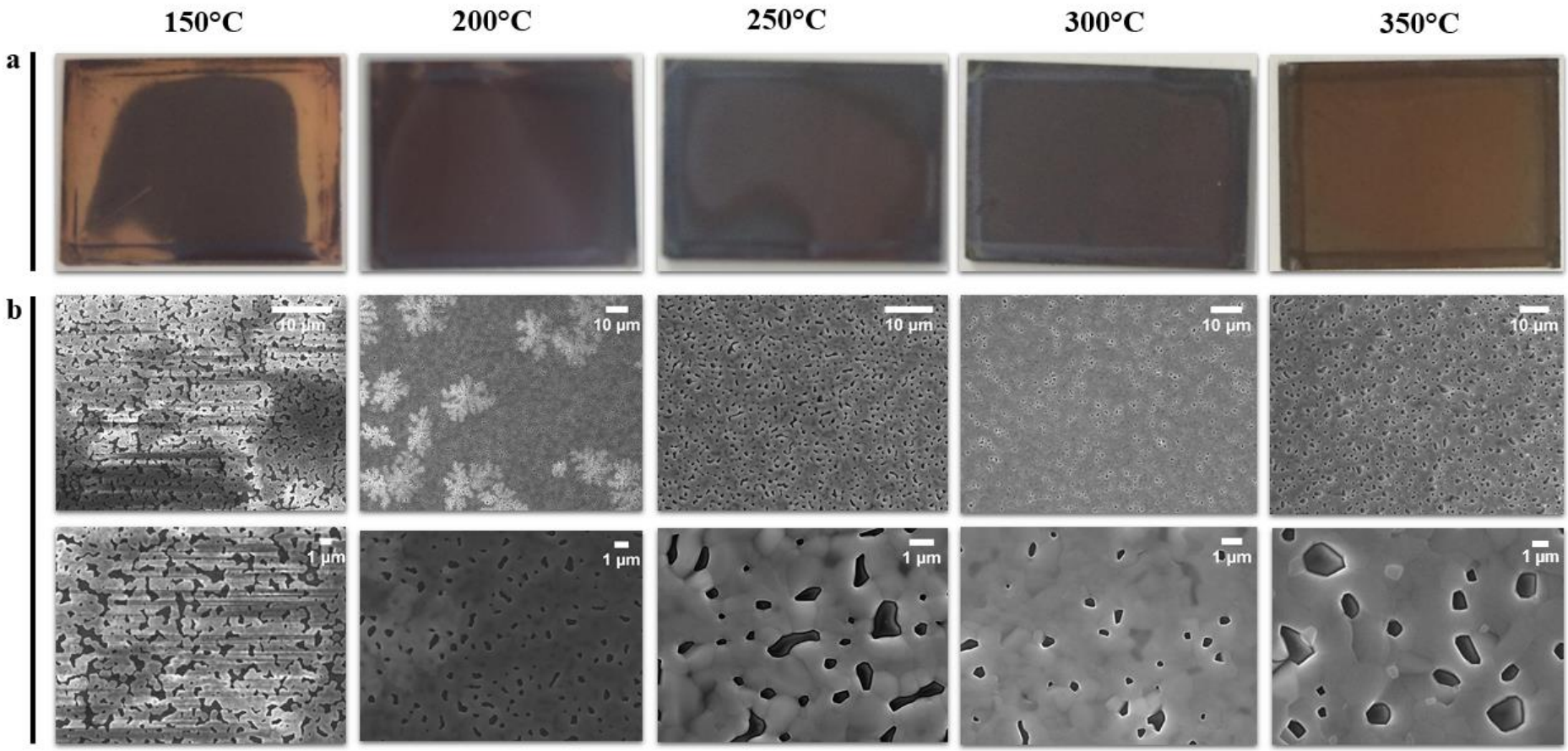


**Fig. 6.3.** Appearance of $CsPbI_2Br$ films deposited on glass *via* one-step solution process and then annealed at 150, 200, 250, 300 and 350°C inside a nitrogen glovebox. a) Photographs of $CsPbI_2Br$ layers (20 x 15 $mm^2$) showing improved uniformity of the film with annealing temperature. b) SEM images, showing an improvement of the homogeneity of the films at $T$ > 250°C. Nevertheless, films show numerous pin-holes, which could cause lower device performance. Images of films annealed at 150°C show striations due to charging, since these samples are highly resistive.

Visual inspection of these $CsPbI_2Br$ films showed that those annealed at 300 and 350°C produced more uniform films. However, analysis by XRD and UV-Vis-IR spectrophotometry showed identical properties for each annealing temperature used. Fig. 6.4a shows XRD results, with peaks at $2\theta = 14.6°$ (100) and 29.6° (200), which is consistent with the XRD patterns presented in the literature and corresponds to a perovskite cubic structure.[5,10] The presence of just two peaks indicates a preferred orientation and that there are no traces of the precursor materials. Optical measurements (Fig. 6.4b), show that both transmittance and reflectance curves are similar for all samples. From these data it was possible to calculate the absorption coefficient and, hence generate the Tauc plots for all films. Fig. 6.4c shows the absorption coefficient for $CsPbI_2Br$ films at all annealing temperatures: a range of $0.5 – 3.5 \cdot 10^5$ $cm^{-1}$ was observed in the visible region for all films. However, the film annealed at 150°C shows an additional absorption feature at 450 – 460 nm (~2.7 - 2.8 eV) which may indicate the presence of secondary phases. The measured direct band gaps were in the range of 1.91-1.92 eV (Fig. 6.4d), which is consistent with literature values.[5,10]

Although both XRD and optical measurements give very similar results for samples having different morphologies and appearances, it should be mentioned that they both sampled the most uniform, central parts of the films which comprised the brown perovskite phase only.

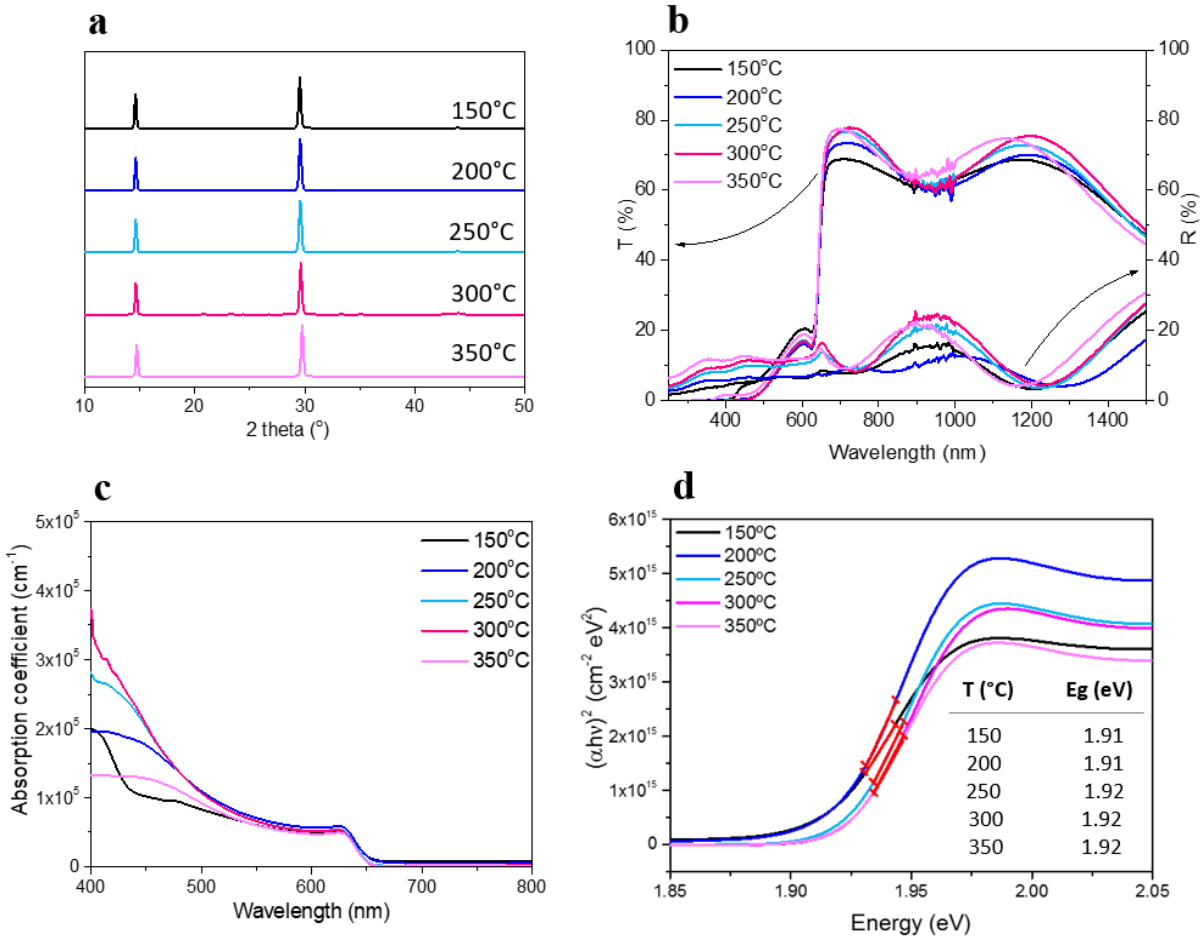


**Fig. 6.4.** Characterisation on $CsPbI_2Br$ films deposited on glass and then annealed at 150, 200, 250, 300 and 350°C. a) XRD patterns showing identical peaks for all films which correspond to the cubic structure of $CsPbI_2Br$ perovskite. b) UV-Vis-IR transmittance and reflectance spectra used to calculate c) the absorption coefficient and d) the Tauc plot, which provides the values of the band gap for all films presented in the inset table (1.91 – 1.92 eV).

Since the Tauc plots in Fig. 6.4d showed insufficient linear portions for precise estimation of the band gap, spectroscopic mode scanning probe microscopy was used to determine the near-edge density of states (DOS) of the perovskite semiconductor in order to make an independent measurement (Fig. 6.5).

A typical DOS spectrum measured by scanning tunneling spectroscopy (STS) of a $CsPbI_2Br$ layer is shown in Fig. 6.5a. During the measurement a sweeping bias was applied to the sample, producing a tunneling current between the semiconductor and the measuring tip (*I*-*V*). In the tunneling conductance (d*I*/d*V*) spectrum (Fig. 6.5a) the positive voltage

shows the position of the conduction band, while negative voltages indicate the position of the valence band, as in those regions electrons are respectively injected and withdrawn.

As STS is an extremely localised measurement, it was necessary to probe numerous sampling points to obtain reliable data. Those are presented in the histograms in Fig. 6.5b, showing the distribution of energies measured for the valence and conduction band edges of the semiconductor.

Overall the measurements reveal a band gap of 1.98 eV which is slightly higher than, but comparable to the values obtained from the Tauc plots (Fig. 6.4d). This difference may arise due to method of determination: since optical and STS measurements determine different properties (energy for the promotion of an electron from valence band to conduction band and tunnelling current respectively), the band gap values extracted may differ. For this reason, the $E_g$ values obtained for $CsPbI_2Br$ are subjected to systematic error.

In addition, the STS measurement shows that the Fermi level is positioned in the middle of the gap, indicating that the $CsPbI_2Br$ is an intrinsic material.

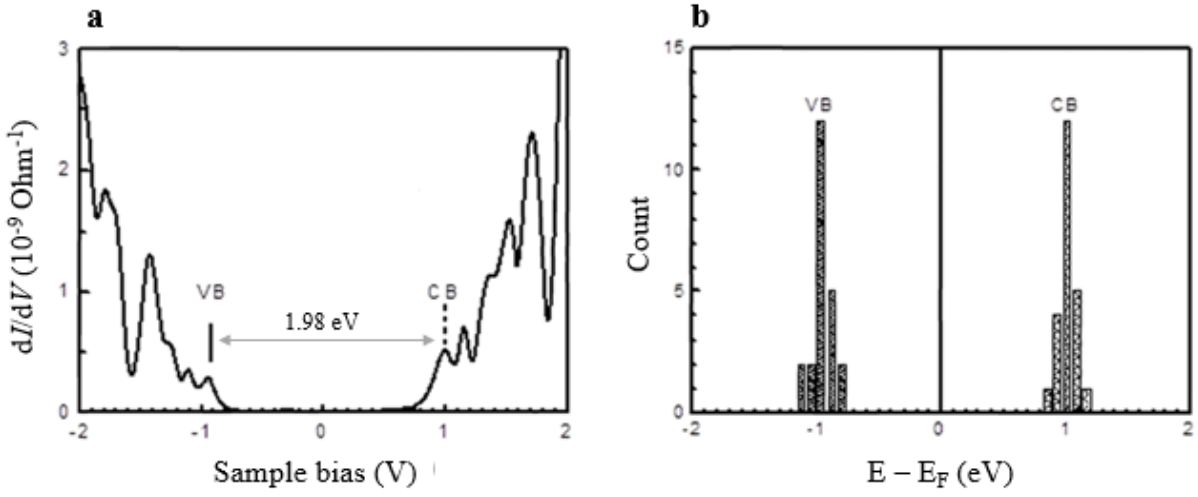


**Fig. 6.5.** Scanning tunneling spectroscopy (STS) measurement performed on $CsPbI_2Br$ film annealed at 350°C, revealing a band gap of 1.98 eV. a) Density of states (DOS) profile (d*I*/d*V*) showing the valence and conduction band (VB and CB) locations. b) Histogram of the valence and conduction band positions from 23 sampling points.

Films were incorporated into devices in order to study the effect of the film preparation conditions on the device performance, as described in the next section. A study of the degradation of the films is deferred until section 6.3.3, since only films made under conditions that gave the best devices (prepared at 350°C) were tested for stability.

### 6.3.2. Characterisation of $CsPbI_2Br$ devices

Devices having the structure glass/ITO/$TiO_2$/$CsPbI_2Br$/spiro-OMeTAD/Au were fabricated using a) different thickness of $TiO_2$ and b) $CsPbI_2Br$ formed at different temperatures. While upwards of 30 devices were made using preparation temperatures between 150 and 350°C, they were found to be unstable in air.

*a) Preliminary device measurements*

This section presents studies for the optimisation of the $TiO_2$ thickness, recording only the data for cells made at 350°C.

An example of the *J-V* curve of a high performing device from this series measured in air, is shown in black in Fig. 6.6, and has a *PCE* of 6.44% ($V_{OC}$ = 1.01 V, $J_{SC}$ = 12.43 mA/cm$^2$, *FF* = 51.24). However, it was necessary to transfer subsequent sets of devices into an air-tight measurement box to permit both the *J-V* and *EQE* measurements required for optimising the $TiO_2$. By measuring the devices in a nitrogen environment a slight improvement in performance was identified: the blue curve in Fig. 6.6 shows *PCE* of 6.64% ($V_{OC}$ = 0.97 V, $J_{SC}$ = 13.80 mA/cm$^2$, *FF* = 49.6). An increased current is recorded compared to devices measured in air, as no degradation was influencing the device performance during the measurement.

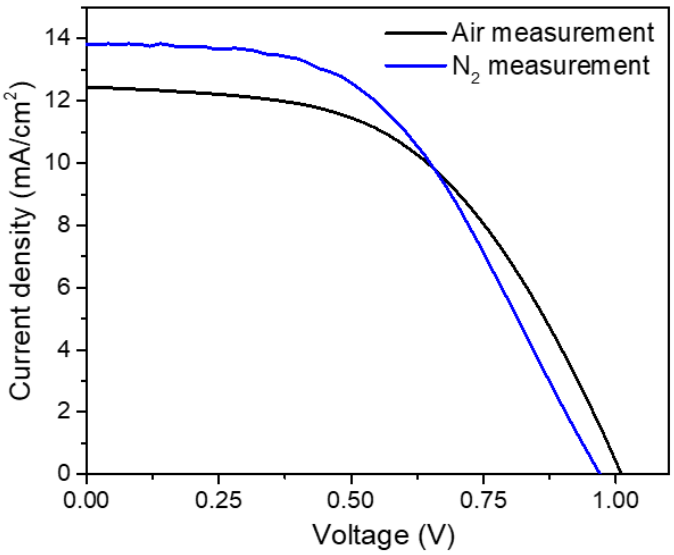


**Fig. 6.6.** *J-V* curve (AM 1.5) of best glass/ITO/$TiO_2$/$CsPbI_2Br$ (350°C)/spiro-OMeTAD/Au device measured in air (black curve) and of a similar cell measured under dry nitrogen inside a measurement box (blue curve).

Although the devices measured in the nitrogen filled box showed an increment of the *PCE*, the *EQE* analysis on these samples showed that the performance of devices could be further improved by thinning the $TiO_2$ layer. Analysing the *EQE* spectra in Fig. 6.7a, it is possible to distinguish three main zones: a low cut off around 310 nm corresponding to the ITO band gap (> 4.1 eV),[24] a shoulder at 370 – 420 nm caused by the onset of absorption of the $TiO_2$ window layer (~3 eV, 415 nm)[25] and a long wavelength cut off at around 650 nm which corresponds to the $CsPbI_2Br$ band gap (1.92 eV). The optical losses at low wavelengths (370 – 420 nm), indicate that photons are absorbed in the window layer. Since the compact $TiO_2$ film made with two layers of Ti-isopropoxide solutions (0.15 M + 0.3 M) (section 5.2.4.a) produces a film with thickness of ~100 – 130 nm, this was reduced to about 50 nm by spin-coating only one solution of Ti-isopropoxide solution. The influence of reducing the thickness of the $TiO_2$ layer on the *EQE* analysis can be seen in the red curve in Fig. 6.7a, showing that the shoulder at 370 – 420 nm wavelengths was reduced and the overall generated current was increased, leading to higher device performances. The general change in *J-V* parameters noticed after thinning the $TiO_2$ layer, was an increment of *c.a.*

20% of the fill factor. Measuring the performances of 8 devices it was observed that the device made with the 0.15 M solution of Ti-isopropoxide produced a champion efficiency of 8% ($V_{OC}$ = 1 V, $J_{SC}$ = 11.56 mA/cm$^2$, *FF* = 69.5%) while the device fabricated with the 0.3 M solution generated a 8.2% efficient device ($V_{OC}$ = 1 V, $J_{SC}$ = 12.68 mA/cm$^2$, *FF* = 67%). Therefore both Ti-isopropoxide solutions used to make single $TiO_2$ layers showed a device efficiency improvement compared to the double $TiO_2$ layer, but as the performance was shown to be slightly higher using the most concentrated precursor solution of $TiO_2$, this was used for the fabrication of devices for the studies presented in the next sections.

The SEM image shown in Fig. 6.7b, demonstrates the device architecture and the thicknesses of the layers: glass/ITO/c-$TiO_2$(50nm)/$CsPbI_2Br$(300-350nm)/spiro-OMeTAD(200nm) for these devices.

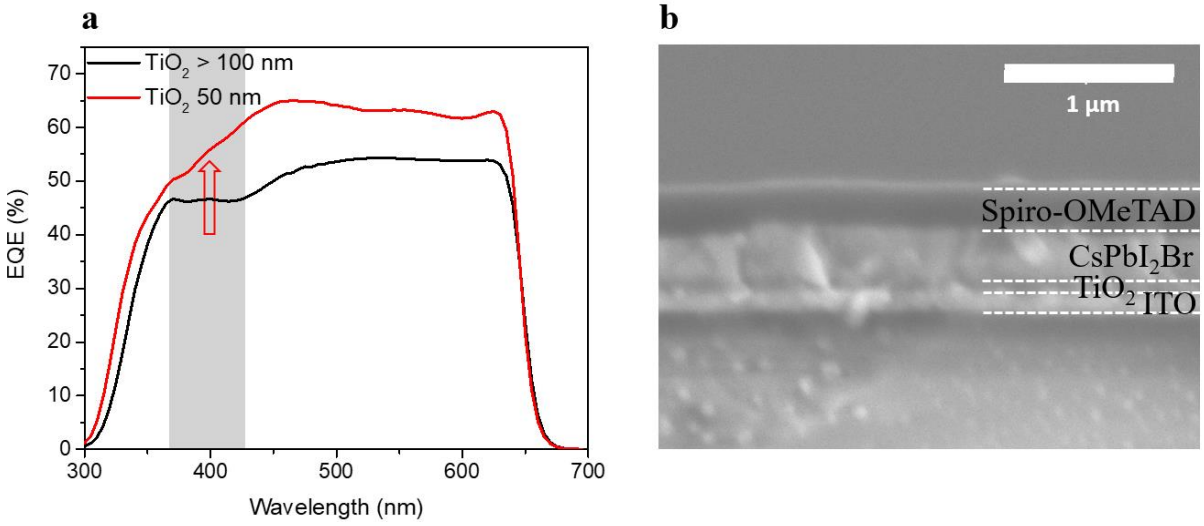


**Fig. 6.7.** a) *EQE* spectra of $CsPbI_2Br$ solar cell devices containing $TiO_2$ layers with different thicknesses. The black curve of the thicker $TiO_2$ layer device (100 -130 nm), show photons absorbed in the window layer below 420 nm. The thinner $TiO_2$ layer corresponding to the red curve (50 nm $TiO_2$ using a 0.3 M solution of Ti-isopropoxide), shows the effect of the improved transparency of the window layer, which produces a more efficient device. b) Cross-section SEM of glass/ITO/$TiO_2$/$CsPbI_2Br$ (350°C annealing)/spiro-OMeTAD/Au device containing a 50 nm $TiO_2$ layer.

Consequently, all devices reported hereon were fabricated using 50 nm thick $TiO_2$ and measured in the air-tight box.

*b) Influence of $CsPbI_2Br$ annealing temperature on device performances*

The effect of the $CsPbI_2Br$ annealing temperature on the device performance was evaluated by making 20 samples: 4 samples at each temperature (150 – 350°C), each of which had 4 contact dots, hence yielding 16 performance results per temperature investigated.

Table 6.3 and Figs. 6.8 and 6.9 present the *J-V* data from these devices. The relationships between the temperature used for the perovskite annealing and the device performance are now described.

Table 6.3 reports the *average* values for *J-V* measurements on fresh and aged devices, however this section focusses only on fresh devices while the discussion on aged devices is deferred until section 6.3.4. *J-V* curves of the champion devices for each annealing temperature used are shown in Fig. 6.8a. The *J-V* curves show that the best performances were achieved for devices prepared with the minimum and the maximum temperatures (150°C and 350°C), however, while the *J-V* curve of the device with $CsPbI_2Br$ annealed at 150°C shows extraordinary current but a poor *FF* (*PCE* = 7.23%, $V_{OC}$ = 1.05 V, $J_{SC}$ = 15.28 mA/cm$^2$ and *FF* = 45.07%), the curve obtained by the device with the 350°C annealed perovskite presents robust *J-V* parameters (*PCE* = 9.08%, $V_{OC}$ = 1.05 V, $J_{SC}$ = 12.68 mA/cm$^2$ and *FF* = 68.4%). However, comparing these results with the averages presented in Table 6.3 (2.29% *PCE* for 150°C and 6.33% *PCE* for the 350°C annealing) it may be speculated that the champion performance of the device annealed at 150°C is exceptional. Considerably lower performances were achieved by devices with the perovskite annealed at 200, 250 and

300°C, as shown from both champion device performances (Fig. 6.8a) and average *PCE* values (1.45%, 1.11% and 1.56% respectively).

The stabilised efficiency of the devices with 350°C annealed $CsPbI_2Br$ was measured, as these were the best performing devices. Fig. 6.8b presents a typical stabilised efficiency analysis of these devices, showing a small drop in efficiency during the first seconds of measurement caused by light soaking settlement, which then stabilises at 6.24% *PCE* for the rest of the evaluation time (70 seconds). Since the *PCE* does not change greatly with time it may be inferred that the *PCE* results presented here are generally reliable.

The relationship between device efficiency and temperature of preparation of $CsPbI_2Br$, is shown more fully in Figs. 6.8c-f which show the averages and standard deviations of all *J-V* parameters (*PCE*, $V_{OC}$, $J_{SC}$ and *FF*) for devices with $CsPbI_2Br$ annealed at 150°C < *T* < 350°C. Graph 6.8c shows a decline of the efficiency between 150°C to a minimum at 250°C and then a rise until 350°C. The increase in performance for higher processing temperature is consistent with the increase in the film continuity shown in the SEM micrographs in Fig. 6.3b and this accounts for the trend in the efficiencies for $T \geq$ 250°C. On the contrary, for $T \leq 250$°C the unexpectedly high *PCE* (best 7.23% and average 2.29%) for the 150°C annealing temperature is inconsistent with the overall trend for $CsPbI_2Br$. Instead it is attributed to presence of phase separation of multiple $CsPbI_{3-x}Br_x$ compositions in the samples prepared at low temperature. This is further discussed in section 6.4.

Comparing the four graphs in Fig. 6.8c-f, the parameter having least influence on the *PCE* trend (Fig. 6.8c) is $V_{OC}$, which is maintained at around 0.7 V between 150 – 300°C and increases by 0.2 V when films are annealed at 350°C (Fig. 6.8d). $J_{SC}$ has a slightly stronger influence, showing a minimum at 250°C and a maximum at 350°C (Fig. 6.8e). The parameter that influences the efficiency most is the fill factor: as shown in Fig. 6.8f, the

trends of *PCE* and *FF* are almost equivalent, with a minimum average *FF* at 250°C of 26.7% and the maximum average *FF* at 350°C of 60.2%, as shown in Table 6.3.

The average results presented in Fig. 6.8c-f, include both forward and reverse scan results for all *J-V* parameters. These $CsPbI_2Br$ devices display significant hysteresis in all PV working parameters, which is illustrated in Fig. 6.9c.

| | | **150°C** | **200°C** | **250°C** | **300°C** | **350°C** |
|---|---|---|---|---|---|---|
| $V_{OC}$ (V) | **Fresh** | 0.67 (± 0.15) | 0.68 (± 0.05) | 0.71 (± 0.10) | 0.73 (± 0.10) | 0.90 (± 0.10) |
| | **Aged** | 0.50 (± 0.08) | 0.51 (± 0.10) | 0.65 (± 0.17) | 0.71 (± 0.07) | 0.79 (± 0.02) |
| $J_{SC}$ ($mA/cm^2$) | **Fresh** | 9.07 (± 2.49) | 7.63 (± 1.56) | 5.83 (± 1.68) | 7.94 (± 1.32) | 11.74 (± 0.68) |
| | **Aged** | 0.16 (± 0.02) | 0.23 (± 0.21) | 0.55 (± 0.72) | 0.26 (± 0.06) | 0.24 (± 0.04) |
| *FF* (%) | **Fresh** | 34.8 (± 5.0) | 28.2 (± 2.3) | 26.7 (± 2.8) | 26.9 (± 3.0) | 60.2 (± 8.3) |
| | **Aged** | 40.6 (± 3.5) | 44.5 (± 6.6) | 42.2 (± 4.7) | 36.2 (± 6.1) | 39.7 (± 2.6) |
| *PCE* (%) | **Fresh** | 2.29 (± 1.37) | 1.45 (± 0.39) | 1.11 (± 0.40) | 1.56 (± 0.41) | 6.33 (± 1.25) |
| | **Aged** | 0.03 (± 0.01) | 0.06 (± 0.06) | 0.18 (± 0.28) | 0.07 (± 0.02) | 0.08 (± 0.01) |

**Table 6.3.** Average PV working parameters for $CsPbI_2Br$ devices prepared at different temperatures ($N \approx 16$). The 'fresh' data is for devices loaded into an airtight box under dry $N_2$ for measurement, whereas the 'aged' devices had been stored in open air for 24 hours.

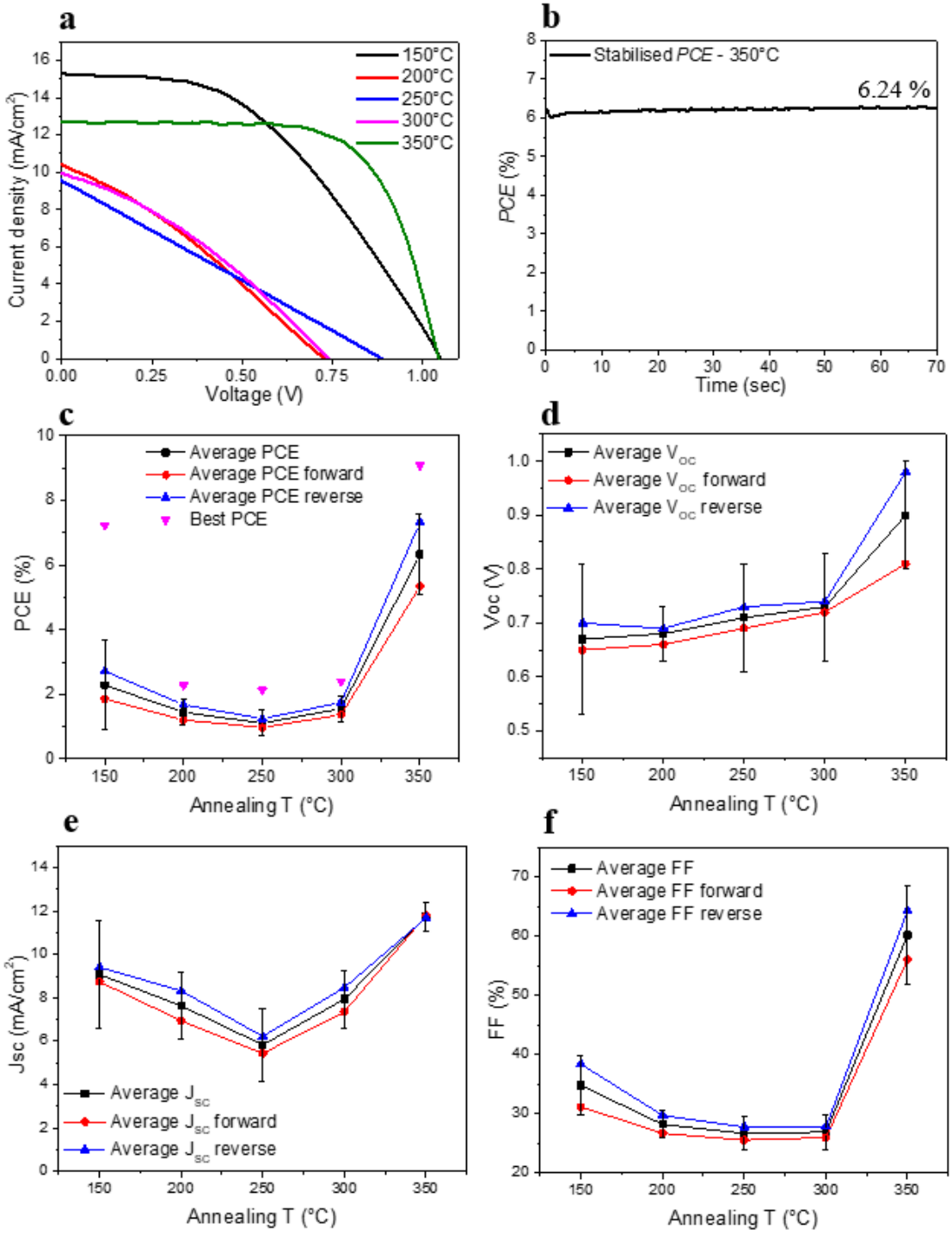


**Fig. 6.8.** *J-V* results on glass/ITO/$TiO_2$/$CsPbI_2Br$/spiro-OMeTAD/Au devices. a) *J-V* (AM1.5) curves of $CsPbI_2Br$ ($T_{annealing}$ = 150°C – 350°C, $\Delta T$ = 50°C) champion devices. b) Stabilised efficiency of an average performing $CsPbI_2Br$ device where the perovskite was annealed at 350°C. c), d), e), f) $CsPbI_2Br$ ($T_{annealing}$ = 150°C – 350°C, $\Delta T$ = 50°C) device performances measured with *J-V* under AM1.5 illumination in forward and reverse scan directions, showing average points and the related standard deviation: best and average efficiencies (a), open circuit voltages (b), short circuit currents (c) and fill factors (d).

Further to the initial stabilisation tests (Fig. 6.8b), the trend of the current shown in Fig. 6.8e was confirmed by the stabilised $J_{SC}$ and the *EQE* responses for devices having $CsPbI_2Br$ annealed at 150 - 350°C temperature range shown in Fig. 6.9a and b. The lowest current was produced by cells containing $CsPbI_2Br$ annealed at 250°C: 7.5 $mA/cm^2$ stabilised $J_{SC}$ and a maximum *EQE* of *c.a.* 40% compared to a maximum stabilised $J_{SC}$ = 9.82 $mA/cm^2$ and 65% *EQE* at 350°C. All devices show a rapid decline in current in the first 10 seconds, followed by steady state behaviour. However the photocurrent stabilises faster for the best performing cells, with the 350°C device achieving a stable current of ~10 $mA/cm^2$ after 10 seconds. For this reason, for reliable *J-V* measurements, samples were measured after a brief light soaking, using a scan rate of 0.19 V/s.

Fig. 6.9c shows the hysteretic behaviour of the glass/ITO/$TiO_2$/$CsPbI_2Br$/spiro-OMeTAD/Au champion device annealed at 350°C and achieving 9.08% efficiency. This performance was achieved with the reverse scan, while the forward scan *J-V* gave a *PCE* of only 6.62%. The average calculated from 16 contacts on devices with $CsPbI_2Br$ grown at 350°C gave 7.32% *PCE* for the reverse and 5.34% for the forward scan. This 2% absolute difference between forward and reverse scans, indicates severe hysteresis of these devices and the reason for this behaviour is further discussed in section 6.4.

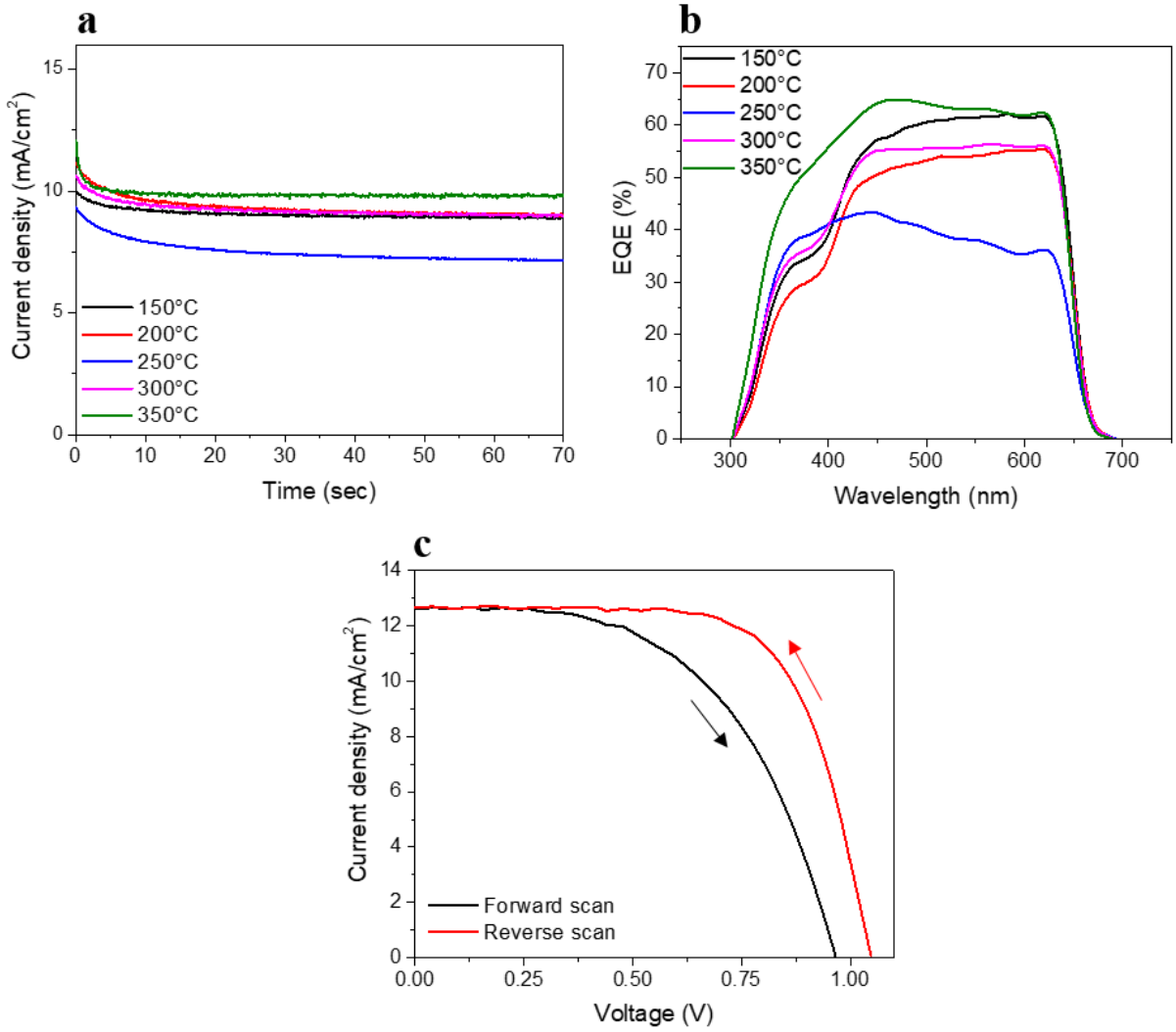


**Fig. 6.9.** Characterisation of $CsPbI_2Br$ devices with films annealed in a temperature range of 150 - 350°C. a) Device's stabilised $J_{SC}$ showing that highest stability and performance is achieved by devices with perovskite annealed at the maximum temperature. b) *EQE* (%) showing that the highest current is produced when $CsPbI_2Br$ is annealed at 350°C. c) High performing device showing hysteresis: higher $V_{OC}$ and *FF* are achieved using a reverse scan rate (*PCE* = 9.08%) compared to the forward scan (*PCE* = 6.62%).

### 6.3.3. $CsPbI_2Br$ material stability

*a) Thin film degradation and characterisation*

As explained previously, when $CsPbI_2Br$ films were removed from the inert atmosphere of the glovebox they underwent a rapid change in colour from brown to pale yellow as shown in Fig. 6.10.

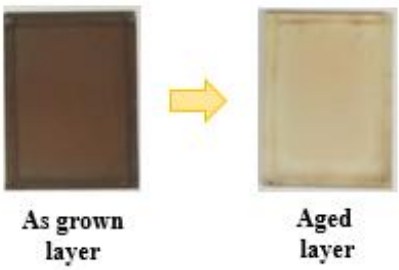


**Fig. 6.10.** Photographs of typical as-grown 'brown' $CsPbI_2Br$ and aged 'yellow' layers (20 x 15 $mm^2$).

Interestingly, it was seen that the degradation to the yellow phase starts from randomly positioned nucleation points in the layer (possibly pin-holes) that evolve to become small circles (see Fig. 6.11a) which merge and slowly cover the whole material. This rapid, spreading transformation can be further observed in Fig. 6.11b, which presents optical micrographs of the $CsPbI_2Br$ degradation in process (one picture every minute, for 32 minutes).

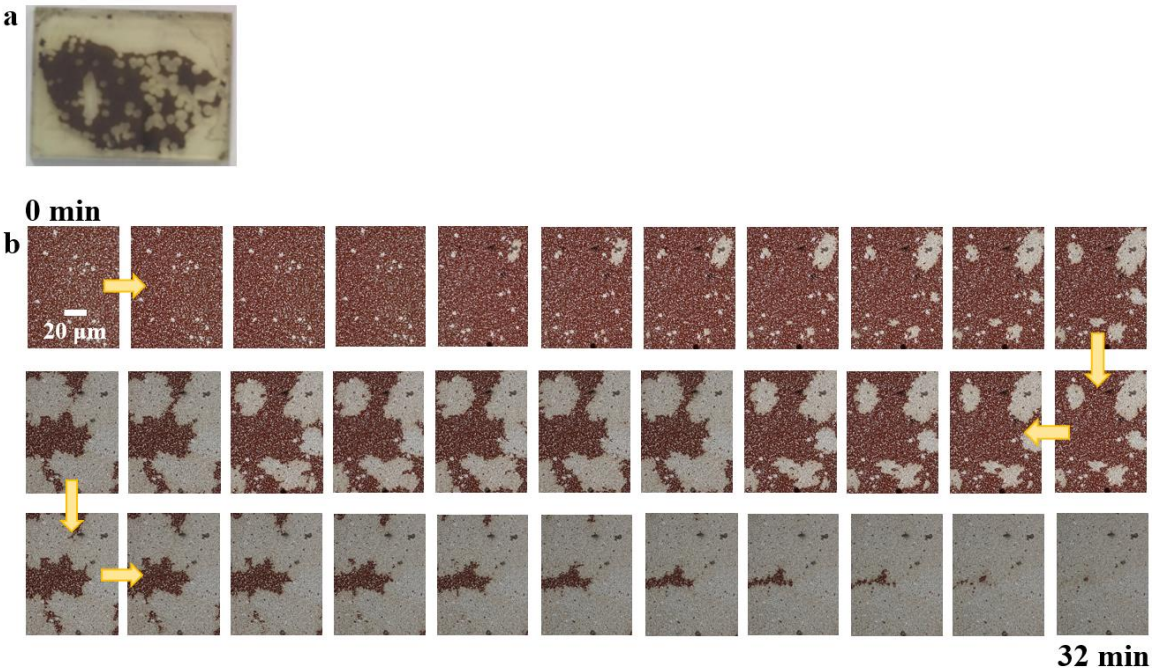


**Fig. 6.11.** Images of $CsPbI_2Br$ layers during degradation. a) Yellow nucleation circles on the surface of a layer deposited on glass (20 x 15 $mm^2$). b) Optical micrographs showing the progression of the spreading degradation. Pictures were taken every minute until the layer became fully transformed into its yellow phase (32 minutes in total).

A systematic study was performed on $CsPbI_2Br$ thin films in order to find the cause of this degradation. The evaluation of the physical state of the samples was performed visually, by XRD analysis and optical characterisation with the results being shown in Fig. 6.12-14. A summary presenting the details of the environmental conditions used and the results obtained from each analysis is presented in Table 6.4 (further details of the environmental tests are given in section 4.3).

*i) Films with up to one week of degradation*

With the exception of '$UV/O_3$' treatment which lasted 54 minutes, exposures to the '$UV/N_2$, 'dark/air' and 'desiccator' environments lasted one week.

As shown in the photographs in Fig. 6.12, '$UV/O_3$' treatment on $CsPbI_2Br$ layers produced only a very weak discolouration of the material. However there was no significant change in the XRD and optical measurements, shown in Fig. 6.13a, b and c, indicating that there is no major modification of the $CsPbI_2Br$ perovskite.

Comparing the analyses on the $CsPbI_2Br$ layers after one week of exposure to the other test conditions ('$UV/N_2$, 'dark/air' and 'desiccator'), shown in Fig. 6.13 a, b and c, it can be noted that $CsPbI_2Br$ layers degrade only in 'dark/air' conditions: XRD patterns (Fig. 6.13a) from this test alone resemble the "yellow/degraded phase" pattern of the degraded control sample. Similarly the transmittance, reflectance and the calculated absorption coefficient (Fig. 6.13b and c respectively) shift to the values expected for the yellow phase solely for the sample exposed to 'dark/air' conditions, *i.e.* the band gap of brown films (1.92 eV) shifts to the $E_g$ of the yellow phase (2.85 eV).

Therefore the results suggest that light (UV-radiation) is not involved in the perovskite's colour change, but air is. Considering that the main reactive molecules in air are oxygen and water, particular focus was given to '$UV/O_3$', 'dark/air' and 'desiccator'

conditions which all include air. However, both 'UV/$O_3$' and 'desiccator' conditions contain abundant oxygen but low water concentrations and do not produce significant changes in the film appearance. Therefore it can be deduced that the only factor that induces degradation is water vapour.


**Fig. 6.12.** Photographs of $CsPbI_2Br$ layers exposed to UV/$O_3$ treatment, taken every minute for 15 min and then every ten minutes, up to a total of 54 minutes. Colour intensity decreases slowly but layers do not show visible degradation, even after almost one hour exposure. The samples measure 15 x 20 $mm^2$.

*ii) Films after one month of degradation*

Compared to the 'one week analysis', the one month degradation analyses (Fig. 6.13d-f and Fig. 6.14) show that prolonged exposure to 'UV/$N_2$' causes degradation in addition to the more rapid effect of 'dark/air' exposure. This shifts and expands XRD patterns and moves the optical absorption towards the yellow phase values. As nitrogen is an inert gas, the degradation factor responsible must be UV radiation. However, it must be considered that the intensity of the UV lamp chosen was particularly strong and positioned very close to the samples. The degradation was visible as yellow patches formed on the surface of 'UV/$N_2$' sample, whereas the samples stored in the desiccator retained its 'as grown' appearance, as shown in Fig. 6.14.

It is possible to conclude that the principal cause of the $CsPbI_2Br$ perovskite transformation is water, followed by a slower sensitivity to strong and continuous UV radiation. Following this statement, it is inferred that the degradation is different from

MAPI's (chapter 5), as the effect of '$UV/O_3$' is barely changing the aspect of $CsPbI_2Br$ layers, even after 54 minutes. Consequently it is inferred that the transformation mechanism of $CsPbI_2Br$ differs from that of MAPI (chapter 5) which has a much more rapid response to '$UV/O_3$' conditions.

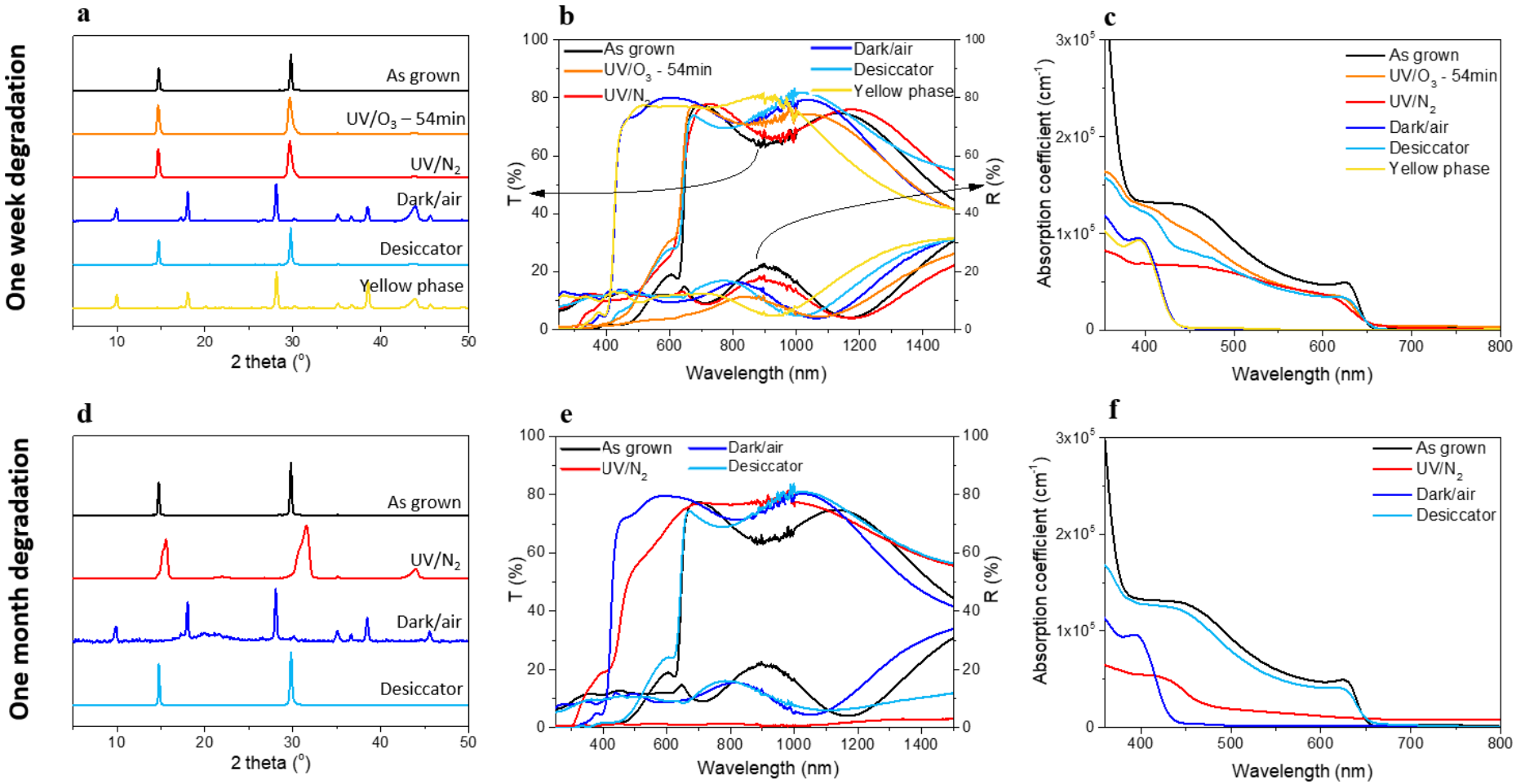


**Fig. 6.13.** XRD (a, d) and optical characterisation (b, c, e, f) for $CsPbI_2Br$ films exposed to degradation conditions after one week (a, b, c) and one month (d, e, f). Results are compared with 'as grown' (measured on the first day) and 'yellow phase' (degraded) films. a) XRD patterns, b) transmittance and reflectance, and c) absorption coefficient analysis of samples exposed to degrading environments for one week, showing the references "as grown" and "yellow phase" for comparison. '$UV/O_3$' condition is included, despite lasting for only 54 minutes. The only exposure showing significant damage on $CsPbI_2Br$ layers is 'dark/air'. d) XRD and e), f) optical characterisation of films after one month of exposure: in addition to 'dark/air', '$UV/N_2$' starts showing significant XRD peaks/band gap changes.

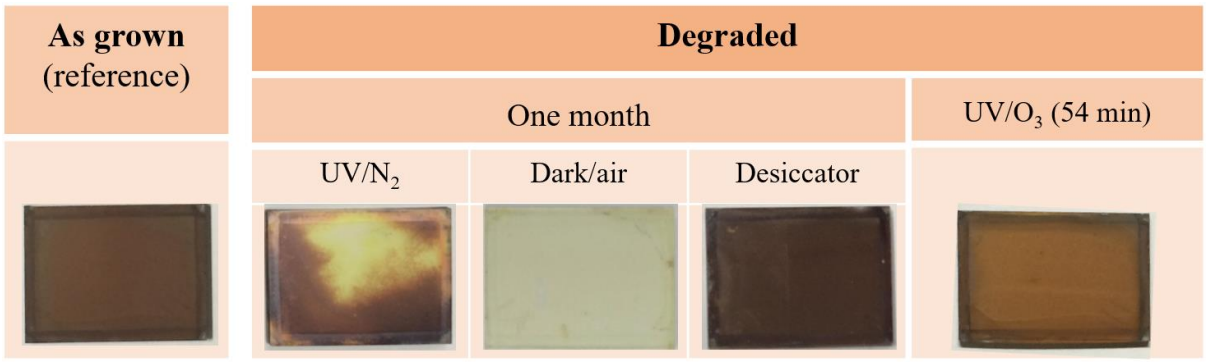


**Fig. 6.14.** Photographs of layers after one month exposure to degradation factors compared to a fresh film. Layers show visible damage in 'dark/air' conditions and partial colour loss in 'UV/$N_2$' containment. The samples measure 15 x 20 $mm^2$.

Table 6.4 summarises the main results of all measurements for each degradation condition, for both one week and one month exposure periods.

Overall it is very clear that strongest degradation occurred when the samples were exposed to air, which is the only condition with high levels of water. It may be therefore concluded that water produces the changes in the $CsPbI_2Br$ perovskite structure. Further studies of this follow in this section and are discussed in section 6.4.

| **Degradation conditions** | | | | | | **Characterisation** | | | |
|---|---|---|---|---|---|---|---|---|---|
| **Test** | **Illumination** | **Containment** | **Atmosphere** | **UV, $O_2$ and/or $H_2O$** | **Duration** | **Visual** | **XRD** | **Optical** | **Conclusion** |
| **"UV/$O_3$"** | UV lamp | UV-ozone cleaner | Dry air with ozone | UV, $O_2$ | 54 minutes | Slightly discoloured but brown | No change | No change | UV and $O_2$/$O_3$ do not affect film |
| **"UV/$N_2$"** | UV lamp | Glovebox | $N_2$ | UV | One week | No change (brown) | No change | No change | Long exposure to strong UV radiation produce small changes on the film structure |
| | | | | | One month | Yellow patches | Shifted peaks | Shifted $E_g$ | |
| **"Dark/air"** | None | Wrapped petridish in drawer | Air (RH > 15%) | $O_2$, $H_2O$ | One week | Yellow | New pattern | Shifted $E_g$ | Humidity changes structure immediately |
| | | | | | One month | Yellow | New pattern | Shifted $E_g$ | |
| **"Desiccator"** | Lab lighting | Desiccator (silica gel in transparent container) | Air (RH < 15%) | $O_2$ (low [$H_2O$]) | One week | No change (brown) | No change | No change | $O_2$ does not affect the structure |
| | | | | | One month | No change (brown) | No change | No change | |

**Table 6.4.** Summary of the result of degradation trials on $CsPbI_2Br$. The most important degradation factor was identified as atmospheric moisture (RH >15%).

*b) Threshold humidity for degradation*

In the previous section, it was shown that humidity affects the $CsPbI_2Br$ structure by inducing degradation. However, $CsPbI_2Br$ layers maintained in a desiccator with RH < 15% did not show any transformation process, even after one month (Fig. 13d, e and f). For this reason, it is postulated that the humidity threat to the perovskite structure occurs above a specific threshold. Since it was not possible to create environments with controlled water concentrations, it is only possible to state that relative humidity levels above 15% may be responsible for $CsPbI_2Br$ degradation, rather than to identify a particular threshold. Nevertheless, a qualitative relationship between air humidity levels and the rate of degradation has been observed: on rainy days the films degraded very quickly, while on sunny days the transformation happened over a longer period of time.

*c) 'Yellow' phase identification and recovery of the 'brown' $CsPbI_2Br$ phase*

Here the nature of the yellow phase that is formed after degradation is investigated.

First, the XRD pattern of the yellow films were compared with the patterns of the series of caesium and lead salts that could possibly be related to the $CsPbI_2Br$. However, as shown in Fig. 6.15, none of the salts revealed matching peaks with the yellow material, and therefore it may be concluded that the material does not decompose into these caesium or lead salts when transforming from the brown to the yellow phase.

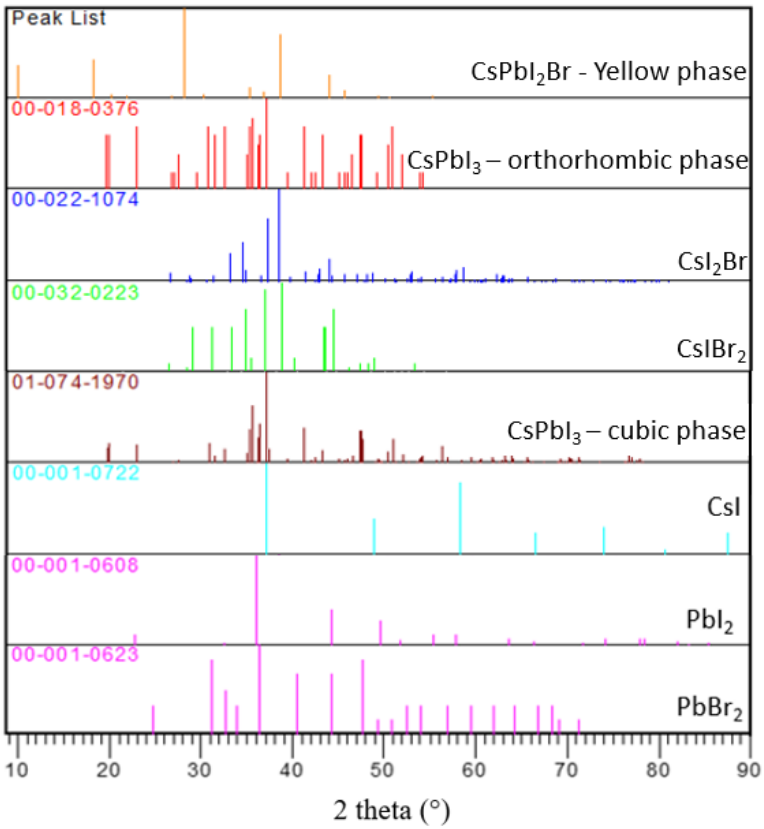


**Fig. 6.15.** XRD characterisation of yellow $CsPbI_2Br$ films: the experimental peak positions (top panel) are compared to reference data for those of Cs and Pb salts which may correspond to the major components of the yellow phase. Each compound peak reference was given by the X'Pert HighScore PANalytical reference systems. No match was found between the yellow phase and any of the salts, implying that the degradation is not a decomposition to the material's components.

Since the formation of the yellow phase occurs as a consequence of the presence of humidity, annealing trials on a hot plate were conducted to remove any possible physisorbed water. Indeed, the yellow films recovered their brown appearance upon annealing: Fig. 6.16 shows the XRD pattern and $CsPbI_2Br$ layer photographs before and after the recovery, revealing that both crystal structure and visual appearance of $CsPbI_2Br$ layers were recovered after re-annealing. The only difference that can be detected comparing the 'fresh' and the 're-annealed' XRD patterns, relates to the presence of a peak at 43.2° 2θ which most probably corresponds to $PbI_2$. The unreacted reagent may suggest that the annealing time

for the recovery process should be increased (> 10 min) in order to complete the conversion to the brown material.

The minimum temperature required to complete the recovery of the material was 250°C, and not 100°C as would have been expected for physisorbed water. Therefore, it was speculated that the water involved could be chemisorbed. This possibility is explored in the next section. Nevertheless, by increasing the temperature above 250°C up to 350°C, the uniformity and the colour of the films improved, similarly to the as grown samples shown in Fig. 6.3a.

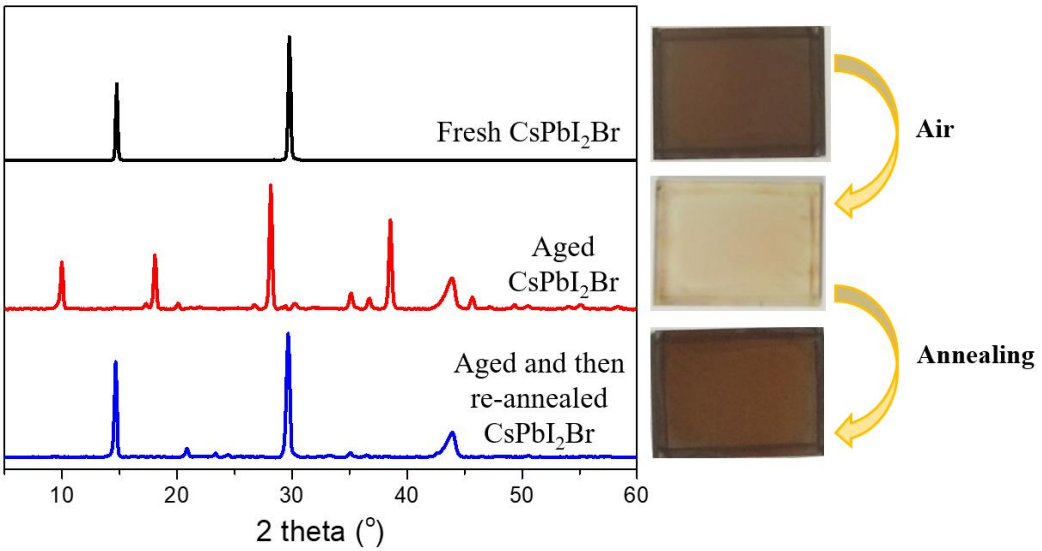


**Fig. 6.16.** XRD patterns and photographs of as grown, aged and re-annealed/recovered $CsPbI_2Br$ thin films deposited on quartz glass (20 x 15 $mm^2$ samples).

*d) The role of water in $CsPbI_2Br$ degradation*

Powder samples of $CsPbI_2Br$ were used in further investigations of the role of water in the degradation process. The visual appearance of fresh powders being degraded in air in only few minutes is shown in Fig. 6.17a. Powders show faster degradation in air compared to thin films, as the surface area is much greater. These degraded powders were compared

to fresh brown $CsPbI_2Br$ powder by using DSC-TGA and $^1H$ NMR analysis and the results are shown in Fig. 6.17b, c.

First, the DSC-TGA analysis (Fig. 6.17b) of the yellow and brown powders shows that the main feature for both samples is an exotherm at 463°C which corresponds to melting, confirming that the material composition of the two samples is identical and stable until high temperatures. However, the aged (yellow) powders present an additional small exotherm at ~255°C, highlighted in the inset, which is not showing weight loss. As there is no evaporation of major components, this trough may indicate a phase transition of the material: indeed, the exotherm temperature matches with the temperature needed to recover aged films on the hotplate, as presented in section 6.3.3.c.

However, further analysis was performed as the proportion of water (if present) might be very small and much lighter compared to the major components of $CsPbI_2Br$. $^1H$ NMR is able to recognise the presence of small quantities of water. However, the only peaks that were identified for both fresh and aged powders correspond to the deuterated solvent DMSO-$d_6$ peaks (quintuplet at 2.5 ppm) and its very small water impurity peak (3.3 ppm),[26] as shown in Fig. 6.17c. Therefore NMR analysis did not show evidence of water in the aged sample, confirming the results obtained from the DSC-TGA analysis.

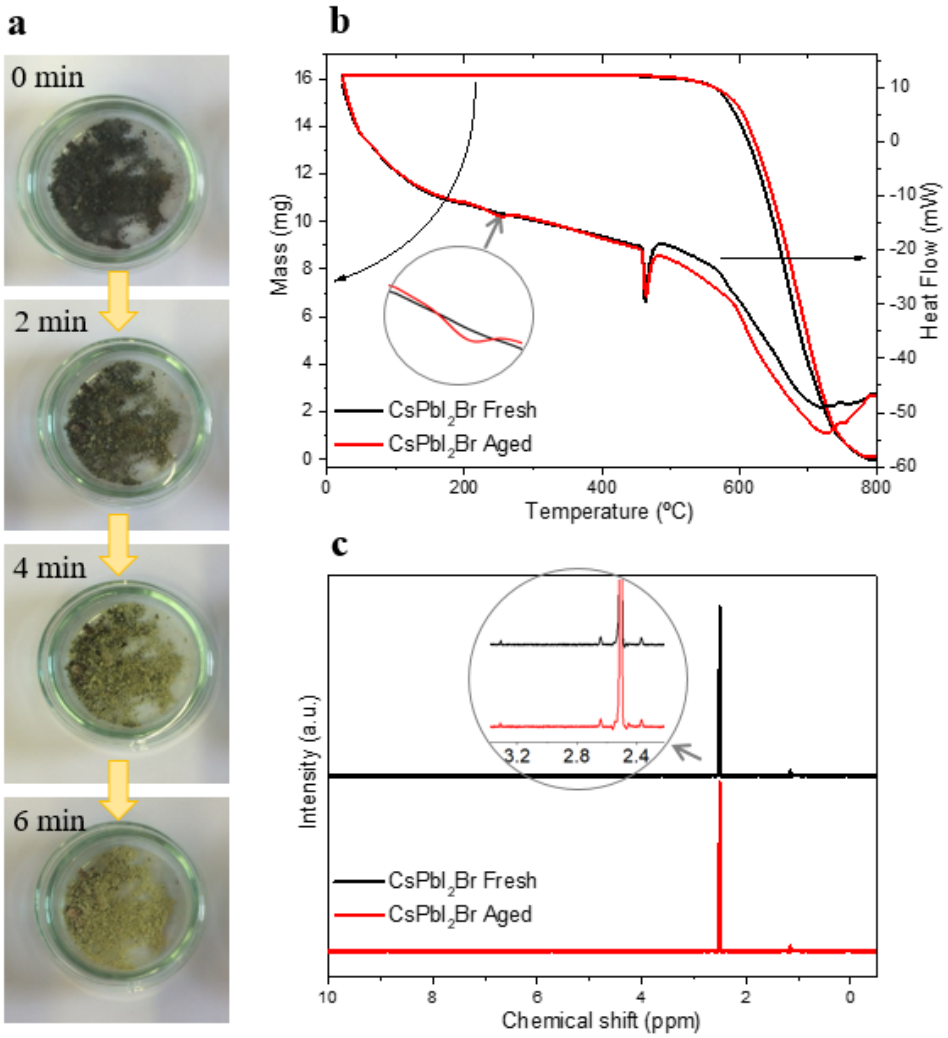


**Fig. 6.17.** $CsPbI_2Br$ powder characterisation. a) Visual appearance of fresh powders degrading quickly in air (RH >> 15%), turning to yellow degraded powders in a very short time. b) DSC – TGA of fresh and aged samples showing a melting peak at 463°C for both samples and a phase transition exotherm at 255°C for the yellow powders. c) $^1H$ NMR analysis on fresh and aged powders: the spectra are identical and do not show the presence of water. The quintuplets at 2.5 ppm correspond to DMSO-$d_6$ solvent and the very small peaks at 3.3 ppm indicate water impurities in the solvent.

Consequently, it was concluded that water is not a major component of the 'degraded' yellow $CsPbI_2Br$, but nevertheless it triggers the transformation from the brown to the yellow material. It is therefore most likely that the transformation is not degradation but a *phase transition*, which is a common feature in many perovskite materials. Further to this, Sharma *et al.* (1992) reported a phase diagram for the whole $CsPbI_{3-x}Br_x$ composition range, as shown in section 3.3.2.a, in which there is a phase change from orthorhombic to

cubic at a composition dependent temperature.[8] For $CsPbI_2Br$ the phase transition from orthorhombic to cubic structure is reported to be at 210°C. Nevertheless it may be inferred that the DSC-TGA exotherm at 255°C (Fig. 6.17b) corresponds to a phase transition from the brown α-cubic high temperature perovskite phase to the room temperature yellow δ-orthorhombic phase of $CsPbI_2Br$.

Overall it may be concluded that it is this phase transition that is responsible for the brown to yellow transformation. Moreover, the as-grown brown films are the metastable high temperature phase and their transformation to the more stable yellow phase is triggered by water vapour.

### 6.3.4. $CsPbI_2Br$ device degradation

Table 6.3 (see section 6.3.2.b), compares the *J-V* parameters of fresh glass/ITO/c-$TiO_2$/$CsPbI_2Br$/spiro-OMeTAD/Au solar cells with these of aged devices after 24 hours of exposure to air. Typical *J-V* curves of 'before' and 'after degradation' devices are shown in Fig. 6.18a, with the behaviours of *PCE* and $V_{OC}$ at different perovskite annealing temperatures in Figs. 6.18b and c respectively.

As shown by the comparison of *J-V* curves of fresh and degraded devices containing $CsPbI_2Br$ annealed at 350°C (Fig. 6.18a), considerable loss of the device efficiency occurred after one day of air exposure, with almost 100% loss of *PCE* being caused by a current drop from 11.74 mA/cm$^2$ to 0.24 mA/cm$^2$ (Table 6.3). This can be directly related to the colour change of the absorber from brown (1.92 eV) to yellow (2.25 eV), and hence from perovskite cubic to the orthorhombic phase. Similar changes occur for devices containing $CsPbI_2Br$ annealed at all temperatures (Table 6.3): overall the *PCE* of the devices after degradation (Fig. 6.18b) is determined by the collapse in $J_{SC}$. However, the open circuit voltages remain remarkably high despite the sample "degradation" (Fig. 6.18c) and retain > 75% of their

original values. The reason for this behaviour might be related to the presence of favourable band line ups for both cubic and orthorhombic phases with the device's hole and electron transporting materials.

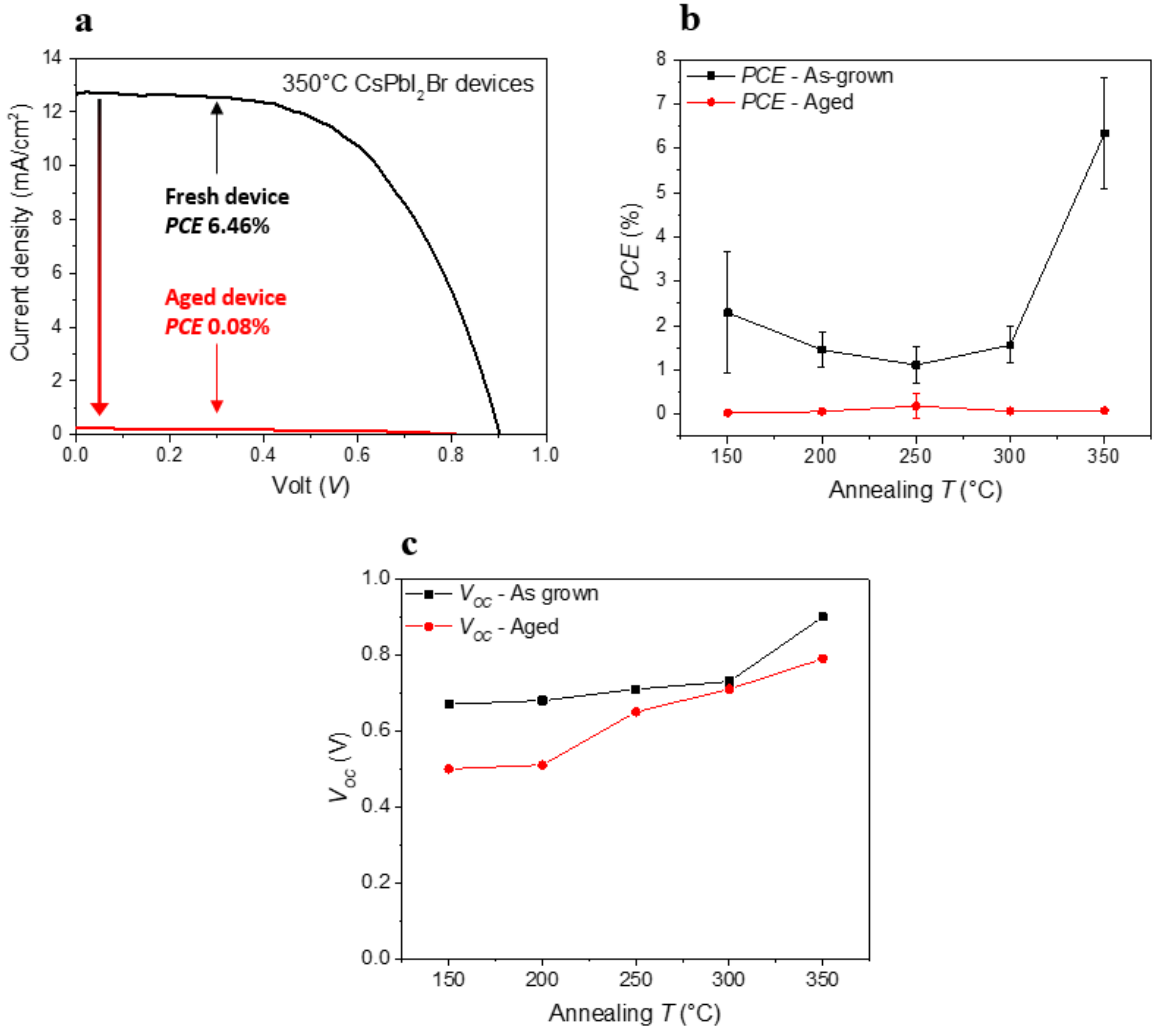


**Fig. 6.18.** As grown and aged device performances: a) illuminated *J-V* curve of a device containing the perovskite annealed at 350°C, presenting the 6.46% *PCE* curve dropping at 0.08% after 24 h in air, showing the collapse in $J_{SC}$ and the retention of $V_{OC}$. b) Fresh and aged efficiencies of devices containing $CsPbI_2Br$ annealed at different annealing temperatures. All *PCE*s collapse to almost 0% after ageing. c) $V_{OC}$ values of fresh and aged devices, with $CsPbI_2Br$ annealed at $T$ = 150 - 350°C, showing an unexpected retention of the open circuit voltage after ageing.

### 6.3.5. Device recovery

A study of the device recovery was performed by preparing fresh and degraded devices on the same day and using the same precursors, in order to produce reliable results

which could be compared (section 6.2.4). For this study, only the devices with the perovskite annealed at 350°C were considered, as this is the temperature that showed best PV performance.

The *J-V* curves of both fresh and recovered devices were measured and compared. Table 6.5 and Fig. 6.19 show examples of *J-V* data of fresh and recovered devices, showing a device *PCE* recovery of 100%, from 5.42% *PCE* of the as grown device, to 5.42% of the recovered device. In addition, Fig. 6.19b shows the stabilised efficiencies of the two devices: the fresh device shows a 4.1% *PCE* while the recovered device 4.3% *PCE* at the end of the measurement (70 seconds). Both show a fast efficiency decay in the first 5 seconds followed by a slower decline, which however does not reach a steady state. Nevertheless, the recovered stabilised efficiency showed slightly better performance than that achieved by the fresh device, in the best case up to 115% of the original performance.

| | **Fresh devices** | **Recovered devices** |
|---|---|---|
| $V_{OC}$ **(V)** | 1.00 | 1.00 |
| $J_{SC}$ **(mA/cm$^2$)** | 9.80 | 9.50 |
| ***FF*** **(%)** | 55.6 | 56.1 |
| ***PCE*** **(%)** | 5.42 | 5.42 |

**Table 6.5.** Example of a 100% recovered $CsPbI_2Br$ device *J-V* performance, showing data collected before the degradation and after the recovery. The related *J-V* curves and stabilised efficiencies are shown in Fig. 6.19.

Generally, the tendency of the recovered materials was to show lower $J_{SC,}$ but higher $V_{OC}$ and *FF*: an example of these behaviours can be seen in the *J-V* curve in Fig. 6.19a. This may be associated with an improvement of the film's quality after the re-annealing process.

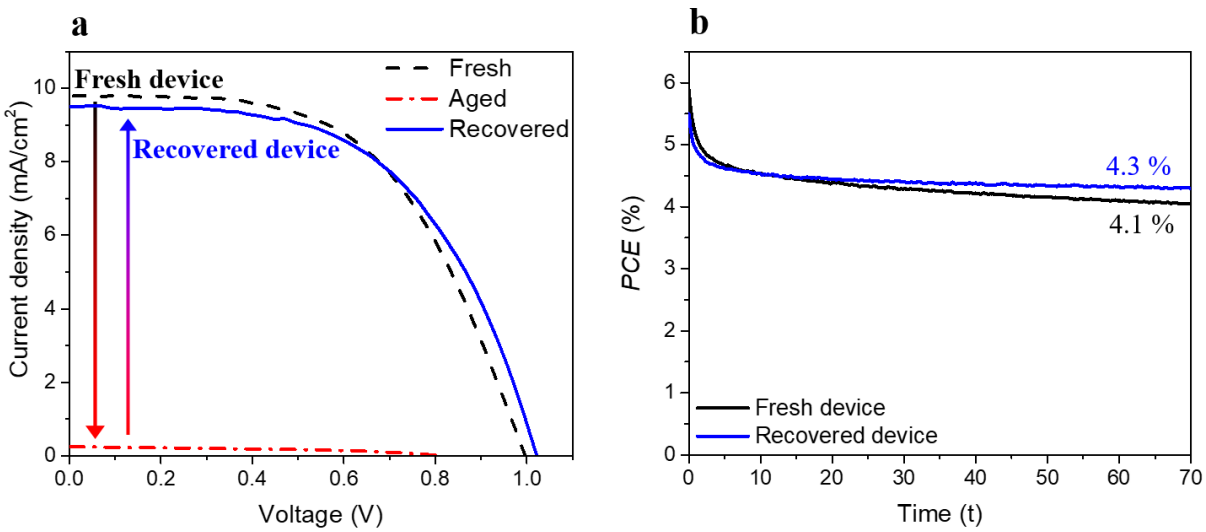


**Fig. 6.19.** *J-V* measurement under AM1.5 illumination of $CsPbI_2Br$ recovered devices. a) Performances of devices starting from fresh, aged and then recovered, showing a 100% recovery. b) Stabilised *PCE* of the fresh and recovered devices, showing an initial drop (5 sec) of *PCE* followed by a *PCE* at 4.3% for the recovered and a 4.1% *PCE* for the fresh device after 70 seconds.

Finally it should be noted that the devices used in the degradation study had lower performances than the best achieved in this work. This may be attributed to the humid local weather conditions at the time. Nevertheless, the high number of samples used (16 as grown and 16 recovered devices) gives confidence that the effects observed are genuine.

## 6.4. Discussion

In this chapter $CsPbI_2Br$ perovskites were studied: films were deposited and their uniformity and structure evaluated over a preparation temperature range 150°C < *T* < 350°C, $\Delta T$ = 50°C, to find the best annealing temperature. Preparation at 350°C generated uniform brown films having a band gap of 1.92 eV which were highly crystalline (cubic) and had grains up to 2 μm and few pin-holes. However, films annealed at 150 and 200°C showed non-uniform colour and were resistive.

The stability of $CsPbI_2Br$ was also investigated. In the literature, this inorganic perovskite has attracted interest due to its thermal stability. However, although the thermal

stability to decomposition was demonstrated by thermo-gravimetrical analysis up to the melting point at 463°C, $CsPbI_2Br$ films prepared in the glovebox rapidly showed discolouration when exposed to air. Since MAPI degraded into its original components turning into a yellow film after exposure to $UV/O_2$ or $H_2O$, the initial hypothesis was that $CsPbI_2Br$ presented the same issue. On the other hand, the compositional similarity of $CsPbI_2Br$ to $CsPbI_3$, which is unstable in its high temperature cubic phase and stable in its orthorhombic phase at room temperature, suggested an alternative mechanistic possibility. Therefore a strategic study was used to investigate the cause of $CsPbI_2Br$ transformation and this identified water vapour as being important. However, no physisorbed or chemisorbed water was found within the 'degraded' compound and similarly no precursor or derivative salts were identified in the material by XRD analysis, suggesting that the yellow phase only corresponded to a different structure of the $CsPbI_2Br$ perovskite rather than to a hydrated phase or a mixture of its component salts.

Concordantly, DSC-TGA analysis performed on yellow $CsPbI_2Br$ powders detected an exotherm at 255°C with no weight loss, which may correspond to the phase transformation which was reported in 1992 by Sharma *et al*.[8] They showed that most perovskite compounds generally change their crystal structure with decreasing temperature, normally following the order cubic, tetragonal, orthorhombic and monoclinic. However, each type of perovskite may show different phase transition temperatures. In the case of the pseudobinary $CsPbI_3$ – $CsPbBr_3$ ($T$ – x) phase diagram shown in Fig. 6.20, the same authors showed a phase boundary separating the low temperature orthorhombic/tetragonal from the high temperature cubic phase. However, while the pure $CsPbBr_3$ presented a tetragonal phase field between the orthorhombic and the cubic phases (88°C > $T$ > 130°C),[27] in $CsPbI_3$ this tetragonal phase was not detected and therefore the transition occurring at 310°C corresponds to a direct orthorhombic – cubic transition.[8] In the case of $CsPbI_2Br$, as it has a

more similar composition to $CsPbI_3$, an orthorhombic – cubic transition may also be likely, but it cannot be excluded that a tetragonal phase is formed in a small range of temperatures. For $CsPbI_2Br$ the transition temperature is reported at 210°C, this being slightly lower than the one identified in the DSC-TGA analysis (255°C), as shown in Fig. 6.20. It may be therefore speculated that the discrepancy between these phase transition temperatures is attributed to the presence of an intermediate $CsPbI_2Br$ tetragonal phase.

Systematic studies of the environmental factors that could cause degradation or other kinds of transformation identified that the most influential factor is water vapour at RH ≥ 15%. The conclusion that best accounts for the experimental observations is therefore as follows: $CsPbI_2Br$ has two phases – the room temperature stable phase being the yellow orthorhombic δ-phase and the high temperature (255°C < $T$ < 463°C) brown cubic α-phase. As grown samples of $CsPbI_2Br$ prepared by annealing at 350°C adopt the brown cubic phase, and this is metastable at room temperature. Exposure to water triggers the transformation of the brown phase to the yellow phase. Heating to $T$ > 255°C regains the brown phase which may again be metastable at room temperature.

It was noticed that the water interaction with the cubic perovskite initiated in small areas, possibly pin-holes with high surface area, which gradually became larger, spreading through the whole film. It is therefore speculated that water interacts with the perovskite surface dangling bonds and/or metal ions. In particular, in the literature it has been shown that CsBr has a high solubility in water[28] which may contribute to destabilising the room temperature metastable cubic crystal structure of $CsPbI_2Br$.

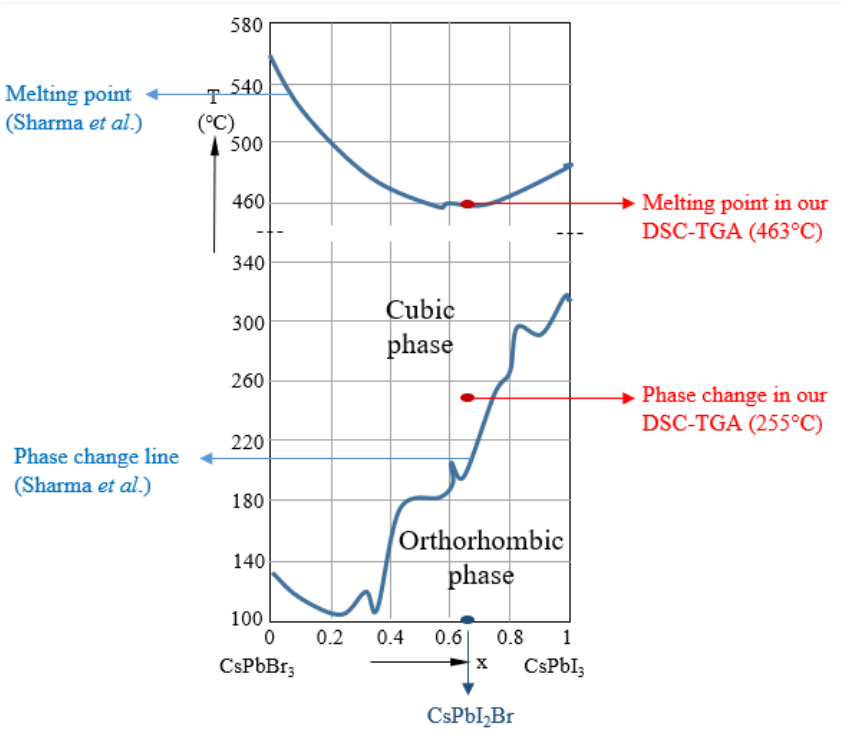


**Fig. 6.20.** $CsPbBr_3$ – $CsPbI_3$ pseudobinary phase diagram re-drawn from Sharma *et al.*[8] Data points for the melting and phase transition temperatures from this work are shown.

$CsPbI_2Br$ devices were fabricated with the superstrate architecture glass/ITO/c-$TiO_2$/$CsPbI_2Br$/spiro-OMeTAD/Au. First, devices were optimised by thinning the $TiO_2$ layer which increased the perovskite's photon absorption between 370 – 420 nm. Furthermore, containment in a dry nitrogen filled box prevented degradation of the devices during the analyses and maintained the perovskite in its brown cubic α-phase. The goal of the device preparation was to find the optimised temperature to anneal $CsPbI_2Br$ thin films: devices were therefore fabricated using the perovskite films annealed at different temperatures and the *J-V* and *EQE* analysis on these devices were measured.

The best device performances were recorded when the $CsPbI_2Br$ films were annealed at 350°C. From the film characterisation it was shown that there had been complete conversion into the brown cubic phase, and that the higher processing temperatures encourage the formation of more uniform films having larger grains and fewer pin holes, as confirmed by visual appearance and SEM analysis. Devices containing these films are

therefore characterised by higher efficiency, mainly improved by the increased *FF*. All films annealed at $T > 250°C$ showed improvement in uniformity and increased crystallinity.

Of all the annealing temperatures used, 250°C was found to be the temperature that gave the minimum device performance. 250°C is also the temperature responsible for the orthorhombic-cubic transition, as was shown by the DSC-TGA analysis, and this is likely to be the cause of the low device performances. Films grown at 250°C were less crystalline and were possibly of mixed phase.

From the phase diagram in Fig. 6.20, at $T < 250°C$ the $CsPbI_2Br$ should be stable in its lower energy yellow orthorhombic δ-phase. Therefore, perovskite layers annealed at $T <$ 250°C should appear yellow and show the orthorhombic structure in the XRD patterns. However, as shown in Fig. 6.3, the layers look brown, non-uniform and present orange patches and in addition, the electron micrographs show resistive films and 'flower-shaped' areas for the 200°C layer. Therefore it may be speculated that there are multiple phases in these films, caused by a miscibility gap of the $CsPbI_{3-x}Br_x$ compound at $T < 250°C$. The effect of possible mixed phases, was also found in devices, as solar cells fabricated using the 150°C annealed $CsPbI_2Br$ showed extraordinary efficiencies (7.23% max *PCE*), not in agreement with the trend of the performances of the other devices, and large standard deviation of the *J-V* parameters (Fig. 6.8). This indicates that the high performance is not consistent and reveals that a spatial variation of mixed phases may be present in the films. Some of these possible phases are reported in Table 6.6. This shows the characteristics of the most important phases of the $CsPbI_{3-x}Br_x$ compounds, such as $CsPbBr_3$, $CsPbI_3$, $CsPbI_2Br$ and $CsPbIBr_2$, and for each compound the temperature range, visual appearance and device performances from the literature are shown, where applicable. Furthermore, the Table considers the possible phases that might be present at an annealing temperature of 150°C. These are the cubic orange $CsPbBr_3$ (visually detected, see Fig. 6.3), the

orthorhombic yellow $CsPbI_3$, the orthorhombic yellow $CsPbI_2Br$ and the black cubic $CsPbIBr_2$. However, while the yellow orthorhombic phases cannot contribute large currents to the device performances, the cubic phases of $CsPbBr_3$ and $CsPbIBr_2$ may be responsible for the high device performances when the perovskite was annealed at 150°C: these compounds alone have produced devices with 5.95% and 8% *PCE* respectively (Table 6.6).[29,30] The similarity of *PCE* between these films and the device with perovskite annealed at 150°C may support the hypothesis that phase separation is responsible. However, absorption coefficient calculations and XRD analysis performed on 150 and 200°C films (Fig. 6.4), show a cubic perovskite phase only. The reason for this may be related to the fact that the non-cubic phases are formed on the corners of the sample, as consequence of the non-uniform hot-plate heating system and the spin-coating technique that forms thinner layers on the corners. Therefore the brown $CsPbI_2Br$ may prefer to crystallise in the centre of the samples and this is the area that is normally investigated by the UV-Vis and X-ray methods, with a small spot size in comparison to the total film area.

| **Compound** | ***T*** | **Crystal structure** | **Phase colour** | **Max *PCE* recorded** | **Ref.** | **Present at 150°C?** |
|---|---|---|---|---|---|---|
| **$CsPbBr_3$** | RT<br>> 88°C<br>> 130°C | Orthorhombic<br>Tetragonal<br>Cubic | Black<br>N/A<br>Orange | -<br>-<br>5.95% | 30 | No<br>No<br>Yes |
| **$CsPbI_3$** | RT<br>>310°C | Orthorhombic<br>Cubic | Yellow<br>Black | -<br>1.7% | 31 | Yes<br>No |
| **$CsPbI_2Br$** | RT<br>> 255°C | Orthorh./Tetrag.*<br>Cubic | Yellow<br>Brown | -<br>9.8 % | 5 | Yes<br>No |
| **$CsPbIBr_2$** | RT<br>> 100°C | Orthorh./Tetrag.*<br>Cubic | N/A<br>Black | -<br>8.0 % | 29 | No<br>Yes |

**Tab 6.6.** Summary of temperature dependent crystal structures of the main $CsPbI_{3-x}Br_x$ compounds, presenting the colour of their phases and the maximum device performances achieved.[5,8–10,27,29–31] *The tetragonal phase was not identified but its existence cannot be excluded.

Overall, the best efficiency recorded with the $CsPbI_2Br$ annealed at 350°C was 9.08% (1.05 V $V_{OC}$, 12.68 mA/cm$^2$ $J_{SC}$ and 60.2% *FF*). Table 6.7 shows a comparison between devices fabricated at the University of Liverpool, University of Oxford and Stanford University, the three highest *PCE*s reported when this work was ongoing. The table includes the highest, average and stabilised efficiencies achieved in each University. The highest *PCE* device was fabricated by Snaith's group,[5] reaching 9.8% compared to 9.1% for this work. Both cases consider the reverse *J-V* scan, as both are strongly affected by hysteresis (2 – 2.5% absolute difference between forward and reverse scans). On the contrary, McGehee's group[10] using an inverted device structure (ITO/PEDOT:PSS/$CsPbI_2Br$/PCBM/BCP/Al) have fabricated almost hysteresis-free $CsPbI_2Br$ devices. Hence, the highest efficiency presented by the Stanford group shows almost comparable results for reverse and forward scans (6.8% and 6.7% respectively), but it is slightly less efficient than the others. These results suggest that the main cause of hysteresis for the fully inorganic perovskite solar cells may be related to the choice of hole and electron transporting materials. In terms of average efficiencies, the devices fabricated in our laboratory show the best results (6.3% *PCE* against 6.0% *PCE* in Oxford). However the highest stabilised efficiency was reached at Stanford University, with a 6.5% *PCE* $CsPbI_2Br$ solar cell device.

| | **Liverpool Univ. (this work)** | **Oxford Univ. (Prof. H. J. Snaith)**[5] | **Stanford Univ. (Prof. M. D. McGehee)**[10] |
|---|---|---|---|
| **Peak *PCE* (%)** | Forward scan 6.6<br>Reverse scan 9.1 | Forward scan 7.8<br>Reverse scan 9.8 | Forward scan 6.7<br>Reverse scan 6.8 |
| **Average *PCE* (%)** | 6.3 | 6.0 | n/a |
| **Stabilised *PCE* (%)** | 6.2 | 5.6 | 6.5 |

**Tab 6.7.** Comparison between champion, average and stabilised efficiencies obtained in our laboratory, University of Oxford and Stanford University (before January 2018).

The work presented on the material stability was further expanded to devices. As for $CsPbI_2Br$ thin films, when devices were exposed to air they underwent degradation as a consequence of the perovskite phase transition. Devices containing the yellow δ-phase $CsPbI_2Br$ lost their performance, as a result of the widening of the band gap (2.85 eV). However, despite the current loss causing *PCE*s < 0.1%, the $V_{OC}$ remained remarkably high, maintaining 75% of the original value (or 86% for devices where the $CsPbI_2Br$ was annealed at 350°C).

A consequence of the transformation from brown to yellow $CsPbI_2Br$ being a phase change and not a material degradation, is that the phase transition can be reversed. After turning yellow, the material could be reconverted into its cubic phase upon annealing above 255°C (ideally at 350°C to recover the high crystallinity), showing a quick transformation to its original brown colour. This $CsPbI_2Br$ perovskite recovery to its cubic phase was also applied to devices. Re-heated perovskite layers regained their photoactive semiconducting properties and therefore restored the device performances, up to as high as 115% of the original average *PCE*. It may be speculated that the reason why devices work better after the recovering process, derives from a reorganisation of defects followed by larger grain size of the crystalline perovskite structure, that yield to an improvement of the devices' fill factor.

## 6.5. Conclusions

Chapter 6 has presented a complete study on the inorganic $CsPbI_2Br$ perovskite material, focussing on the film preparation, device fabrication and optimisation and finally on the material stability and recovery.

$CsPbI_2Br$ films were deposited *via* spin-coating a precursor solution inside a glovebox and then annealed at temperatures between 150°C and 350°C. All annealing

temperatures produced brown films (1.92 eV), however the best film crystallisation was observed in films annealed at the highest temperature (350°C). Nevertheless, all films were used to prepare devices. *J-V* and *EQE* analysis performed on devices confirmed that the best annealing temperature for the films preparation is 350°C, and the champion efficiency obtained was 9.08% using a glass/ITO/c-$TiO_2$(50nm)/$CsPbI_2Br$/spiro-OMeTAD/Au device architecture. The *PCE* recorded is comparable to the world's best *PCE* (9.84%, R. J. Sutton *et al.*),[5] however both results are referred to reverse *J-V* scans, as forward scans produce lower efficiencies (best forward scan 6.6% *PCE*). Hence hysteresis affects devices, but it can be reduced by using different hole and electron transporting materials (R. E. Beal *et al.*).[10]

While the highest performance devices were formed from $CsPbI_2Br$ at 350°C, unexpectedly high performance was found for films fabricated at as low as 150°C. This is speculated to be due to a low temperature miscibility gap between $CsPbI_3$ and $CsPbBr_3$ that could give high performance, although this is not considered to be a valuable route to PV devices in itself since this compound is not sufficiently stable.

The $CsPbI_2Br$ perovskite was confirmed to be thermally stable, melting at 463°C. Furthermore, $CsPbI_2Br$ is more stable than $CsPbI_3$ and has the advantage of having a lower band gap than $CsPbBr_3$. However, this study has shown that despite $CsPbI_2Br$ having a higher stability relative to the pure iodine compound, its brown α-phase is metastable at room temperature. The triggering destabilisation factor was investigated by isolating $CsPbI_2Br$ thin films in specific environments ('UV/$O_3$', 'UV/$N_2$', 'dark/air' and 'desiccator' with RH < 15%) chosen to elucidate the factor responsible for the transformation. The cause of the destabilisation of the brown α-phase was found to be water vapour. However, DSC-TGA and NMR have shown that water only provokes the phase transformation, but it does not form a hydrated perovskite compound. Furthermore, it was proved by XRD and DSC-

TGA analysis that the transformation between brown and yellow material is a phase change rather than a decomposition of the materials into different compounds going from a brown cubic phase (1.92 eV) to yellow non-perovskite phase (2.85 eV). This is similar to the case for $CsPbI_3$. Therefore, yellow films were easily converted to the cubic photoactive form upon reannealing at 350°C. The recovery of the films was extended to devices and it was seen that devices containing degraded yellow phase perovskite and showing *PCE* < 0.1%, recovered up to 115% of their original performance after re-annealing the perovskite film.

In conclusion, $CsPbI_2Br$ perovskite in the brown cubic phase has the potential to be utilised in commercial solar cell devices, in particular in tandem devices as a consequence of the large band gap, but an effective encapsulation would be required to avoid contact with humid air to maintain the brown photoactive perovskite phase.

Future work should involve a deeper study on the effect of prolonged exposure to humidity on encapsulated cells to control the effectiveness of this protection. Furthermore, a passivation study aimed to protect the perovskite's surface could be useful to avoid or delay the humidity effect on the metastable cubic phase. The passivation could also be focussed on reducing the number of pin-holes in the layers which would create larger crystal grains and reduced the grain boundaries surface area, reducing recombination processes and improving the $CsPbI_2Br$ device performances.

## 6.6. References


(1) Conings, B.; Drijkoningen, J.; Gauquelin, N.; Babayigit, A.; D'Haen, J.; D'Olieslaeger, L.; Ethirajan, A.; Verbeeck, J.; Manca, J.; Mosconi, E.; Angelis, F. De; Boyen, H.-G. Intrinsic Thermal Instability of Methylammonium Lead Trihalide Perovskite. *Adv. Energy Mater.* **2015**, *5* (15), 1500477–1500485.

(2) Eperon, G. E.; Stranks, S. D.; Menelaou, C.; Johnston, M. B.; Herz, L. M.; Snaith, H. J. Formamidinium Lead Trihalide: A Broadly Tunable Perovskite for Efficient Planar Heterojunction Solar Cells. *Energy Environ. Sci.* **2014**, *7* (3), 982–988.

(3) Lee, J. W.; Kim, D. H.; Kim, H. S.; Seo, S. W.; Cho, S. M.; Park, N. G. Formamidinium and Cesium Hybridization for Photo- and Moisture-Stable Perovskite Solar Cell. *Adv. Energy Mater.* **2015**, *5* (20), 1501310–1501319.

(4) McMeekin, D. P.; Sadoughi, G.; Rehman, W.; Eperon, G. E.; Saliba, M.; Hörantner, M. T.; Haghighirad, A.; Sakai, N.; Korte, L.; Rech, B.; Johnston, M. B.; Herz, L. M.; Snaith, H. J. A Mixed-Cation Lead Mixed-Halide Perovskite Absorber for Tandem Solar Cells. *Science* **2016**, *351* (6269), 151–155.

(5) Sutton, R. J.; Eperon, G. E.; Miranda, L.; Parrott, E. S.; Kamino, B. A.; Patel, J. B.; Hörantner, M. T.; Johnston, M. B.; Haghighirad, A. A.; Moore, D. T.; Snaith, H. J. Bandgap-Tunable Cesium Lead Halide Perovskites with High Thermal Stability for Efficient Solar Cells. *Adv. Energy Mater.* **2016**, *6*, 150258–150464.

(6) Møller, C. K. The Structure of Perovskite-like Cæsium Plumbo Trihalides. *Mat. Fys. Medd. Dan. Vid. Selsk* **1959**, *32* (2).

(7) Møller, C. K. Crystal Structure and Photoconductivity of Cæsium Plumbohalides. *Nature* **1958**, *182* (4647), 1436–1436.

(8) Sharma, S.; Weiden, N.; Weiss, A. Phase Diagrams of Quasibinary Systems of the Type: $ABX_3$ - $A'BX_3$; $ABX_3$ - $AB'X_3$, and $ABX_3$ — $ABX_3$; X = Halogen Crystal Structure / Phase Diagrams / Phase Transitions / X-Ray Diffraction. **1992**, *175*, 63–80.

(9) Stoumpos, C. C.; Malliakas, C. D.; Peters, J. A.; Liu, Z.; Sebastian, M.; Im, J.; Chasapis, T. C.; Wibowo, A. C.; Chung, D. Y.; Freeman, A. J.; Wessels, B. W.; Kanatzidis, M. G. Crystal Growth of the Perovskite Semiconductor $CsPbBr_3$: A New Material for High-Energy Radiation Detection. *Cryst. Growth Des.* **2013**, *13* (7), 2722–2727.

(10) Beal, R. E.; Slotcavage, D. J.; Leijtens, T.; Bowring, A. R.; Belisle, R. A.; Nguyen, W. H.; Burkhard, G.; Hoke, E. T.; McGehee, M. D. Cesium Lead Halide Perovskites with Improved Stability for Tandem Solar Cells. *J. Phys. Chem. Lett.* **2016**, *7*, 746–751.

(11) Song, J.; Li, J.; Li, X.; Xu, L.; Dong, Y.; Zeng, H. Quantum Dot Light-Emitting Diodes Based on Inorganic Perovskite Cesium Lead Halides ($CsPbX_3$). *Adv. Mater.* **2015**, *27* (44), 7162–7167.

(12) Goldschmidt, V. M. Die Gesetze Der Krystallochemie. *Naturwissenschaften* **1926**, *14* (21), 477–485.

(13) Li, Z.; Yang, M.; Park, J.-S.; Wei, S.-H.; Berry, J. J.; Zhu, K. Stabilizing Perovskite Structures by Tuning Tolerance Factor: Formation of Formamidinium and Cesium Lead Iodide Solid-State Alloys. *Chem. Mater.* **2016**, *28* (1), 284–292.

(14) Hendon, C. H.; Yang, R. X.; Burton, L. A.; Walsh, A. Assessment of Polyanion ($BF_4^-$ and $PF_6^-$) Substitutions in Hybrid Halide Perovskites. *J. Mater. Chem. A* **2015**, *3* (17),

9067–9070.

(15) Shannon, R. D. Revised Effective Ionic Radii and Systematic Studies of Interatomie Distances in Halides and Chaleogenides. *Acta Cryst* **1976**, *32*, 751–768.

(16) Aristidou, N.; Sanchez-Molina, I.; Chotchuangchutchaval, T.; Brown, M.; Martinez, L.; Rath, T.; Haque, S. A. The Role of Oxygen in the Degradation of Methylammonium Lead Trihalide Perovskite Photoactive Layers. *Angew. Chemie - Int. Ed.* **2015**, *54* (28), 8208–8212.

(17) Aristidou, N.; Eames, C.; Sanchez-Molina, I.; Bu, X.; Kosco, J.; Islam, M. S.; Haque, S. A. Fast Oxygen Diffusion and Iodide Defects Mediate Oxygen-Induced Degradation of Perovskite Solar Cells. *Nat. Commun.* **2017**, *8*, 15218–15227.

(18) Bryant, D.; Aristidou, N.; Pont, S.; Sanchez-Molina, I.; Chotchunangatchaval, T.; Wheeler, S.; Durrant, J. R.; Haque, S. A. Light and Oxygen Induced Degradation Limits the Operational Stability of Methylammonium Lead Triiodide Perovskite Solar Cells. *Energy Environ. Sci.* **2016**, *9* (5), 1655–1660.

(19) Asghar, M. I.; Zhang, J.; Wang, H.; Lund, P. D. Device Stability of Perovskite Solar Cells – A Review. *Renew. Sustain. Energy Rev.* **2017**, *77*, 131–146.

(20) Leguy, A. M. A.; Hu, Y.; Campoy-Quiles, M.; Alonso, M. I.; Weber, O. J.; Azarhoosh, P.; van Schilfgaarde, M.; Weller, M. T.; Bein, T.; Nelson, J.; Docampo, P.; Barnes, P. R. F. Reversible Hydration of $CH_3NH_3PbI_3$ in Films, Single Crystals, and Solar Cells. *Chem. Mater.* **2015**, *27* (9), 3397–3407.

(21) Christians, J. A.; Miranda Herrera, P. A.; Kamat, P. V. Transformation of the Excited State and Photovoltaic Efficiency of $CH_3NH_3PbI_3$ Perovskite upon Controlled Exposure to Humidified Air. *J. Am. Chem. Soc.* **2015**, *137* (4), 1530–1538.

(22) Mosconi, E.; Azpiroz, J. M.; De Angelis, F. Ab Initio Molecular Dynamics Simulations of Methylammonium Lead Iodide Perovskite Degradation by Water. *Chem. Mater.* **2015**, *27* (13), 4885–4892.

(23) Correa-Baena, J.-P.; Abate, A.; Saliba, M.; Tress, W.; Jesper Jacobsson, T.; Grätzel, M.; Hagfeldt, A. The Rapid Evolution of Highly Efficient Perovskite Solar Cells. *Energy Environ. Sci.* **2017**, *10* (3), 710–727.

(24) Farhan, M. S.; Zalnezhad, E.; Bushroa, A. R.; Sarhan, A. A. D. Electrical and Optical Properties of Indium-Tin Oxide (ITO) Films by Ion-Assisted Deposition (IAD) at Room Temperature. *Int. J. Precis. Eng. Manuf.* **2013**, *14* (8), 1465–1469.

(25) Pascual, J.; Camassel, J.; Mathieu, H. Resolved Quadrupolar Transition in $TiO_2$. *Phys. Rev. Lett.* **1977**, *39* (23), 1490–1493.

(26) Gottlieb, H. E.; Kotlyar, V.; Nudelman, A. NMR Chemical Shifts of Common Laboratory Solvents as Trace Impurities. *J. Org. Chem.* **1997**, *62* (21), 7512–7515.

(27) Hirotsu, S.; Harada, J.; Iizumi, M.; Gesi, K. Structural Phase Transitions in $CsPbBr_3$. *J. Phys. Soc. Japan* **1974**, *37* (5), 1393–1398.

(28) Wu, L.; Hu, H.; Xu, Y.; Jiang, S.; Chen, M.; Zhong, Q.; Yang, D.; Liu, Q.; Zhao, Y.; Sun, B.; Zhang, Q.; Yin, Y. From Nonluminescent $Cs_4PbX_6$ (X = Cl, Br, I) Nanocrystals to Highly Luminescent $CsPbX_3$ Nanocrystals: Water-Triggered Transformation through a CsX-Stripping Mechanism. *Nano Lett.* **2017**, *17* (9), 5799–5804.

(29) Li, W.; Rothmann, M. U.; Liu, A.; Wang, Z.; Zhang, Y.; Pascoe, A. R.; Lu, J.; Jiang, L.; Chen, Y.; Huang, F.; Peng, Y.; Bao, Q.; Etheridge, J.; Bach, U.; Cheng, Y. B. Phase Segregation Enhanced Ion Movement in Efficient Inorganic $CsPbIBr_2$ Solar Cells. *Adv. Energy Mater.* **2017**, *7* (20), 1700946–1700954.

(30) Kulbak, M.; Cahen, D.; Hodes, G. How Important Is the Organic Part of Lead Halide Perovskite Photovoltaic Cells? Efficient $CsPbBr_3$ Cells. *J. Phys. Chem. Lett.* **2015**, *6* (13), 2452–2456.

(31) Eperon, G. E.; Paternò, G. M.; Sutton, R. J.; Zampetti, A.; Haghighirad, A. A.; Cacialli, F.; Snaith, H. J. Inorganic Caesium Lead Iodide Perovskite Solar Cells. *J. Mater. Chem. A* **2015**, *3* (39), 19688–19695.

# 7. Perovskite/silicon heterojunctions

## 7.1. Introduction

Silicon is the most common material for the fabrication of solar cells,[1,2] and has the advantages of enabling solar devices with high stability and performance. However, compared with fossil fuel generation, PV-generated power from silicon solar cells remains expensive and hence it is not completely viable worldwide for large scale power generation.[3–5] Therefore, numerous research groups are focussing on simplifying silicon solar module manufacturing. For example, an important issue is the energy cost of high temperature silicon processing which may potentially be avoided by using solution processed treatments.[6] Organic materials were therefore proposed in combination with silicon as they may be deposited rapidly and with low-cost processes.[6–9] In particular, in the literature it was shown that it is possible to form silicon heterojunctions with P3HT (poly (3-hexylthiophene)) and PEDOT:PSS (poly(3,4-ethylenedioxythiophene):poly(styrenesulfonate))[6–9] and furthermore, C. Sturm *et al.* showed that by using a silicon/PEDOT heterojunction it is possible to reach a *PCE* of 11.7%, which represents one of the best device performances of this type achieved up to now.[9]

Silicon/polymer heterojunctions are not the only 'new' application using silicon solar cells in the recent years. Perovskite materials were used in the fabrication of tandem solar cells, in order to further increase the silicon solar cell performances by using a facile and low-cost process.[10] Therefore, perovskite materials with large band gaps have been combined with silicon solar cells to form silicon/perovskite tandem solar cells. This device architecture combines two solar cells, a *p-n* silicon junction and a *p-i-n* perovskite junction, using either 2- or 4-terminal connections.[11–15] The perovskite solar cell ($E_g$ = 1.9 eV) is positioned on top of the silicon solar cell to maximise the photon utilisation by minimising hot electron losses. In this way a broad light spectrum can be absorbed by the tandem solar cell and the device performance may be improved compared to that achievable with a single junction.[10,12,14] With this device architecture, K. Catchpole *et al.* have fabricated the latest record efficiency for a perovskite ($RbCsMAFAPbI_{3-x}Br_x$)/silicon tandem solar cell which has shown a *PCE* of 26.4%.[16]

By combining the two ideas of a) combining silicon with a solution processed semiconductor to form a heterojunction and b) using silicon with perovskite solar cells, a new device configuration was proposed and a study of it is presented in this chapter. Silicon and perovskite were combined together forming a single device rather than a combination of two solar cells (tandem solar cell), with the goal of understanding if it is possible to form a heterojunction between silicon and MAPI, thus forming a new type of solar cell device.

## 7.2. Experimental methods

### 7.2.1. Device fabrication

Silicon wafers were cleaned and prepared for perovskite deposition as explained in section 4.1.2. The choice of perovskite material to use for these heterojunctions was determined by the feasibility of their deposition techniques and their stability.

Preliminary studies were conducted using both MAPI and $CsPbI_2Br$ perovskites, but the silicon/$CsPbI_2Br$ heterojunction was quickly dismissed as it was too unstable in air. Therefore the results presented in this chapter refer only to heterojunctions made with MAPI. Both MAPI prepared with the one- and two-step processes were used for the fabrication of devices, however the two-step method showed technical difficulties in the deposition process, forming patchy MAPI layers and leaving large areas of the silicon uncovered. Therefore this deposition technique was abandoned and only MAPI prepared with the one-step deposition technique was used.

A total of 101 devices were fabricated. The best procedure to make devices is described here, for both *n*-Si and *p*-Si/MAPI heterojunctions. Once the wafers were introduced in a nitrogen filled glovebox, device fabrication immediately took place to avoid any contamination of the wafers' surface. In order to facilitate the spin-coating procedure of the thin and fragile wafers, the wafers were glued onto quartz coated glass (20 x 15 $mm^2$, Ossila Ltd.). A film of MAPI was then deposited onto the silicon wafer by using the one-step process. Deposition was difficult compared to the deposition of MAPI on glass or $TiO_2$, as the surface of the wafers was smoother and user skills needed to be developed in the spin-coating process in order to avoid patchy layers and to obtain uniform films. Moreover, the anti-solvent treatment was not used as it was found to give poor reproducibility. The one-step method selected to deposit MAPI on silicon (section 5.2.2.a) was dynamic spin-coating for depositing a precursor solution of $PbI_2/CH_3H_3I$/DMSO solution (1 : 1 : 1 molar ratio) in

0.6 ml DMF (50 µl, 4000 rpm, 25 seconds) followed by annealing (1 minute at 65°C and then 2 minutes at 100°C). See section 5.2.2.a for more information. However, the thickness of MAPI on silicon (~550 nm) showed increased values compared to the thickness produced on glass (~300 nm).

*a) n-Si/MAPI heterojunctions*

Numerous studies of MAPI deposited on crystalline *n*-type silicon wafers (*n*-Si, (100) ± 0.5°, phosphorous doped, 355 – 405 µm thickness, Pi-KEM Ltd) were conducted in order to optimise the device architecture. Preliminary studies were performed on *n*-Si with resistivity of 1 – 10 Ω·cm, and supplementary studies were conducted onto *n*-Si wafer with resistivities of 1 – 5 Ω·cm, 5 – 10 Ω·cm and 10 – 15 Ω·cm ((100), Mi-Net Technology Ltd). Table 7.1 shows the average carrier concentration of these *n*-silicon wafers according to their resistivity.

| **Resistivity (Ω·cm)** | **Carrier concentration ($cm^{-3}$)** |
|---|---|
| 1 - 5 | $8.95 \cdot 10^{14} – 4.83 \cdot 10^{15}$ |
| 5 - 10 | $4.41 \cdot 10^{14} – 8.95 \cdot 10^{14}$ |
| 10 - 15 | $2.92 \cdot 10^{14} – 4.41 \cdot 10^{14}$ |

**Table 7.1.** Carrier concentration of *n*-Si wafer according to resistivity. These values were derived from conversion tables which refer to the type of dopant (phosphorous) and type of silicon (c-Si), considering room temperature conditions.[17]

Initial studies began with depositing only MAPI onto silicon using a substrate configuration, the ultimate device architecture that produced the best working devices was Al/*n*-Si/MAPI/spiro-OMeTAD/Au, as shown in Fig. 7.1a. The evolution of the device architecture to form the silicon/MAPI heterojunctions is described next and an explanation of the reasons of these evolutionary steps is presented in section 7.3.2.

After perovskite annealing, samples were cooled down to room temperature and prepared for the deposition of i) thick gold contacts, or ii) thin (optically transparent) gold layer and then thick gold contacts or iii) spiro-OMeTAD and then gold, as follows:

i) *n*-Si/MAPI samples were coated with 50 nm thick evaporated gold contacts on top of the perovskite using masks with 1 mm lines, over the whole length of the sample, leaving 2 mm between each line.

ii) The perovskite layer was fully covered with an ultra thin layer of gold (5, 10, 15, 20 nm thick, see optimisation study in section 7.3.1.c) and later a second gold evaporation was conducted to deposit 50 nm thick gold lines (1 mm width, every 2 mm). The effect of depositing ultra thin gold layers over the surface of MAPI (where the light enters) was evaluated by characterising the thin layers of gold alone deposited on quartz coated glass: the sheet resistance was measured using a four point probe, whereas the transmittance was analysed by UV-Vis spectrophotometry.

iii) 70 µl of a doped solution of spiro-OMeTAD (2,2',7,7'-Tetrakis-(N,N-di-4-methoxyphenylamino)-9,9'-spirobifluorene) in chlorobenzene (see section 5.2.4b) was dynamically spin-coated at 3000 rpm for 30 seconds on top of MAPI. After 12 hours in a desiccator (RH < 15%) the devices were contacted with gold. An ultra thin layer (5 - 20 nm thick, with 10 nm being the best thickness) of Au was then uniformly deposited over the spiro-OMeTAD layer, followed by a second but thicker gold layer (50 nm thickness) using a shadow mask to form thin lines (1 mm width, every 2 mm).

For all devices, small rectangles (3 x 4 $mm^2$ or 3 x 5 $mm^2$, with contact areas of 0.12 or 0.15 $cm^2$ respectively depending on the sample) were formed by scribing the soft layers (MAPI, spiro-OMeTAD, Au) off. Since these devices have a substrate configuration, the contact area was shadowed by the gold layers, and in particular by the 1 x 4 $mm^2$ thicker gold layer (front contact). Therefore the *PCE* measured from the devices may be

underestimated. As the samples were not very uniform, between 4 and 6 contacts (normally positioned in the centre of the sample) were considered for the measurements for each device.

Finally, a small part on top edge of the sample was scratched off to remove the layers on the silicon and a ~100 nm thick aluminium contact was deposited (see Table 7.2).

The architecture and appearance of the devices prepared with recipe c) are shown in Fig. 7.1a and b. Devices were finally characterised by *J-V*, *EQE* and *C-V* analysis (see section 4.4.1) in air.

*b) p-Si/MAPI heterojunctions*

*p*-type crystalline silicon wafers (*p*-Si (100), boron doped, 380 μm thickness, 1-10 Ω·cm, Pi-KEM Ltd) were used to prepare *p*-Si/MAPI heterojunction devices. Preliminary studies were performed on MAPI deposited onto the wafers with a one-step process with gold contacts evaporated on both the *p*-Si and the MAPI for the back and front Ohmic contact respectively (see Table 7.2).

Au/*p*-Si/MAPI/ZnO/AZO/Au devices were also fabricated. Above the MAPI layer a 100 nm zinc oxide film was deposited by RF sputtering (5 mTorr, 150 Watts, 30 minutes, room temperature, rotation on). As deposition was performed on top of the MAPI (which degrades at $T > 100$°C), deposition was restricted to room temperature. However, the usage of low temperature deposition produces a low *n*-type doping of ZnO. Transparent conductive aluminium doped zinc oxide (AZO) was therefore deposited on top to improve the conductivity. In the same chamber, RF sputtering was used to deposit AZO (2 mTorr, 200 Watts, 3 hours, room temperature, rotation on), producing a film ~300 nm thick. Both ZnO and AZO were deposited forming rectangles of 0.12 $cm^2$ area, by using a mask. 50 nm of gold was then evaporated in thin lines (1 x 4 $mm^2$) on every 0.12 $cm^2$ area to form the front

contacts. Finally on a clean *p*-Si edge, 100 nm of gold was evaporated to form the back contact. A diagram describing the solar cell architecture is shown in Fig. 7.1c.

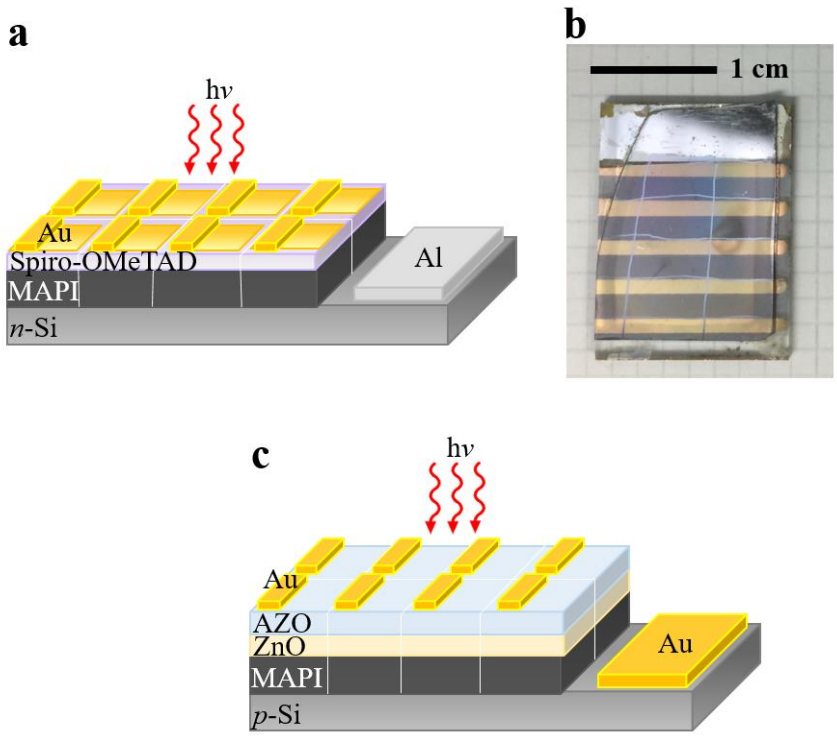


**Fig. 7.1**. a) Diagram and b) photograph of a substrate Al/*n*-Si/MAPI/spiro-OMeTAD/Au solar cell device. c) Diagram of an Au/*p*-Si/MAPI/ZnO/AZO/Au heterojunction device.

### 7.2.2. Samples fabrication for the 'study of the interfaces'

A summary of all the interfaces studied in this chapter is presented in Table 7.2, showing the sections in which they were studied and the behaviour that they showed in the *J-V* analysis (section 7.3.2.b). This study was performed to decouple the layers in the device from the behaviour of the Si/MAPI junction. *J-V* tests were therefore performed on possible interfaces that may form in the devices, either directly or due to the presence of pin holes in the MAPI layer. For example, interfaces such as MAPI/spiro-OMeTAD and MAPI/Au were studied, since MAPI/spiro-OMeTAD is commonly used in the literature (and is reported to have a favourable band alignment[18,19]) but no measurements were found showing how these materials behave electrically together, whereas MAPI/Au was analysed for completeness of

this study. Tests on spiro-OMeTAD/Au were not conducted as their Ohmic behaviour was already shown in the literature.[20,21]

In order to prepare these samples, the same deposition procedures explained in the previous sections were utilised. Each pair of materials taken into consideration for the study were deposited by spin-coating or evaporation and then contacted using Ohmic behaving metals (see Table 7.2). For example, in the case of *n*-Si/Au, gold was evaporated onto the silicon, and the *n*-type silicon was contacted using Al Ohmic contacts. In the case of *n*-Si/spiro-OMeTAD, the hole transporting material was spin-coated onto the silicon and then the substrates were contacted with gold (for spiro-OMeTAD) and aluminium (for *n*-Si).

After the samples were prepared, their electrical behaviour was characterised by *J-V* and *EQE* analysis. However, *EQE* measurements on samples that showed rectifying junctions with no or very little current production were not always possible.

| Section | Junction | Result |
|---|---|---|
| 7.3.1.a, i | *n*-Si/Al | Ohmic |
| | *n*-Si/Au | Rectifying |
| | *p*-Si/Al | Rectifying |
| | *p*-Si/Au | Ohmic |
| 7.3.1.a, ii | MAPI/Au | Ohmic |
| | MAPI/Al | Rectifying |
| 7.3.2.a | *n*-Si/MAPI | Rectifying |
| 7.3.2.b | *n*-Si/spiro-OMeTAD | Rectifying |
| | MAPI/spiro-OMeTAD | Rectifying |
| Literature[20,21] | Spiro-OMeTAD/Au | Ohmic |
| 7.3.3 | *p*-Si/MAPI | Rectifying |

**Table 7.2.** Summary of the junction behaviours obtained by dark *J-V* analysis, showing the sections in which they are reported.

## 7.3. Results

### 7.3.1. Silicon/MAPI heterostructures

The first part of the results section shows how the device architecture of the silicon/MAPI heterojunction devices was developed. Firstly metals to form Ohmic contacts with both silicon and MAPI were investigated. Then the behaviour of the MAPI/silicon interface was observed and finally the device architecture was optimised to improve the device efficiency, for both *n*-type and *p*-type silicon. All these evolutionary steps are presented in the following sections.

*a) Ohmic contacts for silicon/MAPI heterostructures*

*i) Contacts for silicon*

*n*- and *p*-type silicon wafers covered with thin metal lines of Au and Al were measured. The *I-V* responses are shown in Fig. 7.2 together with a diagram showing the sample architecture used for the study. The *I-V* curves show that Ohmic contacts were formed between *n*-Si and Al, and between *p*-Si and Au, whereas rectifying junctions were formed between Au and *n*-Si, and Al and *p*-Si. Therefore for device fabrication, Al was used as a contact for the *n*-type silicon wafers and Au was used with the *p*-type silicon wafers.

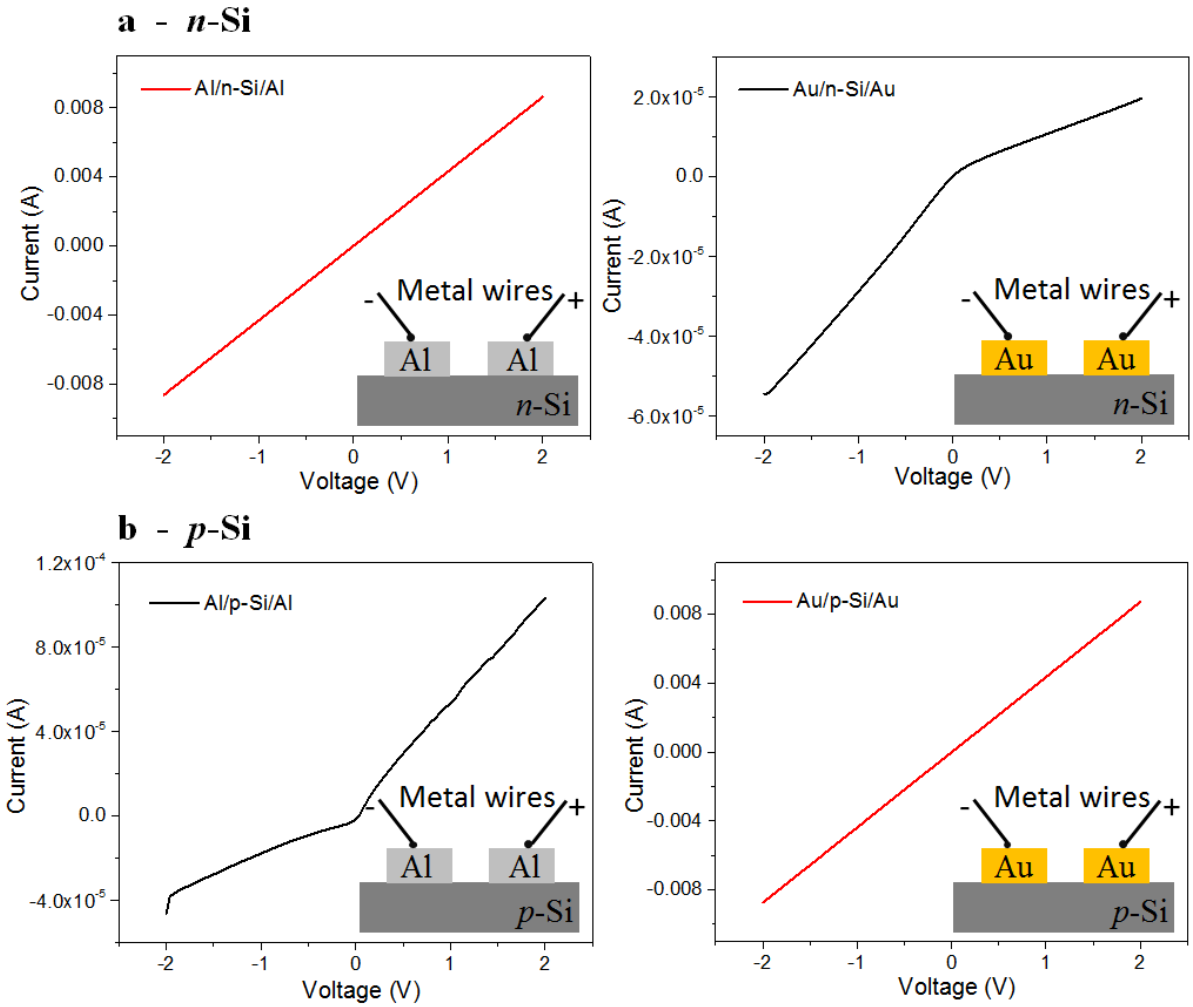


**Fig. 7.2**. Dark *I-V* analysis on Si/metal samples to study their junctions, showing a diagram of the sample architecture for each measurement. a) *n*-Si junctions with Al and Au, forming an Ohmic contact with Al. b) *p*-Si with Al and Au, showing Ohmic behaviour only with Au.

*ii) Contacts for MAPI*

Numerous architectures were fabricated to find the geometry that could investigate the electrical behaviour of Al and Au on MAPI, overcoming the issues caused by a) the soft nature of MAPI (contacting probes scratched the films easily and penetrated the film reaching the substrate) and b) the high resistivity of MAPI (which required metal contacts to be very close for current flow). The final geometries are shown in Fig. 7.3. The related *I-V* curves in Fig. 7.3, show that Au produced an Ohmic junction with MAPI, whereas

Al/MAPI rectified. Therefore, Au was used as contact for MAPI in the heterojunction device fabrication.

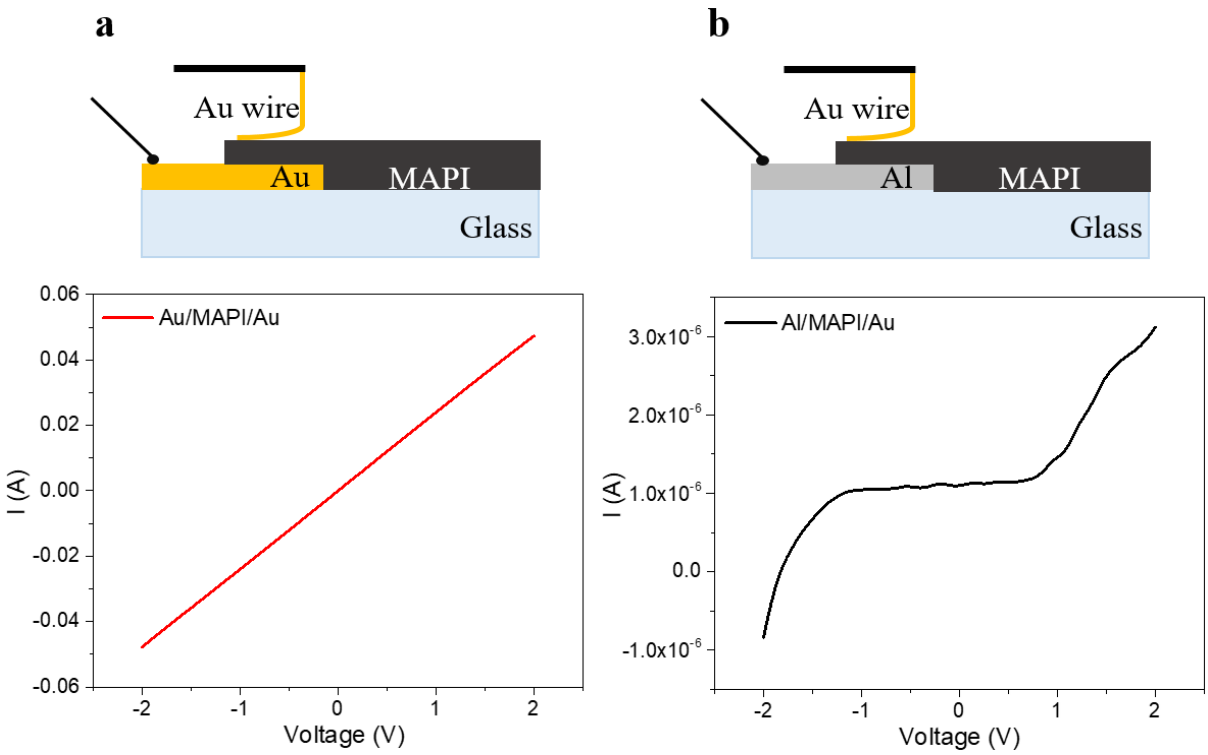


**Fig. 7.3**. Dark *I-V* analysis on MAPI with Au and Al contacts. a) MAPI/Au shows Ohmic behaviour and b) MAPI/Al produces a rectifying junction (forward bias) and shows break down in reverse bias.

*b) Characterisation of MAPI on silicon*

Another important study for the fabrication of the Si/MAPI heterojunctions was to confirm that MAPI could be formed properly by spin-coating onto Si wafers rather than the more usual glass or $TiO_2$ layers. MAPI layers on silicon were therefore investigated by XRD analysis, as shown in Fig. 7.4a and b. The first graph (7.4a), mainly shows the silicon (100) peak at 69.2° 2θ,[22] while the second magnified X-ray pattern in 7.4b shows the MAPI peaks. All the expected tetragonal MAPI perovskite peaks can be identified (see Fig. 5.4 for comparison) and no $PbI_2$ precursor residues were found. These results confirm that the perovskite was grown identically on glass, $TiO_2$ and Si wafer surfaces.

In addition, Fig. 7.4c shows an SEM image of MAPI perovskite deposited on a silicon wafer. Similarly to MAPI layers produced with the one-step solution process on glass (section 5.3.2a), the films contain numerous pin holes.

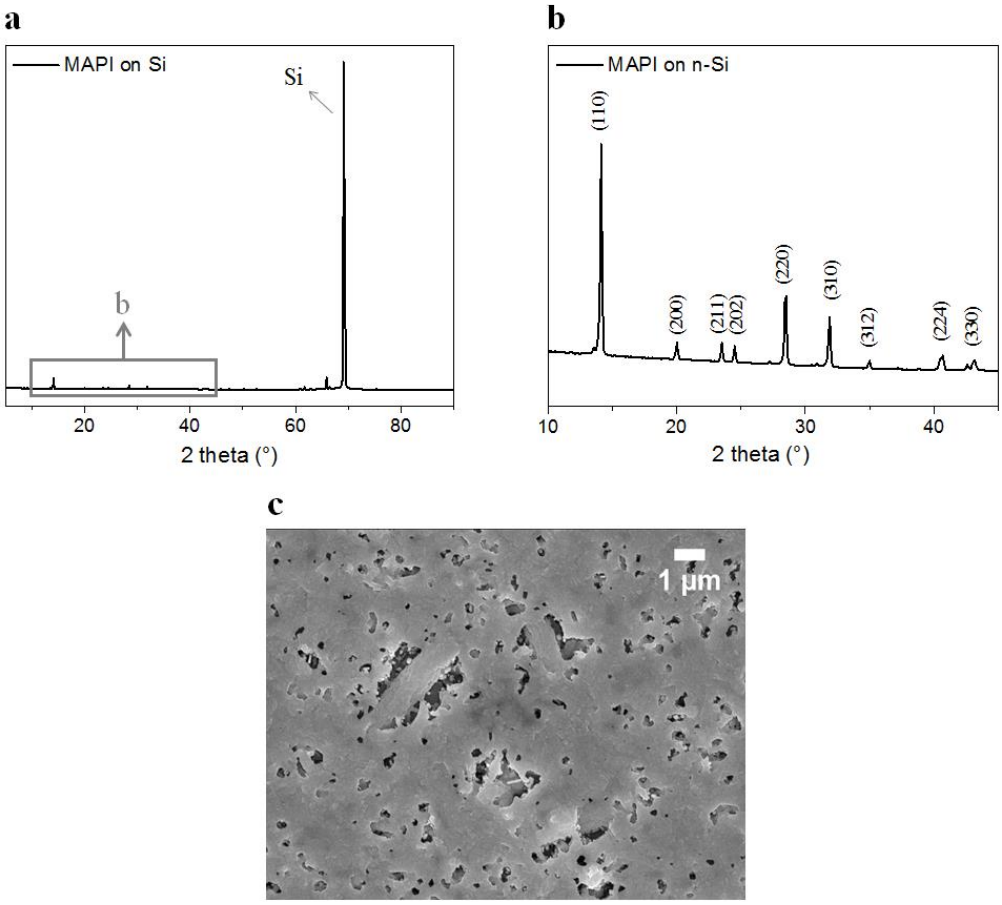


**Fig. 7.4**. Characterisation of MAPI deposited on Si: a) XRD pattern showing the main peak for silicon (100) at 69.2° 2θ and b) magnification of the XRD pattern in Fig.7.4a, showing the 10° - 50° 2θ region where MAPI peaks are assigned with their Miller indices. c) SEM image showing MAPI deposited on silicon. There are numerous pin holes.

*c) First attempts for Si/MAPI heterojunction devices*

Si/MAPI heterojunction devices were fabricated with the following device structures: Al/*n*-Si/MAPI/Au and Au/*p*-Si/MAPI/Au. However, in order to fabricate these devices, some optimisations were needed, as shown by the evolution of the device structure in Fig. 7.5a and b. Initially, the contacting of MAPI's surface was performed by using thick Au contacts as shown in Fig. 7.5a. However, as MAPI showed high resistivity, it was not

possible to measure *J-V* curves of these devices due to a lack of current flow. Therefore, in order to overcome the surface resistivity issue, a very thin Au layer (5 - 20 nm thickness) was deposited onto the whole perovskite surface prior the 50 nm thick Au contacts which are necessary for contacting, as shown in Fig. 7.5b.

First, the effect of depositing the ultra-thin Au layers (5 – 20 nm thick) onto the Si/MAPI was studied by analysing the transmittance and the resistivity of Au films deposited on quartz coated glass: the highest amount of light is required to reach to the absorber layers but thinner Au layers produce higher resistivity, which is counterproductive for solar cell devices. Fig. 7.5c shows the UV-Vis measurement and the sheet resistance values in the inset of the graph. The highest transmittance is reached with the 5 nm Au layer, this being ~70%, but its resistivity was unmeasurably high using the four point probe. 10 and 15 nm thick Au layers show similar transmittance (~60%) in the visible range, but show different resistivity. In particular, in the case of the 10 nm the sheet resistance is of the order of $10^6$ Ω/□, whereas for the 15 nm Au film this is 22.7 Ω/□, which is more similar to that of TCO materials.[23] While the sheet resistance further decreases for the 20 nm thick Au layer (5 Ω/□) its transmittance also decreases, reaching values of 30 – 50%. Therefore, the best balance between transparency and sheet resistance (on glass) was achieved by the 15 nm thick Au layers.

A further analysis of the gold deposited on MAPI is shown in Fig. 7.5d. The SEM image shows an Au film deposited onto MAPI (in this case 10 nm), which reveals that Au forms agglomerations of > 100 nm Ø, rather than a continuous layer. This agglomeration effect may be due to the perovskite's rough surface. Nevertheless, by using Au on the device surface, the samples became measurable by *J-V* analysis.

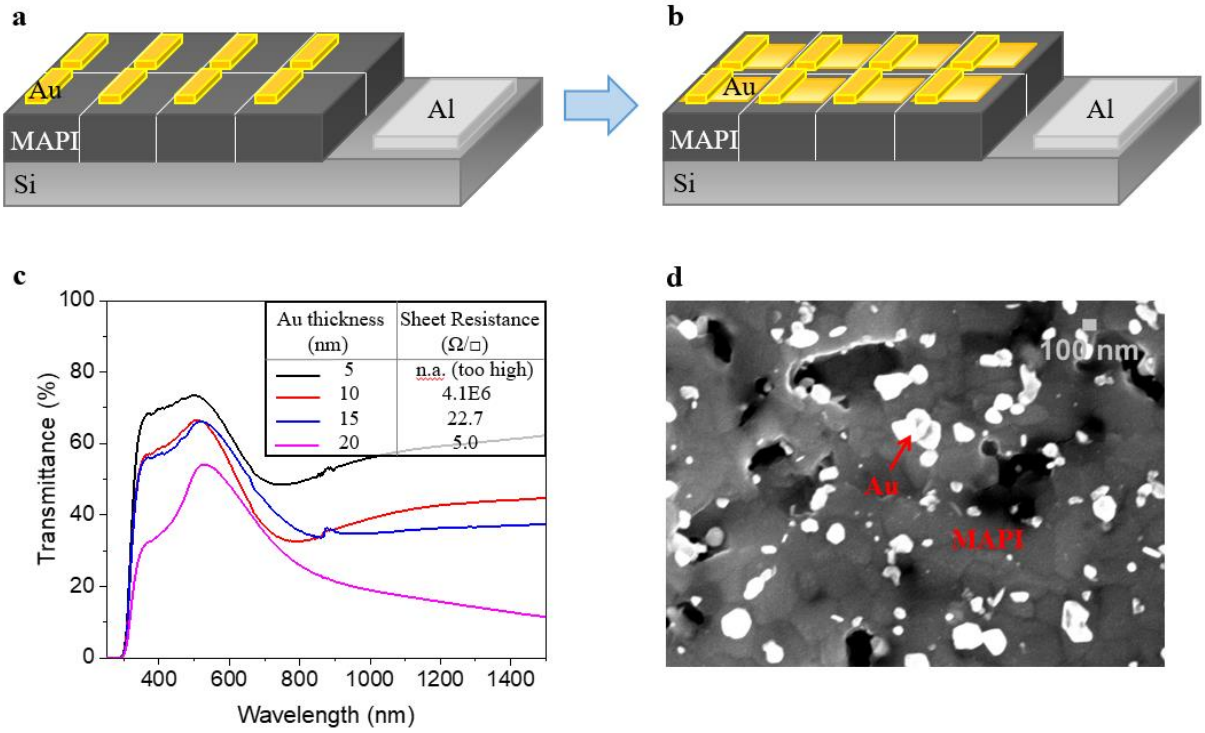


**Fig. 7.5**. Si/MAPI device architecture evolution from a) 50 nm Au contacts to b) 10 nm Au deposited over the whole surface and then 50 nm contacts in smaller areas (1 x 4 $mm^2$). c) Transmittance and resistivity of Au layers (5, 10, 15 and 20 nm thickness) deposited on glass. d) SEM image showing the coverage of 10 nm thick Au on MAPI, mainly represented by gold agglomerations of particles with up to 200 nm diameter.

Results obtained by *J-V* measurements (dark/light) performed onto the device with structure shown in Fig. 7.5b, are shown in Fig. 7.6a and b for *n*-Si/MAPI and *p*-Si/MAPI devices respectively. The curves show rectification between *n*-silicon and MAPI. In addition, the Al/*n*-Si/MAPI/Au device showed the production of a small current under AM1.5, revealing a photoactive junction and producing an average *PCE* of 0.13% ($V_{OC}$ = 0.30 V, $J_{SC}$ = 1.12 mA/$cm^2$, *FF* = 37.7%), measured on 16 contacts.

On the contrary, in the case of MAPI on *p*-Si, nearly Ohmic behaviour was recorded by *J-V* analysis. This phenomenon produced suspicion, as the same behaviour was registered on *p*-Si/Au samples (Fig. 7.2b). Since MAPI showed numerous pin holes (Fig. 7.4c), it may be speculated that shunting occurs: the Au layer deposited on top of MAPI infiltrates the perovskite pin holes to reach the Si wafer, as shown by the cross section diagram in Fig.

7.6c. If this speculation is true, shunting would influence the *n*-Si/MAPI device too, revealing that the *PCE* registered for these devices was not reliable. This issue is resolved in the following sections, for both *n*- and *p*-Si devices.

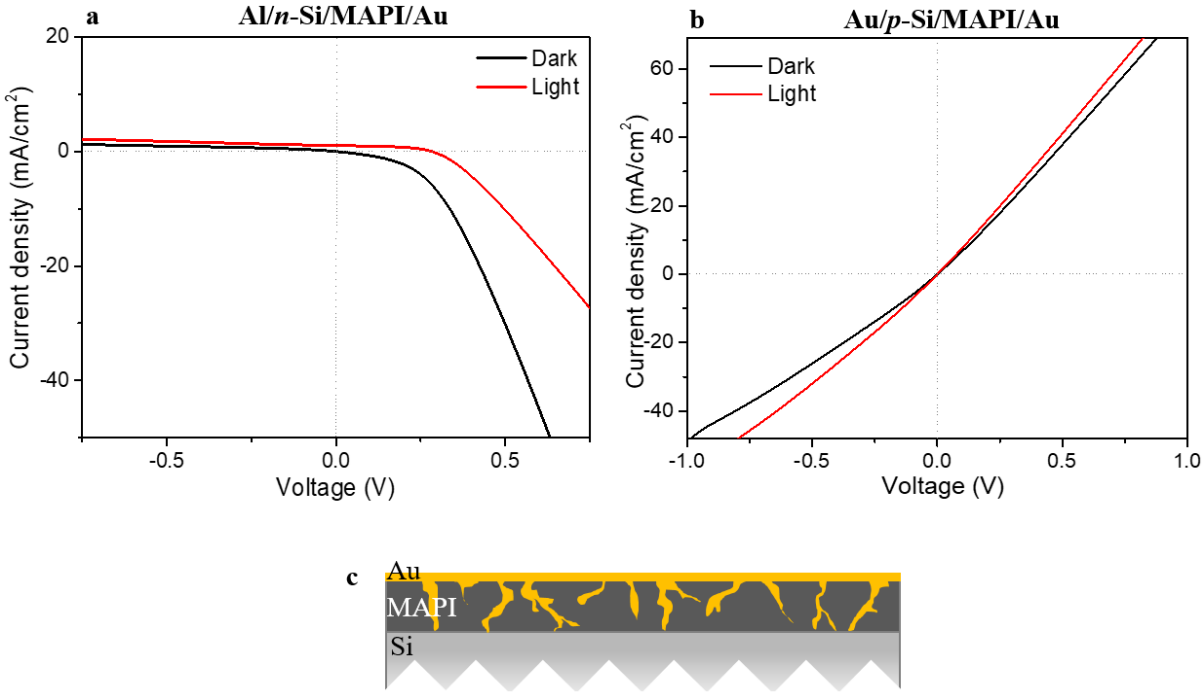


**Fig. 7.6**. *J-V* measurements on a) a rectifying *n*-Si/MAPI junction and b) an Ohmic *p*-Si/MAPI junction. c) Schematic representation of a silicon/MAPI/Au cross section showing MAPI pin holes infiltrating by the gold contact, reaching the silicon surface.

### 7.3.2. *n*-Si/MAPI heterojunctions

*a) n-Si/MAPI/spiro-OMeTAD devices*

In order to avoid the possible shunting issue, another layer was used to separate MAPI and Au. Since spiro-OMeTAD was adopted within devices in chapters 5 and 6 and was therefore well known, this hole transporting material was used in Al/*n*-Si/MAPI/Au devices to form Al/*n*-Si/MAPI/spiro-OMeTAD/Au devices. Considering that MAPI has shown intrinsic properties (see section 5.3.2.a), by using spiro-OMeTAD an *n-i-p* junction may be formed. The structures are shown in Figs. 7.7a and b, and a cross section SEM image

of the device verifying the fabrication of the Al/*n*-Si/MAPI/spiro-OMeTAD/Au devices is shown in Fig. 7.7c.

Furthermore, the effect of using spiro-OMeTAD and Au as top layers of the substrate device was studied by analysing the transmittance of these films deposited on glass. Since the quality of Au films is substrate dependent, the optical transmission of Au/spiro-OMeTAD bilayers on glass was measured relative to Au and spiro-OMeTAD control layers, as shown in Fig. 7.7d. It was observed that by adding the spiro-OMeTAD layer the transmittance of the top Au layer (in this case 10 nm thick) increased by ~5% in the whole spectrum compared to the Au layer alone, and thus also a sheet resistance change was expected. Discussion of this is deferred until section 7.4, but nevertheless this shows that the presence of spiro-OMeTAD is beneficial for the transparency of the ultra thin gold top layer.

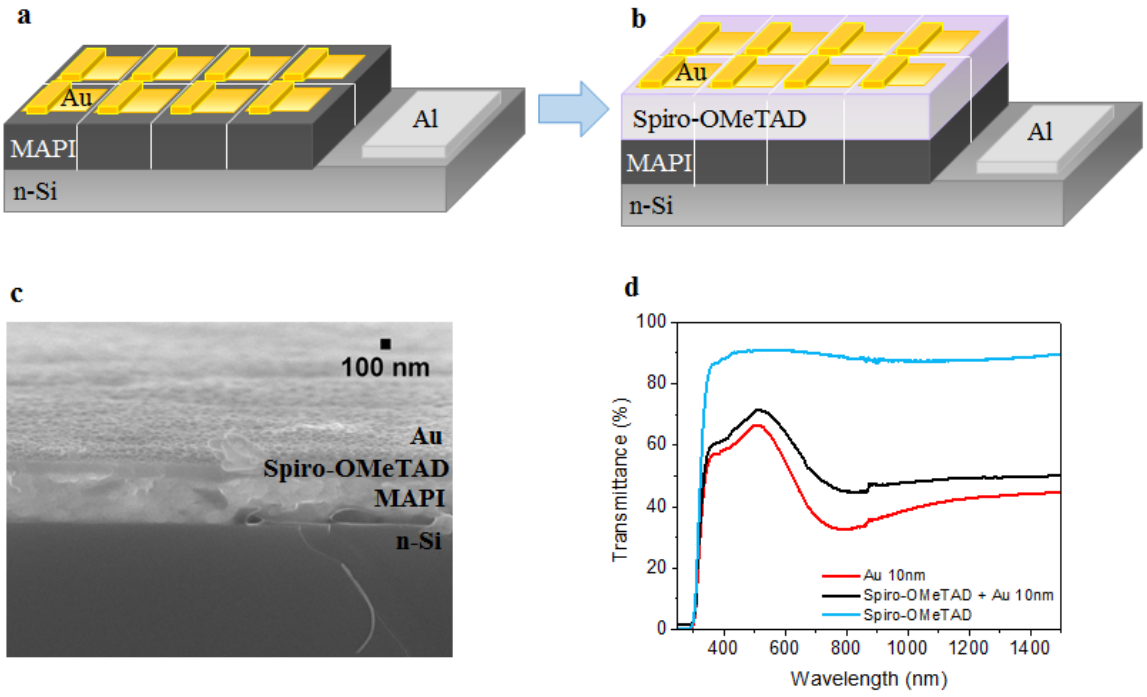


**Fig. 7.7**. Device architecture evolution from a) Al/*n*-Si/MAPI/Au, to b) Al/*n*-Si/MAPI/spiro-OMeTAD/Au. c) SEM cross section image of an Al/*n*-Si/MAPI/spiro-OMeTAD/Au solar cell device. The image was taken in the area covered by both Au layers (~60 nm). d) UV-Vis transmittance spectra showing the beneficial effect of the transparency of 10 nm thick Au deposited onto a spiro-OMeTAD layer. These experiments were performed on layers deposited on quartz coated glass.

The device structure using the hole transporting material showed improved *J-V* performance compared to the Al/*n*-Si/MAPI/Au device, as it may be seen by the *J-V* performances of these devices, presented in Table 7.3 and Fig. 7.8a.

Table 7.3, compares the performances of the devices with and without the hole transporting material, showing best and average results which were calculated from 20 – 25 contacts for each device type. Preliminary studies were performed on both Al/*n*-Si/MAPI/Au and Al/*n*-Si/MAPI/spiro-OMeTAD/Au devices covered with only 10 nm of gold on the top surface. The results show that the devices containing spiro-OMeTAD considerably exceed the performances of the devices without the hole transporting material, showing an average *PCE* of 1.14% against 0.13% respectively. In particular the main improvement was detected in the $V_{OC}$ and $J_{SC}$: devices with the spiro-OMeTAD show 0.49 V and 5.56 mA/cm$^2$ $V_{OC}$ and $J_{SC}$ respectively, compared to 0.3 V and 1.12 mA/cm$^2$ in the case of cells without spiro-OMeTAD. The best *J-V* curves of these devices are compared in Fig. 7.8a, where the increased $V_{OC}$, $J_{SC}$ and thus *PCE* of the devices using the hole transporting material are easily recognisable, with the best Al/*n*-Si/MAPI/spiro-OMeTAD/Au device producing a *PCE* of 1.35% ($V_{OC}$ = 0.5 V, $J_{SC}$ = 6.42 mA/cm$^2$ and *FF* = 42.0 %).

As the Al/*n*-Si/MAPI/spiro-OMeTAD/Au devices showed higher performances compared to those without the hole transporting material, these devices were used for further characterisation. Fig. 7.8b shows that the *J-V* curves do not show significant difference between forward and reverse scans, revealing that hysteretical behaviour is almost absent. Forward and reverse scans show the same $V_{OC}$ (0.5 V) and only a minor difference in the current ($\Delta J_{SC}$ = 0.2 mA/cm$^2$). Furthermore, Fig. 7.8c shows the stabilised efficiency of the Al/*n*-Si/MAPI/spiro-OMeTAD/Au devices, which presents a different behaviour compared to the devices presented in chapters 5 and 6. On standard *p-i-n* junctions, it is common to

register an initial drop of efficiency, which slowly stabilises. In this case however, there is a minor increase of the *PCE* in the first five seconds (from 0.95% to 1%) and then a stable *PCE* throughout the time of measurement (at 1%). These results imply that these heterojunctions are stable. They also show high consistency, as shown by the small standard deviations of the average results presented in Table 7.3.

A typical *EQE* spectra of an Al/*n*-Si/MAPI/spiro-OMeTAD/Au device is shown in Fig. 7.8d. The spectrum shows that at low energy values (high wavelengths) Si dominates, due to its lower band-gap ($E_g$ = 1.1 eV) compared to MAPI's. Then, at around 750 nm, which corresponds to MAPI's band-gap energy (1.6 eV), the *EQE* drops. This abrupt loss in current production reveals that although photons are absorbed in the perovskite the majority of the generated excitons are not extracted as current. Instead it appears that only light transmitted by the MAPI and absorbed in the Si contributes to the *EQE*.

| | | ***PCE*** **(%)** | $V_{OC}$ **(V)** | $J_{SC}$ **(mA/cm$^2$)** | ***FF*** **(%)** |
|---|---|---|---|---|---|
| **W/o spiro-OMeTAD** | AVG | 0.13 (± 0.05) | 0.30 (± 0.03) | 1.12 (± 0.38) | 37.7 (± 7.2) |
| | Best | 0.15 | 0.28 | 1.05 | 50 |
| **With spiro-OMeTAD** | AVG | 1.14 (± 0.12) | 0.49 (± 0.01) | 5.56 (± 0.48) | 41.8 (± 0.7) |
| | Best | 1.35 | 0.50 | 6.42 | 42.0 |

**Table 7.3.** *J-V* parameters of Al/*n*-Si/MAPI/Au and Al/*n*-Si/MAPI/spiro-OMeTAD/Au devices using 10 nm thick Au in the top layer. Standard deviations are shown in brackets ($N \approx$ 20-25 for each type of devices).

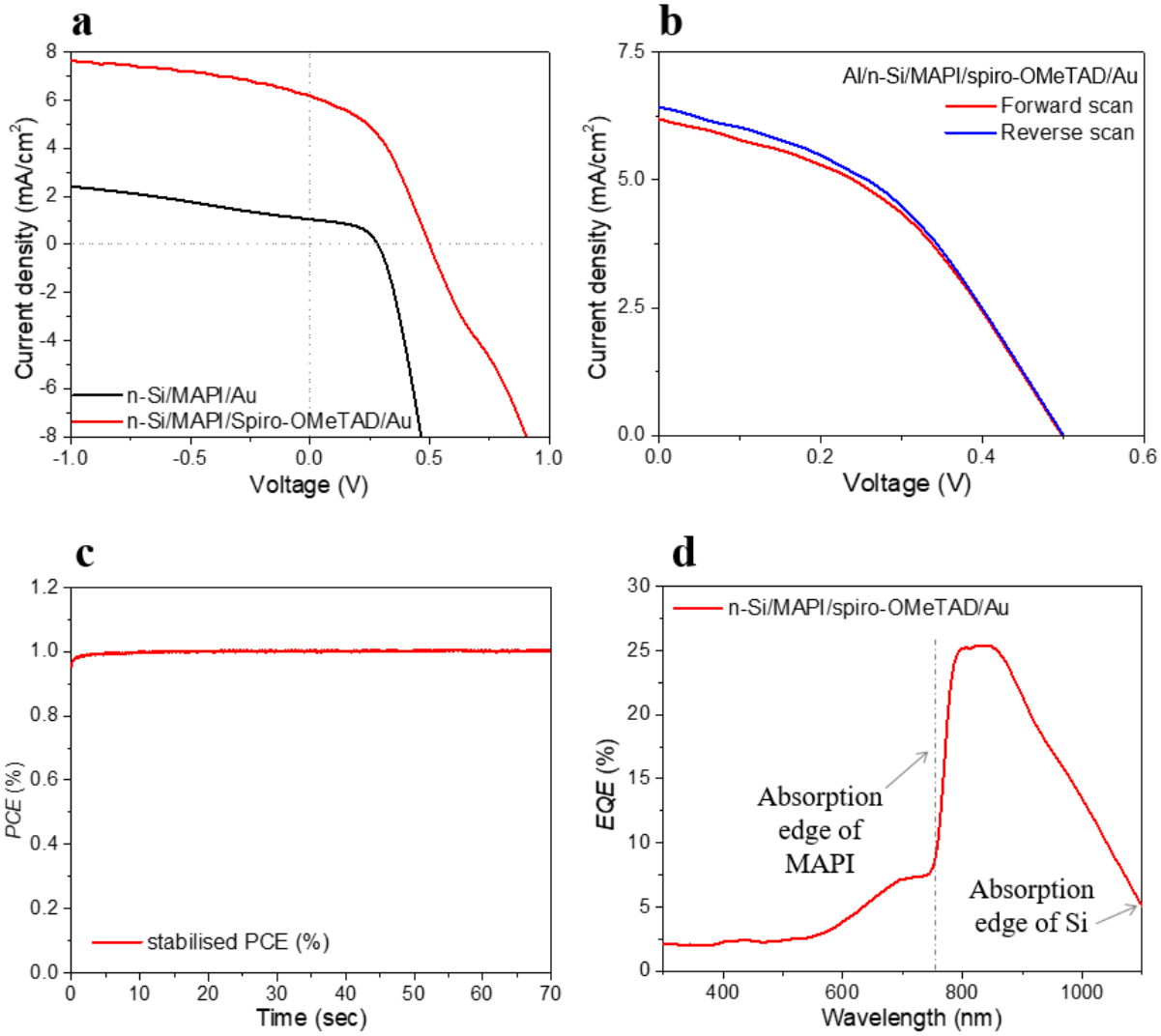


**Fig. 7.8**. *n*-Si/MAPI heterojunction device characterisation. *J-V* analysis showing a) the comparison between *J-V* curves of devices with and without spiro-OMeTAD, b) minor hysteretical behaviour of the Al/*n*-Si/MAPI/spiro-OMeTAD/Au devices, and c) stabilised efficiency at 1% *PCE* for an Al/*n*-Si/MAPI/spiro-OMeTAD/Au device. d) *EQE* analysis of an Al/*n*-Si/MAPI/spiro-OMeTAD/Au device, showing two main absorption edges, corresponding to *n*-Si (at 1100 nm, 1.1 eV) and MAPI (at 780 nm, 1.6 eV).

The effect of using top Au layers with different thicknesses (0 - 20 nm) was studied by measuring the *J-V* performances of the Al/*n*-Si/MAPI/spiro-OMeTAD/Au devices. The *J-V* parameters are reported in Table 7.4 and show the averages for 10 of each device type. The first important result is that the presence of the ultra-thin gold is necessary to produce working devices, as devices without the gold layer produce the lowest *PCE* (0.10%). Minor improvement was observed by using 5 nm of gold (0.13%), whereas the highest performance

was achieved by thicker Au layers (> 10 nm, > 0.92% *PCE*). However it was observed that the improvement of the efficiency is not linear with the Au thickness: the highest performances were shown by devices covered by 10 nm Au (1.14% *PCE*), whereas very similar results were achieved by devices with 15 and 20 nm Au (0.92% and 0.92% *PCE* respectively). Considering the devices containing the Au layer with thickness ≥ 10 nm, the parameter that mainly influenced the device efficiency was the *FF* (41.8% for 10 nm Au and *FF* ≤ 36.6% for 15 and 20 nm), whereas $V_{OC}$ and $J_{SC}$ remain very similar (0.48-0.49 V and 5.2-5.6 mA/cm$^2$ respectively). It was therefore concluded that to optimise the Al/*n*-Si/MAPI/spiro-OMeTAD/Au device performance, a 10 nm ultra thin Au layer was required.

| **Au thickness (nm)** | ***PCE* (%)** | **$V_{OC}$ (V)** | **$J_{SC}$ (mA/cm$^2$)** | ***FF* (%)** |
|---|---|---|---|---|
| **0** | 0.10 (± 0.07) | 0.36 (± 0.02) | 1.02 (± 0.46) | 24.7 (± 6.3) |
| **5** | 0.13 (± 0.05) | 0.43 (± 0.02) | 0.88 (± 0.26) | 32.6 (± 4.1) |
| **10** | 1.14 (± 0.12) | 0.49 (± 0.01) | 5.56 (± 0.48) | 41.8 (± 0.7) |
| **15** | 0.92 (± 0.12) | 0.48 (± 0.01) | 5.35 (± 0.51) | 35.6 (± 1.5) |
| **20** | 0.92 (± 0.16) | 0.48 (± 0.01) | 5.24 (± 0.79) | 36.6 (± 2.5) |

**Table 7.4.** *J-V* parameters of Al/*n*-Si/MAPI/spiro-OMeTAD/Au devices using different thicknesses of the front gold layer. Standard deviations are in brackets ($N \approx 10$ for each thickness).

*b) Study of the interfaces*

In order to fully understand the device performances, every interface of the Al/*n*-Si/MAPI/Au and Al/*n*-Si/MAPI/spiro-OMeTAD/Au devices was studied by light *I-V* and *EQE* analysis, as described in Table 7.5 and shown in Fig. 7.9. Since it was observed in section 7.3.1c that shunting may be an issue in these heterojunction devices, a study focussed

on the possible interfaces that may form as a consequence of MAPI pin holes was required. For example the interfaces forming between *n*-Si and Au or *n*-Si and spiro-OMeTAD may have an influence on the *n*-Si/MAPI heterojunction, representing an obstacle for the main subject of study of this chapter.

Some of the data shown in Table 7.5 summarise the results obtained previously (*n*-Si/Al and *n*-Si/MAPI junctions in section 7.3.1a and 7.3.1c respectively), these showing Ohmic contact and a rectification respectively. It is worth remembering that the *n*-Si/MAPI rectifying junction produced a small photo-activity under light, but showed extremely low efficiencies (0.1% *PCE*), due to low $V_{OC}$ (0.3 V) and $J_{SC}$ (1.1 mA/cm$^2$), as confirmed in the *I-V* curve in Fig. 7.9a (black curve).

Analyses performed on *n*-Si/Au and *n*-Si/spiro-OMeTAD are presented in Table 7.5 and show very important results. In particular, the *n*-Si/Au interface was measured and showed rectification, as also shown in the dark *I-V* analysis shown in Fig. 7.2a. However, under AM 1.5 illumination this junction showed photo-activity, producing a *PCE* of 1.2%. The 'high efficiency' of this junction (compared to the results of the other junctions reported in this work) is mainly associated with the high current density of 13.6 mA/cm$^2$, whereas the $V_{OC}$ is low (0.27 V), as confirmed by the *I-V* curve in Fig. 7.9a (red curve). In parallel, Fig 7.9b shows the *EQE* measurement of the *n*-Si/Au junction, showing a photon absorption in the whole spectrum considered, starting from the band gap of silicon at low energy (1.1 eV, ~1100 nm) reaching a maximum of ~30% *EQE* at ~500 nm, and declining at short wavelengths due to the low blue sensitivity of Si.

In the case of the *n*-Si/spiro-OMeTAD sample, *I-V* measurements show that a junction is formed but that it is only very weakly photoactive (Fig. 7.9a, blue curve). Furthermore, the *EQE* shows that for the *n*-Si/spiro-OMeTAD a small peak is produced

solely in proximity of the hole transporting material's band gap (~3 eV, ~400 nm), confirming the rectifying behaviour seen in the *I-V* curve.

The MAPI/spiro-OMeTAD interface showed a junction but no photo-activity (pink curve, Fig. 7.9a), whereas MAPI/Au interface showed Ohmic behaviour (as seen previously, Fig. 7.3a).

Lastly, it should be mentioned that the spiro-OMeTAD/Au interface is well-known to be Ohmic from the literature and is largely used in classic perovskite *p-i-n* devices.[21]

| **Interface** | ***J-V*** | ***EQE*** | **Notes** |
|---|---|---|---|
| ***n*-Si/Al** | Ohmic | N.A. | |
| ***n*-Si/MAPI** | Rectification: in light AVG *PCE* 0.1%, $V_{OC}$ 0.30 V, $J_{SC}$ 1.1 mA/cm$^2$ | Too low to be measured | Pin holes in MAPI |
| ***n*-Si/Au** | Rectification: in light AVG *PCE* 1.2%, $V_{OC}$ 0.27 V, $J_{SC}$ 13.6 mA/cm$^2$ | Si collects photons in the whole spectrum | |
| ***n*-Si/spiro-OMeTAD** | Rectification but no photo-activity | Photon collected just from the top spiro-OMeTAD layer | |
| **MAPI/spiro-OMeTAD** | Rectification but no photo-activity | N.A. | |
| **MAPI/Au** | Ohmic | N.A. | |
| **spiro-OMeTAD/Au** | Ohmic | N.A. | |

**Table 7.5.** *J-V* and *EQE* results (where possible) for test structure representing the interfaces present in the Al/*n*-Si/MAPI/spiro-OMeTAD/Au devices, including those that may form due to shunting.

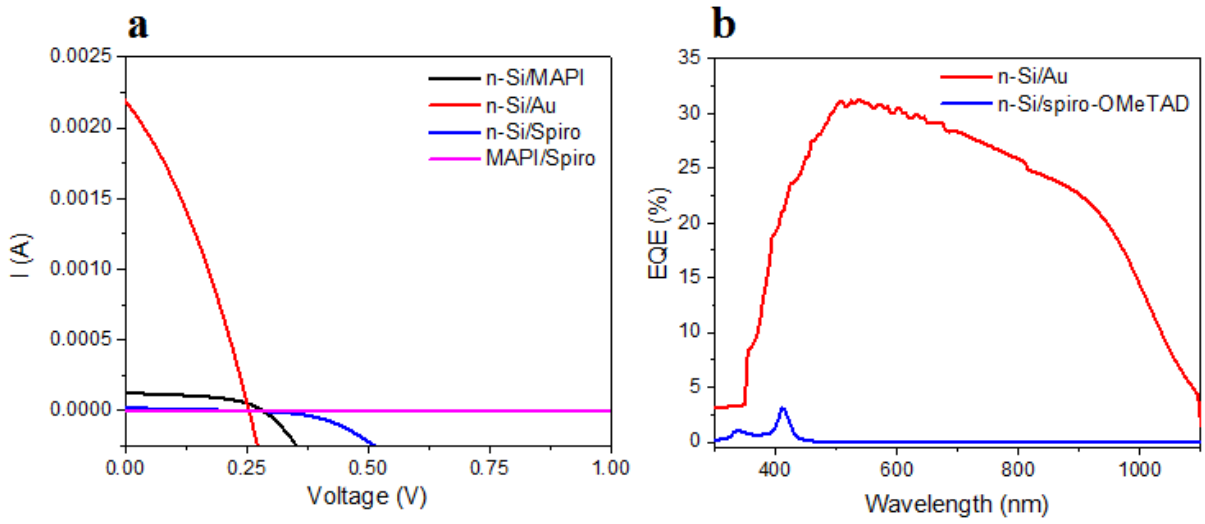


**Fig. 7.9**. Characterisation of the interfaces. a) AM1.5 *I-V* curves of the rectifying junctions showing a strong photodiode response in the *n*-Si/Au junction, the weaker photodiode between *n*-Si/MAPI, a non-photoactive *n*-Si/spiro-OMeTAD and MAPI/spiro-OMeTAD junctions. b) *EQE* (where applicable) of these interfaces, showing the photon collection in the whole spectrum for *n*-Si/Au junction and the absorption in only spiro-OMeTAD in the *n*-Si/ spiro-OMeTAD junction.

The interface study introduced a new perspective to the understanding of the *n*-Si/MAPI junction results shown in Fig. 7.8a. Comparing the results of the device performances of the Al/*n*-Si/MAPI/Au and Al/*n*-Si/MAPI/spiro-OMeTAD/Au devices shown in Table 7.3, similarities may be detected. For example, considering the Al/*n*-Si/MAPI/Au and the *n*-Si/Au interface shown in the interface study, it was seen that their $V_{OC}$ values are similar (0.3 V and 0.27 V respectively), whereas when the spiro-OMeTAD is introduced the $V_{OC}$ increases (0.49 V). As was seen in Table 7.5, Au rectifies with *n*-Si and produced a *PCE* under light, whereas spiro-OMeTAD rectifies but does not produce current. Therefore it may be implied that the Au shunting in the Al/*n*-Si/MAPI/Au devices influenced the performance greatly, whereas the Al/*n*-Si/MAPI/spiro-OMeTAD/Au device architecture is not shunted. In this way, it was possible to isolate the behaviour of the silicon/MAPI junction, which was shown to be photoactive.

*c) Devices on differently n-doped silicon wafers*

Al/*n*-Si/MAPI/spiro-OMeTAD/Au devices were initially fabricated onto Si substrates with a resistivity of 1-10 Ω·cm. This section shows the effect of using different resistivity ranges (1-5 Ω·cm, 5-10 Ω·cm, 10-15 Ω·cm) to observe the effect on the *n*-Si/MAPI junction and the device performance. The devices were measured by *J-V* and *EQE* analysis, as shown in Figs. 7.10 - 7.11 and Table 7.6.

Fig. 7.10 shows the highest performing *J-V* curves and *EQE* spectra recorded for the Al/*n*-Si/MAPI/spiro-OMeTAD/Au devices, and shows that devices manifest similar behaviours despite the different doping concentration of the Si. The best *J-V* curves, shown in Fig. 7.10a, achieved 2.08%, 2.07% and 1.34% *PCE* using 1-5 Ω·cm, 5-10 Ω·cm and 10-15 Ω·cm Si wafers respectively (Table 7.6). The device using the 1-5 Ω·cm Si wafer demonstrated the champion efficiency produced in this work with a *PCE* = 2.08% ($V_{OC}$ = 0.46 V, $J_{SC}$ = 11.77 mA/cm$^2$, *FF* = 38.4%). The increased photovoltaic performance of devices made from the more conductive *n*-Si (*i.e.* lower resistivity, see Table 7.1) is due to the increase in $J_{SC}$, as shown in both the *J-V* and *EQE* curves. However, the *EQE* curves (Fig. 7.10b) show that although both sides of the junction collect charge, the increase is mainly confined to the long wavelength region and is due to collection in the Si. Collection at the wavelength corresponding to the band gap of MAPI (<780 nm) remains low.

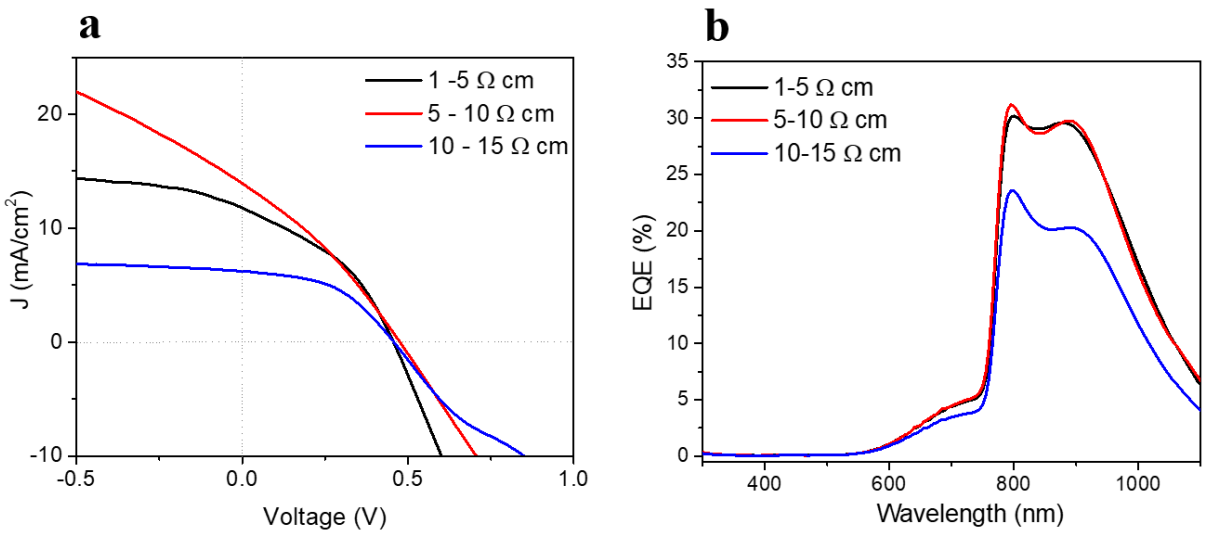


**Fig. 7.10**. Characterisation of Al/*n*-Si/MAPI/spiro-OMeTAD/Au devices containing silicon wafers with different resistivities. a) Best *J-V* curves showing photo-active rectifying junctions producing higher performances when Si wafers with lower resistivities are employed. b) *EQE* spectra showing higher *EQE* % with higher doping levels of the silicon wafers.

In order to improve the understanding of these devices, the *J-V* parameters were analysed further. The highest value, average values and standard deviations of the PV parameters (Table 7.6) are presented in Fig. 7.11. A trend between the Si doping level and the device performance can be noted: higher doping concentrations of Si yield higher device performances. Both the $V_{OC}$ and $J_{SC}$ were consistent between each set of devices (0.42 V, 0.43 V and 0.41 V, and 7.26 mA/cm$^2$, 6.20 mA/cm$^2$ and 6.45 mA/cm$^2$ for the increasing resistivity values, Fig. 7.11b). However, the standard deviation of $J_{SC}$ was large (Fig. 7.11c), revealing the variability of these devices. Finally, Fig. 7.11d shows that similar *FF*s were achieved by the 5-10 Ω·cm and 10-15 Ω·cm devices (37.8% and 39.7% respectively), whereas the 1-5 Ω·cm devices show a step up, reaching 46.2% *FF*, this being the most influential parameter affecting the average device efficiency (note that this differs from the finding that $J_{SC}$ was influential for the highest performing devices as shown in Fig. 7.10). However, it was noted that despite the high average *FF* of the 1-5 Ω·cm devices, the *FF* measured for the best device only achieved 38.4%, revealing that it may yet be possible to

obtain even higher efficiencies for these Al/*n*-Si/MAPI/spiro-OMeTAD/Au heterojunction devices.

| **Silicon resistivity** | | ***PCE*** **(%)** | $V_{OC}$ **(V)** | $J_{SC}$ **(mA/cm$^2$)** | ***FF*** **(%)** |
|---|---|---|---|---|---|
| **1-5 Ω·cm** | Average | 1.26 (± 0.64) | 0.42 (± 0.05) | 7.26 (± 5.28) | 46.2 (± 9.8) |
| | Best | 2.08 | 0.46 | 11.77 | 38.4 |
| **5-10 Ω·cm** | Average | 1.08 (± 0.56) | 0.43 (± 0.06) | 6.20 (± 2.77) | 37.8 (± 9.5) |
| | Best | 2.07 | 0.48 | 13.92 | 30.9 |
| **10-15 Ω·cm** | Average | 1.02 (± 0.22) | 0.41 (± 0.04) | 6.45 (± 1.86) | 39.7 (± 7.1) |
| | Best | 1.34 | 0.46 | 6.22 | 46.7 |

**Table 7.6.** *J*-*V* parameters of Al/*n*-Si/MAPI/spiro-OMeTAD/Au devices using Si wafers with different resistivities. Standard deviations are in brackets ($N \approx 15$ for each set of devices).

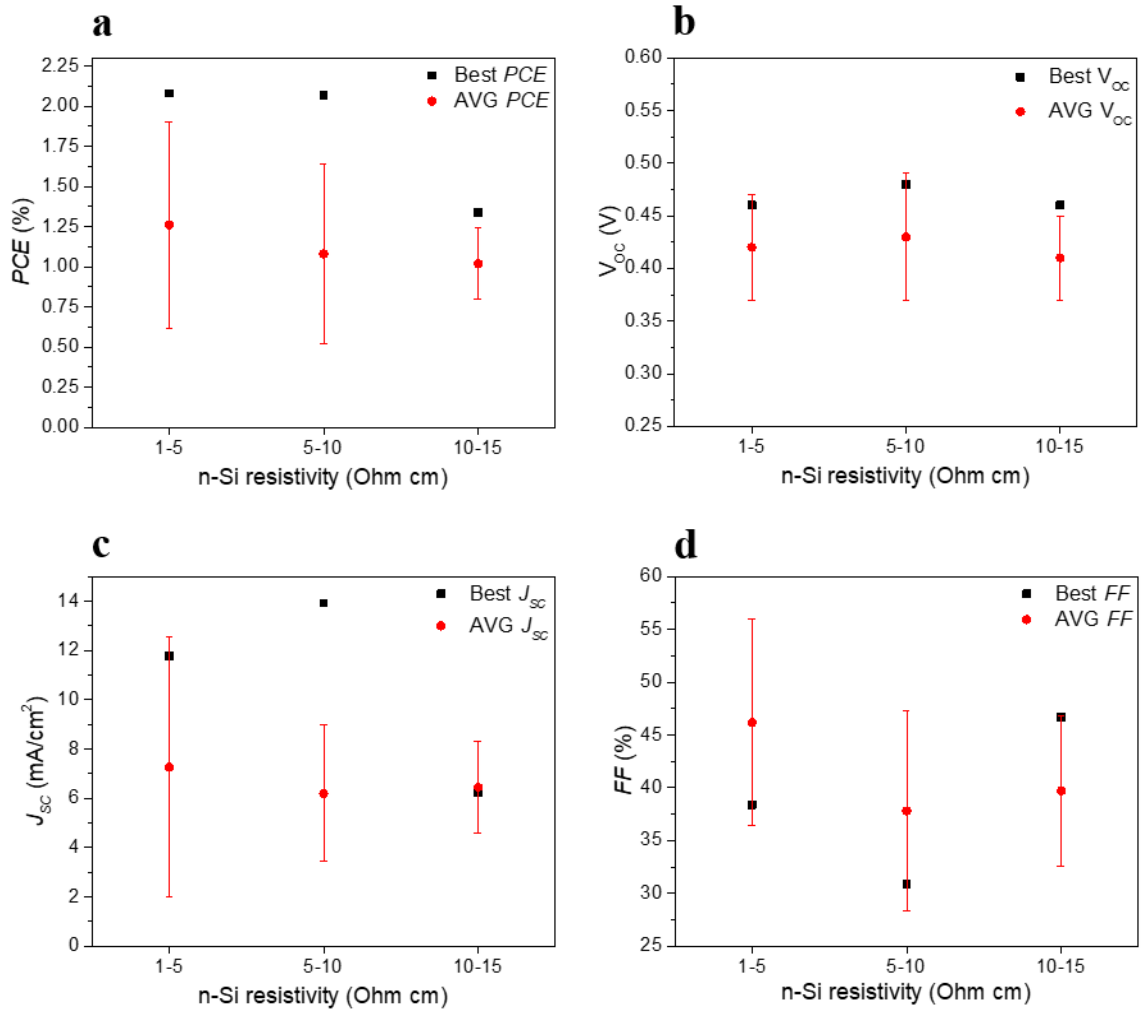


**Fig. 7.11**. *J-V* parameters of Al/*n*-Si/MAPI/spiro-OMeTAD/Au devices fabricated using different Si resistivities (1-5 Ω·cm, 5-10 Ω·cm, 10-15 Ω·cm), showing the best, average and standard deviations.

In order to understand how higher doping concentrations yield increased device performance, a band alignment of the Al/*n*-Si/MAPI/spiro-OMeTAD/Au device structure was constructed and is shown in Fig. 7.12. The band gap energies for each material were taken from the literature[24,25] (Fig. 7.12a), and the positions of the Fermi level for the *n*-Si and spiro-OMeTAD were approximated by their doping properties (*n* and *p*-type respectively). For this reason, Fig. 7.12b and c, show the diagrams for the devices using both low doped and highly doped Si. It can be seen that once the Fermi level is aligned at equilibrium, a spike is formed between the valence bands of MAPI and *n*-Si, the size of

which is dependent on the Si doping level: the higher the doping the smaller the spike. For instance, Fig. 7.12b shows the formation of a spike of 0.56 eV using low doped Si, whereas Fig. 7.12c forms a spike of 0.50 eV by using highly doped silicon. This spike is disadvantageous as it blocks the drift of holes, and thus high doping levels of the *n*-silicon are preferable for the *n*-Si/MAPI heterojunctions. The band offset therefore explains why devices containing the highly doped Si wafer produced higher performances (Table 7.6). The band alignments shown (Fig. 7.12 b and c) were drawn as if the junction was one-sided and positioned in the MAPI. However, since this statement was not established until this point, Fig. 7.12d presents the band diagram in the case of a one-sided junction positioned in the *n*-Si. While the band bendings change direction, the spike between the valence bands of Si and MAPI does not change its size. In contrast, if the junction would be two-sided (with the junction close to the *n*-Si/MAPI interface) the band diagram would be an intermediate situation between Fig. 7.12c and d.

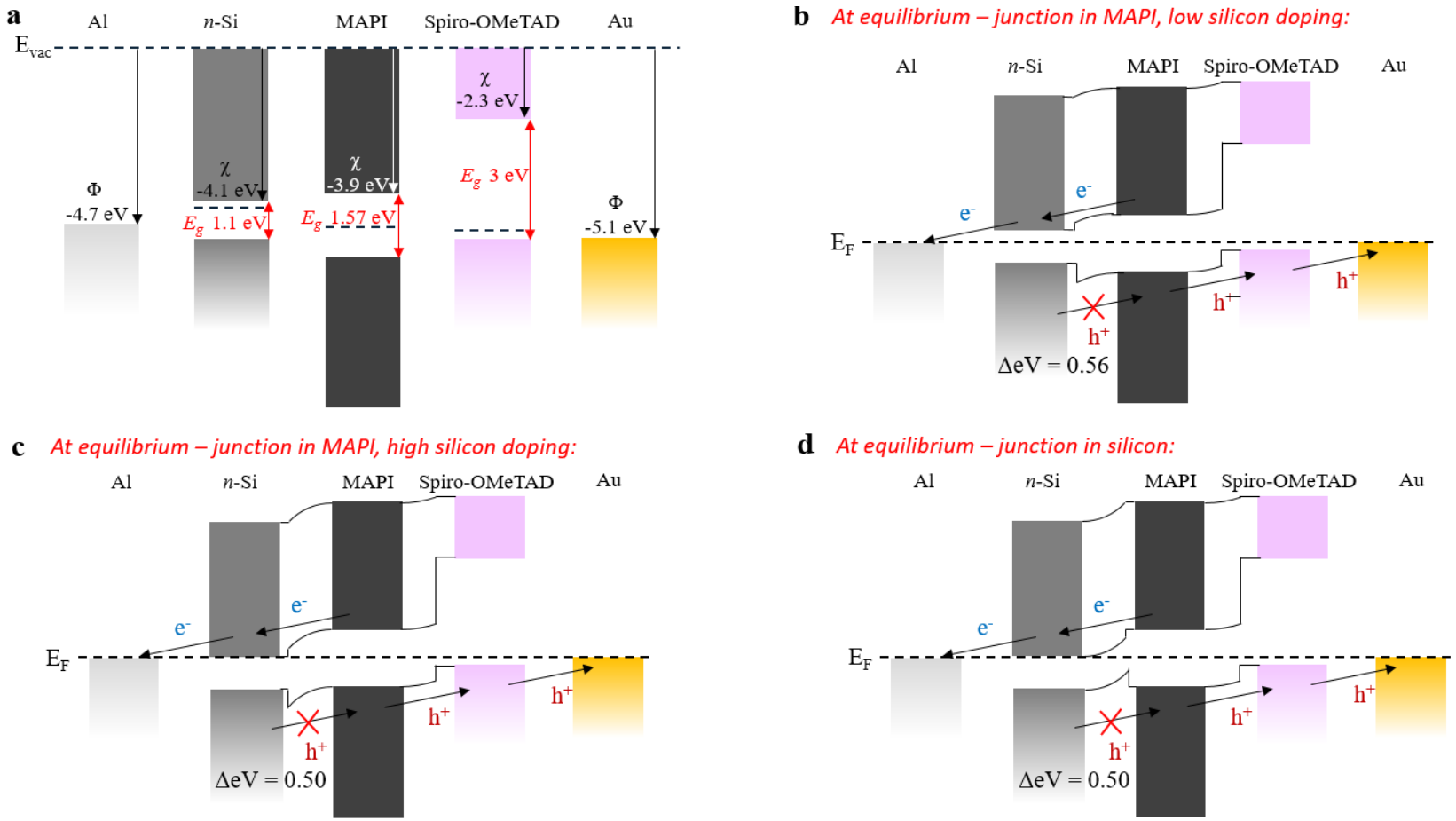


**Fig. 7.12**. Band diagram of Al/*n*-Si/MAPI/spiro-OMeTAD/Au devices. a) Band energies of the materials used in the devices - values were taken from the literature.[24,26] b), c), d) Band offsets at equilibrium, with the one-sided junction positioned in MAPI (b, c) and in Si (d). b) c) Band diagram of *n*-Si/MAPI using *n*-Si with different doping levels showing a downwards spike between conduction bands of Si and MAPI: b) low doped *n*-Si forming a spike of 0.56 eV in the valence band with MAPI, and c) higher doping of the *n*-Si compared to (b), forming a smaller spike with MAPI (0.50 eV). d) Band diagram at equilibrium showing the field in *n*-Si. Now the spike between valence bands of Si and MAPI is upwards, but its size does not change (in the case of highly doped Si this is 0.50 eV).

*C-V* measurements were performed in order to identify the type of junction between Si and MAPI (single or two-sided) and measure the built in voltage ($V_{bi}$) and the carrier concentration from a $1/C^2$ plot (see section 2.2.5). The study was performed on the Al/*n*-Si/MAPI/spiro-OMeTAD/Au devices fabricated with different Si wafer resistivities. Fig. 7.13 presents the *C-V* and $1/C^2$ plots obtained by these devices and applying a frequency of $10^5$ Hz. A main peak in the *C-V* plot (Fig. 7.13a) was recorded at V > 0.5 for all devices. However, it can be noted that there is an unusual peak forming at ~0.25 V for each curve which becomes more evident in the Mott-Shottky plot (Fig. 7.13b, ~0.3V). The intensity of this peak decreases with the increasing doping level of the Si, suggesting that it is related to an interface effect, perhaps between *n*-Si/MAPI valence bands (Fig. 7.12b-d).

The fitting of the x-axis of the Mott-Shottky lines (linear part around 0 V), with intercept ($V_{bi} - kT/q$), provides the built in voltages ($V_{bi}$),[27] whereas the slope of the fitting line determines the carrier concentration of the junction. In the case of built in voltages, similar results between devices that use different Si doping concentrations were measured, showing a built in voltage of 0.70 V, 0.68 V and 0.65 V for the 1-5 Ω·cm, 5-10 Ω·cm and 10-15 Ω·cm device respectively.

While the built in voltages are directly extracted from the Mott-Shottky plot, the determination of the carrier concentration is dependent on the dielectric constant of the materials involved in the junction (section 2.2.5: only one dielectric constant for one-sided junctions and two dielectric constants for two-sided junctions). The carrier concentration results were used to help classify the junction type. A one-sided junction for example, is recognised when the doping concentration of one material is at least two orders of magnitude higher than the other, whereas when the doping concentration of the two materials is similar, a two-sided junction is formed.[27] Since the carrier concentration is known for Si but it is unknown for MAPI, the calculations for both situations were performed and are presented

next, whereas a discussion about which of these possibilities is more appropriate is deferred until section 7.4.

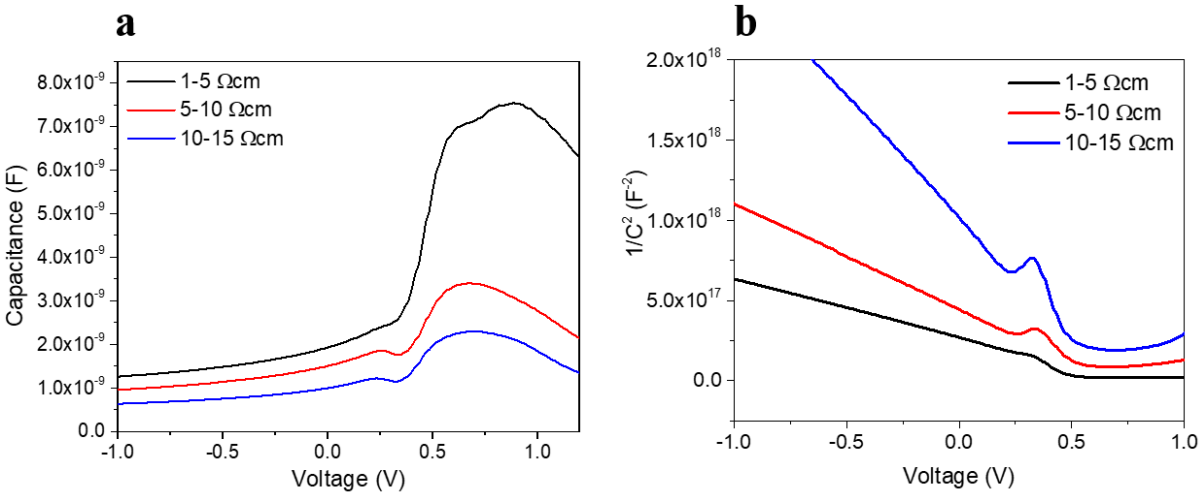


**Fig. 7.13**. *C-V* characterisation of Al/*n*-Si/MAPI/spiro-OMeTAD/Au devices containing Si wafers with different resistivities measured in the dark, applying a frequency of $10^5$ Hz. a) *C-V* plot showing two main peaks: a smaller at V ~0.25 V and a more intense capacitance peak at V > 0.5 V. b) Mott-Shottky plot derived from a *C-V* measurement, which curve fittings provide similar $V_{bi}$ for all devices. Peaks at ~0.3 V are caused by spikes in the band offsets.

*i) One-sided junction*

Assuming that there is a one-sided junction in Si, the carrier concentration was calculated using Equation 2.20 (section 2.2.5.a) for one-sided junctions and using Si's dielectric constant of 11.7,[28] and the results are shown in Table 7.7. The table includes the Si carrier concentrations for comparison with the values obtained by the Mott-Shottky plot: for each Si resistivity the measured and the wafer carrier concentration values are very similar, these being ~$10^{15}$ $cm^{-3}$ for the highly doped Si and ~$10^{14}$ $cm^{-3}$ for the lower doped wafers.

| Si resistivity | $V_{bi}$ (V) | Measured carrier concentration ($cm^{-3}$) | *n*-Si carrier concentration ($cm^{-3}$) |
|---|---|---|---|
| **1-5 Ω·cm** | 0.70 ± 0.01 | $1.39 \cdot 10^{15}$ | $2.86 \cdot 10^{15}$ |
| **5-10 Ω·cm** | 0.68 ± 0.01 | $7.90 \cdot 10^{14}$ | $6.68 \cdot 10^{14}$ |
| **10-15 Ω·cm** | 0.65 ± 0.01 | $3.28 \cdot 10^{14}$ | $3.67 \cdot 10^{14}$ |

**Table 7.7.** Results from *C-V* analysis performed on Al/*n*-Si/MAPI/spiro-OMeTAD/Au devices using Si wafers with different resistivities and applying a frequency of $10^5$ Hz. The assumption is to form a one-sided junction.

*ii) Two-sided junction*

Since the *EQE* (Fig. 7.10b) shows photon collection in both Si and MAPI regions (although in MAPI this is smaller), the junction may form near the interface of the two materials, forming a two-sided junction. If so, then the capacitance of the junction would be influenced by the dielectric constants of both silicon and MAPI (11.7 and 24.1 respectively).[28,29] For simplicity here, it was considered that the depletion region is positioned half in the Si and half in the MAPI. The carrier concentrations of the devices containing Si with the different resistivities were extracted from the Mott-Shottky plot (Fig. 7.13b) and the results are presented in Table 7.8. The calculated carrier concentration and the carrier density of the silicon are compared and showed extremely similar values (~$10^{15}$ $cm^{-3}$ for the highly doped Si and ~$10^{14}$ $cm^{-3}$ for the lower doped wafers). Furthermore, by knowing the carrier concentration of one material participating to the junction (*n*-Si), it was possible to determine the carrier concentration of the second material, *i.e.* MAPI, which has shown to be difficult to measure otherwise.[29] Starting from the equation for the determination of the width of a two-sided junction, it was possible to extract the acceptor

density value of MAPI ($N_A$) (see section 2.2.5.b, Eq. 2.44). The results are shown in Table 7.8 (last column). MAPI's carrier concentration measured in the heterostructure devices showed a carrier concentration of $10^{14}$ - $10^{15}$ $cm^{-3}$ which is very similar to the Si carrier concentration values: the differences in carrier concentration are less than two orders of magnitude which is consistent with the formation of a two-sided junction.[27] Discussion is deferred until section 7.4.

| **Si resistivity** | $V_{bi}$ **(V)** | **Measured carrier concentration ($cm^{-3}$)** | ***n*-Si carrier concentration ($cm^{-3}$)** | **MAPI carrier concentration ($cm^{-3}$)** |
|---|---|---|---|---|
| **1-5 Ω·cm** | 0.70 ± 0.01 | $1.03 \cdot 10^{15}$ | $2.86 \cdot 10^{15}$ | $1.62 \cdot 10^{15}$ |
| **5-10 Ω·cm** | 0.68 ± 0.01 | $5.87 \cdot 10^{14}$ | $6.68 \cdot 10^{14}$ | $7.58 \cdot 10^{15}$ |
| **10-15 Ω·cm** | 0.65 ± 0.01 | $2.44 \cdot 10^{14}$ | $3.67 \cdot 10^{14}$ | $8.30 \cdot 10^{14}$ |

**Table 7.8.** Results from *C-V* analysis performed on Al/*n*-Si/MAPI/spiro-OMeTAD/Au devices using Si wafers with different resistivities and applying a frequency of $10^5$ Hz. A two-sided junction is assumed. The carrier concentration extracted from the $1/C^2$ plot is compared to the Si doping concentration and to the carrier concentration of MAPI derived from Equation 2.44.

### 7.3.3. *p*-Si/MAPI devices

Section 7.3.1c showed that the *p*-Si/MAPI junction was giving an Ohmic response in the *J-V* measurements. However, since pin holes caused shunting, it is clear that the measurements on *p*-Si/MAPI were probably affected by the Ohmic-behaving *p*-Si/Au interface (section 7.3.1a.i).

In order to overcome this problem, an additional layer was introduced in the device, between the MAPI and the gold layer, similarly to the *n*-Si/MAPI devices where spiro-OMeTAD was used as intermediate. In this case however, in order to form a favourable

band alignment an *n*-type intermediate material was chosen, this being ZnO covered by a conductive AZO layer. In this way a *p*-*i*-*n* junction was formed.

Au/*p*-Si/MAPI/ZnO/AZO devices were measured by *J*-*V* analysis, as shown in Fig. 7.14a. Dark and light measurements show rectification, proving that the Ohmic behaviour seen in section 7.3.1c was caused by shunting. However, the difference between dark and light curves is minor, as the average *PCE* measured under AM1.5 showed an efficiency of 0.02% ($V_{OC}$ = 0.35 V, $J_{SC}$ = 0.40 mA/cm$^2$, *FF* = 19.9%). Nevertheless, this result shows that a junction may be formed between *p*-Si and MAPI. However, as the current produced by these devices was very low, it was not possible to perform *EQE* measurements.

The possible explanation for the very low device performance may be inferred from the band offset shown in Fig. 7.14b. Assuming that the ZnO doping level considered is correct, the device architecture shows the formation of a spike between MAPI and ZnO conduction bands, whereas no electron/hole blockages were detected between MAPI and *p*-Si. The spike blocks the electrons generated in MAPI and flowing toward the contact.

However, it was observed that using higher doping of the ZnO would improve the device performance, reducing the size of the spike. Further discussion is presented in section 7.4.

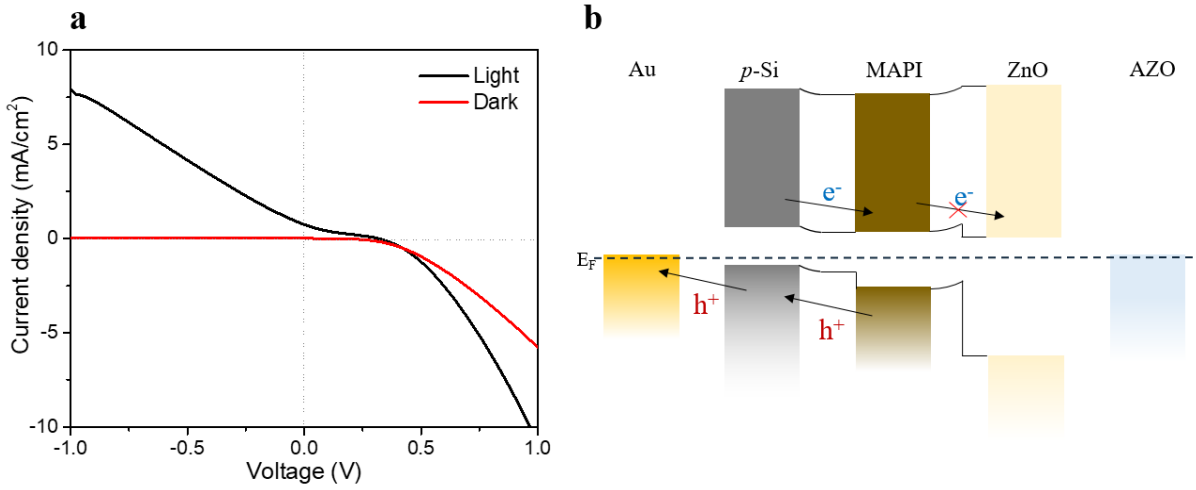


**Fig. 7.14.** Au/*p*-Si/MAPI/ZnO/AZO devices. a) *J-V* analysis in dark and light, showing rectification but only very weak photo-activity. b) Band diagram of the device showing a barrier for electrons generated by MAPI flowing towards the contact. The band energies of each material were taken from the literature (ZnO $E_g$ = 3.2 eV, $\chi$ = 4.3 eV).[24,26,30]

## 7.4. Discussion

In this work, heterojunctions between silicon and MAPI were studied, with the goal of fabricating new devices that were not explored in the literature previously. Through evolutionary steps, the device architecture was developed with the intent of proving the formation of a junction. As the MAPI used in this work showed intrinsic doping properties (see chapter 5), the type of junction formed would not have been a *p-n* junction, but rather an '*n-i*' and '*p-i*' junction with *n*-type and *p*-type Si respectively. Nevertheless, by performing *J-V* and *EQE* analysis it was proven that a photoactive junction between MAPI and Si was formed: photon absorption was observed and efficiencies were recorded under illumination.

The formation of MAPI on Si wafers was verified: the XRD peaks matched with those of MAPI deposited on glass or $TiO_2$, but unfortunately the presence of numerous pin holes was detected (Fig. 7.4c). The main issue related to the pin holes was shunting: Au was an Ohmic contact to MAPI, but it infiltrated in the pin holes and reached the Si. While in

the case of *n*-Si this caused a variation of the *n*-Si/MAPI *J-V* performance (*n*-Si/Au alone gives a *PCE* of 1.2% under AM1.5), in the case of *p*-Si/MAPI heterojunction the shunting produced an Ohmic junction, which was initially thought to be formed by the *p*-Si/MAPI junction. A study performed on the interfaces introduced to the possibility that unwanted junctions forming in the device may produce misleading interpretation of the junction under study (silicon/MAPI). Examples of misleading results caused by shunting issues, but with different materials, were already presented in the literature and it was suggested that the formation of 'weak diode regions'[31] may influence the device performance greatly. Even small numbers of shunts can radically alter the device performance.

Therefore, the employment of an intermediate layer between MAPI and the Au front contact was necessary, however it had to be confirmed that this layer would not interact with the Si. A study was conducted in regard of spiro-OMeTAD and *n*-Si with this aim. It was seen that by introducing the hole transporting material in the Al/*n*-Si/MAPI/Au device, the efficiency of the device was increased considerably (0.13% *PCE* without and 1.14% *PCE* with spiro-OMeTAD). The reason for this improvement is the filling of pin holes in MAPI with spiro-OMeTAD which is favourable as it forms a junction with *n*-Si which although is not itself photoactive, does not degrade the *n*-Si/MAPI interaction measured under light. This 'pin hole blocker' feature is not new for conductive materials in PV devices: other examples in the literature used this effect to overcome shunting issues, for example P3HT with CdTe.[32] The use of Au contacts on top of spiro-OMeTAD was shown to be necessary to measure the heterojunction devices (*PCE* without the Au front contact = 0.10%). When the Au layer thickness was increased from 0 to 5 nm the difference was not significant (0.13%), whereas when thicker layers were deposited (≥ 10 nm) the devices showed *PCE* ≥ 0.92%. Nevertheless, the highest device performances were reached using 10 nm of Au (*PCE* = 1.14%). This difference may be speculated to be due to the different distribution of

Au particles on the surface. Furthermore, it was observed that the 10 nm Au film deposited on spiro-OMeTAD, showed increased transmittance compared to that of 10 nm of Au on quartz-coated glass, hence the use of the hole transporting material had an additional beneficial effect. This increased transmittance might be attributed to a different percolation thickness, or a decrease in the surface roughness (*i.e.* scattering) and reduced reflection loss due to closer refractive index matching in this thin film bilayer system (an example in literature is shown by the ZnO-Ag-ZnO layers which in this configuration become less reflective compared to an Ag layer[33]). A further interesting feature due to the presence of spiro-OMeTAD was seen in the band diagram (Fig. 7.12). By analysing the band offset it can be noted that if the hole transporting material is not present in the device, then the electrons generated in MAPI may equally well drift towards the *n*-Si or the Au, as the difference in energy between the conduction band of MAPI with *n*-Si and with Au are very similar. Hence, holes generated in MAPI and directed towards the Au would lead to recombination.

Nevertheless, by using spiro-OMeTAD it was possible to study the behaviour of the *n*-Si/MAPI junction and devices made from it. A champion device efficiency of 2.08% ($V_{OC}$ = 0.46 V, $J_{SC}$ = 11.77 mA/cm$^2$, *FF* = 38.4%) was obtained using a highly doped *n*-Si wafer (1-5 Ω·cm) and built in voltage values of 0.70 V, 0.68 V and 0.65 V were obtained for the devices using 1-5 Ω·cm, 5-10 Ω·cm, 10-15 Ω·cm Si respectively. However, since $V_{bi}$ values are typically higher than the $V_{OC}$, it may be suggested that there may still be scope to increase the device's open circuit voltage. In addition, a promising feature of the Al/*n*-Si/MAPI/spiro-OMeTAD/Au devices was that they showed very low hysteresis. This suggests that hysteresis in classic *p-i-n* perovskite devices could be mainly related to the capacitive effect at the perovskite/electron transporting material interface, rather than being an intrinsic property of the perovskite material itself.[34]

The *EQE* characterisation of these devices (Fig. 7.10b), showed the collection of photons in both Si and MAPI absorption wavelength regions. However, this showed low intensity in the MAPI region. In order to determine the type of junction formed, EBIC measurements were attempted but it was not possible to collect results due to the high sensitivity of MAPI to electron beam irradiation. Therefore, two main cases were analysed by *C-V* measurements to understand which behaviour seemed to give more appropriate results: a) the formation of a one-sided junction (in the Si) and b) the presence of a two-sided junction.

a) The one-sided junction option was proposed since the *EQE* analysis suggested that reduced photon collection was observed in the MAPI absorption region (< 780 nm) which may be mainly caused by parasitic absorption of MAPI. A similar behaviour was seen in the literature in *EQE* spectra performed on sub-cells of perovskite/Si tandem solar cells (where the silicon cell is positioned at the bottom of the tandem device),[12] of which an example is shown in Fig. 7.15. Comparing the behaviour of the Si sub cell (red curve), it can be noted that this is similar to that obtained by the heterostructure devices fabricated in this work, showing main photocurrent between 780 - 1100 nm in the Si absorption region and a tail corresponding to photoabsorption loss by MAPI. The similarity may therefore suggest that the perovskite layer deposited on Si in this work acts to decrease the photon intensity that reached the silicon. By assuming that the junction between *n*-Si and MAPI is one-sided in the *n*-Si, the carrier concentration determined by *C-V* analysis (~$10^{14}$ - $10^{15}$ $cm^{-3}$ depending on the Si resistivity, Table 7.7) corresponds to the Si carrier concentration itself. Therefore, these results support the assumption of a one-sided junction but nevertheless, it is not clear why an increment of the *EQE* (%) in the MAPI region using lower Si resistivities is observed (Fig.10), if this acts as parasitic absorber.

A further proof of the presence of a junction in the Si (rather than in MAPI) is given by the band diagram shown in Fig. 7.12d, where the field is in the *n*-Si. It may be noted that the spike between Si and MAPI's valence bands is an obstacle for the functioning of the device, although this is true only if the electron/hole pair is generated in the Si. For example, if the junction was one-sided in MAPI (Fig. 7.12b and c), the spike would not cause an obstacle since electrons would drift to Si through the conduction band and holes to spiro-OMeTAD through the valence band, forming efficient devices. The spike between the valence bands of Si and MAPI is therefore harmful only if the field is in the Si which may explain why these devices showed poor performances.

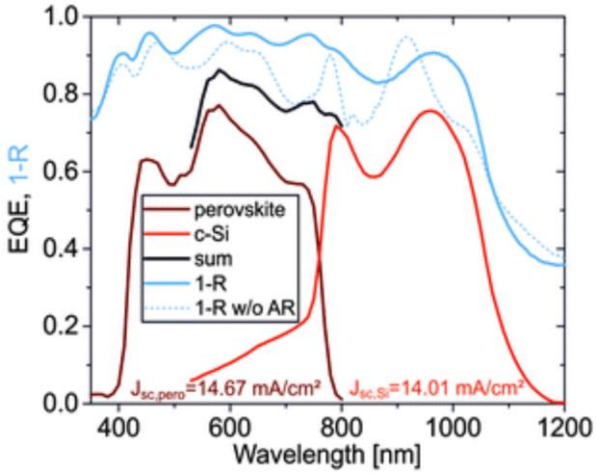


**Fig. 7.15.** Individual sub-cell *EQE* spectra (red and burgundy lines) and sum of spectra (black, and blue with and without antireflective coatings) of a monolithic Si/perovskite tandem device. Graph reproduced with permission from Energy Environ. Sci., ref.[12] (R = reflectance, AR = antireflective coating, LiF).

b) The presence of a two-sided junction was also considered as photon collection was observed in both MAPI and Si regions (*EQE*, Fig. 7.10b). Therefore, it was suggested that the current is collected from two materials, both MAPI *and* Si. The carrier concentration measured by *C-V* analysis showed very similar values compared to the known carrier concentration of Si, and by determining the MAPI carrier concentration attributed to MAPI almost identical values were obtained (~$10^{14}$ - $10^{15}$ $cm^{-3}$). Since in

the literature it is shown that the carrier concentration of MAPI is lower than this ($10^9$ – $10^{14}$ $cm^{-3}$)[29] the results obtained by considering the *n*-Si/MAPI a two-sided junction, may not be reliable. Furthermore, the formation of a spike between *n*-Si and MAPI valence bands may block the natural flow of the charges in presence of the electric field and therefore the Al/*n*-Si/MAPI/spiro-OMeTAD/Au devices containing a two-sided junction may not produce any current.

In conclusion, considering the results obtained by the carrier concentration values the one-sided junction situation (a) seems to be more plausible. In addition the parasitic absorption of MAPI and the presence of the spike between *n*-Si and MAPI valence bands may explain why these devices did not produce high performances. Nevertheless, as devices using the higher doping levels produced higher device efficiencies, it may be speculated that the size of this spike was reduced to minimum by using highly doped *n*-Si wafers (1-5 Ω·cm), in concordance to the band diagram shown in Fig. 7.12b and c.

Regarding the *p*-Si/MAPI devices, the electron transporting material used to block the shunting was ZnO, which represented a poor choice for this device architecture for two main reasons. First, as shown by the band offsets (Fig. 7.14b), ZnO formed a spike with MAPI's conduction band which is strictly dependent to the doping of ZnO. Smaller spikes may be formed using higher doping levels of ZnO, but too high doping levels may produce cliffs, which can also be disadvantageous if their size is large. Hence the exact level of the doping concentration of ZnO should be studied in order to create favourable band alignments. Another electron transporting material that could have been used is $TiO_2$, as it was shown in chapter 5 and 6 that it forms an advantageous band alignment with MAPI. However, the deposition of $TiO_2$ by spin-coating would require solvents which act to destroy the MAPI underneath (as this is a substrate architecture), whereas $TiO_2$ deposition by RF

sputtering requires elevated temperatures (~400°C) which would degrade the MAPI as this is thermally unstable at $T$ > 100°C. Therefore, ZnO seemed the best choice, as it could be sputtered at room temperature. Nevertheless, it is possible that the plasma generated in the sputtering kit was harmful to MAPI, and this could have also contributed to the low performance of the Au/*p*-Si/MAPI/ZnO/AZO devices. Further studies are required in order to identify if *p*-Si/MAPI heterojunctions may form working devices and to determine whether these heterojunctions are one-sided or two-sided.

## 7.5. Conclusions

This chapter presents a work on the fabrication and characterisation of silicon/MAPI heterojunctions, a new device structure that was never studied before. This work was a fundamental study with the goal of understanding if these heterojunctions may be used as solar cell devices in the future. Evolutionary steps in the device fabrication showed that the device architecture that produced the highest device performances was the Al/*n*-Si/MAPI/spiro-OMeTAD/Au device, where by using a crystalline Si wafer having resistivity of 1-5 Ω·cm devices reached a champion device efficiency of 2.08% ($V_{OC}$ = 0.46 V, $J_{SC}$ = 11.77 mA/cm$^2$, $FF$ = 38.4%). The formation of a junction was confirmed by *EQE* measurements and it is suggested that *n*-Si and MAPI form a one-sided junction in the silicon. Although the *EQE* analysis suggests that MAPI acts as a parasitic absorber, its presence is needed to overcome the efficiency produced by the simple Al/*n*-Si/Au devices, which produced a *PCE* of 1.2%, and thus MAPI contributes to the device efficiency. The formation of a one-single junction was proven by *C*-*V* analysis, from which the carrier concentration was determined, this being almost identical to that of Si (~$10^{14}$ - $10^{15}$ cm$^{-3}$). The *C*-*V* characterisation also allowed the determination of the built in voltages of these

heterojunctions, these being in the range of 0.65 – 0.70 V, revealing that the value of the built in voltage is not strongly dependent on the resistivity of the Si used. The effect of using *n*-Si wafers with different doping levels was mainly observed in the *PCE*, showing that higher efficiencies were obtained with higher doping levels of *n*-Si, which was attributed to a decreased size of the spike in the bands between *n*-Si and MAPI.

The formation of a junction was investigated also by using *p*-doped Si with MAPI. Au/*p*-Si/MAPI/ZnO/AZO devices were fabricated and showed rectification and photoactivity under AM1.5. However, the device performance obtained was extremely low (*PCE* = 0.02%, $V_{OC}$ = 0.35 V, $J_{SC}$ = 0.40 mA/cm$^2$, *FF* = 19.9%), although it is not clear if the reason for this is due to the weak junction between *p*-Si and MAPI or the poor choice of the electron transporting material and/or its deposition technique.

Future work should be focused on the study of *p*-Si/MAPI heterojunctions by finding an optimal electron transporting material which a) can be easily deposited onto MAPI, b) does not cause shunting issues and c) produces favourable band alignments with MAPI.

## 7.6. References


(1) Saga, T. Advances in Crystalline Silicon Solar Cell Technology for Industrial Mass Production. *NPG Asia Mater.* **2010**, *2* (3), 96–102.

(2) Shah, A. V.; Schade, H.; Vanecek, M.; Meier, J.; Vallat-Sauvain, E.; Wyrsch, N.; Kroll, U.; Droz, C.; Bailat, J. Thin-Film Silicon Solar Cell Technology. *Prog. Photovoltaics Res. Appl.* **2004**, *12* (23), 113–142.

(3) Louwen, A.; van Sark, W.; Schropp, R.; Faaij, A. A Cost Roadmap for Silicon Heterojunction Solar Cells. *Sol. Energy Mater. Sol. Cells* **2016**, *147*, 295–314.

(4) Reichelstein, S.; Yorston, M. The Prospects for Cost Competitive Solar PV Power. *Energy Policy* **2013**, *55*, 117–127.

(5) Lewis, N. S. Toward Cost-Effective Solar Energy Use. *Science* **2007**, *315* (5813), 798–801.

(6) Chen, T.-G.; Huang, B.-Y.; Chen, E.-C.; Yu, P.; Meng, H.-F. Micro-Textured Conductive Polymer/Silicon Heterojunction Photovoltaic Devices with High

Efficiency. *Appl. Phys. Lett.* **2012**, *101* (3), 033301–033307.

(7) Zhang, F.; Sun, B.; Song, T.; Zhu, X.; Lee, S. Air Stable, Efficient Hybrid Photovoltaic Devices Based on Poly(3-Hexylthiophene) and Silicon Nanostructures. *Chem. Mater.* **2011**, *23* (8), 2084–2090.

(8) Shiu, S.-C.; Chao, J.-J.; Hung, S.-C.; Yeh, C.-L.; Lin, C.-F. Morphology Dependence of Silicon Nanowire/Poly(3,4-Ethylenedioxythiophene):Poly(Styrenesulfonate) Heterojunction Solar Cells. *Chem. Mater.* **2010**, *22* (10), 3108–3113.

(9) Nagamatsu, K. A.; Avasthi, S.; Jhaveri, J.; Sturm, J. C. A 12% Efficient Silicon/PEDOT:PSS Heterojunction Solar Cell Fabricated at < 100°C. *IEEE J. Photovoltaics* **2014**, *4* (1), 260–264.

(10) Werner, J.; Niesen, B.; Ballif, C. Perovskite/Silicon Tandem Solar Cells: Marriage of Convenience or True Love Story? – An Overview. *Adv. Mater. Interfaces* **2018**, *5* (1), 1700731–1700750.

(11) Bush, K. A.; Palmstrom, A. F.; Yu, Z. J.; Boccard, M.; Cheacharoen, R.; Mailoa, J. P.; McMeekin, D. P.; Hoye, R. L. Z.; Bailie, C. D.; Leijtens, T.; Peters, I. M.; Minichetti, M. C.; Rolston, N.; Prasanna, R.; Sofia, S.; Harwood, D.; Ma, W.; Moghadam, F.; Snaith, H. J.; Buonassisi, T.; Holman, Z. C.; Bent, S. F.; McGehee, M. D. 23.6%-Efficient Monolithic Perovskite/Silicon Tandem Solar Cells with Improved Stability. *Nat. Energy* **2017**, *2* (4), 17009–17016.

(12) Albrecht, S.; Saliba, M.; Correa Baena, J. P.; Lang, F.; Kegelmann, L.; Mews, M.; Steier, L.; Abate, A.; Rappich, J.; Korte, L.; Schlatmann, R.; Nazeeruddin, M. K.; Hagfeldt, A.; Grätzel, M.; Rech, B. Monolithic Perovskite/Silicon-Heterojunction Tandem Solar Cells Processed at Low Temperature. *Energy Environ. Sci.* **2016**, *9* (1), 81–88.

(13) Löper, P.; Moon, S.-J.; Martín de Nicolas, S.; Niesen, B.; Ledinsky, M.; Nicolay, S.; Bailat, J.; Yum, J.-H.; De Wolf, S.; Ballif, C. Organic–inorganic Halide Perovskite/Crystalline Silicon Four-Terminal Tandem Solar Cells. *Phys. Chem. Chem. Phys.* **2015**, *17* (3), 1619–1629.

(14) Mailoa, J. P.; Bailie, C. D.; Johlin, E. C.; Hoke, E. T.; Akey, A. J.; Nguyen, W. H.; McGehee, M. D.; Buonassisi, T. A 2-Terminal Perovskite/Silicon Multijunction Solar Cell Enabled by a Silicon Tunnel Junction. *Appl. Phys. Lett.* **2015**, *106* (12), 121105–1201110.

(15) Chen, B.; Bai, Y.; Yu, Z.; Li, T.; Zheng, X.; Dong, Q.; Shen, L.; Boccard, M.; Gruverman, A.; Holman, Z.; Huang, J. Efficient Semitransparent Perovskite Solar Cells for 23.0%-Efficiency Perovskite/Silicon Four-Terminal Tandem Cells. *Adv. Energy Mater.* **2016**, *6* (19), 1601128–1601135.

(16) Duong, T.; Wu, Y.; Shen, H.; Peng, J.; Fu, X.; Jacobs, D.; Wang, E.-C.; Kho, T. C.; Fong, K. C.; Stocks, M.; Franklin, E.; Blakers, A.; Zin, N.; McIntosh, K.; Li, W.; Cheng, Y.-B.; White, T. P.; Weber, K.; Catchpole, K. Rubidium Multication Perovskite with Optimized Bandgap for Perovskite-Silicon Tandem with over 26% Efficiency. *Adv. Energy Mater.* **2017**, *7* (14), 1700228–1700239.

(17) Silicon Wafer Products & Si Wafer Distribution Services - WaferNet, Inc. http://www.wafernet.com/calculator.asp (accessed Aug 1, 2018).

(18) Schulz, P.; Edri, E.; Kirmayer, S.; Hodes, G.; Cahen, D.; Kahn, A. Interface Energetics in Organo-Metal Halide Perovskite-Based Photovoltaic Cells. *Energy Environ. Sci.* **2014**, *7* (4), 1377–1381.

(19) Schölin, R.; Karlsson, M. H.; Eriksson, S. K.; Siegbahn, H.; Johansson, E. M. J.; Rensmo, H. Energy Level Shifts in Spiro-OMeTAD Molecular Thin Films When Adding Li-TFSI. *J. Phys. Chem. C* **2012**, *116* (50), 26300–26305.

(20) Northrop, D. C.; Puddy, D. C. Ohmic Contacts between Evaporated Aluminium and N-Type Silicon. *Nucl. Instruments Methods* **1971**, *94* (3), 557–559.

(21) Behrouznejad, F.; Shahbazi, S.; Taghavinia, N.; Wu, H.-P.; Wei-Guang Diau, E. A Study on Utilizing Different Metals as the Back Contact of $CH_3NH_3PbI_3$ Perovskite Solar Cells. *J. Mater. Chem. A* **2016**, *4* (35), 13488–13498.

(22) Cheragizade, M.; Yousefi, R.; Jamali-Sheini, F.; Mahmoudian, M. R.; Sáaedi, A.; Ming Huang, N. Synthesis and Characterization of PbS Mesostructures as an IR Detector Grown by Hydrogen-Assisted Thermal Evaporation. *Mater. Sci. Semicond. Process.* **2014**, *26*, 704–709.

(23) Lewis, B. G.; Paine, D. C. Applications and Processing of Transparent Conducting Oxides. *MRS Bull.* **2000**, *25* (8), 22–27.

(24) Elumalai, N. K.; Mahmud, M. A.; Wang, D.; Uddin, A. Perovskite Solar Cells: Progress and Advancements. *Energies* **2016**, *9* (11), 861–881.

(25) Haddara, Y. M.; Ashburn, P.; Bagnall, D. M. Silicon-Germanium: Properties, Growth and Applications. In *Springer Handbook of Electronic and Photonic Materials*; Springer International Publishing: Cham, 2017.

(26) Haddara, Y. M.; Ashburn, P.; Bagnall, D. M. Silicon-Germanium: Properties, Growth and Applications. In *Springer Handbook of Electronic and Photonic Materials*; Springer International Publishing: Cham, 2017.

(27) Blood, P.; Orton, J. W. *The Electrical Characterization of Semiconductors:Majority Carriers and Eletron States*; Academic Press, 1992.

(28) Dunlap, W. C.; Watters, R. L. Direct Measurement of the Dielectric Constants of Silicon and Germanium. *Phys. Rev.* **1953**, *92* (6), 1396–1397.

(29) Walsh, A.; Scanlon, D. O.; Chen, S.; Gong, X. G.; Wei, S. H. Self-Regulation Mechanism for Charged Point Defects in Hybrid Halide Perovskites. *Angew. Chemie - Int. Ed.* **2015**, *54* (6), 1791–1794.

(30) Wilson, S. S.; Bosco, J. P.; Tolstova, Y.; Scanlon, D. O.; Watson, G. W.; Atwater, H. A. Interface Stoichiometry Control to Improve Device Voltage and Modify Band Alignment in ZnO/$Cu_2O$ Heterojunction Solar Cells. *Energy Environ. Sci.* **2014**, *7* (11), 3606–3610.

(31) Koishiyev, G. T.; Sites, J. R. Effect of Weak Diodes on the Performance of CdTe Thin-Film Modules. In *2009 34th IEEE Photovoltaic Specialists Conference (PVSC)*; IEEE, 2009; pp 001978–001981.

(32) Major, J. D.; Phillips, L. J.; Al Turkestani, M.; Bowen, L.; Whittles, T. J.; Dhanak, V. R.; Durose, K. P3HT as a Pinhole Blocking Back Contact for CdTe Thin Film Solar Cells. *Sol. Energy Mater. Sol. Cells* **2017**, *172*, 1–10.

(33) Sahu, D. R.; Lin, S.-Y.; Huang, J.-L. ZnO/Ag/ZnO Multilayer Films for the Application of a Very Low Resistance Transparent Electrode. *Appl. Surf. Sci.* **2006**, *252* (20), 7509–7514.

(34) Chen, B.; Yang, M.; Priya, S.; Zhu, K. Origin of J – V Hysteresis in Perovskite Solar Cells. *J. Phys. Chem. Lett.* **2016**, *7* (5), 905–917.

# 8. Discussion

In this thesis, the perovskite materials MAPI and $CsPbI_2Br$ were studied to determine their properties and to develop photovoltaic devices from them.

The perovskite thin films were deposited by spin-coating precursor solutions. In particular, MAPI thin films were prepared with two spin-coating techniques, these being a one-step solution process and a two-step interdiffusion process. The one-step process uses a single solution that forms MAPI upon annealing immediately after the spinning. On the contrary, the two-step process involves the spinning of two different precursor solutions to form methylammonium iodide and lead iodide which form MAPI when they combine. Both procedures formed MAPI thin films having similar band gaps (1.57 eV and 1.61 eV for the one-step and the two-step processes respectively) with intrinsic doping, having the expected tetragonal structure at room temperature and high absorption coefficients ($\sim 10^5$ $cm^{-1}$ in the visible region). The main difference observed between the two deposition techniques was the uniformity of the films and the crystal size. While the one-step process produced large crystals (~500 nm Ø) and numerous pin-holes, the two-step process showed smaller crystals (~100 nm Ø) but higher uniformity. This difference is likely to reflect the fundamental

difference between the two film formation mechanisms – in the case of one-step growth the film forms directly by crystallisation from the solvent whereas in the two-step process the two component iodides must diffuse together in order to form the film.

However, the quality of the one-step processed films was significantly improved by using toluene as an anti-solvent. It was observed that with the toluene treatment the size of the crystals decreased from ~500 to ~100 nm Ø and formed highly uniform films. The reason for this is likely to be that MAPI is insoluble or at least less soluble in toluene than in DMF. Hence as toluene is added it displaces the DMF and hence the MAPI increases in concentration in each remaining solvent droplet. In this way the supersaturation necessary for the nucleation of crystal formation is encouraged. Since the grain size is smaller it may be inferred that the density of nucleation sites is increased. Moreover, this high density of nucleation points generates more uniform coverage and highly compact films without pinholes. Overall, although the grain size is reduced, the coverage is improved which on balance might be expected to be beneficial for photovoltaic devices.

These MAPI films were subsequently used for the fabrication of devices using the *n-i-p* structure most widely reported in the literature, *i.e.* glass/ITO/$TiO_2$/MAPI/spiro-OMeTAD/Au. With this configuration the champion devices made in this work showed 9.36% *PCE* ($V_{OC}$ = 0.92 V, $J_{SC}$ = 20.23 mA/cm$^2$, *FF* = 50.3%) and 8.45% *PCE* ($V_{OC}$ = 0.98 V, $J_{SC}$ = 16.57 mA/cm$^2$, *FF* = 52.1%), for the one-step process (with anti-solvent treatment) and the two-step process respectively. Therefore, similar device performances were achieved by using the two deposition techniques. Nevertheless, the two sets of devices aged differently. In particular, for the two-step material only, an increase in the efficiency of the devices was recorded by ageing the devices for 24 hours in a desiccator (RH < 15%, ambient light). This reached a maximum of 11.8% *PCE* ($V_{OC}$ = 1 V, $J_{SC}$ = 20.87 mA/cm$^2$, *FF* = 56.5%). Although the exact cause of this was not investigated, it is suggested that this

improvement of *PCE* was due to the time spent in the environmental conditions of the desiccator. For example, beneficial oxidation processes may have been involved in the spiro-OMeTAD, increasing the conductivity of the hole transporting material. Overall though, the efficiencies of the MAPI devices presented in this work were lower than the record for MAPI devices presented at the time of this study (2015), which had reached a maximum of ~18% *PCE*.[1] By this time there were already dozens of laboratories working on perovskite PV and the difference between the value obtained in this work and the 2015 record probably reflects the relative levels of effort expended on device development, which may be related to the differences in materials quality arising from details of the solution processing in the preparation of the MAPI and the electron and hole transporting materials which might also have been optimised empirically in this work. While the effects of such optimisation are generally difficult to specify, it is possible to be specific in occasional cases. For example, in the case of the two-step MAPI, the reduced efficiency may be related specifically to the presence of unreacted $PbI_2$ precursor. Therefore optimisation of the concentration of the precursor solutions may improve the device performance.[5] At the time of writing this thesis perovskite solar cells achieved up to ~22%,[2–4] however it should be considered that these highly efficient devices did not use MAPI, but rather mixed cation/halide compounds and therefore it is not possible to make a direct comparison.

The fully inorganic perovskite $CsPbI_2Br$ was deposited by spin-coating using a one-step process only. The annealing temperature was optimised, and achieved the highest crystallinity when the layers were heated at 350°C. The material showed an optical band gap of 1.92 eV in agreement with literature values,[6] intrinsic doping properties, a high absorption coefficient (~$10^5$ $cm^{-1}$) and a dark cubic phase. The films comprised crystals up to 2 μm Ø, with few pin-holes visible on the surface. Although the relatively large band gap of these material makes them more useful in tandem solar cells, single junction devices were

fabricated using the same architecture adopted for MAPI, *i.e.* glass/ITO/$TiO_2$/$CsPbI_2Br$/spiro-OMeTAD/Au. With this configuration devices produced an efficiency of 9.1% ($V_{OC}$ = 1.05 V, $J_{SC}$ = 12.68 mA/cm$^2$ and *FF* = 60.2%), which, at the time this work was performed, was comparable to the world record device made from this material, reported by Sutton *et al*. in 2016 (9.8%).[6] Subsequently, however, a new record of 14.78% *PCE* was achieved by Yin *et al.* in 2018.[7]

The devices made from both MAPI and $CsPbI_2Br$ all showed hysteresis. This was measured as giving 2 percentage points in *PCE* difference between forward and reverse scans for $CsPbI_2Br$ devices, and 4.20 and 1.65 percentage point differences for the one- and two-step MAPI devices respectively. This is a severe level of hysteresis, but comparable to that reported by other workers for perovskite solar cells.[8] There are many reports of hysteresis and it has been linked to many factors, including the choice of solar cell structure and materials, the preparation conditions of the materials, the film thicknesses, and the scan rate used during the measurement.[8] Physical processes such as ion migration and charge accumulation have been invoked. It has been shown that by using different hole and electron transporting materials the hysteresis may be decreased. For example, by employing the *p-i-n* device architecture (rather than *n-i-p* structures) the hysteresis effect can be drastically decreased.[9] The reason for this is that in the *p-i-n* structure the materials used as hole and electron transporting materials at the heterointerfaces with MAPI confer benefits. For example, PCBM, commonly used as electron transporter, becomes doped by MAPI from the interface and therefore its conductivity is increased. This has the effect of eliminating charge accumulation resulting from ion migration. In addition, by using fullerene ($C_{60}$, used as interfacial selective electron transporter material in *p-i-n* devices) it is believed that trap states are passivated, either by blocking the ion migration phenomenon or simply by extracting the electrons more efficiently due to its high conductivity.[10]

Further comparison between MAPI and $CsPbI_2Br$ devices arises from considering the influence of the thickness of the electron transporting material on the device performance. It was observed that both one-step process MAPI and $CsPbI_2Br$ (which is also a one-step process) yielded higher device performances when only 50 nm of $TiO_2$ were employed. On the contrary, the two-step process MAPI devices showed higher efficiency using thicker $TiO_2$ layers (~100 nm). The principal difference between one- and two-step films is that the latter requires interdiffusion of methylammonium iodide with lead iodide to form the films, whereas one-step processing does not. Hence it is possible that the two-step films contain unreacted lead iodide and that this somehow requires thicker $TiO_2$ in order to achieve the best device performance. Therefore it may be suggested that while thinner $TiO_2$ layers act to generally positively affect the performances of the solar cells, the $PbI_2$ residues present in the MAPI prepared with the two-step process may adversely influence the performance. For example, it was seen that devices using MAPI with high levels of impurities of $PbI_2$, show poorer electron injection.[5] Since the 100 nm $TiO_2$ layer comprises two differently $TiO_2$ layers (with the most concentrated being at the interface with MAPI), the resulting materials profile may improve the electric drift toward the contact balancing the poorer electron injection from MAPI toward $TiO_2$, caused by the unreacted $PbI_2$. On the contrary the benefits of thin $TiO_2$ (in one-step processed devices) may have an explanation in the minimisation of optical absorption in the $TiO_2$ or else the minimisation of series resistance loss.

Chapters 5 and 6 presented studies of the stability of the perovskite materials. Initial studies of MAPI showed that films prepared using a two-step process produced more stable layers compared to those prepared with the one-step process, but nevertheless the triggering factors for degradation were identical for both, and were UV in combination with oxygen. The reason why the two-step processed MAPI showed higher stability, may be related to its

highly compact films which may have protected against the infiltration of oxygen into the films through voids and grain boundaries. Yet more importantly, significant differences were observed between the stabilities of MAPI and $CsPbI_2Br$ films – which has a consequence for devices. Although MAPI and $CsPbI_2Br$ are both perovskite materials, their stabilities differ. Their main aspects are compared in Table 8.1 which shows the degradation conditions used on the perovskite layers and their main effects on both MAPI and $CsPbI_2Br$.

| **Degradation conditions:** | **MAPI** | **$CsPbI_2Br$** |
|---|---|---|
| **"UV/$O_3$"** | The structure completely changes in only 19 minutes. | After 54 minutes no changes were detected. |
| **"UV/$N_2$"** | UV exposure changes the structure. | UV exposure produces only small changes to the structure. |
| **"Dark/air"** | Oxygen or humidity alone do not affect the structure. | Humidity produces changes immediately. |
| **"Desiccator"** | Ambient light and oxygen combined produce changes in the structure. | No changes are produced by oxygen or ambient light. |

**Table 8.1.** Degradation conditions and their effect on MAPI and $CsPbI_2Br$, after one month exposure (except for UV/$O_3$ which lasted for 19 minutes and 54 minutes for MAPI and $CsPbI_2Br$ respectively).

Overall, Table 8.1 shows that in this study MAPI degradation was observed in films exposed to UV light and oxygen together, while in the case of $CsPbI_2Br$ degradation occurred in presence of water vapour. For MAPI, the findings for UV and oxygen are confirmed in the literature, but there are additional reports published that also implicate water vapour as a degrading factor.[11,12] In this work maximum humidity values used were in the range of 40 - 60% RH, which is relatively low. Hence it is possible that this phenomenon was not observed here due to the choice of low-humidity environments. This could imply that there is a minimum threshold for water vapour to make a contribution to degradation.

Nevertheless it is important to mention that the mechanism of degradation of $CsPbI_2Br$ with water is intrinsically different from that of MAPI. In the case of MAPI, both UV/oxygen and water degradation affect the chemical composition, transforming the MAPI irreversibly into its precursors ($PbI_2$, MAI) and other by-products ($CH_3NH_2$, $I_2$, HI, $H_2O$).[13] On the contrary, for $CsPbI_2Br$ the water acts by changing the crystalline structure from a cubic to a yellow orthorhombic phase, but there is no chemical reaction with water. Instead water triggers a phase transition. The advantage of being only a phase transition (and not a chemical transformation) is that this process is reversible. The effectiveness of the $CsPbI_2Br$ recovery was demonstrated on thin films and on devices: by exposing the orthorhombic phase to heat, the cubic structure was re-established and in the case of devices these regained up to 115% of their original efficiency. At room temperature the stable phase of $CsPbI_2Br$ is orthorhombic (a wide gap yellow phase) while the dark cubic phase of $CsPbI_2Br$ that is useful for PV is only metastable at room temperature. Water triggers the metastable dark cubic phase to transform to the room temperature stable yellow phase, while heating to above the transition temperature recovers the brown phase. A similar metastable behaviour was observed also for $CsPbI_3$ (pure iodine compound),[14] but this was not found to be caused by water vapour.

Since, contrarily to the case for MAPI, UV and low humidity air do not harm $CsPbI_2Br$, it may be suggested that $CsPbI_2Br$ is more resistant to illumination and hence more suitable for the fabrication of solar cells – providing of course that adequate encapsulation is employed to protect against water vapour. Overall, stability is a significant issue for both hybrid and all-inorganic materials for use in photovoltaics. The requirements for stability are very stringent since the design life of solar photovoltaic modules for use in all outdoor environments is 25 – 30 years.

The perovskite materials explored in this thesis were also used for the fabrication of heterostructures with silicon, with the intent of fabricating a new solar cell device. However, the rapid phase transition of $CsPbI_2Br$ in highly humid air made trials with this impractical. Therefore, MAPI was preferred, and in particular the one-step process was favoured because for its ease of deposition onto silicon. Both *n*-doped and *p*-doped silicon wafers were used, and MAPI was directly deposited onto the silicon surface. Since these MAPI films contained numerous pin-holes, "pin-hole blockers" were used to avoid shunting, these being spiro-OMeTAD and ZnO for *n*-Si/MAPI and *p*-Si/MAPI devices respectively, forming the following devices: Al/*n*-Si/MAPI/spiro-OMeTAD/Au and Au/*p*-Si/MAPI/ZnO/AZO devices.

Al/*n*-Si/MAPI/spiro-OMeTAD/Au devices showed rectification and photoactivity under illumination: by using highly doped silicon (1-5 Ω·cm) devices achieved a hysteresis-free champion *PCE* of 2.1% % ($V_{OC}$ = 0.46 V, $J_{SC}$ = 11.77 mA/cm$^2$, *FF* = 38.4%). The negligible hysteresis of these devices may be due to the absence of the $TiO_2$ transporting material, suggesting that $TiO_2$ may make a significant contribution to the mechanism of hysteresis in *n-i-p* perovskite devices. By analysing the *n*-Si/MAPI junction it was determined that a one-sided junction was formed, this being in the silicon, and that MAPI performed only as a parasitic light absorber rather than a positive contributor to photocurrent. This assumption was made since the *EQE* analysis showed photon collection in the silicon and only very little in the MAPI absorption regions. The reason why a single junction is formed, is related to the carrier concentration of the two materials involved in the junction. If the materials (*i.e.* MAPI and *n*-silicon) show a difference in the carrier concentration of at least two orders of magnitude, then the junction is one-sided. Considering that in the champion devices the carrier concentration of the silicon was of $10^{15}$ cm$^{-3}$ (1-5 Ω·cm), the carrier concentration of the MAPI must be $\leq 10^{13}$ cm$^{-3}$ or $\geq 10^{17}$ cm$^{-3}$. Since in

the literature the carrier concentration of MAPI is shown to be in the range $10^9$ - $10^{14}$ $cm^{-3}$,[15,16] the first option ($\leq 10^{13}$ $cm^{-3}$) would seem more plausible, however since one-sided junctions are typically located in the less conductive side, it is implied that the MAPI having higher carrier concentration ($\geq 10^{17}$ $cm^{-3}$) is a more realistic possibility. Although this situation may seems to disagree with the carrier concentration of MAPI presented in the literature,[15,16] researchers have shown that MAPI's carrier concentration strictly depends on the solution and film preparation, indicating that a high carrier concentration ($\geq 10^{14}$ $cm^{-3}$) may exist.[17]

In order to form a two-sided junction the carrier concentration of MAPI and/or silicon would require to be of similar values (*i.e.* less than two orders of magnitude difference).[18] For instance, considering the carrier concentration of the silicon being still $10^{15}$ $cm^{-3}$, by using MAPI with carrier concentration between $10^{13}$ $cm^{-3}$ and $10^{15}$ $cm^{-3}$ a two-sided junction should form: absorption and hole/electron collection would derive from both materials, and maybe improve the device performance.

Structures on *p*-silicon were also investigated. Au/*p*-Si/MAPI/ZnO/AZO devices showed rectification, revealing that a junction between *p*-Si and MAPI is formed, but no photoactivity was recorded. The study of the junction requires more work to determine if the absent photoactivity is due to the *p*-Si/MAPI junction itself or due to a poor choice of the electron transporting material: both band alignment and deposition methods do not favour the ZnO combination with MAPI. For example, an organic electron transporting material such as PCBM may be used, since it has shown to be electrically compatible with MAPI and because its deposition may be performed on MAPI's surface.[19]

## 8.1. References


(1) Wu, C. G.; Chiang, C. H.; Tseng, Z. L.; Nazeeruddin, M. K.; Hagfeldt, A.; Grätzel, M. High Efficiency Stable Inverted Perovskite Solar Cells without Current Hysteresis. *Energy Environ. Sci.* **2015**, *8* (9), 2725–2733.

(2) NREL efficiency chart 2018 https://www.nrel.gov/pv/assets/images/efficiency-chart.png (accessed Jul 5, 2018).

(3) Bi, D.; Yi, C.; Luo, J.; Décoppet, J.-D.; Zhang, F.; Zakeeruddin, S. M.; Li, X.; Hagfeldt, A.; Grätzel, M. Polymer-Templated Nucleation and Crystal Growth of Perovskite Films for Solar Cells with Efficiency Greater than 21%. *Nat. Energy* **2016**, *1* (10), 16142–16147.

(4) Yang, W. S.; Park, B. W.; Jung, E. H.; Jeon, N. J.; Kim, Y. C.; Lee, D. U.; Shin, S. S.; Seo, J.; Kim, E. K.; Noh, J. H.; Seok, S. Il. Iodide Management in Formamidinium-Lead-Halide-Based Perovskite Layers for Efficient Solar Cells. *Science.* **2017**, *356* (6345), 1376–1379.

(5) Bi, D.; El-Zohry, A. M.; Hagfeldt, A.; Boschloo, G. Unraveling the Effect of $PbI_2$ Concentration on Charge Recombination Kinetics in Perovskite Solar Cells. *ACS Photonics* **2015**, *2* (5), 589–594.

(6) Sutton, R. J.; Eperon, G. E.; Miranda, L.; Parrott, E. S.; Kamino, B. A.; Patel, J. B.; Hörantner, M. T.; Johnston, M. B.; Haghighirad, A. A.; Moore, D. T.; Snaith, H. J. Bandgap-Tunable Cesium Lead Halide Perovskites with High Thermal Stability for Efficient Solar Cells. *Adv. Energy Mater.* **2016**, *6*, 150258–150464.

(7) Yin, G.; Zhao, H.; Jiang, H.; Yuan, S.; Niu, T.; Zhao, K.; Liu, Z.; Liu, S. F. Precursor Engineering for All-Inorganic $CsPbI_2Br$ Perovskite Solar Cells with 14.78% Efficiency. *Adv. Funct. Mater.* **2018**, 1803269–1803279.

(8) Snaith, H. J.; Abate, A.; Ball, J. M.; Eperon, G. E.; Leijtens, T.; Noel, N. K.; Stranks, S. D.; Wang, J. T. W.; Wojciechowski, K.; Zhang, W. Anomalous Hysteresis in Perovskite Solar Cells. *J. Phys. Chem. Lett.* **2014**, *5* (9), 1511–1515.

(9) Bryant, D.; Wheeler, S.; O'Regan, B. C.; Watson, T.; Barnes, P. R. F.; Worsley, D.; Durrant, J. Observable Hysteresis at Low Temperature in "Hysteresis Free" Organic-Inorganic Lead Halide Perovskite Solar Cells. *J. Phys. Chem. Lett.* **2015**, *6* (16), 3190–3194.

(10) Bai, Y.; Meng, X.; Yang, S. Interface Engineering for Highly Efficient and Stable Planar P-i-n Perovskite Solar Cells. *Adv. Energy Mater.* **2018**, *8* (5), 1701883–1701901.

(11) Yang, J.; Siempelkamp, B. D.; Liu, D.; Kelly, T. L. Investigation of $CH_3NH_3PbI_3$ Degradation Rates and Mechanisms in Controlled Humidity Environments Using in Situ Techniques. *ACS Nano* **2015**, *9* (2), 1955–1963.

(12) Leguy, A. M. A.; Hu, Y.; Campoy-Quiles, M.; Alonso, M. I.; Weber, O. J.;

Azarhoosh, P.; van Schilfgaarde, M.; Weller, M. T.; Bein, T.; Nelson, J.; Docampo, P.; Barnes, P. R. F. Reversible Hydration of $CH_3NH_3PbI_3$ in Films, Single Crystals, and Solar Cells. *Chem. Mater.* **2015**, *27* (9), 3397–3407.

(13) Niu, G.; Guo, X.; Wang, L. Review of Recent Progress in Chemical Stability of Perovskite Solar Cells. *J. Mater. Chem. A* **2015**, *3* (17), 8970–8980.

(14) Eperon, G. E.; Paternò, G. M.; Sutton, R. J.; Zampetti, A.; Haghighirad, A. A.; Cacialli, F.; Snaith, H. J. Inorganic Caesium Lead Iodide Perovskite Solar Cells. *J. Mater. Chem. A* **2015**, *3* (39), 19688–19695.

(15) Walsh, A.; Scanlon, D. O.; Chen, S.; Gong, X. G.; Wei, S. H. Self-Regulation Mechanism for Charged Point Defects in Hybrid Halide Perovskites. *Angew. Chemie - Int. Ed.* **2015**, *54* (6), 1791–1794.

(16) Zohar, A.; Levine, I.; Gupta, S.; Davidson, O.; Azulay, D.; Millo, O.; Balberg, I.; Hodes, G.; Cahen, D. What Is the Mechanism of $MAPbI_3$ p-Doping by $I_2$? Insights from Optoelectronic Properties. *ACS Energy Lett.* **2017**, *2* (10), 2408–2414.

(17) Wang, Q.; Shao, Y.; Xie, H.; Lyu, L.; Liu, X.; Gao, Y.; Huang, J. Qualifying Composition Dependent p and n Self-Doping in $CH_3NH_3PbI_3$. *Appl. Phys. Lett.* **2014**, *105* (16), 163508–163516.

(18) Blood, P.; Orton, J. W. *The Electrical Characterization of Semiconductors:Majority Carriers and Eletron States*; Academic Press, 1992.

(19) Docampo, P.; Ball, J. M.; Darwich, M.; Eperon, G. E.; Snaith, H. J. Efficient Organometal Trihalide Perovskite Planar-Heterojunction Solar Cells on Flexible Polymer Substrates. *Nat. Commun.* **2013**, *4*, 2761.

# 9. Conclusion and future work

In this thesis, hybrid and inorganic plumbo halide MAPI and $CsPbI_2Br$ perovskites were studied. Their films were prepared, evaluated for stability and then used for the fabrication of perovskite solar cell devices, using the most common *n-i-p* device architecture known in literature and a new device heterojunction with silicon.

In chapter 5, MAPI thin films deposited with a one-step and a two-step solution process were utilised for the film characterisation, stability tests and then further employed for the fabrication of solar cells. While both deposition methods produced MAPI thin films with properties agreeing to those presented in the literature, the crystallinity of the films was considerably better in the case of two-step deposition processed MAPI. However, an anti-solvent treatment performed with toluene on the one-step process films was demonstrated to improve the coverage and crystallinity of the films. Nevertheless, these films produced poorly performing devices. Using the glass/ITO/$TiO_2$/MAPI/spiro-OMeTAD/Au device architecture, the highest *PCE* was achieved by the one-step process MAPI films treated with anti-solvent (9.4%). Moreover, the two-step process deposited MAPI device measured after 24 hours of ageing achieved 11.8% *PCE*. However, in the literature numerous reports were published, showing higher device performances using the same device architectures,[1] which

reveal that additional improvement on the perovskite material and deposition should be done.

The stability of the MAPI thin films was also investigated. When this work was ongoing, this was a current and rapidly evolving topic for research. Although unpublished, the results obtained are similar to those presented in the literature. MAPI films were exposed to different degradation conditions for different amounts of time and then analysed. It was found that MAPI was particularly sensitive towards two factors: UV light and oxygen. However, these did not individually affect the MAPI structure, whereas their combination did. In the literature this behaviour was confimred,[2] however it was also shown that MAPI is unstable towards water,[3] a factor that was not revealed in this work. The main reason of this, may be due to the adoption here of degradation factors involving weakly humid environments.

Since MAPI has shown precarious stability toward ambient environments, numerous research groups have been focused on the change in the perovskite with the aim to form a highly stable and efficient material. The fully inorganic $CsPbI_2Br$ compound, for example, has been proposed as an all-inorganic alternative with environmental stability possibly exceeding that of hybrid organic-inorganic perovskites. This was explored in chapter 6. $CsPbI_2Br$ thin films were prepared using a solution processing technique and then characterised in order to verify formation of the compound. The material had a band gap of 1.92 eV and the cubic perovskite phase and the films were adopted for the fabrication of *n-i-p* solar cells. Using the structure glass/ITO/$TiO_2$/$CsPbI_2Br$/spiro-OMeTAD/Au, device with champion efficiency of 9.1% were fabricated in this work. Although these presented significant hysteresis, the device performances were comparable to the world record device efficiency (9.8%, Sutton *et al.*).[4] Recent work by other authors however, showed further increases in *PCE* for this material, achieving 14.78%.[5]

A rather important finding in chapter 6, relates to the stability of the $CsPbI_2Br$ thin films and devices. By adopting the same degradation environments used for testing MAPI, the $CsPbI_2Br$ was shown to have great sensitivity towards water vapour. While UV light and oxygen did not produce any significant change in the material's structure, air humidity produced immediate effects in the $CsPbI_2Br$, visibly recognisable by the change in colour of the films changing from brown to yellow. However, these studies showed that water does not chemically interact with $CsPbI_2Br$, but rather it promotes a phase transition (from cubic to orthorhombic). Unlike the case of the chemical degradation of MAPI, this phase transition is reversible. Therefore, both films and devices could be recovered by heating. In particular, the devices could regain up to 115% of their original *PCE*.

Although this material has shown poor stability towards water, easy protection could be applied in practice. For example, effective encapsulation may protect devices form water and permit their functionality for long periods of time. However, the large band gap of $CsPbI_2Br$ makes them more suitable for tandem applications (both silicon/perovskite and perovskite/perovskite tandems). Future work should therefore be aimed at fabricating such tandem devices.

Chapter 7 presented a study on the fabrication of MAPI/silicon heterojunctions. In the literature a vast number of works have been published on the fabrication of tandem solar cells, however no work presented a direct heterojunction between silicon and MAPI. Here, silicon/MAPI devices were fabricated. Since their fabrication was new, most of the effort was given to the optimisation of the device architecture, leading to Al/*n*-Si/MAPI/spiro-OMeTAD/Au and Au/*p*-Si/MAPI/ZnO/AZO devices.

Particular attention was given to the Al/*n*-Si/MAPI/spiro-OMeTAD/Au devices, which achieved a *PCE* of 2.1%. However, by analysing these devices carefully it was discovered that *n*-Si and MAPI formed a one-sided junction in the silicon, where MAPI only

acted as a parasitic absorber and did not contribute to the photocurrent. Hence, additional work should be performed on changing the doping concentration of MAPI and of the silicon in order to form a two-sided junction device and maybe improving the device efficiency.

Regarding the *p*-doped silicon and its device comprising Au/*p*-Si/MAPI/ZnO/AZO, no significant photoactivity was recorded under illumination. However, rectification was observed. Additional work should be carried out in order to identify if the lack of photoactivity was related to the junction *p*-Si/MAPI or the choice of the electron transporting material, ZnO, which was sputtered, a process that could damage the MAPI. For example, other electron transporters may be employed that do not affect the MAPI on which they are deposited. Moreover, interface studies could be used to determine if the transporter creates shunting issues.

## 9.1. References


(1) NREL. Efficiency chart https://www.nrel.gov/pv/assets/images/efficiency-chart.png (accessed Feb 12, 2018).

(2) Aristidou, N.; Eames, C.; Sanchez-Molina, I.; Bu, X.; Kosco, J.; Islam, M. S.; Haque, S. A. Fast Oxygen Diffusion and Iodide Defects Mediate Oxygen-Induced Degradation of Perovskite Solar Cells. *Nat. Commun.* **2017**, *8*, 15218–15227.

(3) Niu, G.; Guo, X.; Wang, L. Review of Recent Progress in Chemical Stability of Perovskite Solar Cells. *J. Mater. Chem. A* **2015**, *3* (17), 8970–8980.

(4) Sutton, R. J.; Eperon, G. E.; Miranda, L.; Parrott, E. S.; Kamino, B. A.; Patel, J. B.; Hörantner, M. T.; Johnston, M. B.; Haghighirad, A. A.; Moore, D. T.; Snaith, H. J. Bandgap-Tunable Cesium Lead Halide Perovskites with High Thermal Stability for Efficient Solar Cells. *Adv. Energy Mater.* **2016**, *6*, 150258–150464.

(5) Yin, G.; Zhao, H.; Jiang, H.; Yuan, S.; Niu, T.; Zhao, K.; Liu, Z.; Liu, S. F. Precursor Engineering for All-Inorganic $CsPbI_2Br$ Perovskite Solar Cells with 14.78% Efficiency. *Adv. Funct. Mater.* **2018**, 1803269–1803279.